



HAL
open science

Reduced Order Models for the Navier-Stokes equations for aeroelasticity

Fabrizio Di Donfrancesco

► **To cite this version:**

Fabrizio Di Donfrancesco. Reduced Order Models for the Navier-Stokes equations for aeroelasticity. Biomechanics [physics.med-ph]. Sorbonne Université, 2019. English. NNT : 2019SORUS603 . tel-02972425v2

HAL Id: tel-02972425

<https://theses.hal.science/tel-02972425v2>

Submitted on 9 Sep 2021

HAL is a multi-disciplinary open access archive for the deposit and dissemination of scientific research documents, whether they are published or not. The documents may come from teaching and research institutions in France or abroad, or from public or private research centers.

L'archive ouverte pluridisciplinaire **HAL**, est destinée au dépôt et à la diffusion de documents scientifiques de niveau recherche, publiés ou non, émanant des établissements d'enseignement et de recherche français ou étrangers, des laboratoires publics ou privés.

THÈSE de DOCTORAT

Opérée au sein de :

Sorbonne Université

Ecole Doctorale 391

Sciences mécaniques, acoustique, électronique et robotique de Paris

Spécialité de doctorat : Mécanique

Soutenue publiquement le 13/12/2019, par :

Fabrizio Di Donfrancesco

**Reduced Order Models for the Navier-Stokes equations
for aeroelasticity**

Devant le jury composé de :

Christophe Airiau

Professeur des Universités, Université Paul Sabatier

Marianna Braza

Directrice de recherche, Institut de Mécanique des Fluides de Toulouse

Jean-Camille Chassaing

Professeur des Universités, Sorbonne Université

Jose-Maria Fullana

Professeur des Universités, Sorbonne Université

Aziz Hamdouni

Professeur des Universités, Université de La Rochelle

Antoine Placzek

Docteur, ONERA

Jean-Christophe Robinet

Professeur des Universités, ENSAM

Rapporteur

Examinatrice

Directeur de thèse

Examineur

Examineur

Éncadrant de thèse

Rapporteur

Contents

Introduction	1
1 State of the art	3
1.1 Stability and accuracy	4
1.2 Dealing with nonlinearities	8
1.3 ROMs in aeroelasticity and fluid-structure interaction	9
1.4 Parametric investigation	12
2 Construction of a projection-based ROM for nonlinear systems	13
2.1 Introduction	13
2.2 From the nonlinear system to the reduced system	14
2.3 Low-rank approximation by Proper Orthogonal Decomposition	16
2.4 Galerkin and Petrov-Galerkin projection	18
2.5 Masked projections	20
2.6 Practical implementation of a nonlinear reduced order model using masked projection	27
2.7 Construction of a reduced order model for periodic flows	28
2.7.1 Time Spectral Method	29
2.7.2 Reduced Order Time Spectral Method	33
2.8 Conclusions	36
3 Construction and implementation of a nonlinear projection-based ROM for the compressible Navier-Stokes equations	37
3.1 Introduction	38
3.2 Formulation of the compressible Navier-Stokes equations	38
3.3 Computation of the POD modes of a flow around a fixed cylinder at low Reynolds number	41
3.3.1 Numerical simulation of the flow around a fixed cylinder at low Reynolds	41
3.3.2 Computation of the POD modes	43
3.4 Numerical integration of the nonlinear projection-based ROM of a flow around a fixed cylinder at low Reynolds	47
3.4.1 Effect of the time-step on the response of the projection-based nonlinear ROM	48
3.4.2 Effect of the POD basis truncation on the response of the projection-based nonlinear ROM	49
3.4.3 Choice of the formulation for the projection-based nonlinear ROM with masked projection	50

3.4.4	Influence of the number of the DEIM interpolation points . . .	54
3.5	Assessment of the performance of the masked projection techniques in fluid dynamics applications	55
3.5.1	Zero incidence transonic flow around a NACA 0012 airfoil at moderate Reynolds number	56
3.5.2	High incidence flow around a NACA 0012 airfoil	62
3.6	Conclusions	67
4	Adaptation of a nonlinear ALE-based reduced order model of the Navier- Stokes equations for aeroelasticity	69
4.1	Introduction	70
4.2	Projection of the Arbitrary Lagrangian-Eulerian formulation of the Navier-Stokes equations	70
4.2.1	Computation of the POD modes of a flow configuration with deforming mesh	72
4.2.2	Nonlinear ROM adaptation for non-autonomous systems . . .	73
4.2.3	Alternative centering of the snapshot collection	73
4.2.4	Practical adaptation of an ALE-based nonlinear reduced order model	75
4.3	Numerical integration of the nonlinear ALE-based ROM of a flow around a cylinder in forced motion at low Reynolds	76
4.3.1	Adaptation of the ALE-based nonlinear ROM for a new pa- rameter configuration	85
4.3.2	Numerical integration of the adapted nonlinear ALE-based ROM for new motion parameters	89
4.3.3	Discussion	96
4.4	Numerical integration of an aeroelastic reduced order system: flow around a cylinder in free motion	97
4.5	Conclusions	104
5	Construction of a Reduced Order Time Spectral Model for the compress- ible ALE-based Navier-Stokes equations	105
5.1	Introduction	105
5.2	Formulation of the ROTSM for the compressible ALE-based Navier- Stokes equations	106
5.3	Numerical integration of the nonlinear ROTSM of a transonic flow around an oscillating airfoil	108
5.3.1	1 harmonic test case	110
5.3.2	3 harmonics test case	112
5.4	Numerical integration of the parametric ROTSM: Mach number vari- ation	114
5.5	Conclusions	123

Contents

Conclusions and perspectives	125
Appendices	131
A Preliminary investigation of a Reduced Order Model for the URANS formulation of the Navier-Stokes equations	133
B Integration of a projection-based ROM for the subsonic Euler equations	137
Bibliography	139

List of Figures

2.1	An example of a masked projection algorithm resulting in a finite volume selection on the computational domain for the flow around a fixed cylinder at $M = 0.2$ and $Re = 100$, where the number of cells is $n \sim 55000$, the number of selected cells (red triangles) is $f = 20$ and the number of selected cells plus the neighbor to complete the stencils (considering, for example, a second-order approximation) is $g = f + 6 \times f$.	22
2.2	A graphical description of the initialization of the ROTSM by projecting onto the POD subspace.	36
3.1	Computational domain for the two-dimensional cylinder configuration.	42
3.2	Instantaneous density field for the flow past a cylinder at $Re = 100$.	42
3.3	Time evolution of the aerodynamic coefficients C_L and C_D of a fixed circular cylinder at $Re = 100$ and $M = 0.2$. Corresponding Strouhal number: $St = 0.164$.	43
3.4	Proper orthogonal eigenvalue spectrum for a flow past a cylinder at $Re = 100$.	44
3.5	First proper orthogonal mode (POM of density) for the flow around a fixed cylinder at $Re = 100$.	44
3.6	Proper orthogonal eigenvalue spectrum for the flow past a cylinder at $Re = 100$ for the snapshot set with subtraction of the time average field.	45
3.7	First to 6 th density proper orthogonal mode (POM) for the flow around a fixed cylinder at $Re = 100$.	45
3.8	The time evolution of the aerodynamic coefficients of a fixed circular cylinder at $Re = 100$ and $m = 0.2$.	46
3.9	Evolution of the aerodynamic coefficients for the nonlinear ROM using 10 POD modes and various time-steps for the time integration.	49
3.10	Evolution of the aerodynamic coefficients for the nonlinear ROM using various POD basis truncations.	50
3.11	Evolution of the aerodynamic coefficients for the nonlinear ROM using the 2 different formulations reported in Section 3.4.3.	52
3.12	Evolution of the aerodynamic coefficients for the nonlinear ROM using different values of the number of interpolation points p for the DEIM approximation.	54

3.13	Illustrative example of a masked projection selected cell (dark grey) and the related cells (light grey) to be initialized in order to compute the flux balance of the FOM.	56
3.14	Proper orthogonal eigenvalue spectrum for the flow around a NACA-0012 airfoil at different flow conditions.	57
3.15	The first four density POD modes for $Re = 5000$, $M = 0.85$ at zero incidence.	57
3.16	$Re = 5000$, $M = 0.85$, $\alpha = 0^\circ$: a) FOM density instantaneous snapshot of the flow for the last time instance of the sampled vortex shedding period; density fields absolute difference between the FOM and: b) the ROM-DEIM with 12 nonlinear modes, c) the ROM-DEIM with 20 nonlinear modes, d) the ROM-QDEIM with 12 nonlinear modes, e) the ROM-QDEIM with 20 nonlinear modes.	59
3.17	$Re = 10000$, $M = 0.85$, $\alpha = 0^\circ$: a) FOM density instantaneous snapshot of the flow for the last time instance of the sampled vortex shedding period; b) density fields absolute difference between the FOM and the ROM-DEIM with 40 nonlinear modes.	60
3.18	The 50 th amplitude and nonlinear mode for the flow at $Re = 10000$	60
3.19	$Re = 10000$, $M = 0.85$, $\alpha = 0^\circ$: a) FOM density instantaneous snapshot of the flow for the last time instance of the sampled vortex shedding period; density fields absolute difference between the FOM and: b) the ROM-QDEIM with 12 nonlinear modes, c) the ROM-QDEIM with 20 nonlinear modes, d) the ROM-QDEIM with 30 nonlinear modes, e) the ROM-QDEIM with 40 nonlinear modes, e) the ROM-QDEIM with 50 nonlinear modes.	61
3.20	$Re = 10000$, $M = 0.85$, $\alpha = 0^\circ$: on the left axis the wall pressure reference in black and on the right axis the wall pressure differences for different p in blue. On the left for $t = T/2$ and on the right at the end the cycle $t = T$	62
3.21	Instantaneous density field for $Re = 5000$, $M = 0.2$, $\alpha = 10^\circ$ on the left and for $Re = 1000$, $M = 0.2$, $\alpha = 20^\circ$ on the right.	63
3.22	Instantaneous density fields absolute difference between the ROM and the FOM plotted in Fig.3.21 for the BDEIM adaptation using $p = 60$ nonlinear modes (and $f = 240$ fitting points) on the left, and using the BQDEIM adaptation using $p = 10$ nonlinear modes (and $f = 40$ fitting points) on the right.	64
3.23	Instantaneous density fields absolute difference between the ROM and the FOM plotted in Fig.3.21 for the BQDEIM adaptation using $p = 20$ nonlinear modes (and $f = 80$ fitting points) on the left, and using the BQDEIM adaptation using $p = 30$ nonlinear modes (and $f = 120$ fitting points) on the right.	64

List of Figures

3.24	$Re = 5000$, $M = 0.2$, $\alpha = 10^\circ$: on the left axis the wall pressure reference in black and in blue on the right axis the wall pressure differences for different p at the last time instance of the vortex shedding cycle.	65
3.25	Instantaneous density fields difference between the ROM and the FOM plotted in Fig.3.21 for the BDEIM adaptation using $p = 20$ nonlinear modes (and $f = 80$ fitting points) on the left, and using the BQDEIM adaptation using $p = 10$ nonlinear modes (and $f = 40$ fitting points) on the right.	66
3.26	Instantaneous density fields difference between the ROM and the FOM plotted in Fig.3.21 for the BDEIM adaptation using $p = 40$ nonlinear modes (and $f = 160$ fitting points) on the left, and using the BQDEIM adaptation using $p = 10$ nonlinear modes (and $f = 40$ fitting points) on the right.	66
3.27	Instantaneous density fields difference between the ROM and the FOM plotted in Fig.3.21 for the BQDEIM adaptation using $p = 20$ nonlinear modes (and $f = 80$ fitting points).	67
4.1	Normalized vortex shedding frequency f_s by the shedding frequency of the fixed cylinder configuration f_0 as a function of the f_r for different A_e , where $f_{s,P}$ and $f_{s,S}$ are the primary and secondary frequencies of f_s , respectively [128].	77
4.2	Instantaneous density field of a flow around a vertically oscillating cylinder at $Re = 185$, $A_e = 0.2$ and $f_r = 0.8$	77
4.3	Energy distribution of the solution POD modes for the cases of a flow around a vertically oscillating cylinder at $Re = 185$ and $M = 0.2$ for two different sets of forced motion parameters.	78
4.4	First to 6 th density proper orthogonal mode (POM) for the flow around a vertically oscillating cylinder at $Re = 185$ and $(A_e, f_r) = (0.2, 0.8)$	78
4.5	On the left axis: time history of the first 6 POD modes amplitudes for the case at $(A_e, f_r) = (0.2, 0.8)$; results obtained for the nonlinear ALE-based ROM without any masked projection. On the right axis: the respective absolute error $ a_{FOM} - a_{ROM} $ (red dotted plot).	79
4.6	On the left axis: time history of the first 6 POD modes amplitudes for the case at $(A_e, f_r) = (0.2, 0.8)$; results obtained for the nonlinear ALE-based ROM with the use of the BQDEIM approach by using 14 nonlinear POD modes (and $14 \times 4 = 56$ fitting points). On the right axis: the respective absolute error $ a_{FOM} - a_{ROM} $ (red dotted plot).	79

4.7	Relative error (in percentage) of the density field for the last time step of the ROM simulation: results obtained for the nonlinear ALE-based ROM with the use of the BQDEIM approach by using 14 nonlinear POD modes (and $14 \times 4 = 56$ fitting points).	80
4.8	Instantaneous density field of a flow around a vertically oscillating cylinder at $Re = 185$, $A_e = 0.5$ and $f_r = 1.2$	81
4.9	On the left axis: time history of the first 6 POD modes amplitudes for the case at $(A_e, f_r) = (0.5, 1.2)$; results obtained for the nonlinear ALE-based ROM without any masked projection. On the right axis: the respective absolute error $ a_{FOM} - a_{ROM} $ (red dotted plot).	82
4.10	Illustrative scheme of the application of the selection algorithm for each conservative block variable itself decomposed in other 5 additional blocks.	82
4.11	Spatial location of the 800 cells selected using the block-adapted masked projection using 20 blocks and 40 nonlinear POD modes . . .	83
4.12	On the left axis: time history of the first 6 POD modes amplitudes for the case at $(A_e, f_r) = (0.5, 1.2)$; results obtained for the nonlinear ALE-based ROM with the use of the BQDEIM approach by using 40 nonlinear POD modes (and $40 \times 20 = 800$ fitting points). On the right axis: the respective absolute error $ a_{FOM} - a_{ROM} $ (red dotted plot).	83
4.13	Relative error (in percentage) for the density field for the last time step of the ROM simulation for the case at $(A_e, f_r) = (0.5, 1.2)$: results obtained for the nonlinear ALE-based ROM with the use of the BQDEIM approach by using 40 nonlinear POD modes (and $40 \times 20 = 800$ fitting points).	84
4.14	Selection of the time window for the extraction of the set of snapshots that would be the basis for nonlinear ROM. Such a procedure is necessary in order to perform a proper interpolation for the off-reference initial condition $w_0(\mu_*)$	87
4.15	Initial conditions w_0 at different values of A_e and the related interpolated field.	87
4.16	Singular values distribution for the global POD approach reported in Algorithm 8 between the operating points $(A_e, f_r) = (0.2, 0.8)$ and $(A_e, f_r) = (0.2, 0.9)$	90
4.17	On the left axis: time history of the first 6 POD modes amplitudes of eq.(4.16) for the interpolated case at $(A_e, f_r) = (0.2, 0.85)$; results obtained for the nonlinear ALE-based ROM without the use of any masked projection approach. On the right axis: the respective absolute error $ a_{FOM} - a_{ROM}^* $ (red dotted plot).	91

List of Figures

4.18	On the left axis: time history of the first 6 POD modes amplitudes of eq.(4.16) for the interpolated case at $(A_e, f_r) = (0.2, 0.85)$; results obtained for the nonlinear ALE-based ROM with the use of the BQDEIM approach by using 24 nonlinear POD modes (and $24 \times 4 = 96$ fitting points). On the right axis: the respective absolute error $ a_{FOM} - a_{ROM}^* $ (red dotted plot).	92
4.19	Relative error (in percentage) for the density field for the last time step of the ROM simulation for the interpolated case at $(A_e, f_r) = (0.2, 0.85)$; results obtained with the use of the BQDEIM approach by using 24 nonlinear POD modes (and $24 \times 4 = 96$ fitting points).	92
4.20	Difference between the ROM first amplitude a_1^* (see eq.(4.16)), obtained from a long-term ROM simulation without any masked projection, and its FOM counterpart.	93
4.21	Singular values distribution for the global POD approach reported in Algorithm 8 between the operating points $(A_e, f_r) = (0.2, 0.8)$ and $(A_e, f_r) = (0.4, 0.8)$	94
4.22	On the left axis: time history of the first 6 POD modes amplitudes of eq.(4.16) for the interpolated case at $(A_e, f_r) = (0.3, 0.8)$; results obtained for the nonlinear ALE-based ROM without the use of any masked projection approach. On the right axis: the respective absolute error $ a_{FOM} - a_{ROM}^* $ (red dotted plot).	95
4.23	On the left axis: time history of the first 6 POD modes amplitudes of eq.(4.16) for the interpolated case at $(A_e, f_r) = (0.3, 0.8)$; results obtained for the nonlinear ALE-based ROM with the use of the BQDEIM approach by using 24 nonlinear POD modes (and $24 \times 20 = 480$ fitting points). On the right axis: the respective absolute error $ a_{FOM} - a_{ROM}^* $ (red dotted plot).	95
4.24	Relative error (in percentage) for the density field for the last time step of the ROM simulation for the interpolated case at $(A_e, f_r) = (0.3, 0.8)$; results obtained with the use of the BQDEIM approach by using 24 nonlinear POD modes (and $24 \times 20 = 480$ fitting points).	96
4.25	Illustrative scheme of the <i>predictor-corrector</i> procedure for the determination of the number of interpolation points for the parametric nonlinear ROM.	97
4.26	Computational domain for the two-dimensional cylinder configuration in transverse free-motion.	98
4.27	Illustrative scheme for the <i>weak coupled</i> fluid structure system.	99
4.28	Time history of the displacement y of the cylinder in transverse free motion immersed in a uniform flow for $Re = 110$ and $M = 0.2$	99
4.29	Singular values distribution of the POD for flow around a cylinder in free transverse motion at $Re = 110$	100

4.30	First to 6 th density proper orthogonal mode (POM) for the flow around a cylinder in free transverse motion at $Re = 110$	100
4.31	Time history of the position of the center of the cylinder y (top) and of the lift coefficient c_L (bottom) for the case of a cylinder in free transverse motion at $Re = 110$	102
4.32	Time history of the first six amplitudes for the coupled ROM and the FOM for the case of a cylinder in free transverse motion at $Re = 110$	102
4.33	Lift coefficient and displacement phase portrait for the coupled ROM and the FOM of a cylinder in free transverse motion at $Re = 110$	103
4.34	Time history of the lift coefficients for the coupled ROM for different parameters used in the masked projection approach.	103
5.1	Mach fields for three different instants of the finite volume resolution of the unsteady Euler equations.	109
5.2	Comparison of the aerodynamic force coefficients between the finite volume solver and the TSM solver.	109
5.3	Density fields of the 3 proper orthogonal modes (POMs) composing the POD basis for the ROTSM for $N = 1$	110
5.4	Comparison of the Euclidean norm of the density residual for the full order and the reduced order TSM. Note the different abscissa related to the two approaches.	111
5.5	On the first line, the density fields at the 3 time instances of the TSM. On the second line, the density fields absolute difference between the ROTSM and the FOTSM density fields.	111
5.6	Density fields of the 7 proper orthogonal modes (POMs) composing the POD bases for the ROTSM for $N = 3$	112
5.7	The Euclidean norm of the density residual for the 7 steady state fields of the ROTSM.	113
5.8	On the first line, the density fields at the seven time instances of the TSM. On the second line, the density fields absolute difference between the ROTSM and the FOTSM density fields.	113
5.9	Mach steady states for three different free-stream Mach numbers in the operating points set. Left: $M_\infty = 0.52$, middle: $M_\infty = 0.68$, right: $M_\infty = 0.80$,	114
5.10	Singular values distribution of the POD computed for the matrix collection \mathbf{W} of the ROTSM solutions for different Mach numbers included in Λ_{M_∞} (eq.(5.7)).	115
5.11	Density fields of the 24 proper orthogonal modes (POMs) composing the GPOD basis for the parametric ROTSM (sorted from left to right from the top to the bottom).	116
5.12	Density fields at the 3 time instances of the TSM for $M_\infty = 0.58$. Results obtained with the reference ROTSM.	118

List of Figures

5.13	Comparison of the Euclidean norm of the density residual for the ROTSM with different interpolation approaches for $M_\infty = 0.58$. In black, the respective reference ROTSM.	119
5.14	Density fields absolute difference between the reference ROTSM and the adapted ROTSM density fields at the 3 time instances for $M_\infty = 0.58$: on the first line with GPOD, on the second line with truncated GPOD and on the third line with the interpolated basis on a tangent space of the Grassmann manifold.	120
5.15	Density fields at the 3 time instances of the TSM for $M_\infty = 0.78$. Results obtained with the reference ROTSM.	121
5.16	Comparison of the Euclidean norm of the density residual for the ROTSM with different interpolation approaches for $M_\infty = 0.78$. In black, the respective reference ROTSM.	121
5.17	Density fields absolute difference between the reference ROTSM and the adapted ROTSM density fields at the 3 time instances for $M_\infty = 0.78$: on the first line with GPOD, on the second line with truncated GPOD and on the third line with the interpolated basis on a tangent space of the Grassmann manifold.	122
A.1	Instantaneous snapshots of the field of an URANS simulation of a flow around a NACA-0012 airfoil at $\alpha = 20^\circ$, $Re = 20000$ and $M = 0.5$, using the $k - \omega$ turbulent model: a) density field, b) ρk field, c) $\rho\omega$ field.	134
A.2	Absolute error on the amplitudes related to the POD modes between FOM simulation and the ROM using a constant average eddy viscosity: flow around a NACA-0012 airfoil at $\alpha = 20^\circ$, $Re = 20000$ and $M = 0.5$, using the $k - \omega$ turbulent model.	135
A.3	Aerodynamic force coefficients for a flow around a NACA-0012 airfoil at $\alpha = 20^\circ$, $Re = 20000$ and $M = 0.5$, using the $k - \omega$ turbulent model: comparison between FOM simulation and the ROM using a constant average eddy viscosity.	135
A.4	Absolute error on the amplitudes related to the POD modes between FOM simulation and the ROM using a constant average eddy viscosity: flow around a NACA-0012 airfoil at $\alpha = 20^\circ$, $Re = 20000$ and $M = 0.5$, using the $k - \omega$ turbulent model.	136
B.1	Proper orthogonal eigenvalue spectrum.	137
B.2	Density fields of the first two proper orthogonal modes (POMs) for the inviscid flow of the reference CT5 [144].	137
B.3	Comparison of the first 3 modal coordinates a_i computed as the solution of the projection based ROM and of the reference modal coordinates for the test case defined in reference CT5 [144].	138

List of Tables

1.1	Summary of bibliography: ROMs and the related stability methods. Legend: N-S = Navier-Stokes equations, K-S = Kuramoto-Sivashinsky equation, MEMS = pressure sensor behaviour dynamic system, Gal. = Galerkin, Pet.Gal. = Petrov-Galerkin, ^{lam} = laminar, ^{inv} = inviscid, ^{inc/s.c.} = incompressible/slightly compressible.	7
1.2	Summary of bibliography: ROMs for aeroelasticity. Legend: N-S = Navier-Stokes equations, ^{inv} = inviscid, ^{inc/s.c.} = incompressible/slightly compressible, Gal. = Galerkin, Pet.Gal. = Petrov-Galerkin, FOM = non-linear term computed using the Full Order Model, LCO = limit cycle oscillations, NL-HBM = nonlinear Harmonic Balance Method.	11
2.1	Computational cost associated to the different masked projection algorithms, given n equal to the number of degree of freedom of the system and p the number of the retained nonlinear modes.	26
3.1	Value of E_{N_m} eq.(2.13) for the flow past a cylinder at $Re = 100$ for the snapshot set with subtraction of the time average field.	45
3.2	Root-mean-square deviation (RMSD) of the reconstructed C_D and C_L using m proper orthogonal modes with respect to the reference solution.	47
4.1	Summary table of the matrices and vectors with their respective size computed during the offline phase of the nonlinear ROM for the Navier-Stokes equations.	86
5.1	Sum of the absolute density error and max absolute error over the entire mesh for the different basis adaptation approaches for the 3 different instances of the TSM for the case at $M_\infty = 0.58$	119
5.2	Sum of the absolute density error and max absolute error over the entire mesh for the different basis adaptation approaches for the 3 different instances of the TSM for the case at $M_\infty = 0.78$	122

List of Symbols

The next list describes several symbols that will be later used within the body of the document:

α	Angle of incidence
\bar{w}	Time-average of the system variables column vector
$\partial \Omega$	Boundary of the computational spatial domain
$\mathcal{V}(\Omega)$	Volume related to a discretized cell
Ω	Computational spatial domain
ω	Oscillation frequency
ρU	Momentum per unit of volume
ρ	Density
σ	Singular value
\mathbf{P}	Mask matrix for the masked projection approach
Φ	POD basis of the solution
Σ	Singular values diagonal matrix
a	Column vector of the amplitudes related to the POD modes
c	Column vector of the amplitudes related to the POD modes of the nonlinear term
F_c	Convective flux operator
F_d	Diffusive flux operator
f_p	Operator which computes the nonlinear term for the points selected by the masked projection approach
F	Snapshots matrix collection of the nonlinear term
f	General nonlinear functions column vector
J	Jacobian operator
s	Grid velocity

U	POD basis of the nonlinear term
V	Right singular vectors resulting from a SVD
W	Snapshots matrix collection of the solution
w	System variables column vector
$\tilde{\mathbf{P}}$	Points selector operator which includes the f points selected by \mathbf{P} plus the neighbor points
b	Number of blocks for the block-adaptation of the masked projection approach
E	Total energy per unit of mass
f	Number of points for the masked projection approach
M	Mach number
m	Number of retained modes for the POD basis
N	Number of harmonics
n	Number of degrees of freedom of the system
N_x	Dimension of the discretized domain
p	Number of retained nonlinear term modes for the POD basis
r	Rank of a matrix
Re	Reynolds number
T	Oscillation period
\mathbf{R}_Ω	Non-linear residual operator that computes the flux balance of the Navier-Stokes equations for each cell of a computational discretized domain

Introduction

Dynamical systems are the basic framework for high-fidelity modeling and control of a large variety of complex systems of engineering interest or industrial value. For example, in the aeronautic and aerospace fields, dynamical systems model the response of some complex phenomena such as fluid-structure interaction, shock interaction, flow separation, limit-cycle oscillations and so on. During the last three decades, the computing barriers for such high-fidelity numerical simulations have been broken by hardware enhancements and improved numerical methods and resolution algorithms. However, the growing need for an improved accuracy is still critical for applications involving **many-query** problems. This class of problems consists in the numerical simulations that require to be accomplished systematically and, possibly, in short time. Examples include nonlinear models for fluid control or **flow induced vibrations in aeroelasticity**. The latter, in particular, is the main objective of this dissertation. It involves computational models that are components of a more comprehensive (multiphysics) problem, demanding to be run for a large number of system parameters and configurations. In such circumstances, the different simulation times must be significantly decreased in order to complete the analysis within a reasonable overall computational time. Examples include aeroelastic investigation, optimization and uncertainty quantification.

The hierarchical physics approaches are an attractive alternative to address this issue. Their peculiarity is to replace the high-fidelity model by less accurate models with stronger assumptions on the physics (e.g. Navier-Stokes→Euler→Doublet Lattice Method,...). When available, this kind of techniques compromises the physics of the problem and results in lower global complexity achieving limited speedups. The present thesis focuses on the reduction of the compressible Navier-Stokes equations involving deforming meshes in the case of aeroelastic investigations. Thus, the hierarchical approaches are not suitable because they become inaccurate when complex physics are involved, like, for example, transonic or rotational flows. In this application scenario, the model reduction techniques have been deeply investigated and enhanced in last two decades. Two main classes of reduction approaches can be distinguished. The first one is the surrogate model approach that provides an empirical estimation of the system by employing some interpolation technique on the basis of a certain number of given high-fidelity solutions. This kind of “black-box” approaches ensures a high speedup albeit there is no assurance of the preservation of accuracy and physical properties of the solution. An exhaustive review of surrogate models is available, for example, in the book by Forrester *et al.* [1]. It is worth mentioning that an intermediate class of model reduction techniques is available which combines the hierarchical approaches with the surrogate models. Such approaches are designed to improve the surrogate models and some examples are given in references [2], [3]. The second one is the class of the **projection-based reduced order**

models (ROM). ROMs are physics based methods and capture the principal characteristics of the high-fidelity full order model (FOM) potentially yielding very high speedups. To decrease the dimension of the model, these methods first execute an ‘offline phase’: expensive computations (e.g. high-fidelity simulations, matrix operations etc.) are carried out in order to build the physical basis of the model such as the low-dimensional subspace that captures the dominant physical behavior of the model. Then, during the “online” phase, the reduced order simulation provides an approximated solution in this low-dimensional subspace. The complexity of the applications envisaged in this thesis has led us to favor ROMs over the other modeling approaches because they provides a low-dimensional model that is built on the basis of a relatively low number of high-fidelity evaluations and still keeps/preserves the physics of the system. To date, ROMs have been studied for a broad variety of challenging fluid dynamics problems. However, significant problems may arise when considering complex nonlinear systems. Thus, the goal of the model reduction methods presented in this thesis is to generate a low-order model that captures the nonlinearity of the unsteady Navier-Stokes equations and the further complexity induced by a moving or deforming domain. Frequently, the model reduction is accomplished without regard to a priori long-term numerical stability and convergence, but this could represent an important limitation for more challenging nonlinear periodic configurations. A further accomplishment of this thesis is the formulation of a reduced order model that exploits the periodicity of the envisaged configuration to derive an a priori stable nonlinear ROM. Finally, in order to simulate these complex systems the high fidelity model is often modeled by an industrial solver and, for this reason, the ROM is designed to satisfy the requirement of a minimal intrusiveness with respect to the FOM.

The thesis is organized as follows. In Chapter 1 the state of the art of the main projection-based ROMs for nonlinear fluid dynamics and their derivation in aeroelastic and parametric contexts is provided. Chapter 2 outlines the mathematical formulation and the related issues of a ROM for a general nonlinear system. The strategy to deal with the nonlinearity and the formulation for periodic systems is also presented. Chapter 3 illustrates the application of the nonlinear ROM presented in Chapter 2 to the compressible Navier-Stokes equations with fixed meshes. Here, test cases of increasing complexity are studied. Then, Chapter 4 and 5 present the adaptation of the nonlinear ROM respectively for deforming meshes configurations and nonlinear periodic configurations. The last chapter concludes the thesis and highlights some suggestions for future works.

CHAPTER 1

State of the art

The present section summarizes the relevant literature on model order reduction with a specific focus on nonlinear fluid dynamics projection-based ROMs and their aeroelastic and parametric applications. Anyway, it is worth mentioning that, for linear time invariant systems, an exhaustive review of reduced order modeling methods is available, for example, in the book by Antoulas [4]. This includes methods such as balanced truncation, empirical balanced truncation, moment matching and Loewner framework that could be used to produce ROMs with stability guarantees and error bounds. The level of knowledge is quite different when considering ROMs for non-linear dynamical systems, whose awareness and progress are still an open question.

Concerning nonlinear model reduction in fluid mechanics, the most popular approaches are based on the approximation of the state vector by linear combinations of a relatively small number of basis functions. Thus, the first essential ingredient of all projection-based model reduction techniques is the construction of such basis functions. In this regard, data-driven techniques have been widely used in recent years in order to provide a low-dimensional basis computed from a known ensemble of numerical (or experimental) solutions. Some of the most used techniques are summarized in the review by Taira *et al.* [5] and its more recent sequel with applications and further perspectives [6]. Also recently, a new technique has been proposed by Towne *et al.* [7] in order to characterize the flow structures that evolve coherently in space and time. Among all the proposed techniques, the Proper Orthogonal Decomposition (POD), also known in other disciplines as Karhunen-Loève decomposition, principal component analysis or empirical eigenfunctions method, was first introduced in fluid dynamics by Lumley [8] as an unbiased definition of the coherent structures existing in a turbulent flow. A complete review of the POD theory can be found in [9]. Basically, it consists of looking for the deterministic function that is most similar in an average sense to an ensemble of representative systems solutions (snapshots). The POD problem is formulated as an eigenvalue problem and the eigenmodes are the POD spatial modes that are orthonormal and thus form a basis. The POD remains one of the most widely used techniques for the definition of the approximation basis for linear and nonlinear model order reduction.

There are two possible approaches for performing the projection characterizing the projection-based model reduction: continuous and discrete projection. The continuous approach implies that the governing PDEs are projected at a continuous level with a continuous inner product. Its similarity to spectral numerical approx-

imation methods allows the use of analysis techniques employed by the spectral methods community [10]. However, it is tied to a subsequent discretization, e.g., for the interpolation of discrete reduced order bases or for the evaluation of the continuous inner products by using a numerical quadrature. Kalashnikova *et al.* [11] outline this point for linear time invariant systems by emphasizing the differences between the continuous and discrete approach. However, in the majority of applications of reduced order modeling for compressible fluid dynamics, a discrete projection formulation is employed. Contrary to its continuous counterpart, such an approach is linked to the numerical scheme used to solve the FOM. This implies that the properties of the numerical scheme as well as the boundary conditions are often inherited intrinsically by the related ROM [11].

1.1 Stability and accuracy

The main question about this kind of nonlinear ROMs concerns the lack of any guarantee of stability and accuracy [12]. In the last years, two categories of approaches have been introduced to tackle this issue. The a priori stabilization methods involve the application of stabilization techniques based on preliminary or empirical adjustments of the ROM while the a posteriori stabilization methods calibrate the ROM operators on the basis of a reference precomputed solution. Concerning the former class of stabilization approaches, methods that involve the inclusion of an artificial viscosity or the modification of the projection basis (Petrov-Galerkin projection) are widely used. For example, Iollo *et al.* [13] explicitly add an artificial dissipation term whose construction is similar to the Lax-Wendroff type artificial diffusion term. Alternatively, a different choice of the norm used for the POD is shown to improve stability. Iollo *et al.* [14] deal with this last aspect by employing the scalar product on a Sobolev H^1 space while Kirby [15] defines a scalar product for a Sobolev space by employing higher order derivatives. In both cases, although an improved stabilization is reported, the methods require an empirical calibration of the parameters defined in the scalar products. Xiao *et al.* [16] improve the stability of the POD based non-linear ROM using a Petrov-Galerkin method based on the use of the cosine rule between the advection direction in Cartesian space-time and the solution gradient direction. Leblond *et al.* [17] develop and test an optimal projection method for incompressible flows providing variables separation. Sabetghadam *et al.* [18] suggest an α -regularization (Helmholtz filtering) in order to improve the stability of the POD-Galerkin models while Östh *et al.* [19] and Protas *et al.* [20] investigate a hierarchy of eddy-viscosity terms to account for the large fraction of unresolved truncated POD modes. Balajewicz *et al.* [21] develop a stabilization approach that modifies the projection subspace in order to capture more of the low-energy and high dissipative scales of the flow solutions. Coherently, Baiges *et al.* [22] integrate the ROM by including a model for the unresolved subscales of the POD modes built by using an

1.1. Stability and accuracy

a posteriori least-squares procedure. Bergmann *et al.* [23] achieve a good stability feature using a domain decomposition and performing the ROM only to update the unsteady boundary conditions. Reddy *et al.* [24] provide a constrained ROM within user-defined bounds in order to enhance robustness, while de Pando *et al.* [25] report robust and accurate results using a distinct approach for the linear and non-linear part of the ROM. More recently, Stabile *et al.* [26] propose and compare two different pressure stabilization strategies for the incompressible Navier-Stokes equations. The Gauss-Newton with Approximated Tensors (GNAT) method of Carlberg *et al.* [27] shows stability properties using a fully discrete formulation for the ROM and a Petrov-Galerkin projection. Amsallem *et al.* [28] combine the GNAT and a local-basis technique in order to take into account multiple configurations without any lack of robustness.

On the other hand, various a posteriori calibration methods have been developed to enhance the stability of POD-Galerkin models. They are based on the introduction of calibration terms to account for the unresolved fine-scale fluctuations neglected by the POD truncation. These calibration terms are normally calculated by resolving appropriate constrained minimisation problems. Galletti *et al.* [29] calibrate a corrective term for the linear operator to take into account the pressure term that is generally neglected in incompressible flows. Couplet *et al.* [30] generalize and expand this method for any coefficient of the ROM. Bourguet *et al.* [31] compare different types of functional to be minimized for the calibration and a summary of different calibration methods is reported by Cordier *et al.* [32] and Gloerfelt [33]. Giere *et al.* [34] present a numerical analysis for the definition of appropriate stabilization parameters for a Streamline-Upwind Petrov-Galerkin (SUPG) ROMs for convection dominated problems. To the knowledge of the author, in last years more progress has been made concerning the a priori stabilization methods from a point of view of efficiency and application developments.

Alternatively, Loiseau *et al.* [35] avoid the numerical stability issues related to the projection-based ROMs by using a system identification approach to determine the amplitudes associated to the POD modes of a two-dimensional flow past a cylinder and a shear-driven cavity flow. In other words, the amplitudes associated to the POD modes are not computed as a result of the integration of the projected governing equations, but they are identified via a regression model formulated in reference [36]. Shinde *et al.* [37] overcome the numerical issues associated to the standard POD-Galerkin ROMs by using a Galerkin-free approach in a parametric context. They compute from the high-fidelity solutions the POD spatial modes and their related time amplitudes. Then, two interpolations for the spatial POD modes and the amplitudes are performed in order to compute the flow for a new flow configuration. Similarly, Oulghelou *et al.* [38] formulate a non intrusive ROM, which is independent of the governing equations, by providing POD spatial and temporal modes to be interpolated and calibrated in order to reconstruct the solution for new configuration parameters. With such approaches, the stability problems arising

from the projection of the Navier-Stokes equations are avoided since no dynamical system has to be integrated. Table 1.1 is given to summarize the state of the art for non-linear ROMs and the related a priori stability and accuracy methods.

Flow type	Projection	Stabilization	Non-linearity	Ref.
K-S	Gal.	Sobolev scalar product	Explicit multilinear	Kirby [15]
N-S ^{lam}	Gal.	Artificial viscosity	Explicit multilinear	Iollo <i>et al.</i> [13]
N-S	Gal.	H^1 scalar product	Full Order Model	Iollo <i>et al.</i> [14]
K-S	Gal.	α regularization	Explicit multilinear	Sabetghadam <i>et al.</i> [18]
MEMS	Pet.-Gal.	GNAT + local bases	Approxim. tensors	Amsallem <i>et al.</i> [28]
N-S ^{inv}	Gal	Domain decomposition	Explicit multilinear	Bergmann <i>et al.</i> [23]
N-S ^{inc}	Pet.-Gal.	Petrov-Galerkin projection	Explicit multilinear	Xiao <i>et al.</i> [16]
N-S ^{inc}	Gal.	Eddy viscosity addition	Explicit multilinear	Östh <i>et al.</i> [19]
N-S ^{s.c.}	Gal.	Eddy viscosity addition	Explicit multilinear	Protas <i>et al.</i> [20]
N-S ^{s.c.}	Gal.	Minimal subspace rotation	Explicit multilinear	Balajewicz <i>et al.</i> [21]
N-S	Pet.-Gal.	GNAT	Approxim. tensors	Carlberg <i>et al.</i> [27]
N-S	Gal.	Adjoint linear	DEIM	de Pando <i>et al.</i> [25]

Table 1.1 Summary of bibliography: ROMs and the related stability methods. Legend: N-S = Navier-Stokes equations, K-S = Kuramoto-Sivashinsky equation, MEMS = pressure sensor behaviour dynamic system, Gal. = Galerkin, Pet.Gal. = Petrov-Galerkin, ^{lam} = laminar, ^{inv} = inviscid, ^{inc/s.c.} = incompressible/slightly compressible.

1.2 Dealing with nonlinearities

For PDEs characterized by polynomial nonlinear functions, projection-based ROMs can be easily formulated in terms of precomputed reduced operators, resulting in ROMs whose evaluations are independent of the dimensions of the FOM. This is not the case for systems with non-polynomial nonlinearities (such as the compressible Navier-Stokes equations) whose reduction becomes inefficient because the nonlinear term must be evaluated systematically during the online ROM computation. To overcome this computational bottleneck, various approaches have been developed to recover the efficiency of projection-based model reductions for nonlinear problems. Masked projection approaches approximate a given general nonlinear term by interpolating (or fitting) it on the basis of a certain number of judiciously selected points. The key ingredient distinguishing the different approaches is the greedy algorithm that selects the interpolation/fitting grid points. However, all techniques minimize a representation error of the nonlinear terms. The Missing Point Estimation (MPE), developed by Astrid *et al.* [39], provides an algorithm for the selection of the sub-optimal set of fitting points for the nonlinear term using a heuristic optimization inspired by the Gappy POD method [40]. Since it is highly costly, the standard MPE entailed the recent work by Zimmermann *et al.* [41] who derive a fast and more efficient surrogate of the standard MPE algorithm that slightly raises the error indicator. Alternatively, another widely used selection algorithm is the Discrete Empirical Interpolation Method (DEIM) which has been proposed by Chaturantabut *et al.* [42], entailed by its continuous counterpart the Empirical Interpolation Method (EIM) by Barrault *et al.* [43]. This method selects a limited number of interpolation points while remaining sub-optimal with respect to the error introduced by the approximation of the nonlinear term. More recently, Drmac *et al.* [44] provide a variation that implies a better upper bound for the DEIM error indicator. Also, Peherstorfer *et al.* [45] formulate a randomized oversampling technique aiming to stabilize the interpolation of the nonlinearity in the presence of Gaussian noise. Sargsyan *et al.* [46] develop a genetic search algorithm for online improvement of the interpolation points of the DEIM approach. Dimitriu *et al.* [47] provide a comparative study focused on the efficiency and accuracy of different hyper-reduction techniques applied to a biological model describing the spatio-temporal dynamics of a predator-prey community. All these methods have been widely used in fluid mechanics context and their implementation and applications will be discussed and explored in Section 3.

1.3 ROMs in aeroelasticity and fluid-structure interaction

Anttonen *et al.* [48] outlined that an additional level of difficulty is reached when considering aeroelastic non-linear dynamical systems. In fluid-structure interaction cases, especially when adopting high-fidelity aerodynamics, there are some theoretical limits arising from the POD theory formulated in a deformable domain. The POD is based on a definition of a spatial correlation of the system, but the snapshots resulting from an aeroelastic CFD solver cannot ensure this point as, notoriously, the mesh is moving and deforming during the simulation. The loss of the spatial correlation and the increasingly important problems of stability and accuracy make the aeroelastic ROMs study widely challenging. Recently, Freno *et al.* [49] reported with numerical examples involving a moving airfoil that, when an index based domain like the one considered by Anttonen *et al.* [48] is used to build the ROM, the formulation is not affected by the aforementioned limitation when the mesh is deforming in a consistent manner, that is when the index numbering is preserved during the numerical simulation. When a rigid body motion is taken into account, an interesting manner to avoid this issue is presented by Lewin *et al.* [50] and Placzek [51]. They perform the projection of the governing equations in a noninertial reference frame in order to preserve the consistency of the POD formulation. Anyway, stability problems appear when considering highly non-linear flows. Bourguet *et al.* [52] propose a Hadamard formulation to take into account small wall deformations. Then an a posteriori calibration is performed to improve the stability. Troshin *et al.* [53] outline an alternative POD methodology for a flow field in a domain with moving boundaries. The moving or deforming domain is mapped to a stationary domain by combining a transfinite interpolation and an algorithm for volumes adjustment. Liberge *et al.* [54] implement a multiphase method that allows to perform a POD on a moving domain using characteristic functions to follow the fluid-structure interface. More recently, Falaize *et al.* [55] extend such formulation for flows induced by rigid bodies in forced rotation. Also, they include parametric changes in the proposed model. Longatte *et al.* [56] explore the behavior of POD-multiphase ROM presented in 2010 [54] when the parameter values are different from those used to build the POD basis. Stankiewicz *et al.* [57], [58] deepen the study of Anttonen *et al.* [48] with test cases of increasing complexity also considering parametric changes. The aforementioned aeroelastic studies do not consider systems with non-polynomial nonlinearities. Freno *et al.* [49], [59] deal with general non-linear systems in aeroelastic context. They use dynamic basis functions to take into account the domain deformation dynamics by defining a dynamics for the projection basis related to the instantaneous deformed configuration. In addition, they consider a fully non-linear system but, since it is impossible to make it explicit, they use the FOM to evaluate the non-linear term at each time-step. As a result, the

computational efficiency of the ROM is reduced significantly. Also, recently, Shinde *et al.* [60] extend the Galerkin-free approach to fluid-structure interaction problems by interpolating POD bases including mesh deformations.

Alternatively, Thomas *et al.* [61] develop a nonlinear ROM for dynamically nonlinear solvers for limit cycle oscillation analysis. They use a nonlinear frequency-domain harmonic balance method [62] in conjunction with a Taylor series expansion and Proper Orthogonal Decomposition to create a frequency-domain nonlinear ROM.

In the context of system identification approaches, Chen *et al.* [63] develop a Support-Vector-Machine- (SVM-) based ROM for predicting the limit cycle oscillation induced by the nonlinear aerodynamics of an aeroelastic system. Mannarino *et al.* [64], [65] develop a neural network-based ROM technique in the discrete time domain in order to deal with nonlinearities in fluid-structure interaction problems. Kou *et al.* [66] derive a ROM for the investigation of limit cycle oscillations and flutter behaviors of an airfoil by combining linear autoregressive with exogenous input (ARX) model with radial basis function neural network (RBFNN) model for the nonlinear approximation.

Finally the progress for linear aeroelastic systems should be mentioned. For aerodynamic models like the Doublet Lattice Method (DLM) and linearized frequency domain methods, the aerodynamic ROM can be easily coupled with the structure one. As a consequence, “fully coupled” aeroelastic computations can be performed, as shown in the works by Bui-Thanh *et al.* [67], Farhat *et al.* [68], Vetrano *et al.* [69], Kim [70] and Winter *et al.* [71]. Table 1.2 is given to summarize the state of the art for ROMs in aeroelasticity distinguishing linear and non linear applications and the related approaches.

Flow type	Projection	Aeroelastic issue approach	Non-linearity (if any)	Ref.
Lin. N-S ^{inv}	Gal.	Small-disturbance frequency-domain	-	Thomas <i>et al.</i> [72]
Lin. N-S ^{inv}	Pet.-Gal.	Explicit affine function for geometry variation	-	Bui-Thanh <i>et al.</i> [67]
Lin. N-S ^{inv}	-	Radial Basis Funct. vs Chebyshev polynomials	-	Winter <i>et al.</i> [71]
N-S ^{inv}	Gal.	Non-inertial reference	Explicit multilinear	Lewin <i>et al.</i> [50]
N-S ^{s.c.}	Gal.	Non-inertial reference	Explicit multilinear	Placzek [51]
Potential	Gal.	Index-based POD	Explicit multilinear	Anttonen <i>et al.</i> [73]
N-S ^{inc}	Gal.	Index-based POD + interpolation	Explicit multilinear	Stankiewicz <i>et al.</i> [57]
N-S ^{s.c.}	Gal.	Hadamard formulation + calibration	Explicit multilinear	Bourguet <i>et al.</i> [52]
N-S ^{inc.}	Gal.	Multiphase method	Explicit multilinear	Liberge <i>et al.</i> [54]
N-S ^{inc.}	Gal.	Index-based POD + calibration	Explicit multilinear	Stankiewicz <i>et al.</i> [58]
N-S	Gal.	Dynamic basis functions	FOM	Freno <i>et al.</i> [49], [59]
N-S (LCO)	Gal.	NL-HBM	FOM (in the frequency domain)	Thomas <i>et al.</i> [61]

Table 1.2 Summary of bibliography: ROMs for aeroelasticity. Legend: N-S = Navier-Stokes equations, ^{inv} = inviscid, ^{inc/s.c.} = incompressible/slightly compressible, Gal. = Galerkin, Pet.Gal. = Petrov-Galerkin, FOM = non-linear term computed using the Full Order Model, LCO = limit cycle oscillations, NL-HBM = nonlinear Harmonic Balance Method.

1.4 Parametric investigation

Another very significant topic for ROMs is the parametric investigation. For example, parametric ROMs capturing the coupled fluid dynamic and structural dynamic behavior of an aircraft configuration enable rapid characterization of the aircraft's flight envelope. In such an application scenario, ROMs avoid such expensive computations as the aerodynamic responses related to a set of system parameters are requested systematically. However, the construction of a parametric ROM is a non-trivial task. For example, Bergmann *et al.* [23] show that for a POD based non linear parametric ROM, a set of snapshots for different configurations are required to build the reduced order model. But when the investigated configuration is not included among the sampled configurations there is no guarantee that the reduced basis will adequately approximate the solution. In the ROM community it was realized that parameter domains could be decomposed into subdomains for which local ROMs can be formulated or more easily adapted. As a consequence, the partitioning of the parameter domain and the ROM adaptation become an issue of intense investigations. These include applying sampling methods to build a basis from a sufficiently representative collection of simulations and eventually clustering them [74]–[80], replacing coefficients in the reduced order models with functions fitted from data [81] or adjusting the model basis by extrapolation, [82]–[84] or interpolation, [38], [69], [85]–[89]. Benner *et al.* [81] survey the methods in projection-based model reduction by highlighting the important role played in the parametric domain.

Construction of a projection-based ROM for nonlinear systems

Contents

2.1	Introduction	13
2.2	From the nonlinear system to the reduced system	14
2.3	Low-rank approximation by Proper Orthogonal Decomposition	16
2.4	Galerkin and Petrov-Galerkin projection	18
2.5	Masked projections	20
2.6	Practical implementation of a nonlinear reduced order model using masked projection	27
2.7	Construction of a reduced order model for periodic flows	28
2.7.1	Time Spectral Method	29
2.7.2	Reduced Order Time Spectral Method	33
2.8	Conclusions	36

2.1 Introduction

The present chapter provides the mathematical guidelines for the construction of a nonlinear ROM. The reader should be aware that the presented framework is far from being a complete review of the full range of possible approaches for nonlinear model order reduction. Different sections mention the relevant literature and develop the methods which impacted on the present doctoral work on the basis of the following characteristics:

- documented relevance and performance
- implementation affordability and/or feasibility
- envisaged application

In section 2.2 the mathematical framework at the basis of the construction of a projection-based nonlinear model reduction is presented. In the subsequent sections, the tools allowing model reduction are detailed and the resulting choices are

motivated. In section 2.3 the Proper Orthogonal Decomposition is introduced in order to construct a lower dimensional approximation for the high-fidelity system. In section 2.4 the subject of the projection operator is addressed. Then, the reduction of the nonlinearity complexity is introduced in a projection-based framework by performing the evaluation onto a subset of the domain. This approach is known as masked projection and detailed in section 2.5. In section 2.6 the practical implementation of a projection based ROM is presented in order to summarize and explain the succession of the procedures illustrated before. Finally, in section 2.7, in the particular case of periodic systems, an efficient time-domain harmonic method is introduced with its related reduced order derivation.

2.2 From the nonlinear system to the reduced system

A generic nonlinear spatio-temporal dynamical system is governed by an autonomous system of coupled equations which may be written in the semi-discretized form as:

$$\frac{d\mathbf{w}(t)}{dt} = \mathbf{f}(\mathbf{w}(t)) \quad (2.1)$$

where $\mathbf{w} \in \mathbb{R}^n$ is the time-dependent spatially discretized unknown vector including the k different physical variables discretized in a spatial domain \mathbb{R}^{N_x} (N_x is the number of cells in a finite volume discretization, the number of elements in a finite elements discretization and so on) so that $n = N_x \times k$:

$$\mathbf{w}(t) = \begin{pmatrix} \mathbf{w}_1(t) \\ \mathbf{w}_2(t) \\ \vdots \\ \mathbf{w}_k(t) \end{pmatrix} \quad (2.2)$$

and $\mathbf{f}(\mathbf{w}(t))$ is a general non-linear term. Consequently, the coupled system of eq.(2.1) can be written in a matrix form, as:

$$\begin{pmatrix} \frac{d\mathbf{w}_1(t)}{dt} \\ \frac{d\mathbf{w}_2(t)}{dt} \\ \vdots \\ \frac{d\mathbf{w}_k(t)}{dt} \end{pmatrix} = \begin{pmatrix} \mathbf{f}_1(\mathbf{w}(t)) \\ \mathbf{f}_2(\mathbf{w}(t)) \\ \vdots \\ \mathbf{f}_k(\mathbf{w}(t)) \end{pmatrix} \quad (2.3)$$

where the \mathbf{f}_i with $i = 1 \dots k$ are the different nonlinear function components related to each different physical variable.

2.2. From the nonlinear system to the reduced system

Projection techniques for model-order reduction seek to approximate the state vector \mathbf{w} by an element in a low-rank vector subspace spanned by a matrix $\Phi \in \mathbb{R}^{n \times m}$ whose column vectors $\Phi_i = [\Phi_i^{(1)}, \Phi_i^{(2)}, \dots, \Phi_i^{(k)}]^T$ with $i = 1, 2, \dots, m$ form a basis for the subspace, with $m \ll n$. The state vector is then approximated as a linear combination of the basis vectors:

$$\mathbf{w}(t) \approx \sum_{i=1}^m \Phi_i a_i(t) = \Phi \mathbf{a}(t) \quad (2.4)$$

where $\mathbf{a} \in \mathbb{R}^m$ is a column vector. Substituting eq.(2.4) in eq.(2.1) yields an overdetermined system of n nonlinear equations with m unknowns:

$$\Phi \frac{d\mathbf{a}(t)}{dt} = \mathbf{f}(\Phi \mathbf{a}(t)) \quad (2.5)$$

Then, m constraints are introduced by enforcing the orthogonality to a left subspace spanned by the column vectors of $\Psi \in \mathbb{R}^{n \times m}$. Therefore, projection based ROMs accomplish the model reduction by projecting the system onto a suitably chosen left subspace Ψ . Using the inner product given by $(\Psi, \Phi) = \Psi^T \Phi$ results in the reduced system of m equations with m unknowns:

$$\Psi^T \Phi \frac{d\mathbf{a}(t)}{dt} = \Psi^T \mathbf{f}(\Phi \mathbf{a}(t)) \quad (2.6)$$

where the superscript ' T ' denotes the transpose operation. The presented formulation can be easily extended to any choice of inner products. A classical criterion to choose the left subspace is $\Psi = \Phi$, that is equivalent to force the residual of eq.(2.6) to be orthogonal to the subspace generated by the columns of Φ . This is known as *Galerkin* projection. More general strategies for which $\Psi \neq \Phi$ are referred to as *Petrov-Galerkin* projections.

The presented projection-based model reduction approach is efficient for problems where the matrix operators are constructed only once and can be assembled a priori. For example, for linear time-invariant or polynomial systems, the dynamical system do have a canonical form characterized explicitly by an affine decomposition of linear operators. In more detail, supposing \mathbf{f} to be affine such that $\mathbf{f}(\mathbf{w}, t) = \mathbf{A} \mathbf{w}(t) + \mathbf{B}$, the system in eq.(2.6) becomes:

$$\Psi^T \Phi \frac{d\mathbf{a}(t)}{dt} = \Psi^T \mathbf{A} \Phi \mathbf{a}(t) + \Psi^T \mathbf{B} \quad (2.7)$$

In such a case, the projected spatial operators $\Psi^T \Phi$, $\Psi^T \mathbf{A} \Phi$ and $\Psi^T \mathbf{B}$ may be efficiently precomputed once and for all. This phase is known as the *offline* phase. Finally the *online* phase involves the time integration of the reduced system eq.(2.7) which can achieve potentially real-time responses. This is not the case for non-affine problems with general non-polynomial nonlinearities: despite the subspace Ψ and

Φ are computed in the offline phase, the evaluation of the reduced form of the nonlinearity $\Psi^T f(\Phi \mathbf{a}(t))$ is involved during the online stage. Such a nonlinear term requires the use of the FOM to be evaluated and finally projected at each time step of the ROM time integration. These operations lead to a computational cost that still scales as the dimension of the FOM and therefore undermine the computation gain of the projection-based ROMs. Different approaches have been developed in order to efficiently reduce the burden limit of scalability of the nonlinearity by maintaining the nonlinear structure of the system. One of these methods avoids the full evaluation of the nonlinear term by approximating it via interpolation (or fitting) over a judiciously selected subset of points significantly smaller than the large-scale full model dimension n . This approximation approach is called *masked projection* approach and will be discussed in section 2.5. Once the reduced system of eq.(2.6) is introduced, the focus is placed on the definition of Φ and Ψ . These topics are addressed respectively in sections 2.3 and 2.4.

2.3 Low-rank approximation by Proper Orthogonal Decomposition

The Proper Orthogonal Decomposition (POD) is a classical technique for data analysis used in a broad variety of mathematical contexts. This method consists in looking for the deterministic function that is most similar in an average sense to an ensemble of representative systems solutions so that the original variables of the system are transformed into a new set (called POD basis) of uncorrelated vectors ranked in descending order with respect to their average energy. A lower dimensional representation of the solutions is thus obtained by truncating the basis. In the theory of stochastic processes this procedure is known as Karhunen-Loève (KL) decomposition, whereas in multivariate statistics it is known as Principal Component Analysis (PCA). In fluid mechanics, the POD was introduced for turbulent flows by Lumley [8] as a technique to identify the *coherent structures* of a flow.

In the context of reduced order modeling, the POD method has been mostly used, in conjunction with (Petrov-)Galerkin projection methods, for the construction of reduced-order models of time-dependent problems [25], [48], [90] and, more recently, in the context of parametrized systems [81], [91].

Consider a set of observations (also called *snapshots*) $\{\mathbf{W}(\mathbf{x}, t_n), (\mathbf{x}, t_n) \in \mathcal{H}\}$ with \mathcal{H} an Hilbert space. The snapshots are obtained at N_t different time steps t_n over a spatial domain Ω ($\mathbf{x} = (x, y, z) \in \Omega$) and could be experimental measurements or numerical solutions of any dynamical system. The proper orthogonal modes for the system are obtained by maximizing the quantity [92]:

$$\max_{\Psi \in \mathcal{H}} \frac{\langle \langle \mathbf{W}, \Psi \rangle^2 \rangle}{\|\Psi\|^2} = \frac{\langle \langle \mathbf{W}, \Phi \rangle^2 \rangle}{\|\Phi\|^2}, \quad (2.8)$$

2.3. Low-rank approximation by Proper Orthogonal Decomposition

with respect to:

$$(\Psi, \Psi) = \|\Psi\|^2 = 1.$$

Commonly, $\langle \cdot \rangle$ could be a temporal, spatial, ensemble etc. average, while (\cdot, \cdot) and $\|\cdot\|$ denote an inner product and norm over \mathcal{H} , but it could be possible to use different inner products, to obtain different notions of optimality [92]. In the case of interest, the snapshots collected in \mathbf{W} are the numerical solutions of the nonlinear system (2.1) at N_t time steps, so that \mathbf{W} can be represented by a matrix of size $\mathbf{W} \in \mathbb{R}^{n \times N_t}$. Thus, eq.(2.8) can be written in the discretized form as:

$$\max_{\Psi \in \mathbb{R}^n} \frac{\langle (\mathbf{W}, \Psi)^2 \rangle}{\|\Psi\|^2} = \frac{\langle (\mathbf{W}, \Phi)^2 \rangle}{\|\Phi\|^2}, \quad (2.9)$$

with the relative euclidean n -inner product. In a fluid mechanics context and thus assuming that \mathbf{W} is collection of state vectors, the euclidean n -inner product is a natural space since it induces an “energy” defined norm. However, for the case of compressible flows, some precautions should be taken since the velocity variables are dynamically coupled with the thermodynamic variables [93]. Considering a temporal average, the problem of eq.(2.9) reduces to an eigenvalue problem as [92]:

$$\mathbf{R}\Phi = \Phi\Lambda, \quad (2.10)$$

where $\mathbf{R} = \mathbf{W}\mathbf{W}^T$ is the two-point spatial correlation tensor and $\Lambda \in \mathbb{R}^{r \times r}$ is a diagonal matrix including the eigenvalues of the problem, with $r = \text{rank}(\mathbf{W}) \leq \min(n, N_t)$. The solution of the eigenvalue problem is equivalent to the computation of a singular value decomposition (SVD) of the matrix \mathbf{W} , so that:

$$\mathbf{W} = \Xi\Sigma\mathbf{V}^T \quad (2.11)$$

where $\Sigma \in \mathbb{R}^{r \times r}$ is a diagonal matrix which contains the singular values of \mathbf{W} listed in order of decreasing magnitude and $\Xi \in \mathbb{R}^{n \times r}$ and $\mathbf{V}^T \in \mathbb{R}^{r \times N_t}$ are orthonormal matrices. Indeed, given eq.(2.11), $\mathbf{R} = \Xi\Sigma\mathbf{V}^T\mathbf{V}\Sigma\Xi^T = \Xi\Sigma^2\Xi^T$ and by right multiplying by Ξ we obtain:

$$\underbrace{\Xi\Sigma^2\Xi^T}_{\mathbf{R}}\Xi = \Xi\Sigma^2, \quad (2.12)$$

where the equality is obtained given the orthonormality of Ξ . Hence, by comparing eq.(2.10) and eq.(2.12), it is evident that the left-singular vectors of \mathbf{W} are the Proper Orthogonal Modes (POMs) resulting from the problem of eq.(2.9) and the singular values of \mathbf{W} are the square roots of the eigenvalues of the related eigenvalue problem (2.10). If we define the diagonal element of Σ as σ_i the rate of “energy” captured by the first m modes is given by

$$E_m = \frac{\sum_{i=1}^m \sigma_i^2}{\sum_{i=1}^r \sigma_i^2} \quad (2.13)$$

In order to obtain a low-rank approximation of the system solution one can choose a cutoff value requiring to contain a given percentage (e.g. $E_m = 99.99\%$ as in references [52], [94], [95]) of the total energy $\sum_{i=1}^r \sigma_i^2$ so that a reduced number of POD modes are retained. The reader interested in further details of the POD method is referred to the works by Towne *et al.* [7] and Cordier *et al.* [92].

From now on, the symbol Φ will denote the POD basis which contains a reduced number of singular modes computed as described in Algorithm 1.

Algorithm 1 POD basis computation.

Input: Snapshot matrix $\mathbf{W} \in \mathbb{R}^{n \times N_t}$

Output: POD basis $\Phi \in \mathbb{R}^{n \times m}$

- 1: Compute the thin SVD: $\mathbf{W} = \Phi \Sigma \mathbf{V}^T$
 - 2: Choose a cutoff condition for $\Phi \in \mathbb{R}^{n \times r}$
 - 3: Truncate the basis $\Phi \in \mathbb{R}^{n \times m}$ with $m \ll r$
-

In this work, the POD will be used to compute the subspace for the approximated solution. This choice is motivated by the numerous advantages that make it particularly suited for the construction of ROMs. Among them, we mention that the POD is a linear method but no linear hypothesis is imposed on the process, so that it does not neglect the nonlinearities of the original vector field. Also, the method is computationally tractable with a rigorous mathematical framework so that it represents a powerful mean for generating low dimensional models of dynamical systems with a large number of degrees of freedom (e.g. fluid mechanics cases). However, some limitations related to POD should not be neglected. For example, the energy truncation of the POD basis still remains arbitrary and there is no guarantee about a fixed value of E_m which can absolutely ensure a good representation of the relevant scales of the system and therefore a good accuracy of the ROM. Finally, the POD basis functions are closely related to the reference data from which they have been derived rather than to the operators of the governing dynamical system. Therefore, a POD basis can properly reproduce the dynamics of a system for the reference condition but may fail if an off-reference condition is envisaged. In such a case, the POD basis needs to be improved through an adaptive or interpolation procedure.

2.4 Galerkin and Petrov-Galerkin projection

As mentioned above, two possible types of projection can be distinguished in the construction of a ROM. In this section, a brief discussion of the Galerkin and Petrov-Galerkin projection is reported. On the basis of eq.(2.6) and of the low-rank POD approximation, by performing a Galerkin projection, that is $\Psi = \Phi$, and given the orthonormality of the basis, we obtain:

$$\frac{d\mathbf{a}(t)}{dt} = \Phi^T \mathbf{f}(\Phi \mathbf{a}(t)) \quad (2.14)$$

2.4. Galerkin and Petrov-Galerkin projection

Evidently, this approach leads to a small system to be integrated in time. However, in order to obtain computational efficiency, it is necessary to reduce the computational complexity of repeatedly computing matrix-vector products of the form $\Phi^T f$, otherwise the method is sometimes referred to as *inflation* in structural mechanics [96] and as *subspace projection* in fluid mechanics [97].

Galerkin projection is the most popular technique for ROMs. In particular for linear problems, under certain conditions, Galerkin projection techniques lead to a priori stable ROMs [86]. Then, in the context of the incompressible Navier-Stokes equations, error estimates for Galerkin projection are provided [90], [98]. However, in some cases and specifically in nonlinear cases this technique has led to unstable and inaccurate long-time responses. Such a scenario might be aggravated for systems with non-symmetric operators like fluid dynamics systems [27], [99]. In this context, Carlberg *et al.* [27] provided a mathematical proof that Galerkin projection ensures a minimal l^2 -norm of the residual of the system at a *time-continuous* level but can lose such a property at a *time-discrete* level. Various techniques have been introduced to improve numerical stability, however the main drawback of the majority of the stabilization methods is that they are formulated *a posteriori* and there are always some parameters to optimize in order to ensure an accurate match with the full order solution. Consequently, the ROM will be stable and accurate only for the particular configuration for which it has been tuned with no guarantee for off-reference conditions. An alternative *a priori* stabilization technique has been proposed by Carlberg *et al.* [100]. If we rearrange eq.(2.6) in a residual form as:

$$\Psi^T R(\mathbf{a}(t)) = \Psi^T \Phi \frac{d\mathbf{a}(t)}{dt} - \Psi^T \mathbf{f}(\Phi \mathbf{a}(t)) = 0 \quad (2.15)$$

it can be shown that a Petrov-Galerkin projection of the system in eq.(2.15) onto the test basis $\Psi = \mathbf{J}\Phi$, where $\mathbf{J} = \partial R(\mathbf{a}(t))/\partial(\Phi \mathbf{a}(t))$, leads to an optimal projection associated to residual minimization at the time-discrete level. This technique has been successfully used for a large-scale compressible fluid-dynamics with turbulence modeling configuration, for which it has been proved that Galerkin projection leads to instability. For theoretical details, equivalence conditions and error analysis the reader is referred to reference [27]. It should be emphasized that the choice of such a type of projection subspace implies the computation of a Jacobian operator and therefore the use of the FOM at each time step of the time integration. Furthermore, the Jacobian might be difficult to compute (or even unavailable) and this undermines the implementation feasibility of the ROM. This problematic entails the formulation by Carlberg *et al.* [95] which introduces in the model reduction a second level of approximation for the tensors involved in the Petrov-Galerkin projection introduced just before. Even though this and other Petrov-Galerkin stabilization techniques have been proposed with some benefits, Galerkin projection still remains the most successfully used technique in the context of nonlinear ROMs [50], [58], [59]. For this reason, in this work, the initial approach to nonlinear ROMs is based on

Galerkin projection, then, other techniques will be explored for the long-term stability issues.

2.5 Masked projections

In this section, the question of the efficient computation of the projected nonlinear operator $\Phi^T f(\Phi \mathbf{a}(t))$ is addressed. As mentioned above, even if at the reduced order level the state $\mathbf{a}(t)$ lives in a low-dimensional subspace of order m , computing such a term would require to lift back to the full n -dimensional subspace systematically and therefore compromises the possibility to devise an offline/online decomposition. Evidently, this negatively affects the computational efficiency of the ROM because the nonlinear term entails computations with costs that scale with the number of the degrees of freedom n of the full system. Among different solutions, masked projections have been successfully used during the last 20 years.

These approaches imply the introduction of a further approximation for the nonlinear term by projecting it onto a subspace that approximates the space generated by the nonlinear function as:

$$f(\Phi \mathbf{a}(t)) \approx U \mathbf{c}(t) \quad (2.16)$$

where $U \in \mathbb{R}^{n \times p}$ is a matrix whose column vectors form a basis for the nonlinear term subspace, and $\mathbf{c}(t) \in \mathbb{R}^p$ is a column vector. The former is involved in the offline phase of the ROM, while the latter is computed during the online phase. The most common choice for the computation of U is to employ a POD of the nonlinear term since it provides an optimal basis that captures the dynamics of the space generated from the snapshots of the nonlinear function at different time steps. In other words, Algorithm 1 (presented on p. 18) can be applied by substituting the input matrix with the following snapshot matrix of the nonlinear term at different time instances

$$F = \begin{bmatrix} f_1(\mathbf{w}(t_0)) & f_1(\mathbf{w}(t_1)) & \dots & f_1(\mathbf{w}(t_{N_t})) \\ f_2(\mathbf{w}(t_0)) & f_2(\mathbf{w}(t_1)) & \dots & f_2(\mathbf{w}(t_{N_t})) \\ \vdots & \vdots & \dots & \vdots \\ f_k(\mathbf{w}(t_0)) & f_k(\mathbf{w}(t_1)) & \dots & f_k(\mathbf{w}(t_{N_t})) \end{bmatrix} \quad (2.17)$$

2.5. Masked projections

so that the output becomes a new POD basis $\mathbf{U} \in \mathbb{R}^{n \times p}$:

$$\mathbf{U} = \begin{bmatrix} \mathbf{U}_{11} & \mathbf{U}_{12} & \dots & \mathbf{U}_{1p} \\ \mathbf{U}_{21} & \mathbf{U}_{22} & \dots & \mathbf{U}_{2p} \\ \vdots & \vdots & \dots & \vdots \\ \mathbf{U}_{k1} & \mathbf{U}_{k2} & \dots & \mathbf{U}_{kp} \end{bmatrix} = [\mathbf{U}_1 \ \mathbf{U}_2 \ \dots \ \mathbf{U}_p] \quad (2.18)$$

The solution of the system of eq.(2.16) for the amplitudes vector $\mathbf{c}(t)$ is overdetermined because it involves n equations for p unknowns. Obviously, solving (or fitting) the system would require the availability of the full scale nonlinear term $\mathbf{f}(\Phi \mathbf{a}(t))$; hence, the computation of $\mathbf{c}(t)$ would be redundant for the purpose of the time integration in eq.(2.14). Therefore, the objective is to solve the system (2.16) provided that the entire term $\mathbf{f}(\Phi \mathbf{a}(t))$ is not available. In this context, the so-called *mask matrix* is employed to select a certain number of equations $f \geq p$ and $f \ll n$ of the system in eq.(2.16) in order to obtain a smaller system to solve. More specifically, if e_{φ_i} is the φ_i -th column of the identity operator of size $n \times n$, the mask-matrix is the column-orthogonal matrix $\mathbf{P} = [e_{\varphi_1}, \dots, e_{\varphi_f}] \in \mathbb{R}^{n \times f}$ so that the following masked subsystem is obtained:

$$\mathbf{P}^T \mathbf{f}(\Phi \mathbf{a}(t)) \approx (\mathbf{P}^T \mathbf{U}) \mathbf{c}(t) \quad (2.19)$$

In particular, when $f = p$ the eq.(2.19) of size $f \times p$ can be inverted (provided the positive definiteness), otherwise a least-square fitting is required. At this stage, it is important to point out that the selection operation $\mathbf{P}^T \mathbf{f}(\Phi \mathbf{a}(t))$ is not a simply “point-wise function”. Consequently, we are not allowed to apply the row-selection matrix \mathbf{P}^T to its argument as $\mathbf{f}(\mathbf{P}^T \Phi \mathbf{a}(t))$. As an example, we consider the common nonlinear 1D advection operator for fluid dynamics $f(w) = w \frac{\partial w}{\partial x}$. Using a finite difference discretization approach with a fixed Δx and a second order approximation of the derivative, the nonlinearity can be written as:

$$\begin{bmatrix} \vdots \\ \vdots \\ w_j \frac{\partial w_j}{\partial x} \\ \vdots \\ \vdots \end{bmatrix} \approx \begin{bmatrix} \ddots & & & & \\ & \ddots & & & \\ & & w_j & & \\ & & & \ddots & \\ & & & & \ddots \end{bmatrix} \begin{bmatrix} \ddots & \ddots & & & \\ \ddots & \ddots & \ddots & & \\ & \frac{-1}{2\Delta x} & 0 & \frac{1}{2\Delta x} & \\ & & \ddots & \ddots & \ddots \\ & & & \ddots & \ddots \end{bmatrix} \begin{bmatrix} \vdots \\ \vdots \\ w_{j-1} \\ w_j \\ w_{j+1} \\ \vdots \end{bmatrix} \quad (2.20)$$

For simplicity, we assume that the operator \mathbf{P}^T selects only the j^{th} row of the nonlinear term and the corresponding selected argument is highlighted in grey in eq.(2.20). It is evident that selecting only the j^{th} row of the argument of the function \mathbf{f} is not sufficient to compute the j^{th} row of the nonlinear term because the evaluation of the spatial derivative approximation by a finite-difference/volume/element derivative

Chapter 2. Construction of a projection-based ROM for nonlinear systems

requires additional values of the state vector (highlighted in orange in eq.(2.20)), depending on the stencil of the discretization scheme. However, we can overcome this issue by taking into account such neighbor mesh points required for the computation of the derivatives of each selected point. In other words, at each step of the *online* time integration, the computation of $\mathbf{P}^T f(\Phi \mathbf{a}(t))$ is performed using the following steps:

1. define $\tilde{\mathbf{P}}^T \in \mathbb{R}^{n \times g}$ as a selector operator which includes the f points selected by \mathbf{P}^T plus the neighbor points required to complete the stencils, so that $g > f$;
2. initialize the field for the selected points and the related stencils $\tilde{\mathbf{P}}^T \Phi \mathbf{a}(t)$;
3. compute the nonlinearity locally as $f_{\mathbf{P}}(\tilde{\mathbf{P}}^T \Phi \mathbf{a}(t))$, where the subscript \mathbf{P} points out that the nonlinear term is computed locally, only for the f selected points using the required stencils.

Such an implementation still remains suitable if we compare the huge number of degrees of freedom normally involved in fluid dynamics applications with respect to a set of degrees of freedom including f points plus their related stencils. In Fig.2.1, an example of a masked projection selection on cells of a finite volume mesh is shown to give the reader an idea of the gain affordable using masked projection.

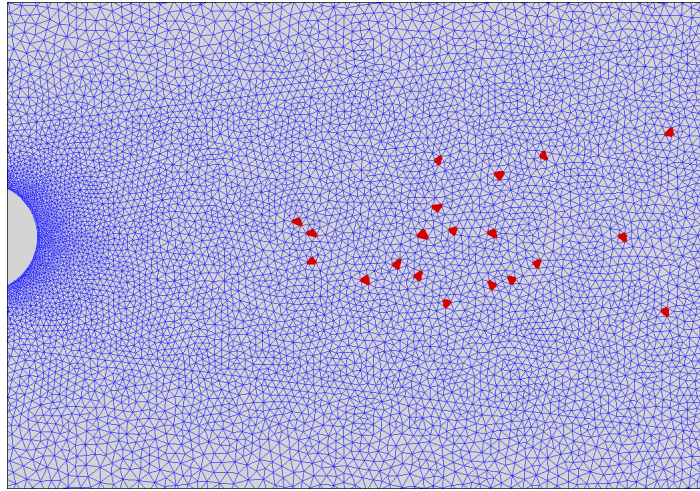


Figure 2.1 An example of a masked projection algorithm resulting in a finite volume selection on the computational domain for the flow around a fixed cylinder at $M = 0.2$ and $Re = 100$, where the number of cells is $n \sim 55000$, the number of selected cells (red triangles) is $f = 20$ and the number of selected cells plus the neighbor to complete the stencils (considering, for example, a second-order approximation) is $g = f + 6 \times f$.

Besides, such an implementation is affordable provided that an intrusive operation into the FOM is performed in order to extract the term $f_{\mathbf{P}}(\tilde{\mathbf{P}}^T \Phi \mathbf{a}(t))$ for some isolated selected narrow stencils.

2.5. Masked projections

The amplitudes related to the nonlinear modes in eq.(2.19) can be obtained by an interpolation (matrix inversion) or a regression (Moore-Penrose pseudo-inversion):

$$\mathbf{c}(t) \approx \begin{cases} (\mathbf{P}^T \mathbf{U})^{-1} \mathbf{f}_P(\tilde{\mathbf{P}}^T \Phi \mathbf{a}(t)), & \text{if } f = p, \\ (\mathbf{U}^T \mathbf{P} \mathbf{P}^T \mathbf{U})^{-1} \mathbf{U}^T \mathbf{P} \mathbf{f}_P(\tilde{\mathbf{P}}^T \Phi \mathbf{a}(t)), & \text{if } f > p. \end{cases} \quad (2.21)$$

and the full nonlinear term is approximated by

$$\mathbf{f}(\Phi \mathbf{a}(t)) \approx \hat{\mathbf{f}}(\Phi \mathbf{a}(t)) = \begin{cases} \mathbf{U}(\mathbf{P}^T \mathbf{U})^{-1} \mathbf{f}_P(\tilde{\mathbf{P}}^T \Phi \mathbf{a}(t)), & \text{if } f = p, \\ \mathbf{U}(\mathbf{U}^T \mathbf{P} \mathbf{P}^T \mathbf{U})^{-1} \mathbf{U}^T \mathbf{P} \mathbf{f}_P(\tilde{\mathbf{P}}^T \Phi \mathbf{a}(t)), & \text{if } f > p. \end{cases} \quad (2.22)$$

so that the following projection based nonlinear ROM is obtained:

$$\frac{d\mathbf{a}(t)}{dt} = \Phi^T \begin{cases} \mathbf{U}(\mathbf{P}^T \mathbf{U})^{-1} \mathbf{f}_P(\tilde{\mathbf{P}}^T \Phi \mathbf{a}(t)), & \text{if } f = p, \\ \mathbf{U}(\mathbf{U}^T \mathbf{P} \mathbf{P}^T \mathbf{U})^{-1} \mathbf{U}^T \mathbf{P} \mathbf{f}_P(\tilde{\mathbf{P}}^T \Phi \mathbf{a}(t)), & \text{if } f > p. \end{cases} \quad (2.23)$$

Chaturantabut *et al.* [42] and more recently Zimmermann *et al.* [41] for the case of overdetermined mask matrix (oblique projection) provide an estimation of the error introduced by the masked projection of eq.(2.22):

$$\|\mathbf{f}(\Phi \mathbf{a}(t)) - \hat{\mathbf{f}}(\Phi \mathbf{a}(t))\|_2 \leq C \|\mathbf{f}(\Phi \mathbf{a}(t)) - \mathbf{U} \mathbf{U}^T \mathbf{f}(\Phi \mathbf{a}(t))\|_2, \quad (2.24)$$

where

$$C = \begin{cases} \|(\mathbf{P}^T \mathbf{U})^{-1}\|_2, & \text{if } f = l. \\ \frac{1}{\sigma_{\min}(\mathbf{P}^T \mathbf{U})} \leq \|(\mathbf{U}^T \mathbf{P} \mathbf{P}^T \mathbf{U})^{-1}\|_2, & \text{if } f > l. \end{cases} \quad (2.25)$$

with $\sigma_{\min}(\mathbf{P}^T \mathbf{U})$ the smallest singular-value of the matrix $\mathbf{P}^T \mathbf{U}$. The reader interested in mathematical proofs is referred to references [42] and [41]. Selecting the optimal set of rows for \mathbf{P} is a combinatorial problem [101]. When feasible, the resolution of such a problem is highly inefficient in terms of computational time for most practical applications and would affect the performance of the model or even would make it more time-consuming than the FOM. Various algorithms of points selection are available in literature that avoid the direct approach to such a combinatorial problem by minimizing sequentially the local growth of the quantity C .

The Discrete Empirical Interpolation Method (DEIM) [42] is the pioneer and one of the most popular selection algorithm which forces the mask operator \mathbf{P} to seek p linearly independent rows of \mathbf{U} such that the growth of the spectral norm of $(\mathbf{P}^T \mathbf{U})^{-1}$ is limited via a greedy search, as implemented in Algorithm 2. Such a selection algorithm has been widely applied and adapted in different scientific applications, as for example in references [102]–[105].

The QDEIM [44] is a recent variation of the DEIM that provides a better upper bound for the condition number C than the DEIM algorithm using a QR factorization with column pivoting of \mathbf{U} (see Algorithm 3).

Algorithm 2 DEIM (Discrete Empirical Interpolation Method). [42]

Input: POD basis of the nonlinear term $U \in \mathbb{R}^{n \times p}$

Output: Masked projection operator $P \in \mathbb{R}^{n \times p}$

- 1: $[|\rho|, \varphi_1] = \max\{|u_1|\}$, $U = [u_1]$, $P = [e_{\varphi_1}]$
 - 2: **for** $i = 2$ to p **do**
 - 3: Solve $P^T U c = P^T u_i$ for c
 - 4: $r = u_i - U c$
 - 5: $[|\rho|, \varphi_i] = \max\{|r|\}$
 - 6: $U \leftarrow [U \ u_i]$, $P \leftarrow [P \ e_{\varphi_i}]$
 - 7: **end for**
-

Algorithm 3 QDEIM [44].

Input: POD basis of the nonlinear term $U \in \mathbb{R}^{n \times p}$

Output: Masked projection operator $P \in \mathbb{R}^{n \times p}$

- 1: $[Q, R, S] = \text{QR decomposition of } (U^T)$
 - 2: $P = S(1 : p)$
-

Both algorithms select a number of interpolation points equal to the number of basis vectors of U such that $f = p$.

Astrid *et al.* [39] introduced the Missing Point Estimation (MPE) with the derivation of an algorithm for the selection of the optimal mask matrix, which allows oversampling (that is $f > p$), using a heuristic optimization inspired by the Gappy POD method [40]. Since it is highly costly, the standard MPE entailed the recent work by Zimmermann *et al.* [41] who derives a fast and more efficient surrogate of the standard MPE algorithm that slightly raises the error indicator C . This accelerated surrogate algorithm reduces to $O(np^2)$ the computational cost per iteration, compared to a cost larger than $O(np^3)$ with the standard MPE. Basically, in order to find the suitable points for the masked projection, the accelerated MPE sorts an arbitrary set of candidate vectors according to certain properties of their components preventing the resolution of an eigenvalue problem. However, the computational cost still depends on the number of degrees of freedom of the system n which could be very large depending on the related test case.

Another approach which approximates the nonlinear term with a sparse oversampling is the Gauss-Newton with approximated tensors (GNAT) method by Carlberg *et al.* [95], [100]. It achieves a dimension reduction by a Petrov-Galerkin projection scheme along with a gappy POD technique for approximating the nonlinear function and the Jacobian matrix. In this context, the work of de Pando *et al.* [25] is of particular importance since they present an efficient implementation of the DEIM method for nonlinear reduction of a compressible flow solver. In particular, they exploit an efficient procedure for evaluating matrix-vectors products involving the Jacobian for the construction of a nonlinear ROM using DEIM. This work is ad-

2.5. Masked projections

dressed to high-order numerical solvers for which the resulting operators are dense and characterized by wide stencils. Both the GNAT [100] and the approach of de Pando *et al.* [25] seem to be concrete alternatives to undertake the application scenarios envisaged in this thesis. However, they require the use of the Jacobian which is not always available, especially when dealing with industrial codes.

In the construction of a reduced order model for nonlinear systems, usually we have to deal with a huge number n of degrees of freedom so that it is better to avoid selection algorithms whose computational cost depends on n . Consequently, the DEIM (as well as its recent alternative QDEIM) is appropriate since it implies a computational cost of only $\sim \mathcal{O}(p^3)$ where p is the number of retained nonlinear modes, usually quite small. But, as mentioned above, this kind of algorithms provides a **number of interpolation points equal to the number of basis vectors** resulting in a limiting factor, since oversampling is beneficial or even explicitly required for some applications. To avoid this problem, an adaptation of the DEIM algorithm is proposed by Zhou [106]. At each iteration, one can observe that the greedy search of the interpolation points is done over the entire nonlinear mode vectors of U (see eq.(2.18)) without any distinction among the k different state variables. This leads to an important sensitivity of the algorithm to different scales and dynamics involved in the nonlinear system. The greedy selection algorithm can be applied to the nonlinear modes of the conservative variables separately by exploiting independently the physical variables of the system. In other words, the DEIM (or QDEIM) algorithm is applied block-wise to the matrix U . Consequently, the number of the selected rows is equal to pb with $b \in \mathbb{N}$ the chosen number of blocks. For the case of Zhou [106], $b = k = 4$ is chosen equal to the number of physical unknowns of the system for the two-dimensional Navier-Stokes system. This choice leads to an approach referred to as *scalar-valued DEIM*.

Algorithm 4 Block-wise DEIM/QDEIM (BDEIM/BQDEIM).

Input: Nonlinear snapshot matrix $U \in \mathbb{R}^{n \times p}$, number of conservative variables k , discretized domain dimension N_x

Output: Masked projection operator $\mathbf{P} \in \mathbb{R}^{n \times kp}$

```

1:  $\mathbf{P} = [ ]$ 
2: for  $i = 0$  to  $(k - 1)$  do
3:    $U^{(i)} = U[(N_x \cdot i) : (N_x \cdot (i + 1)), :]$ 
4:    $\mathbf{P}^{(i)} = \text{DEIM/QDEIM}(U^{(i)})$ 
5:    $\mathbf{P} \leftarrow [\mathbf{P} \ \mathbf{P}^{(i)}]$ 
6: end for

```

In the same way, the value of b can be increased, enabling the selection of a higher number of interpolation (or fitting) points. In this work, the approach of Zhou [106] is referred simply as block-wise masked projection and it is implemented in Algorithm 4. It will be explicitly reported when the value of b is higher than the number

Chapter 2. Construction of a projection-based ROM for nonlinear systems

Method	Computational cost
MPE standard [39]	$\sim O(np^3)$
MPE improved [41]	$O(np^2)$
DEIM [42]/QDEIM [44]	$O\left(\frac{p(p+1)(2p+1)}{6}\right)$
DEIM/QDEIM with k block	$O\left(\frac{p(p+1)(2p+1)}{6}k\right)$

Table 2.1 Computational cost associated to the different masked projection algorithms, given n equal to the number of degree of freedom of the system and p the number of the retained nonlinear modes.

of unknown variables k .

With the increase of the number of blocks the block-wise masked-projection is still suboptimal and provides a better upper-bound with respect to the standard DEIM (or QDEIM). In table 2.1 the computational costs of the most common points selection procedures are reported and compared with the adaptations presented just above. As can be seen, the block adaptation is well suited for CFD applications, that is when $n \gg p$.

Other selection procedures have been introduced in literature addressing particular test cases or problems in the formulation of ROMs [43], [103], [104], [107]. Anyway, to the knowledge of the author, the whole of selection algorithms presented so far represents the most relevant and successful methods in the construction of nonlinear ROMs for fluid mechanics which is the field of interest of this thesis.

It is worth mentioning the work of Freno *et al.* [59] for nonlinear ROMs which addresses complex fluid dynamics test cases involving moving discontinuities. They do not use any kind of masked projection in the construction of the ROM but focuses on the difficulties related to the POD bases used for the approximation. The ROM still remains costly because the nonlinear term is projected at each time step. However, in highly nonlinear cases, it is quite possible that the additional approximation introduced by the masked projection must be avoided in order to ensure the performance of the ROM.

2.6. Practical implementation of a nonlinear reduced order model using masked projection

2.6 Practical implementation of a nonlinear reduced order model using masked projection

A summary of the nonlinear ROM procedures employed in the present work and leading to the ROM described in eq.(2.23) is presented in Algorithm 5. All steps of the offline phase involve the procedure presented in the previous sections.

Algorithm 5 Nonlinear model-order reduction (eq.(2.23))

Offline phase:

- 1: Generate snapshot sequences $\mathbf{W} \in \mathbb{R}^{n \times N_t}$ for the solution and $\mathbf{F} \in \mathbb{R}^{n \times N_t}$ for the nonlinear term using the FOM solver
- 2: Construct $\Phi \in \mathbb{R}^{n \times m}$ using POD via Algorithm 1 with input \mathbf{W}
- 3: Construct $\mathbf{U} \in \mathbb{R}^{n \times p}$ using POD via Algorithm 1 with input \mathbf{F}
- 4: Construct masked projection matrix \mathbf{P} via Algorithm 2,3 or 4 with input \mathbf{U}
- 5: **if** Algorithm 2 or 3 is chosen **then**
- 6: $\mathbf{P} \in \mathbb{R}^{n \times p}$
- 7: Compute the matrix operations of eq.(2.23) once and for all: $\Phi^T \mathbf{U} (\mathbf{P}^T \mathbf{U})^{-1}$
- 8: **else if** Algorithm 4 is chosen **then**
- 9: $\mathbf{P} \in \mathbb{R}^{n \times kp}$
- 10: Compute the matrix operations of eq.(2.23) once and for all: $\Phi^T \mathbf{U} (\mathbf{U}^T \mathbf{P} \mathbf{P}^T \mathbf{U})^{-1} \mathbf{U}^T \mathbf{P}$
- 11: **end if**
- 12: Construct the nonlinear operator $f_{\mathbf{P}}(\tilde{\mathbf{P}}^T \Phi \mathbf{a}(t))$

Online phase:

Input: The initial value for \mathbf{a}_0

Output: The time discrete response for the vector amplitudes $\mathbf{a} \in \mathbb{R}^{m \times N_t}$

- 1: Compute $f_{\mathbf{P}}(\tilde{\mathbf{P}}^T \Phi \mathbf{a}_0)$
 - 2: Integrate in time eq.(2.23) for \mathbf{a}_1
 - 3: $\mathbf{a} \leftarrow [\mathbf{a}_1]$
 - 4: **for** $i = 2$ to N_t **do**
 - 5: Compute $f_{\mathbf{P}}(\tilde{\mathbf{P}}^T \Phi \mathbf{a}_{i-1})$
 - 6: Integrate in time eq.(2.23) for \mathbf{a}_i
 - 7: $\mathbf{a} \leftarrow [\mathbf{a} \ \mathbf{a}_i]$
 - 8: **end for**
-

It should be noted that the construction of the nonlinear operator $f_P(\tilde{\mathbf{P}}^T \Phi \mathbf{a}(t))$ (step 12 of the *offline* phase) here is included in the *offline* phase because we considered dynamical systems governed by a general autonomous system. If now we consider a non-autonomous system in the semi-discretized form:

$$\frac{d\mathbf{w}(t)}{dt} = \mathbf{f}(\mathbf{w}(t), t) \quad (2.26)$$

the nonlinear function \mathbf{f} depends not only on the state vector \mathbf{w} , but also on time t . This would imply one main difference in the construction of the masked projection operator presented in Algorithm 5. Indeed, for autonomous systems the operator $f_P(\tilde{\mathbf{P}}^T \Phi \mathbf{a}(t))$ can be constructed in the *offline* phase and its evaluation during the *online* phase is straightforward. On the contrary, for non-autonomous systems, the respective operator $f_P(\tilde{\mathbf{P}}^T \Phi \mathbf{a}(t), t)$ cannot be constructed *offline* once and for all because the nonlinear function depends on time. Consequently, it must be updated at each time step of the time integration which corresponds to an additional step to the *online* phase of the nonlinear model-order reduction.

Concerning the ROM time integration, in principle, the same time integrator as the one used in the FOM could be the most appropriate choice. In most cases, implicit solvers are used at the full order level and this would require the computation of the Jacobian at each ROM time step. On the contrary, using an explicit solver would typically require very small time steps compared to those used with implicit solvers. Apparently, this amounts to a substantial problem: on the one hand, we want to avoid the use of implicit solvers because of the related computational complexity, and on the other hand, the use of an explicit solver would require a huge number of very small time steps in order to cover the FOM time period, thus undermining the computational efficiency of the ROM. In this scenario, the POD plays a primary role. Indeed, the energy truncation applied in the POD basis computation (see Algorithm 1) accounts for a filtering of those modes related to high frequency dynamics of the system. For this reason, it is reasonable (and quite common in literature) to use explicit solver with moderately large time steps for ROMs. In this work, integration in time is carried out using a 4th order Runge-Kutta scheme and it will be explicitly specified when a different time integrator is used.

2.7 Construction of a reduced order model for periodic flows

The nonlinear ROM presented until now is general and can be used for periodic as well as for arbitrary transient solutions. However, for the simulation of time periodic solutions only the periodic steady state is of concern and furthermore the long-term behaviour of the projection based ROM could be challenging in terms of

2.7. Construction of a reduced order model for periodic flows

stability. The most evident issue is related to the approximation error that accumulates over the time integration leading to divergence in most cases. Another explanation is that the projection based ROMs filter the low energy modes as a result of the POD truncation so that they fail to account for the dynamics related to those unresolved modes and the interaction between resolved and unresolved modes [108]. To overcome this problem, different solutions like the addition of artificial viscosity or the use of data-driven closure terms have been investigated [108]–[110]. Anyway, the long term stability of fully non-linear time-dependent problems is still an open question.

Another solution would be to consider a different FOM that intrinsically takes into account the periodicity of the solution at the full order level. Indeed, classical unsteady techniques can be avoided when considering systems that are periodic in time. Harmonic methods take advantage of the time periodicity of a problem to decompose its solution into a mean part plus several harmonic contributions and thus simplify a full unsteady problem into a set of coupled steady problems. Different harmonic methods exist in literature and they consider variables either in the time-domain or in the frequency-domain. In the context of fluid dynamics, an efficient time-domain method dedicated to time-periodic flows has been developed. Following the direction suggested by Hall *et al.* [111], Gopinath *et al.* [112] introduced the Time Spectral Method (TSM), which casts the unsteady governing equations in a set of coupled steady equations. More specifically, a Fourier representation with N harmonics is used for the time evolution of the system so that the periodicity is directly enforced and hence the solution does not have to evolve through transients to reach a periodic steady-state. Then, casting back the equations into the time domain, the time derivative appears as a high-order central difference formula coupling a set of $2N + 1$ steady equations related to different instances corresponding to a uniform sampling of the time period. These steady equations can then be solved using standard steady methods with convergence acceleration techniques such as local time stepping and multigrid. The convergence of a steady computation is better mastered than the transient needed by an unsteady computation to reach the periodic state. This method proved to be efficient for periodic problem computations such as vortex shedding [113], flutter and turbomachinery applications [62], [111], [114]–[116] for example.

2.7.1 Time Spectral Method

The Nyquist-Shannon theorem states that $2N + 1$ time instances evenly distributed in the time period $T = 2\pi/\omega$ of a signal, where ω is the oscillating frequency, allow to compute at best the N -th harmonic of the fundamental frequency. Therefore,

Chapter 2. Construction of a projection-based ROM for nonlinear systems

considering the Fourier series decomposition of $\mathbf{w}(t)$ truncated to the N -th harmonic

$$\mathbf{w}(t) = \sum_{k=-N}^N \hat{\mathbf{w}}_k \exp(ik\omega t) \quad (2.27)$$

the k -th Fourier coefficient $\hat{\mathbf{w}}_k$ can be accurately computed using the Discrete Fourier Transform (DFT) over $2N + 1$ time instances evenly distributed over the time period. The analytic expression of this discrete DFT is given by:

$$\hat{\mathbf{w}}_k = \frac{1}{2N + 1} \sum_{j=0}^{2N} \mathbf{w}_j \exp(-ik\omega j\Delta t) \quad (2.28)$$

with $\mathbf{w}_j = \mathbf{w}(j\Delta t)$ and $\Delta t = T/(2N + 1)$. The main idea of the time domain spectral methods is to look for these solutions \mathbf{w}_j in order to evaluate the solution $\mathbf{w}(t)$ at any time t in the period using eq.(2.27). Conversely the Inverse Discrete Fourier Transform (IDFT) allows to retrieve \mathbf{w}_n using the harmonics:

$$\mathbf{w}_j = \sum_{k=-N}^N \hat{\mathbf{w}}_k \exp(ik\omega j\Delta t) \quad (2.29)$$

These relations can be written in matrix form:

$$\widehat{\mathbf{W}} = \mathcal{E}\mathbf{W} \quad \text{and} \quad \mathbf{W} = \mathcal{E}^{-1}\widehat{\mathbf{W}} \quad (2.30)$$

where $\widehat{\mathbf{W}} = (\hat{\mathbf{w}}_{-N}, \hat{\mathbf{w}}_{-N+1}, \dots, \hat{\mathbf{w}}_N)^T$ and $\mathbf{W} = (\mathbf{w}_0, \mathbf{w}_1, \dots, \mathbf{w}_{2N})^T$. The general term matrices of the DFT and IDFT are given by:

$$\mathcal{E}_{k,j} = \frac{1}{2N + 1} \exp\left(-2i\pi k \frac{j}{2N + 1}\right), \quad \mathcal{E}_{k,j}^{-1} = \exp\left(2i\pi k \frac{j}{2N + 1}\right) \quad (2.31)$$

With these premises, the Fourier series of eq.(2.1) is obtained:

$$\sum_{k=-N}^N (ik\omega \hat{\mathbf{w}}_k + \hat{\mathbf{f}}_k) \exp(ik\omega t) = 0 \quad (2.32)$$

where $\hat{\mathbf{w}}_k$ and $\hat{\mathbf{f}}_k$ are the Fourier coefficients of \mathbf{w} and \mathbf{f} . The complex exponential family forming an orthogonal basis, the only way for eq.(2.32) to be true is that each of $(2N + 1)$ components $(ik\omega \hat{\mathbf{w}}_k + \hat{\mathbf{f}}_k)$ is zero. Therefore, by noting $\hat{\mathbf{f}}(\mathbf{W}) = (\hat{\mathbf{f}}_{-N}, \hat{\mathbf{f}}_{-N+1}, \dots, \hat{\mathbf{f}}_N)^T$, the eq.(2.32) can be rewritten as the equivalent system:

$$\mathcal{D}\mathcal{E}\mathbf{W} - \hat{\mathbf{f}}(\mathbf{W}) = 0 \quad (2.33)$$

where \mathcal{D} is a diagonal matrix with elements defined by $\mathcal{D}_{kk} = ik\omega$. These equations are not independent due to the non linearity of the operator $\hat{\mathbf{f}}(\mathbf{W})$: indeed $\hat{\mathbf{f}}_k$

2.7. Construction of a reduced order model for periodic flows

cannot be computed directly from $\hat{\mathbf{w}}_k$, but only from the nonlinear function in the time domain $f(\mathbf{w})$. As a result, a continuous going back and forth from the time to the frequency domain is required in order to solve eq.(2.33). Evidently, such an elaborated procedure may represent a non-negligible computational burden when dealing with complex time domain solvers like CFD solvers. Alternatively, the application of the IDFT to $\hat{f}(\mathbf{W})$ leads to the original expression f because the DFT is bijective. Besides, the IDFT of the term $\mathcal{D}\mathcal{E}\mathbf{W}$ produces a source term that couples all the time instants:

$$\mathcal{E}^{-1} \left(\mathcal{D}\mathcal{E}\mathbf{W} - \hat{f}(\mathbf{W}) \right) = \underbrace{\mathcal{E}^{-1} \mathcal{D}\mathcal{E}\mathbf{W}}_{D_t(\mathbf{W})} - f(\mathbf{W}) = 0 \quad (2.34)$$

Let us denote D_t the spectral operator approximating the physical derivative d/dt of eq.(2.1):

$$D_t(\mathbf{W}) = \mathcal{E}^{-1} \mathcal{D}\mathcal{E}\mathbf{W} \approx \frac{d\mathbf{W}}{dt} \quad (2.35)$$

Gopinath and Jameson Gopinath *et al.* [112] have provided a detailed expression of this matrix spectral operator for each instant j :

$$D_t \mathbf{w}_j = \sum_{i=-N}^N d_i \mathbf{w}_{j+i} \quad (2.36)$$

with

$$d_i = \begin{cases} \frac{\pi}{T} (-1)^{i+1} \csc\left(\frac{\pi i}{2N+1}\right) & , \quad i \neq 0 \\ 0 & , \quad i = 0 \end{cases} \quad (2.37)$$

Note that $d_{-i} = -d_i$ and $d_i = d_{i-N}$, so that the coefficients d_i need to be computed for $i \in [0; N]$ only. Using eq.(2.36) to approximate the time derivative at t_j , the TSM version of system (2.1) becomes

$$D_t(\mathbf{w}_j) - f(\mathbf{w}_j) = 0 \quad , \quad 0 \leq j \leq 2N + 1. \quad (2.38)$$

The resolution of eq.(2.38) can be challenging and pseudo-time stepping techniques are used to time march the equations to the steady-state solutions:

$$\frac{\partial \mathbf{w}_j}{\partial \tau_j} + D_t(\mathbf{w}_j) - f(\mathbf{w}_j) = 0 \quad , \quad 0 \leq j \leq 2N + 1. \quad (2.39)$$

The term $D_t(\mathbf{w}_j)$ appears as a source term that represents a high order formulation of the initial time derivative in eq.(2.1). For stability reasons, the computation of the local time step is modified to take into account such an additional source term. Hall *et al.* [62] observed that the convergence of the method speeds down for increasing N . This issue leads to the use of significantly small local time steps when explicit schemes are used to carry out the pseudo-time integration. Conversely, implicit

Chapter 2. Construction of a projection-based ROM for nonlinear systems

schemes are more stable and allow larger local time steps. For the sake of clarity, the eq.(2.39) is written as:

$$\frac{\partial \mathbf{W}}{\partial \tau} + R_{TSM}(\mathbf{W}) = \mathbf{0} \quad (2.40)$$

where, $R_{TSM}(\mathbf{W}) = D_t(\mathbf{W}) - \mathbf{f}(\mathbf{W})$. Noting the increment $\Delta \mathbf{W} = \mathbf{W}^{q+1} - \mathbf{W}^q$, the linearization of $R_{TSM}(\mathbf{W}^{q+1})$ is

$$R_{TSM}(\mathbf{W}^{q+1}) = R_{TSM}(\mathbf{W}^q) + \mathbf{J}\Delta \mathbf{W} + O(\Delta \mathbf{W}^2). \quad (2.41)$$

Equations (2.40) and (2.41) lead to the following linear system

$$\left(\frac{\mathbf{I}}{\Delta \tau} + \mathbf{J} \right) \Delta \mathbf{W} = -R_{TSM}(\mathbf{W}^q). \quad (2.42)$$

The definition of the Jacobian term \mathbf{J} leads to two different formulations known as semi-implicit and fully-implicit formulations.

2.7.1.1 Semi-implicit formulation

This approach is the results of the definition $\mathbf{J} = -\partial \mathbf{f}(\mathbf{W})/\partial \mathbf{W}$ leading to the augmented system

$$\begin{pmatrix} \boxed{\frac{\mathbf{I}}{\Delta \tau_0} + J_0} & 0 & \dots & 0 \\ 0 & \boxed{\frac{\mathbf{I}}{\Delta \tau_1} + J_1} & \ddots & \vdots \\ \vdots & \ddots & \ddots & 0 \\ 0 & \dots & 0 & \boxed{\frac{\mathbf{I}}{\Delta \tau_{2N}} + J_{2N}} \end{pmatrix} \begin{pmatrix} \Delta \mathbf{w}_0 \\ \Delta \mathbf{w}_1 \\ \vdots \\ \Delta \mathbf{w}_{2N} \end{pmatrix} = - \begin{pmatrix} R_{TSM}(\mathbf{w}_0^q) \\ R_{TSM}(\mathbf{w}_1^q) \\ \vdots \\ R_{TSM}(\mathbf{w}_{2N}^q) \end{pmatrix}, \quad (2.43)$$

where $J_j = -\partial \mathbf{f}(\mathbf{w}_j)/\partial \mathbf{w}_j$. In other words, in such an approach, only the nonlinear term of eq.(2.39) is linearized, but not the source term $D_t(\mathbf{w}_j)$. Eq.(2.43) is block diagonal and a LU-SSOR algorithm can be applied independently on each instant j . This is clearly an advantage from a numerical point of view, however Sicot *et al.* [115] show that convergence may not be achieved easily unless small time steps are used when increasing number of harmonics N .

2.7. Construction of a reduced order model for periodic flows

2.7.1.2 Fully-implicit formulation

This approach is the results of the more general definition $\mathbf{J} = \partial R_{TSM}(\mathbf{W})/\partial \mathbf{W}$ leading to the augmented system

$$\begin{pmatrix} \boxed{\frac{I}{\Delta\tau_0} + J_0} & d_1 I & \dots & d_{-1} I \\ d_{-1} I & \boxed{\frac{I}{\Delta\tau_1} + J_1} & \ddots & \vdots \\ \vdots & \ddots & \ddots & d_1 I \\ d_1 I & \dots & d_{-1} I & \boxed{\frac{I}{\Delta\tau_{2N}} + J_{2N}} \end{pmatrix} \begin{pmatrix} \Delta \mathbf{w}_0 \\ \Delta \mathbf{w}_1 \\ \vdots \\ \Delta \mathbf{w}_{2N} \end{pmatrix} = - \begin{pmatrix} R_{TSM}(\mathbf{w}_0^q) \\ R_{TSM}(\mathbf{w}_1^q) \\ \vdots \\ R_{TSM}(\mathbf{w}_{2N}^q) \end{pmatrix}, \quad (2.44)$$

where, analogously to eq.(2.43), $J_j = -\partial f(\mathbf{w}_j)/\partial \mathbf{w}_j$. The new left-hand side matrix is no longer block-sparse and couples all the increments $\Delta \mathbf{w}_j$ of all instants j . Furthermore, as $d_m = -d_{-m}$ the sum of the coefficients d_m vanishes along the diagonals so that the left-hand side matrix is diagonally dominant. This allows the use of an iterative Block-Jacobi method, for the resolution of the fully implicit formulation. The reader interested to the mathematical derivation of this method is referred to the reference [115]. The presented implicit time integration enables much larger time steps and make the TSM more efficient.

In this work, semi-implicit and fully-implicit TSM implementations approaches are used. It should be stressed that the TSM is defined on the basis of two strong hypotheses. First, the solution must be periodic with a given a priori known period T . This can be considered a very strong hypothesis, but, in the context of this work, and of a variety of internal and external aeronautical applications the envisaged fluid dynamics meets this requirement. Furthermore, this method (together with its reduced version presented in the next section) is intrinsically immune to long-term stability which makes it really appealing. Second, an arbitrary number N of harmonics for the Fourier series approximation must be chosen. However, it is reasonable to select a small number (e.g., from 5 to 10) of harmonics to cover a wide range of the periodic phenomena involved in aeronautical applications.

2.7.2 Reduced Order Time Spectral Method

In this section we introduce a Reduced Order Time Spectral Method (ROTSM) which implies a lower computational complexity and a better convergence performance than the Full Order Time Spectral Method (FOTSM).

For the construction of the ROTSM, analogously to Algorithm 1 (presented at p.18), a POD of the solutions of the TSM at different time instants $\mathbf{W} \in \mathbb{R}^{n \times (2N+1)}$ is

Chapter 2. Construction of a projection-based ROM for nonlinear systems

performed without any cutoff operation in order to obtain the basis $\Phi \in \mathbb{R}^{n \times (2N+1)}$. The obtained POD modes span a subspace that contains the TSM solutions. In such a case, no energy truncation of the POD basis is done. Then the solution is expressed as:

$$\mathbf{w}_j = \Phi \mathbf{a}_j, \quad 0 \leq j < 2N + 1. \quad (2.45)$$

By substituting eq.(2.45) in eq.(2.38) the following coupled system of $(2N + 1) \times n$ steady equations involving $(2N + 1)^2$ unknowns is obtained:

$$\mathcal{R}_{TSM}(\mathbf{a}_j) = D_t \Phi \mathbf{a}_j - \mathbf{f}(\Phi \mathbf{a}_j) = 0, \quad 0 \leq j < 2N + 1 \quad (2.46)$$

A steady-state solution is typically sought using a pseudo-time stepping technique. This approach is a common choice when starting from a poor initial guess (such as uniform flow). However, when a good starting guess is available it can be more efficient to apply the Newton's method directly. Applying Newton's method to solve the fully coupled system (2.46) with all amplitudes gathered in vector $\mathbf{a} = (\mathbf{a}_0, \mathbf{a}_1, \dots, \mathbf{a}_{2N+1}) \in \mathbb{R}^{(2N+1)^2}$ results in the following iterations. For $k = 1 \dots K$

$$\mathbf{A}^k \Delta \mathbf{a}^k = -\mathcal{R}_{TSM}(\mathbf{a}^k), \quad (2.47)$$

with K determined by the threshold of a convergence criterion. The resulting Jacobian matrix is defined as:

$$\mathbf{A}^k = \mathbf{J}^k \Phi_D = \begin{bmatrix} \mathbf{J}_{f_0}^k & d_1 \mathbf{I} & \dots & d_{-1} \mathbf{I} \\ d_{-1} \mathbf{I} & \mathbf{J}_{f_1}^k & \ddots & \vdots \\ \vdots & \ddots & \ddots & d_1 \mathbf{I} \\ d_1 \mathbf{I} & \dots & d_{-1} \mathbf{I} & \mathbf{J}_{f_{(2N)}}^k \end{bmatrix} \begin{bmatrix} \Phi & \mathbf{0} & \dots & \mathbf{0} \\ \mathbf{0} & \Phi & \ddots & \vdots \\ \vdots & \ddots & \ddots & \mathbf{0} \\ \mathbf{0} & \dots & \mathbf{0} & \Phi \end{bmatrix}, \quad (2.48)$$

with the Jacobian $\mathbf{J}_{f_j} = \partial \mathbf{f}(\mathbf{a}_j) / \partial (\Phi \mathbf{a}_j)$. The matrix dimensions involved in the previous equation are: $\mathbf{J}^k \in \mathbb{R}^{[n(2N+1)]^2}$, $\Phi_D \in \mathbb{R}^{n(2N+1) \times (2N+1)^2}$. It is worth recalling that n is the number of degrees of freedom of the system and N is the number of retained harmonics for the TSM, thus $n \gg N$. As a consequence, the construction of matrix \mathbf{A}^k can be very computationally expensive, but, since matrix Φ_D is block-diagonal, it can be constructed block-wise. The system of equations (2.47) can be solved in a least-square sense by using the Gauss-Newton algorithm:

$$\Delta \mathbf{a}^k = \left\{ \Delta \mathbf{a}^k \in \mathbb{R}^{(2N+1)^2} : \|\mathbf{A}^k \Delta \mathbf{a}^k + \mathcal{R}_{TSM}(\mathbf{a}^k)\|_2^2 \text{ is minimized} \right\}, \quad (2.49)$$

that is:

$$\Delta \mathbf{a}^k = -(\Phi_D^T \mathbf{J}^{kT} \mathbf{J}^k \Phi_D)^{-1} (\Phi_D^T \mathbf{J}^{kT}) \mathcal{R}_{TSM}(\mathbf{a}^k). \quad (2.50)$$

It can be noted that the previous resolution of the Gauss-Newton algorithm is equivalent to the resolution of the Petrov-Galerkin projection of the system in eq.(2.47) onto the subspace $\mathcal{L} = (\mathbf{J}^k \Phi_D)$.

2.7. Construction of a reduced order model for periodic flows

Alternatively, the system in eq.(2.47) can be projected (using a Galerkin projection) onto the subspace $\mathcal{L} = \Phi_D$. Such a projection leads to a much simpler system of $2N + 1$ equations in $2N + 1$ unknowns:

$$(\Phi_D^T \mathbf{J}^k \Phi_D) \Delta \mathbf{a}^k = -\Phi_D^T \mathcal{R}_{TSM}(\mathbf{a}^k), \quad (2.51)$$

that can be easily solved by matrix inversion provided the positive definiteness of the matrix $(\Phi_D^T \mathbf{J}^k \Phi_D) \in \mathbb{R}^{(2N+1)^2 \times (2N+1)^2}$:

$$\Delta \mathbf{a}^k = -(\Phi_D^T \mathbf{J}^k \Phi_D)^{-1} \Phi_D^T \mathcal{R}_{TSM}(\mathbf{a}^k). \quad (2.52)$$

On the one hand, from a computational point of view, such an approach is much more beneficial with respect to the one derived in eq.(2.50) because most of the matrix operations of size $(2N + 1) \times n$ that must be computed at each iteration are avoided. On the other hand, as discussed in Section 2.4, using a Galerkin projection, convergence problems may occur.

The presented ROTSM is beneficial for two important aspects. First, the solution is sought in a subspace that is a priori suitable as a result of the POD so that the number of unknown variables switches from n to $2N + 1$. Second, the matrices involved in the numerical resolution have smaller dimensions. Indeed, if we consider the Jacobian matrix A^k , it involves $(2N + 1) \times n$ columns for the FOTSM, whereas it reduces to only $(2N + 1)^2$ for the ROTSM.

To conclude, it should be noted that the ROTSM should not be referred to as a reduced order model in a strict sense because there is not any truncation in the construction of the basis Φ . However, the reduced order approximation can be related to the Fourier series decomposition truncation at the basis of the FOTSM and the ROTSM may help reducing the computational time and improving the rate of convergence of the FOTSM that is an excellent and well-suited property when dealing with nonlinear, time periodic, unsteady problems.

Definition of the initial guess

The success of the presented ROTSM depends on the quality of the starting guess \mathbf{a}^0 since a poor starting guess would require time marching techniques in order to improve the convergence of the solution. In the absence of other suitable alternatives, the FOTSM initial guess is set as a uniform solution \mathbf{w}_u . If we define \mathbf{w}_j^* as the exact solution of system (2.46), the quality of the ROTSM initial guess is represented by the error:

$$\mathbf{e} = \mathbf{w}_j^* - \mathbf{w}_u = \mathbf{e}_{\parallel} + \mathbf{e}_{\perp} = \underbrace{\mathbf{w}_j^* - \Phi(\Phi^T \mathbf{w}_{fs})}_{\mathbf{e}_{\parallel}} - \underbrace{(I - \Phi\Phi^T)\mathbf{w}_{fs}}_{\mathbf{e}_{\perp}} \quad (2.53)$$

where $\mathbf{e}_{\parallel} \in \text{span}(\Phi)$ and $\mathbf{e}_{\perp} \in \text{span}(\Phi^{\perp})$. By construction of the POD basis, the solution $\mathbf{w}_j^* \in \text{span}(\Phi)$. As a consequence, if we define the initial guess as the projection

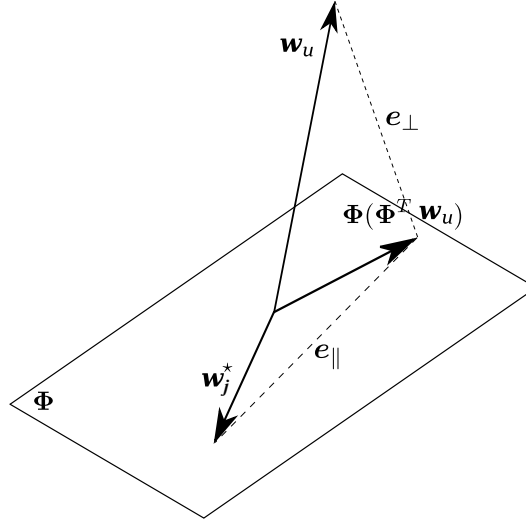


Figure 2.2 A graphical description of the initialization of the ROTSM by projecting onto the POD subspace.

of the snapshot w_u onto the POD basis Φ

$$a_j^0 = \Phi^T w_u \quad (2.54)$$

the contribution of e_{\perp} is eliminated from the first iteration onwards, resulting in a more suitable initial guess for the Newton algorithm. The mentioned procedure is graphically depicted in Fig.2.2.

2.8 Conclusions

In this chapter, the mathematical formulation of the different tools required for the construction of a ROM for a general nonlinear system has been presented. The POD turned out to be appropriate in order to construct a low-rank approximation for data characterized by a moderate time history and a high spatial resolution. Then, the choice of a Galerkin projection, with respect to a Petrov-Galerkin projection, has been discussed. In order to complete the construction of the ROM, it has been necessary to reduce the computational complexity of the projected nonlinear term. To this end, masked projection techniques have been introduced in order to provide an approximation for the projected nonlinear term by interpolating (or fitting) it onto a small subset of the spatial domain. Finally, in the particular case of periodic systems at a given period T , an efficient time-domain method for periodic systems has been presented together with a new formulation for its reduced order counterpart.

In the next chapters, the presented nonlinear ROM will be used and eventually adapted for aerodynamics and then aeroelastic applications envisaged in this thesis.

Construction and implementation of a nonlinear projection-based ROM for the compressible Navier-Stokes equations

Contents

3.1	Introduction	38
3.2	Formulation of the compressible Navier-Stokes equations	38
3.3	Computation of the POD modes of a flow around a fixed cylinder at low Reynolds number	41
3.3.1	Numerical simulation of the flow around a fixed cylinder at low Reynolds	41
3.3.2	Computation of the POD modes	43
3.4	Numerical integration of the nonlinear projection-based ROM of a flow around a fixed cylinder at low Reynolds	47
3.4.1	Effect of the time-step on the response of the projection-based nonlinear ROM	48
3.4.2	Effect of the POD basis truncation on the response of the projection-based nonlinear ROM	49
3.4.3	Choice of the formulation for the projection-based nonlinear ROM with masked projection	50
3.4.4	Influence of the number of the DEIM interpolation points	54
3.5	Assessment of the performance of the masked projection techniques in fluid dynamics applications	55
3.5.1	Zero incidence transonic flow around a NACA 0012 airfoil at moderate Reynolds number	56
3.5.2	High incidence flow around a NACA 0012 airfoil	62
3.6	Conclusions	67

3.1 Introduction

The aim of this chapter is to go through the processes for the construction of the nonlinear ROM (presented in Chapter 2) in the case of fluid mechanics systems. This will be the basis for the further objectives of this dissertation. For this purpose, firstly the fluid mechanics governing equations are presented in a semi-discretized form and will represent the FOM to be reduced. Then, the different steps of the ROM illustrated in Algorithm 5 (presented at p.27) are separately addressed by highlighting the related implementation procedures. The effect on the results related to the different parameters to be fixed for the construction of the ROM is investigated. Finally, particular attention is directed to the masked projection approaches and some examples of increasing complexity are presented in order to assess the accuracy related to these approaches.

3.2 Formulation of the compressible Navier-Stokes equations

Within the framework of a continuous regime, the macroscopic description of the dynamic and thermodynamic behaviour of a fluid (in general air) is described by the Navier-Stokes equations, supplemented by behaviour and state laws¹. These equations are presented in the form of partial derivative equations allowing to determine the evolution, from specified initial conditions, of the fields of the density ρ , the momentum per unit of volume $\rho\mathbf{U}$ and of the total energy per unit of volume ρE , the total energy per unit of mass E being equal to the sum of the internal energy e and kinetic energy per unit of mass $\frac{1}{2}\mathbf{U}^2$. The Navier-Stokes equations are written:

$$\frac{\partial \rho}{\partial t} + \nabla \cdot (\rho\mathbf{U}) = 0. \quad (3.1)$$

$$\frac{\partial \rho\mathbf{U}}{\partial t} + \nabla \cdot (\rho\mathbf{U} \otimes \mathbf{U} + p\mathbf{I} - \boldsymbol{\tau}) = 0. \quad (3.2)$$

$$\frac{\partial \rho E}{\partial t} + \nabla \cdot (\rho E\mathbf{U} + p\mathbf{U} - \boldsymbol{\tau} \cdot \mathbf{U} + \mathbf{q}) = 0. \quad (3.3)$$

In these equations, \mathbf{U} indicates the absolute velocity field; p , $\boldsymbol{\tau}$ and \mathbf{q} respectively represent the pressure, the stress tensor due to viscosity and the heat flux vector due to thermal conductivity. To close the problem, it is thus necessary to specify the expression of the scalar p , of the tensor $\boldsymbol{\tau}$ and of the vector \mathbf{q} .

¹ This supposes that all the scale length characteristics of the flow are large with respect to the mean free path of the molecules constitutive of the gas.

3.2. Formulation of the compressible Navier-Stokes equations

Laws of behaviour

For a Newtonian fluid, the stress tensor $\boldsymbol{\tau}$ is given by the law:

$$\boldsymbol{\tau} = \lambda (\nabla \cdot \mathbf{U}) \mathbf{I} + 2\mu \mathbf{D}, \quad (3.4)$$

where \mathbf{D} is the tensor of the rates of deformation, i.e. the symmetrical part of the velocity gradient, and where λ and μ are the two viscosity coefficients of the fluid. By supposing valid the Stokes hypothesis, $3\lambda + 2\mu = 0$, the volumic viscosity coefficient λ is given as a function of μ by:

$$\lambda = -\frac{2}{3}\mu. \quad (3.5)$$

The heat flux vector is given by the Fourier law:

$$\mathbf{q} = -K_T \nabla T, \quad (3.6)$$

where K_T indicates the thermal coefficient of conductivity and T the absolute temperature.

Laws of state

The laws of state make it possible to express the internal energy e , the pressure p and the viscosity and thermal conductivity coefficients μ and K_T according to the temperature T . By supposing a perfect gas, with constant specific heats of ratio $\gamma = c_p/c_v$, the internal energy e and the pressure p are specified by:

$$e = c_v T, \quad (3.7)$$

$$p = r_{gas} \rho T, \quad (3.8)$$

where r_{gas} represents the ratio of the universal constant of perfect gases to the molar mass of the gas considered. For a thermodynamically perfect gas, the pressure p and the temperature T are thus specified as functions of the internal energy e by:

$$p = (\gamma - 1) \rho e. \quad (3.9)$$

$$T = \frac{(\gamma - 1)}{r_{gas}} e. \quad (3.10)$$

The viscosity coefficient is given according to temperature by the Sutherland law:

$$\mu = \frac{\beta_s \sqrt{T}}{1 + C_s/T}, \quad (3.11)$$

where β_s and C_s are two parameters depending on the nature of the considered gas. Finally, the thermal conductivity coefficient K_T is proportional to the viscosity coefficient according to the Fourier law:

$$K_T = c_p \frac{\mu}{Pr}, \quad (3.12)$$

where Pr is the (assumed to be constant) *Prandtl number*.

Semi-discrete formulation

We consider the system of conservation laws eq.(3.1), (3.2), (3.3) in the following integral form:

$$\frac{d}{dt} \int_{\Omega} \mathbf{w} d\Omega + \oint_{\partial\Omega} \mathbf{F}_c(\mathbf{w}) \cdot \mathbf{n} d\Sigma + \oint_{\partial\Omega} \mathbf{F}_d(\mathbf{w}) \cdot \mathbf{n} d\Sigma = \mathbf{0}, \quad (3.13)$$

where Ω is the computational domain, of boundary $\partial\Omega$ of unit external normal \mathbf{n} . In the preceding formulation, we distinguish the following terms :

- the vector of conservative variables:

$$\mathbf{w} = \begin{pmatrix} \rho \\ \rho\mathbf{U} \\ \rho E \end{pmatrix}. \quad (3.14)$$

- the convective flux:

$$\oint_{\partial\Omega} \mathbf{F}_c(\mathbf{w}) \cdot \mathbf{n} d\Sigma = \begin{pmatrix} \oint_{\partial\Omega} \rho\mathbf{U} \cdot \mathbf{n} d\Sigma \\ \oint_{\partial\Omega} (\rho\mathbf{U} \otimes \mathbf{U} + p\mathbf{I}) \cdot \mathbf{n} d\Sigma \\ \oint_{\partial\Omega} (\rho E\mathbf{U} + p\mathbf{U}) \cdot \mathbf{n} d\Sigma \end{pmatrix}. \quad (3.15)$$

- the diffusive flux:

$$\oint_{\partial\Omega} \mathbf{F}_d(\mathbf{w}) \cdot \mathbf{n} d\Sigma = \begin{pmatrix} \mathbf{0} \\ -\oint_{\partial\Omega} \boldsymbol{\tau} \cdot \mathbf{n} d\Sigma \\ -\oint_{\partial\Omega} (\boldsymbol{\tau}\mathbf{U} - \mathbf{q}) \cdot \mathbf{n} d\Sigma \end{pmatrix}. \quad (3.16)$$

If we consider a computational domain discretized in a system of elementary *hexahedral* cells, we can write the semi-discrete formulation for eq.(3.13):

$$\frac{d}{dt} \int_{\Omega} \mathbf{w} d\Omega = - \sum_{i=1}^6 \int_{\Sigma_i} [\mathbf{F}_c(\mathbf{w}) + \mathbf{F}_d(\mathbf{w})] \cdot \mathbf{n} d\Sigma, \quad (3.17)$$

where Σ_i represents the i -th face of the *hexahedral* cell considered in the mesh. Then, the average of the conservative variables \mathbf{w} in the cell Ω can be defined as:

$$\mathbf{w}_{\Omega} = \frac{1}{\mathcal{V}(\Omega)} \int_{\Omega(t)} \mathbf{w} d\Omega, \quad (3.18)$$

where $\mathcal{V}(\Omega)$ is the volume of the related cell. By substituting such a term in eq.(3.17), we can write:

$$\frac{d \mathcal{V}(\Omega) \mathbf{w}_{\Omega}}{dt} = -\mathbf{R}_{\Omega}(\mathbf{w}_{\Omega}), \quad (3.19)$$

3.3. Computation of the POD modes of a flow around a fixed cylinder at low Reynolds number

where \mathbf{R}_Ω is a non-linear residual operator that computes the flux balance for each cell. Since the discretized domain is fixed, the cell volumes $\mathcal{V}(\Omega)$ does not depend on time and eq.(3.19) can be rearranged as:

$$\frac{d \mathbf{w}_\Omega}{dt} = -\frac{\mathbf{R}_\Omega(\mathbf{w}_\Omega)}{\mathcal{V}(\Omega)} = \mathbf{f}_\Omega(\mathbf{w}_\Omega). \quad (3.20)$$

In order to relax the notation, the subscript Ω can be omitted so that the following equation is obtained:

$$\frac{d \mathbf{w}(t)}{dt} = \mathbf{f}(\mathbf{w}(t)). \quad (3.21)$$

The previous equation is formally analogous to eq.(2.1). As a consequence, the nonlinear ROM formulations presented in Chapter 2 and illustrated in Algorithm 5 (p.27) can be deployed within this compressible fluid dynamics scenario.

3.3 Computation of the POD modes of a flow around a fixed cylinder at low Reynolds number

In this section, the *offline* phase of the nonlinear ROM for the compressible Navier-Stokes equations is assessed on the classical configuration of a two-dimensional uniform flow past a circular cylinder at Reynolds number $Re = 100$ and Mach $M = 0.2$. This particular configuration could be analyzed with the incompressible Navier-Stokes equations, from which an explicit formulation of the ROM including the nonlinear terms can be derived [17], [99]. However, it was considered appropriate to validate the implementation of the nonlinear ROM based on the compressible Navier-Stokes equations starting with a classical case and subsequently test the accuracy and robustness of the model with more challenging and relevant configurations.

3.3.1 Numerical simulation of the flow around a fixed cylinder at low Reynolds

The computational domain is shown in Fig.3.1 and discretized with 53278 unstructured triangular finite volumes. Uniform steady boundary conditions are imposed on the external boundaries and a no-slip boundary condition is prescribed on the cylinder surface. A second order cell-centered finite-volume solver is used to compute the laminar Navier-Stokes equations [117], [118]. Convection fluxes are evaluated using Roe's approximate Riemann solver. Time integration is performed with a fully implicit second-order scheme that combines dual time stepping and the LU-SGS method. The simulation is initialized with a solution resulting from a previous steady simulation. After a transient phase, the aerodynamic field begins to oscillate

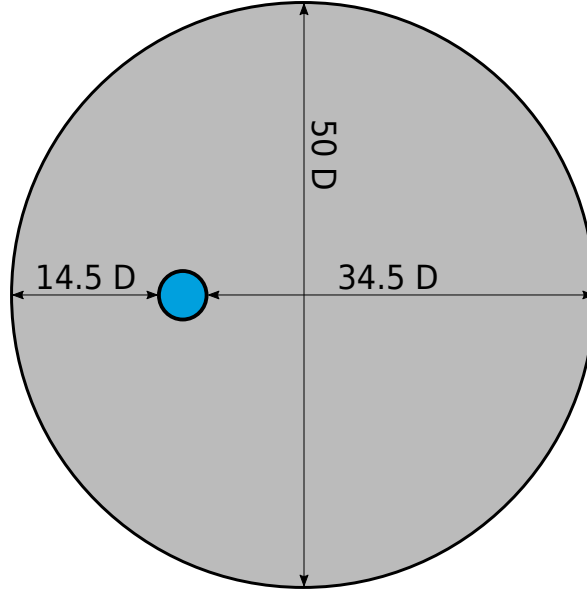


Figure 3.1 Computational domain for the two-dimensional cylinder configuration.

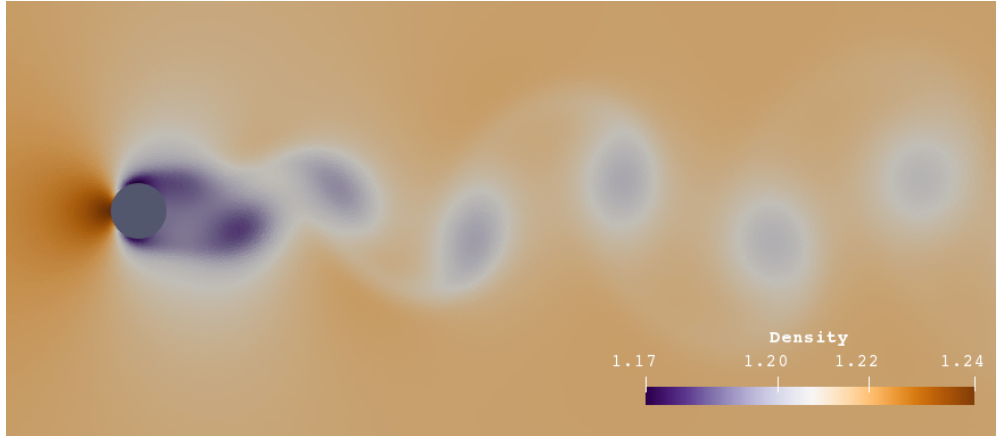


Figure 3.2 Instantaneous density field for the flow past a cylinder at $Re = 100$.

periodically because of a vortex shedding instability in the wake. An instantaneous snapshot that shows the spatial scales of density is depicted in Fig.3.2. The *offline* phase and the following *online* phase will be validated on the basis of a proper reproduction of this unsteady periodic phenomenon. This can be characterized by the time evolution of the aerodynamic force coefficients of lift C_L and drag C_D :

$$C_L(t) = \frac{F_L(t)}{0.5\rho_\infty U_\infty^2 D} \quad \text{and} \quad C_D(t) = \frac{F_D(t)}{0.5\rho_\infty U_\infty^2 D}, \quad (3.22)$$

where F_L and F_D are the aerodynamic forces projected respectively on the perpendicular and the parallel axes of the freestream direction. The time evolution of the aerodynamic force coefficients of a fixed circular cylinder at $Re = 100$ is presented in Fig.3.3 with respect to the adimensional time $t^* = t/T$ where T is the Strouhal period

3.3. Computation of the POD modes of a flow around a fixed cylinder at low Reynolds number

related to the vortex shedding, validated with respect to reference [99] as well.

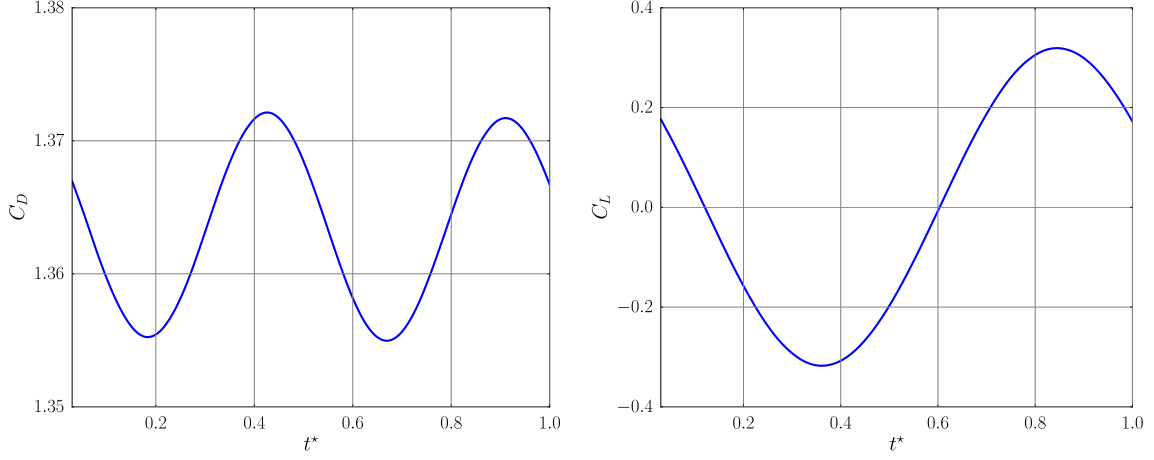


Figure 3.3 Time evolution of the aerodynamic coefficients C_L and C_D of a fixed circular cylinder at $Re = 100$ and $M = 0.2$. Corresponding Strohal number: $St = 0.164$.

3.3.2 Computation of the POD modes

In order to perform the POD, according to Algorithm 1 (presented at p.18), a set of N_t snapshots of the conservative state variables $\mathbf{w} = [\rho, \rho U, \rho V, \rho E]^T$ is equally sampled throughout the simulated vortex shedding cycle. In Fig.3.4 the energy contribution associated to each POD mode, computed following Algorithm 1 (p.18), is shown. The plot represents the portion of energy captured by the different POD modes with respect to the relative singular values, according to eq.(2.11). The number of snapshots chosen to sample the oscillation period of the system seems to slightly affect the spectrum of the POD modes. From now on, in order to allow a wider range of possibilities for the number of retained POD modes, the case for $N_t = 40$ is analyzed. Fig.3.5 depicts the topology of the first and most energetic POD mode which resembles the mean flow of the unsteady solution². This corroborates the common practice of centering the snapshot collection with respect to a reference state $\bar{\mathbf{w}}$. Depending on the application, the field $\bar{\mathbf{w}}$ can be a time-averaged flow field, a steady solution or the initial solution. This last option is proven to lead to a *consistent* approximation in the framework of the GNAT ROM formulation [100]. As a consequence, the approximation of eq.(2.4) can be decomposed using the affine decomposition as:

$$\mathbf{w}(t) \approx \bar{\mathbf{w}} + \Phi \mathbf{a}(t), \quad (3.23)$$

and the snapshot collection for the POD becomes $\mathbf{W} = [\mathbf{w}(t_0) - \bar{\mathbf{w}}, \mathbf{w}(t_1) - \bar{\mathbf{w}}, \dots, \mathbf{w}(t_{N_t}) - \bar{\mathbf{w}}]$, with $\mathbf{W} \in \mathbb{R}^{n \times N_t}$. In such a case, the POD spectrum for a sampling of 40 snapshots

²Actually, here there is a misuse of language because the ‘shape’ of the POD mode corresponds to the whole vector $\Phi_{(i)} = [\Phi_{\rho(i)}, \Phi_{\rho U(i)}, \Phi_{\rho E(i)}]^T$, whereas only the $\Phi_{\rho(i)}$ is shown in the figure.

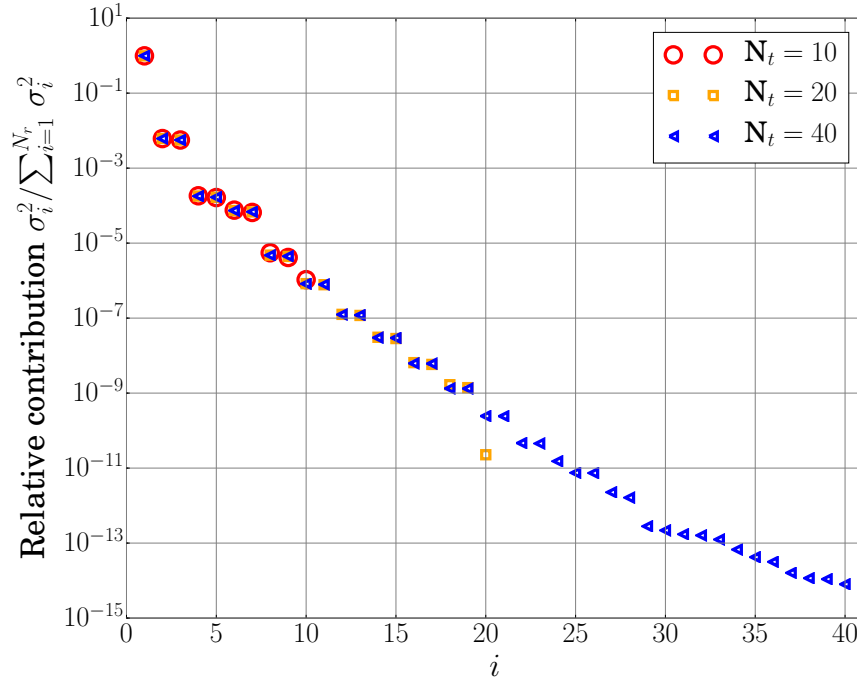


Figure 3.4 Proper orthogonal eigenvalue spectrum for a flow past a cylinder at $Re = 100$.



Figure 3.5 First proper orthogonal mode (POM of density) for the flow around a fixed cylinder at $Re = 100$.

with subtraction of the time average $\bar{\mathbf{w}} = \langle \mathbf{w} \rangle = \frac{1}{N_t} \sum_{i=1}^{N_t} \mathbf{w}(t_i)$ is plotted in Fig.3.6. The rank of the matrix \mathbf{W} has been reduced by 1 corresponding to the impact of the first singular value related to the case without any subtraction. Except for the first singular value, the average subtraction leaves basically intact the remaining spectrum. The value of E_{N_m} (eq.(2.13)) representing the increasing rate of energy included with the first m modes is reported in Tab.3.1.

From Fig.3.4 and also Fig.3.6, we can see that the other relevant singular values appear in pairs. This clustering can be attributed to the progressive and symmetric convection of the vortex structures in the wake of the flow. This feature is usually observed in the unsteady wake of a cylinder and an airfoil as well when periodic

3.3. Computation of the POD modes of a flow around a fixed cylinder at low Reynolds number

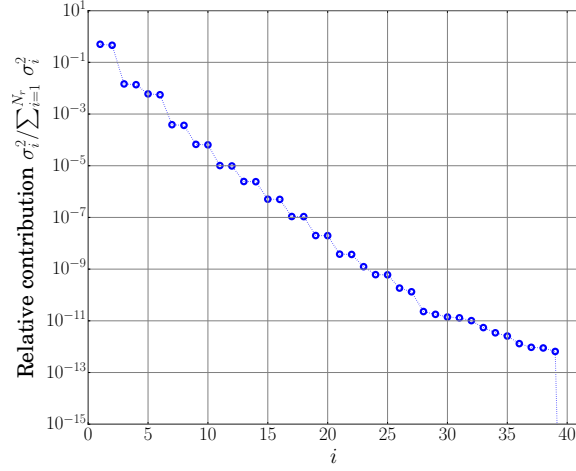


Figure 3.6 Proper orthogonal eigenvalue spectrum for the flow past a cylinder at $Re = 100$ for the snapshot set with subtraction of the time average field.

m	2	4	6	8	10	20
E_{N_m}	0.9592	0.9875	0.9909	0.9998	0.9999	≈ 1

Table 3.1 Value of E_{N_m} eq.(2.13) for the flow past a cylinder at $Re = 100$ for the snapshot set with subtraction of the time average field.

vortex shedding is observed [119]. If we look at the shape of the other proper orthogonal modes in Fig.3.7, the spatial structures of the modes are analogously grouped in pairs (1-2),(3-4),(5-6) and represent the convected counter-rotating vortex pair, characteristic of the Von Kármán instabilities. Also, it should be noted that the spa-

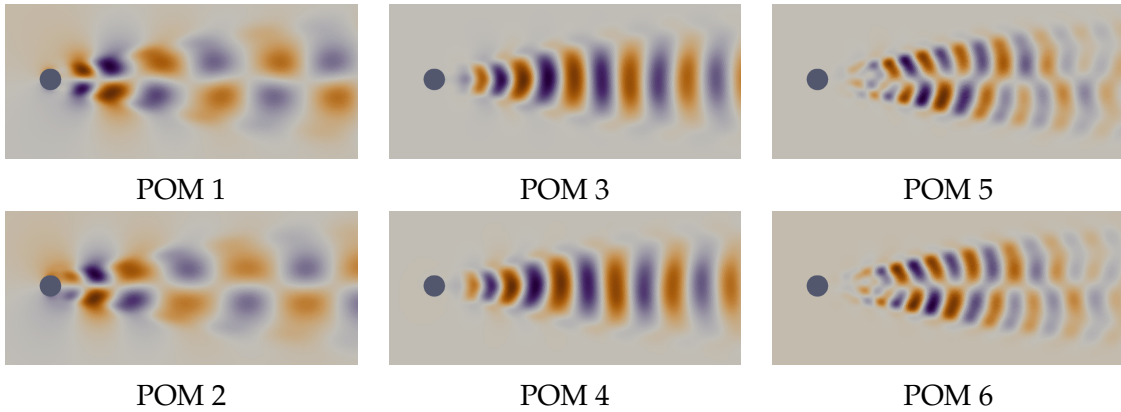


Figure 3.7 First to 6th density proper orthogonal mode (POM) for the flow around a fixed cylinder at $Re = 100$.

tial scales reduce with the decreasing of the related singular value. This means that the higher order modes contribute to smaller spatial scales. In particular, under certain conditions, a similar behavior is found on the Fourier modes and on structural eigenmodes as well [120].

Chapter 3. Construction and implementation of a nonlinear projection-based ROM for the compressible Navier-Stokes equations

From now on, the formulation of eq.(3.23) with the time average flow subtraction is considered. Once the POD modes are computed, a cutoff condition, defining the number of modes m to retain, is required (see Algorithm 1 at p.18). As proposed in Section 2.3, the $m = 6$ first modes could be selected in order to construct a low-rank approximation of the solution including the 99% of the total energy (see eq.(2.13)). This value is arbitrary and comes from common practice. In order to state the suitable value for m , we can reconstruct the set of snapshots \mathbf{W} using the truncated POD basis by retaining the first m modes.

$$\mathbf{w}_{(m)}(t_i) = \bar{\mathbf{w}} + \sum_{j=1}^m \Phi_j a_j(t_i) = \bar{\mathbf{w}} + \Phi_{(m)} \mathbf{a}_{(m)}. \quad (3.24)$$

The related modal amplitudes can be evaluated either using the previous SVD computation of eq.(2.11) so that:

$$\mathbf{a}_{(m)} = \Sigma \mathbf{V}_{(m)}^T \quad (3.25)$$

or by exploiting the orthonormality of the POD modes with respect to the euclidean scalar product $(\mathbf{A}, \mathbf{B}) = \mathbf{A}^T \mathbf{B}$, so that:

$$\mathbf{a}_{(m)}(t_i) = \Phi_{(m)}^T (\mathbf{w}(t_i) - \bar{\mathbf{w}}) \quad \text{for } i = 1, \dots, N_t. \quad (3.26)$$

Once the modal amplitudes are computed, the snapshots are reconstructed as a linear combination of the POD modes using eq.(2.4). Fig.3.8 shows the time evolution of the aerodynamic force coefficients for the flows reconstructed with different values of m .

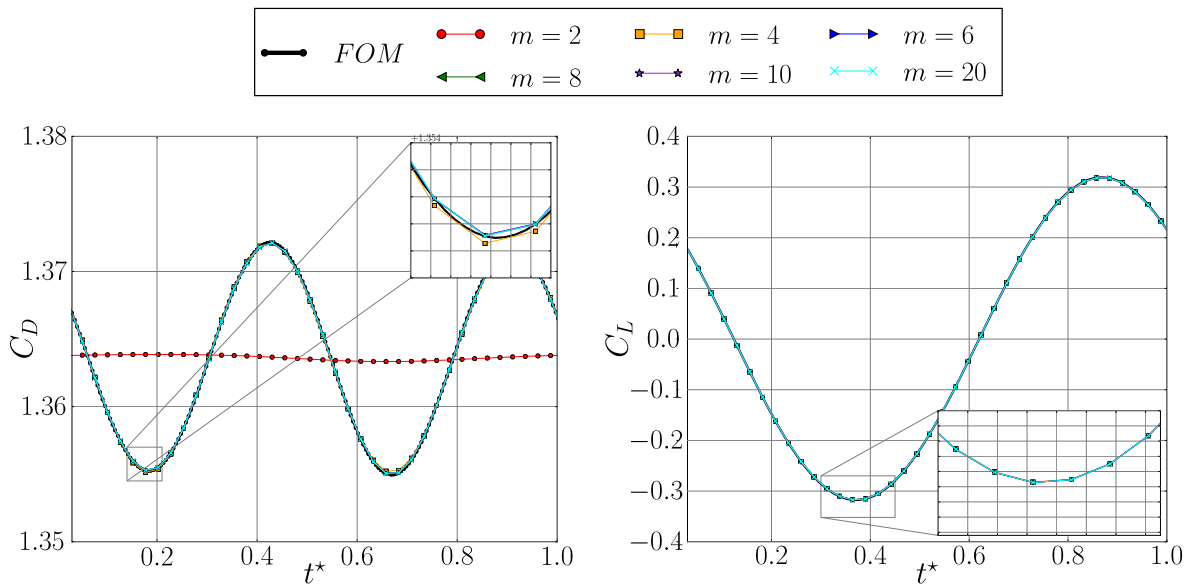


Figure 3.8 The time evolution of the aerodynamic coefficients of a fixed circular cylinder at $Re = 100$ and $m = 0.2$.

3.4. Numerical integration of the nonlinear projection-based ROM of a flow around a fixed cylinder at low Reynolds

Including only the first 2 POMs is already sufficient for a proper reconstruction of C_L . Indeed, if we increase m there is not a remarkable increase in the fidelity of the reconstruction for the lift. On the contrary, the accurate reconstruction of the drag is ensured starting from $m = 4$ and it is slightly enhanced up to $m = 20$. However, according to Tab.3.2, the aerodynamics coefficients root-mean-square deviation (RMSD)

$$\text{RMSD}(\mathbf{x}) = \sqrt{\frac{1}{N_t} \sum_{i=1}^{N_t} |\Delta x_i|^2}, \quad (3.27)$$

for the low-rank approximation is still very low even using a small number of modes.

m	2	4	6	8	10	20
RMSD(C_D)	3.37e-05	1.11e-08	2.66e-10	1.87e-10	1.38e-10	6.60e-11
RMSD(C_L)	2.18e-07	9.21e-08	1.05e-08	9.71e-09	8.43e-09	7.40e-09

Table 3.2 Root-mean-square deviation (RMSD) of the reconstructed C_D and C_L using m proper orthogonal modes with respect to the reference solution.

3.4 Numerical integration of the nonlinear projection-based ROM of a flow around a fixed cylinder at low Reynolds

In the previous section, the different steps of the *offline* phase of the construction of a nonlinear ROM have been discussed. In this section, the *online* phase is studied and the performance of the ROM for the compressible Navier-Stokes equations is assessed with a configuration of a two-dimensional uniform flow past a circular cylinder at Reynolds number $Re = 100$ and $M = 0.2$. Hence, the objective is to perform and validate all the steps of the online phase of Algorithm 5 (p.27). As explained in Section 2.5, the use of the masked projection approximation allows to overcome a bottleneck issue that would undermine the performance of the ROM. However, a preliminary validation is done without any masked projection, in order to assess all the other aspects of the online integration of the nonlinear ROM.

On the basis of the decomposition for the flow solution introduced in the previous section, we can use the approximation of eq.(3.23) so that, by substituting and projecting analogously to eq.(2.14) we obtain the following system to integrate:

$$\frac{d\mathbf{a}(t)}{dt} = \mathbf{\Phi}^T \mathbf{f}(\bar{\mathbf{w}} + \mathbf{\Phi} \mathbf{a}(t)). \quad (3.28)$$

For this example $\bar{\mathbf{w}}$ is the time average flow field. The ordinary differential nonlinear equations (3.28) (ODE) of the system represents the nonlinear ROM and must be

Chapter 3. Construction and implementation of a nonlinear projection-based ROM for the compressible Navier-Stokes equations

completed by the m initial conditions, indicated as \mathbf{a}_0 , in order to guarantee the well-posedness. For example, the ROM can be initialized using the steady solution of the flow or the first snapshot of the collection \mathbf{W} . Thus, the initial amplitudes \mathbf{a}_0 can be obtained by projecting the chosen initial solution \mathbf{w}_0 onto the POD basis as:

$$\mathbf{a}_0 = \Phi^T(\mathbf{w}_0 - \bar{\mathbf{w}}). \quad (3.29)$$

Eq.(3.28) of the ROM are integrated using the 4th-order Runge-Kutta scheme. Finally, in a subsequent phase the masked approach will be introduced and investigated. In Sections 3.4.1 and 3.4.2 the effect of the time-step and the influence of the truncation of the POD basis on the accuracy of the ROM are investigated. Then, the possible formulations for the nonlinear ROM with masked projection are analyzed in Section 3.4.3. Finally, in Section 3.4.4 the accuracy of the masked projection approach is studied.

3.4.1 Effect of the time-step on the response of the projection-based nonlinear ROM

First of all, the impact of the time-step on the time integration is studied. Given the POD spectrum in Fig.3.6, and following the considerations of the retained rate of energy E_{N_m} of Section 3.3.2, a number of POD modes $m = 10$ is chosen. We remind that the FOM is integrated using an implicit integrator and therefore the use of an explicit integrator for the ROM should imply a smaller CFL condition in order to prevent numerical divergence. Actually, the time-step for the ROM can be significantly increased because the POD acts as a *low-pass* filter by eliminating the high frequencies that typically require a small CFL for the time integration [121]. This behavior is confirmed in Fig.3.9 where the time history of the aerodynamic coefficients are shown for different ROM time-steps: the ROM time-step can be increased up to 10 times the FOM time step without affecting significantly accuracy. However, a visible discrepancy is detected when the time-step is increased up to 20 times the FOM time step. As a result, for next ROM test cases on this configuration, a time-step equal to 10 times the FOM time-step is used.

An opposite effect may, however, occur in more complex cases: the use of smaller and smaller time-steps requires a greater number of evaluations of the nonlinearity associated to the approximated solution. This could result in an increasing approximation error which accumulates more frequently over the time integration and potentially leads to divergence. In such a case, the time-step must be chosen as a compromise to take into account this counter-intuitive behavior (for example see Appendix A).

3.4. Numerical integration of the nonlinear projection-based ROM of a flow around a fixed cylinder at low Reynolds

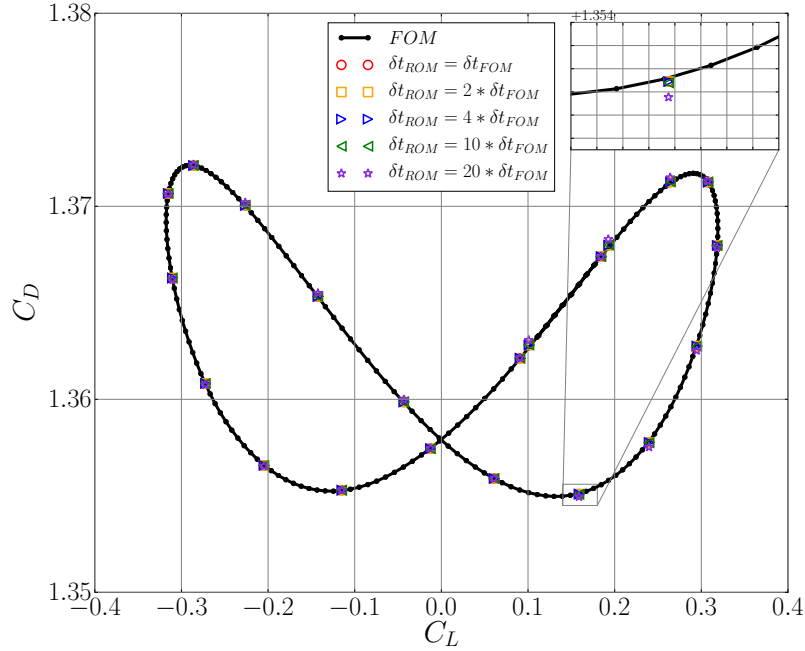


Figure 3.9 Evolution of the aerodynamic coefficients for the nonlinear ROM using 10 POD modes and various time-steps for the time integration.

3.4.2 Effect of the POD basis truncation on the response of the projection-based nonlinear ROM

In Section 3.3.2 the question of the choice of the number of modes for the ROM **reconstruction** related to the *offline* phase has been discussed. However, the energy condition of eq.(2.13) as well as the study in Fig.3.8 cannot ensure a priori that the nonlinear ROM is integrated accurately during the *online* phase. In this section, a study about the required number of POD modes for the online ROM integration is performed. In Fig.3.10 the time history of the aerodynamic coefficients for different numbers of POMs m is shown. In accordance with Fig.3.8 the case for $m = 2$ can be just excluded because the modes are not sufficient to reproduce correctly the aerodynamic coefficients even if the coordinated associated to the modes were computed correctly. Then, although 4 modes could be sufficient according to the energy condition of Section 3.3.2 (see Fig.3.6 and Tab.3.1), in order to compute correctly the aerodynamic coefficients (see Fig.3.8), the integration of the nonlinear ROM with only $m = 4$ leads to a significant inaccuracy and divergence. Switching to $m = 6$ the discrepancy substantially reduces and the ROM converges toward the correct vortex shedding cycle. However, using 6 and 8 POMs still implies a non-negligible deviation with respect to the reference aerodynamic coefficients which is almost eliminated for $m = 10$. Finally, the accuracy of the nonlinear ROM is slightly increased from $m = 10$ to $m = 20$.

We can conclude that the global performance appears to be reasonable as the

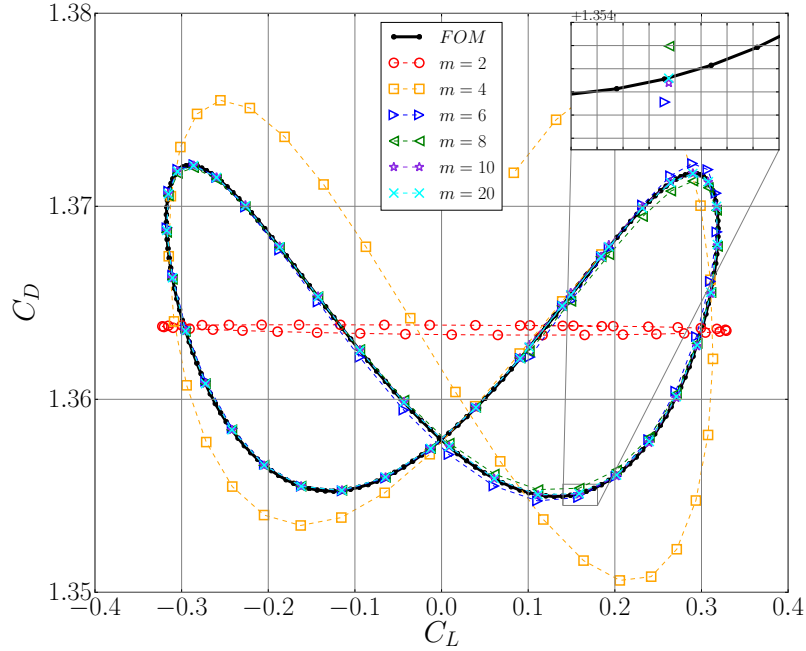


Figure 3.10 Evolution of the aerodynamic coefficients for the nonlinear ROM using various POD basis truncations.

aerodynamic force prediction of the ROM is monotonically enhanced with an increasing number of POD modes m . The usual process of the POD truncation which neglects the least relevant modes or, in other words, the small-scale spatial structures of the dynamical system could be generally successful for very simple dynamics of the flow, for which the energy transfer from low index POD modes to higher index POD modes is weak. However, in many other cases the smaller spatial structures are essential for energy processes that are fundamental for the physics of the fluid dynamic systems. In this context, the extension of the *energy cascade* concept to the POD sequence and the forward energy transfer between POD modes was numerically investigated by Couplet *et al.* [122]. For this reason, closure model strategies could be eventually introduced in ROMs in order to ensure an accurate integration of the ROM keeping a small number of POD modes to strike a balance between efficiency and accuracy [109]. Finally, for this quite simple test case, a suitable number of modes m ranges from 10 to 20 and no additional closure model is required.

3.4.3 Choice of the formulation for the projection-based nonlinear ROM with masked projection

So far, eq.(3.28) has been used for the nonlinear ROM formulation. As explained in Section 2.5, such a formulation is inappropriate because the evaluation of the nonlinear term requires to lift back to the full-order system systematically at each

3.4. Numerical integration of the nonlinear projection-based ROM of a flow around a fixed cylinder at low Reynolds

step of the ROM time integration. This significantly undermines the performance of the ROM, so that masked projection techniques are introduced at this stage. In this section, the formulation of masked projection techniques for nonlinear fluid dynamic systems is developed. This kind of approaches are based on the formulation of eq.(2.16) with the approximation eq.(3.23) of the conservative field, so that the nonlinear term can be rewritten as:

$$\mathbf{f}(\tilde{\mathbf{w}}) \approx \mathbf{U}\mathbf{c}(t), \quad (3.30)$$

where $\tilde{\mathbf{w}} = \bar{\mathbf{w}} + \Phi \mathbf{a}(t)$. Following the masked projection process detailed in Section 2.5, the ROM system to integrate in time becomes (referred to as *formulation A*):

$$\text{formulation A: } \frac{d\mathbf{a}(t)}{dt} = \Phi^T \begin{cases} \mathbf{U}(\mathbf{P}^T \mathbf{U})^{-1} \mathbf{f}_P(\tilde{\mathbf{P}}^T \tilde{\mathbf{w}}(t)), & \text{if } f = p. \\ \mathbf{U}(\mathbf{U}^T \mathbf{P} \mathbf{P}^T \mathbf{U})^{-1} \mathbf{U}^T \mathbf{P} \mathbf{f}_P(\tilde{\mathbf{P}}^T \tilde{\mathbf{w}}(t)), & \text{if } f > p. \end{cases} \quad (3.31)$$

An alternative formulation can be defined starting from the following decomposition:

$$\Phi^T \mathbf{f}(\tilde{\mathbf{w}}) = \Phi^T [\mathbf{f}(\tilde{\mathbf{w}}) + \mathbf{f}(\mathbf{w}_0) - \mathbf{f}(\mathbf{w}_0)] = \Phi^T \mathbf{f}(\mathbf{w}_0) + \Phi^T [\mathbf{f}(\tilde{\mathbf{w}}) - \mathbf{f}(\mathbf{w}_0)]. \quad (3.32)$$

where the term $\Phi^T \mathbf{f}(\mathbf{w}_0)$ can be computed *a priori* during the offline phase and the masked projection approach operates only on the *fluctuation* term as:

$$\mathbf{f}(\tilde{\mathbf{w}}) - \mathbf{f}(\mathbf{w}_0) \approx \mathbf{U}\mathbf{c}(t). \quad (3.33)$$

Such an equation is similar to eq.(2.16), but here the basis $\mathbf{U} \in \mathbb{R}^{n \times p}$ is computed via a POD of the nonlinear snapshot collection whose columns are subtracted by the term $\mathbf{f}(\mathbf{w}_0)$. This rearrangement leads to a new nonlinear ROM formulation that will be referred to as *formulation B*:

$$\text{formulation B: } \frac{d\mathbf{a}(t)}{dt} = \Phi^T \mathbf{f}(\mathbf{w}_0) + \Phi^T \begin{cases} \mathbf{U}(\mathbf{P}^T \mathbf{U})^{-1} \left(\mathbf{f}_P(\tilde{\mathbf{P}}^T \tilde{\mathbf{w}}(t)) - \mathbf{P}^T \mathbf{f}(\mathbf{w}_0) \right), & \text{if } f = p. \\ \mathbf{U}(\mathbf{U}^T \mathbf{P} \mathbf{P}^T \mathbf{U})^{-1} \mathbf{U}^T \mathbf{P} \left(\mathbf{f}_P(\tilde{\mathbf{P}}^T \tilde{\mathbf{w}}(t)) - \mathbf{P}^T \mathbf{f}(\mathbf{w}_0) \right), & \text{if } f > p. \end{cases} \quad (3.34)$$

To summarize, provided the additional offline step for the nonlinear snapshot centering with respect to $\mathbf{f}(\mathbf{w}_0)$, the simple decomposition of eq(3.32) allows us to approximate via masked projection only the fluctuation nonlinear term of eq.(3.33) and not the whole nonlinear term as is the case of *formulation A*.

In order to compare these two formulations the nonlinear ROM is integrated using $m = 20$ POD modes for the conservative variables snapshots and the DEIM masked projection using $f = p = 20$ POD modes for the nonlinear term snapshots (see Sec.2.5). The time history of the aerodynamics coefficients for the two formulations are compared in Fig.3.11. All other parameters being the same, the *formulation*

Chapter 3. Construction and implementation of a nonlinear projection-based ROM for the compressible Navier-Stokes equations

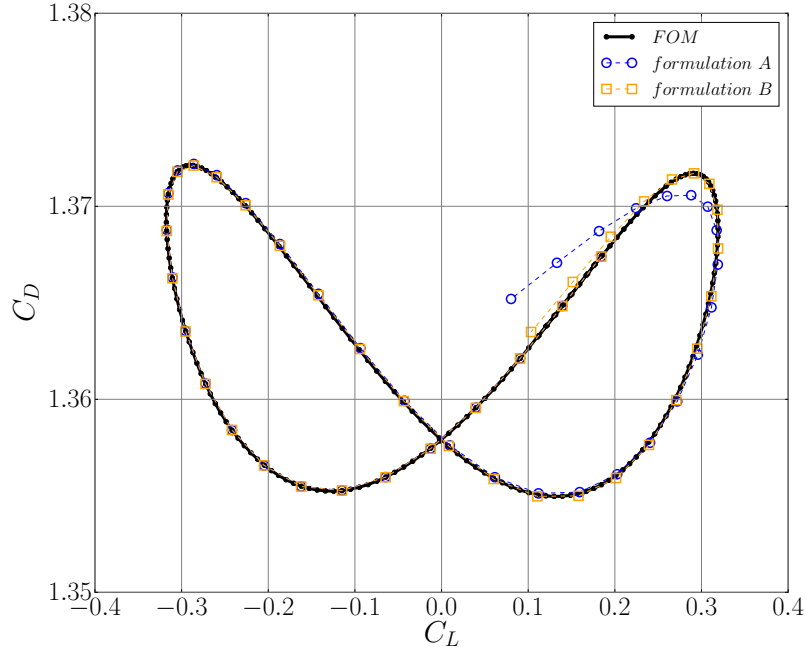


Figure 3.11 Evolution of the aerodynamic coefficients for the nonlinear ROM using the 2 different formulations reported in Section 3.4.3.

B is more stable and accurate than *formulation A*. Indeed the use of the *formulation B* allows to complete the integration of an entire cycle of oscillation with an error significantly smaller than with the use of *formulation A*. For this reason, *formulation B* is chosen and employed for the rest of this study. In this context, de Pando *et al.* [25] propose a more general formulation which includes the Jacobian term in the decomposition of eq.(3.32) in order to capture the linear dynamics included in the nonlinear term. More specifically, they generalize eq.(3.32) using the first two Taylor-expansion terms about $\bar{\mathbf{w}}$:

$$\mathbf{f}(\bar{\mathbf{w}} + \mathbf{w}') = \mathbf{f}(\bar{\mathbf{w}}) + \mathbf{J}(\bar{\mathbf{w}}) \mathbf{w}' + \mathbf{f}_{NL}(\bar{\mathbf{w}}, \bar{\mathbf{w}}), \quad (3.35)$$

where $\mathbf{J} = \left. \frac{\partial \mathbf{f}}{\partial \bar{\mathbf{w}}} \right|_{\bar{\mathbf{w}}}$. In this way, the DEIM masked projection approach is used only to approximate the higher-order nonlinear terms. This seems to be a well-suited formulation, anyway it requires the computation of the Jacobian term which is not always affordable and/or available.

3.4. Numerical integration of the nonlinear projection-based ROM of a flow around a fixed cylinder at low Reynolds

3.4.3.1 Practical implementation of a nonlinear reduced order model for compressible fluid dynamics

All previous considerations lead to the construction of a nonlinear ROM for fluid dynamic applications. Some adjustments with respect to the formulation in Chapter 2 for a general nonlinear system have been introduced. As a consequence, all the steps of a nonlinear ROM for the compressible Navier-Stokes equations are detailed in Algorithm 6 and the adjustments with respect to the general Algorithm 5 (p.27) are highlighted in blue color.

Algorithm 6 Nonlinear model-order reduction for the Navier-Stokes equations

Offline phase:

- 1: Generate snapshot sequences $\mathbf{W} \in \mathbb{R}^{n \times N_t}$ for the solution and $\mathbf{F} \in \mathbb{R}^{n \times N_t}$ for the nonlinear term using the FOM solver with subtraction of $\bar{\mathbf{w}}$ and $\mathbf{f}(\mathbf{w}_0)$
- 2: Construct $\Phi \in \mathbb{R}^{n \times m}$ using POD via Algorithm 1 with input \mathbf{W}
- 3: Construct $\mathbf{U} \in \mathbb{R}^{n \times p}$ using POD via Algorithm 1 with input \mathbf{F}
- 4: Construct masked projection matrix \mathbf{P} via Algorithm 2,3 or 4 with input \mathbf{U}
- 5: **if** Algorithm 2 or 3 is chosen **then**
- 6: $\mathbf{P} \in \mathbb{R}^{n \times p}$
- 7: Compute the matrix operations of eq.(3.34) once and for all: $\Phi^T \mathbf{f}(\mathbf{w}_0)$, $\mathbf{P}^T \mathbf{f}(\mathbf{w}_0)$ and $\Phi^T \mathbf{U}(\mathbf{P}^T \mathbf{U})^{-1}$
- 8: **else if** Algorithm 4 is chosen **then**
- 9: $\mathbf{P} \in \mathbb{R}^{n \times kp}$
- 10: Compute the matrix operations of eq.(3.34) once and for all: $\Phi^T \mathbf{f}(\mathbf{w}_0)$, $\mathbf{P}^T \mathbf{f}(\mathbf{w}_0)$ and $\Phi^T \mathbf{U}(\mathbf{U}^T \mathbf{P} \mathbf{P}^T \mathbf{U})^{-1} \mathbf{U}^T \mathbf{P}$
- 11: **end if**
- 12: Construct the nonlinear operator $f_P(\tilde{\mathbf{P}}^T \tilde{\mathbf{w}}(t))$

Online phase:

Input: The initial value for \mathbf{a}_0 from eq.(3.29)

Output: The time discrete response for the vector amplitudes $\mathbf{a} \in \mathbb{R}^{m \times N_t}$

- 1: Compute $f_P(\tilde{\mathbf{P}}^T \Phi \mathbf{a}_0)$
 - 2: Integrate in time eq.(3.34) for \mathbf{a}_1
 - 3: $\mathbf{a} \leftarrow [\mathbf{a}_1]$
 - 4: **for** $i = 2$ to N_t **do**
 - 5: Compute $f_P(\tilde{\mathbf{P}}^T \tilde{\mathbf{w}}(t_{i-1})) - \mathbf{P}^T \mathbf{f}(\mathbf{w}_0)$
 - 6: Integrate in time eq.(3.34) for \mathbf{a}_i
 - 7: $\mathbf{a} \leftarrow [\mathbf{a} \ \mathbf{a}_i]$
 - 8: **end for**
-

3.4.4 Influence of the number of the DEIM interpolation points

In the previous section, the DEIM masked projection has been introduced using $p = 20$ nonlinear modes for preliminary demonstration purpose. We remind that this technique allows to approximate the nonlinear term by interpolating it over a judiciously selected subset of points significantly smaller than the large-scale full model dimension n . The purpose of this and the following sections is to study the performance of these techniques for fluid dynamic applications. As previously explained, the original DEIM selection algorithm provides a number of interpolation points f equal to the number of the retained nonlinear POD modes p . Thus, the performance of the DEIM can be studied for different values of p . For this purpose, in Fig.3.12 the trajectory of the aerodynamics coefficients computed by the nonlinear ROM detailed in Algorithm 6 (presented at p.53) for $m = 20$ and different values of p is plotted.

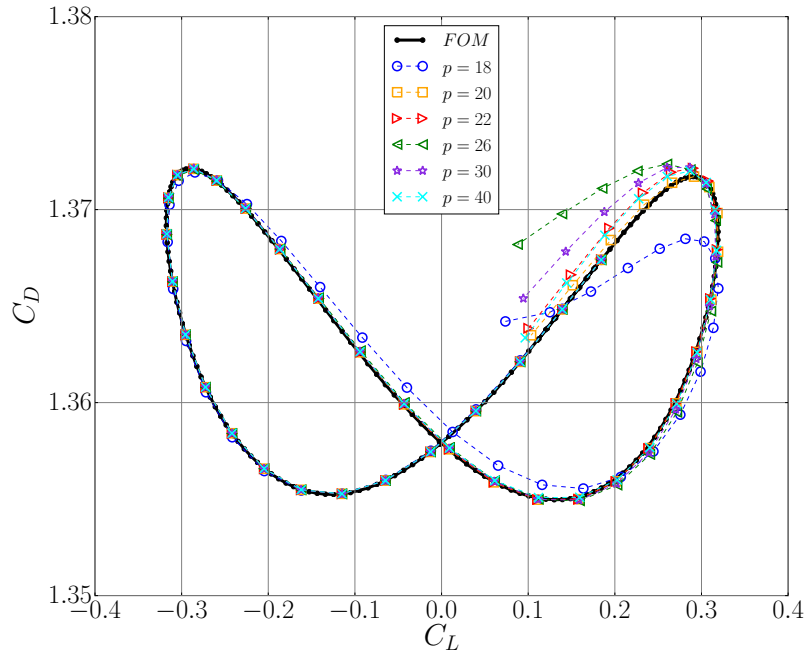


Figure 3.12 Evolution of the aerodynamic coefficients for the nonlinear ROM using different values of the number of interpolation points p for the DEIM approximation.

As in the DEIM the value p corresponds to the number of interpolation points, the accuracy improvement detected by switching from $p = 18$ to $p = 20$ seems reasonable. According to this coherent behavior, a monotonic trend of both p and the accuracy of the model is expected. On the contrary, this is not the case for higher values of p and indeed a reversal of this trend is reported. The accuracy is deteriorated until $p = 26$ and then is progressively improved until $p = 40$. However, the best performance is obtained for $p = 20$. These last results, albeit preliminary, seem undesirable and entail the next study of this thesis about the assessment of

3.5. Assessment of the performance of the masked projection techniques in fluid dynamics applications

the masked projection techniques (and the related selection algorithms) for fluid dynamic applications (Section 3.5).

Finally, from Fig.3.12, it should be noted that here the best DEIM performance involves a non-negligible residual error at the end of the vortex-shedding cycle which entails stability issues for long-term simulations. This problematic will be addressed from an alternative point of view with respect to the usual stabilization techniques in Chapter 5.

3.5 Assessment of the performance of the masked projection techniques in fluid dynamics applications

As detailed in Section 2.5, the family of masked projection approaches is based on the efficient resolution of eq.(2.16) (or equivalently eq.(3.33)). The procedure proposed is based on the application of a mask matrix to the full order nonlinear term of the system in order to select a relatively small number of lines to solve. This is equivalent to use a relatively small set of points of the system domain for interpolating (or fitting) the nonlinear term. Methods listed in Section 2.5 differ only by the algorithm for the selection of interpolation points.

In order to ensure the computational gain of masked projection approaches, the problematic related to the point-wise evaluation of the nonlinear function has been discussed in Chapter 2. Indeed, when the concerned system is represented by the semi-discretized Navier-Stokes equations in a finite volume context, the nonlinear operator consists in the convective and diffusive fluxes balance. Evidently, it cannot be point-wise because the cell flux balance depends on the field of the related neighbor cells. Consequently, to compute the flux balance for some isolated cells it is necessary to initialize the involved cells plus the neighbor cells required by the space discretization to complete the stencil (see Fig.3.13). The selector operator which includes the f points selected by the masked projection plus the neighbor points required to complete the stencil is indicated as $\tilde{\mathbf{P}}^T$. For common industrial CFD solvers this is still convenient if we compare the huge number of degrees of freedom normally involved in fluid dynamics with respect to a small set of stencils. Anyway, the same may not be true if we consider high-order numerical flow solvers that have wide stencil and dense resulting operator [25]. For the solvers used in this thesis, second order spatial discretization schemes are employed so that the relative sparse operator is suitable for masked projection approaches.

The practical application of the masked approach is involved in steps 4 and 12 of the offline phase of Algorithm 6 (presented at p.53). The implementation of such phases has been comprehensively summarised in the 3 steps of Section 2.5 (p.22). It should be noted that such an implementation presupposes a moderate level of intrusiveness into the FOM flow solver. In this thesis and in the following test cases,

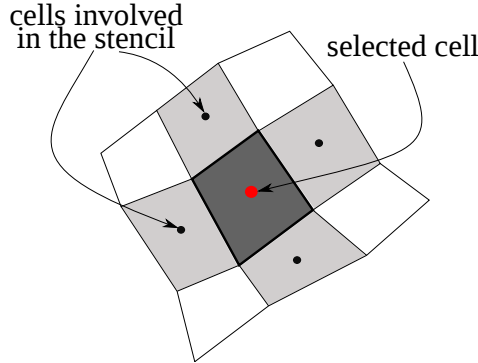


Figure 3.13 Illustrative example of a masked projection selected cell (dark grey) and the related cells (light grey) to be initialized in order to compute the flux balance of the FOM.

the industrial finite volume solver *elsA* [123] is used and its high level of complexity coupled with the wide range of applications and formulations would require an important programming effort in order to construct the nonlinear operator $f_P(\tilde{\mathbf{P}}^T \tilde{\mathbf{w}}(t))$. For this reason, it was considered appropriate to bypass this intrusive implementation for a preliminary validation [124]. As a consequence for the following test cases, at each time-step of the ROM integration the flux balance is computed over the whole spatial domain and the value for the selected cells is extracted a posteriori (with the operation $\mathbf{P}^T f(\tilde{\mathbf{w}})$).

In the sections below, a study for the assessment of masked projection techniques is conducted on test cases of increasing complexity.

3.5.1 Zero incidence transonic flow around a NACA 0012 airfoil at moderate Reynolds number

For the first test-case, a fixed NACA 0012 airfoil is set at an incidence of $\alpha = 0^\circ$ with the flow parameters $M = 0.85$ and $Re = 5000$ or $Re = 10000$. Under these conditions the flow is laminar. A structured C-grid is used with about 3×10^4 finite volumes. The farfield distance is set to 10 chord lengths. With a preliminary steady configuration as initial condition, two unsteady FOM simulations are performed with the Backward Euler scheme and the Dual Time Step acceleration technique. As showed by Bourguet *et al.* [125], it develops an unsteadiness corresponding to a near-wake von Kármán instability. The timestep is set such that the vortex shedding cycle is sampled with 100 snapshots. The energy distribution of the solution POD modes for the case at $Re = 5000$ is plotted in Fig.3.14 and the first four density POD modes for $Re = 5000$ are depicted in Fig.3.15. A similar shape is observed for the modes related to the $Re = 10000$ configuration at $\alpha = 0^\circ$ (not shown). For the reduced order model, the dimension of the solution POD basis is set to $m = 12$ and the ROM is integrated in time using the 4th order Runge-Kutta explicit scheme. The choice of the basis dimension is done according to the value $E_m = \sum_{i=1}^m \sigma_i^2 / \sum_{i=1}^r \sigma_i^2$

3.5. Assessment of the performance of the masked projection techniques in fluid dynamics applications

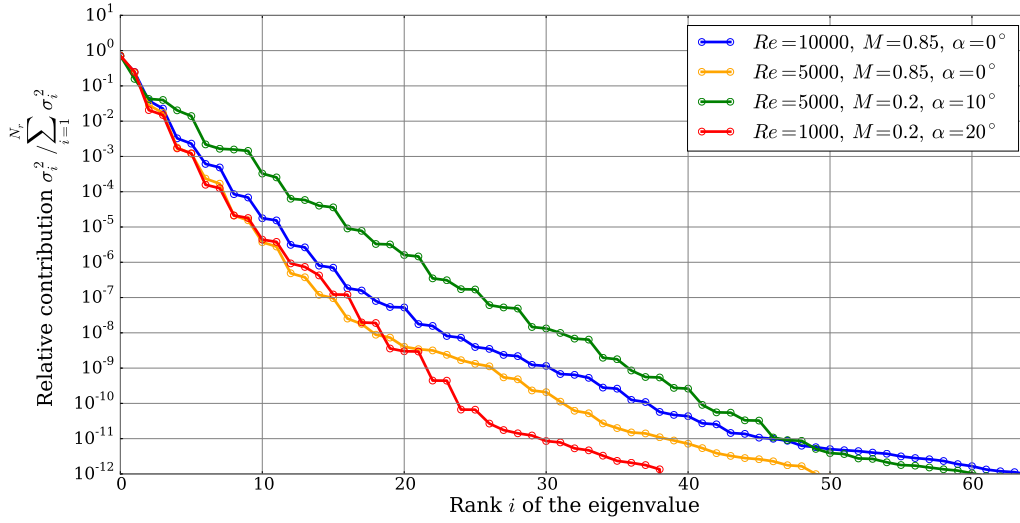


Figure 3.14 Proper orthogonal eigenvalue spectrum for the flow around a NACA-0012 airfoil at different flow conditions.

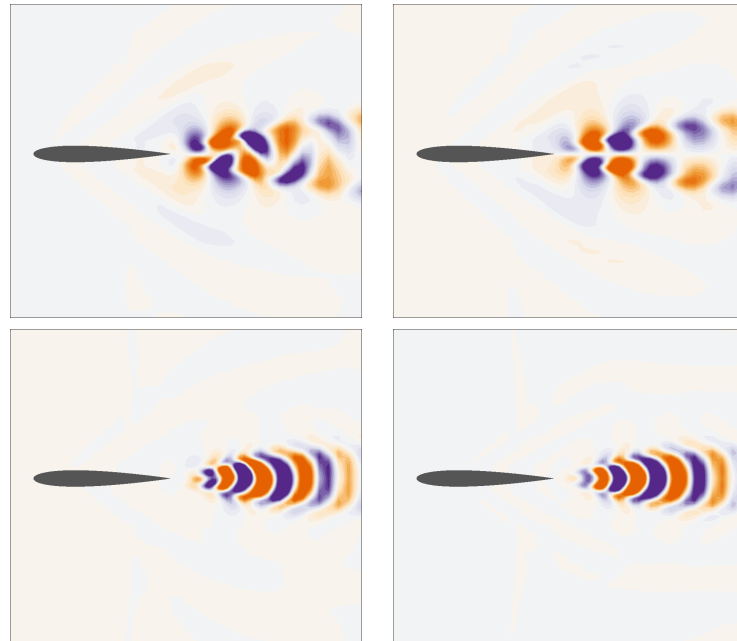


Figure 3.15 The first four density POD modes for $Re = 5000, M = 0.85$ at zero incidence.

that, for $m = 12$, is already over 0.9999. The alternative QDEIM approach is analyzed with respect to the standard DEIM approach. For both masked projection methods, the number of interpolation points is equal to the number p of the selected nonlinear modes ranging from 12 to 50.

For the case at $Re = 5000$, the ROM is integrated using the DEIM and the QDEIM for a single cycle of vortex shedding. In both cases the model is integrated suc-

Chapter 3. Construction and implementation of a nonlinear projection-based ROM for the compressible Navier-Stokes equations

cessfully. Nevertheless different levels of accuracy are detected when switching the masked projection algorithms and/or changing the number of interpolation points. Fig.3.16 presents the density snapshot corresponding to the last time instance of the vortex shedding cycle for the FOM (a) and the absolute error $|\rho_{FOM} - \rho_{ROM}|$ with respect to such a snapshot resulting from the ROM integration with different masked projection approaches and number of interpolation points (b-e). In line with its theoretical derivation, the QDEIM is globally more accurate than the DEIM. However, there is not a monotonic relationship between the accuracy and the number of retained non-linear modes (and interpolation points): indeed the best accuracy is reached using 12 nonlinear POD modes. This undesirable and counterintuitive trend, highlighted also in the previous Section 3.4.4, often recurs when using masked projection approaches and will be analyzed in the next test case.

For the case at $Re = 10000$, the ROM is integrated using the DEIM and the QDEIM for the cycle of vortex shedding. In this case, the DEIM fails and the system always diverges except when using 40 nonlinear POD modes as shown in Fig.3.17. As discussed above, there is no guarantee that increasing the number of interpolation points enhances accuracy as, also in this case, the change from 40 to 50 points deteriorates the solution leading to divergence. This is due to the limitations of the DEIM algorithm that requires a number of interpolation points equal to the number of nonlinear POD modes. In other words, the extension of the nonlinear term basis with a new lower energy nonlinear mode is required in order to add one new interpolation point. Such a mode can contain the low energy numerical fluctuations that involve potentially destabilizing dynamics. Moreover, the inclusion of these low energy modes leads to the selection of those cells that are mostly affected by numerical fluctuation. The use of such cells for the interpolation would potentially introduce spurious oscillations that inevitably affect the performance of the ROM. As a consequence, whilst a high number of interpolation points would certainly enhance the performance of the interpolation, it implies the use of low energy nonlinear modes that could involve chaotic fluctuations of the flow and compromise the stability of the model. As an example, the 50th nonlinear mode and the related amplitude are depicted in Fig.3.18 in order to show the nature of low energy modes. On the other hand, the benefits of the QDEIM approach are highlighted in Fig.3.19. First of all, divergence never occurs and the best accuracy is reached using 20 interpolation points. Increasing further implies a bigger error with respect to the FOM. The same trend can be observed for the wall pressure in Fig.3.20. As one can see, the error slightly increases during the cycle but for the QDEIM ROMs it is always lower than 1% for any choice of the size of the nonlinear basis. So it is evident that, the improved error bound provided theoretically by the QDEIM implies better performances with an unchanged computational cost.

3.5. Assessment of the performance of the masked projection techniques in fluid dynamics applications

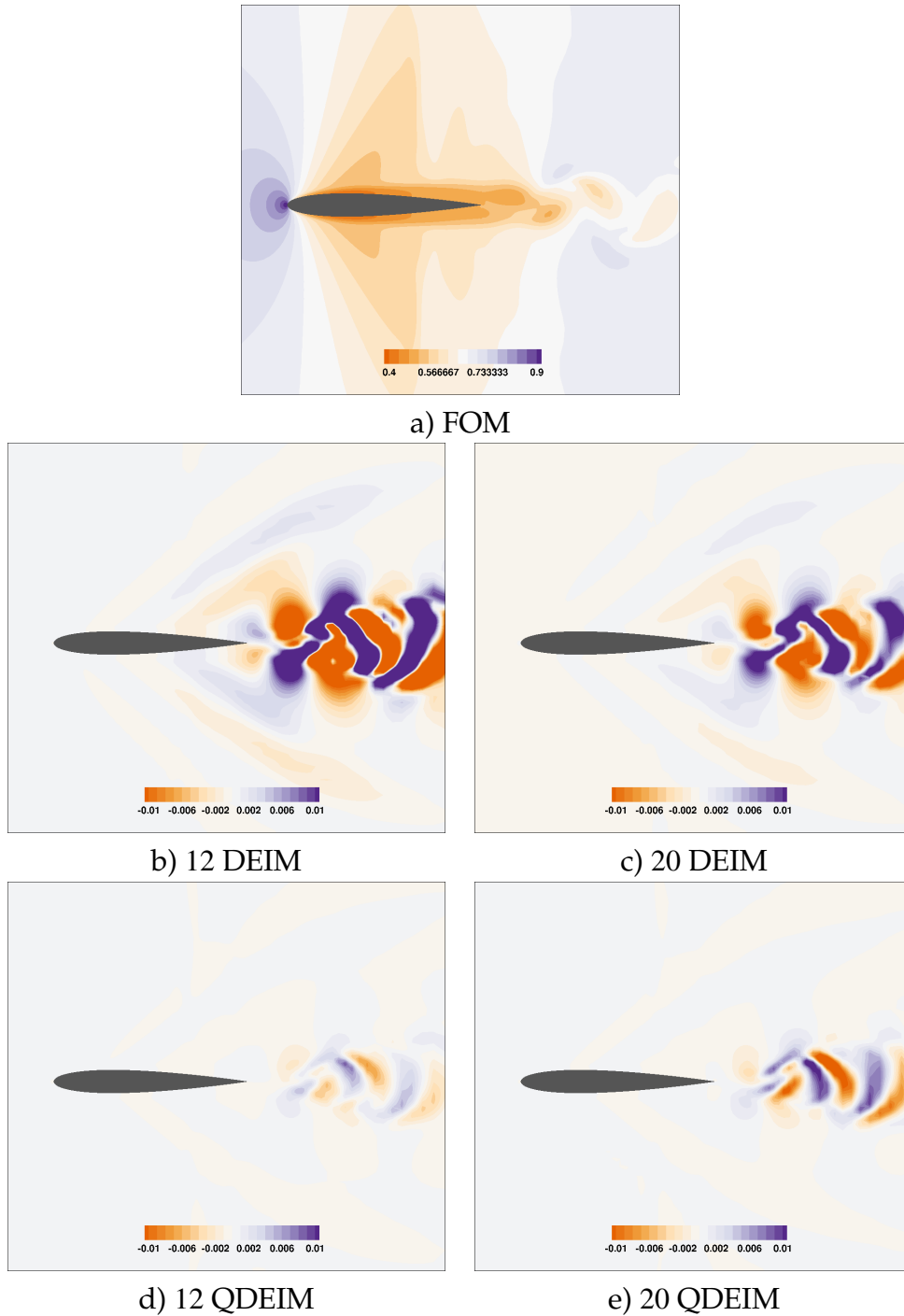


Figure 3.16 $Re = 5000$, $M = 0.85$, $\alpha = 0^\circ$: a) FOM density instantaneous snapshot of the flow for the last time instance of the sampled vortex shedding period; density fields absolute difference between the FOM and: b) the ROM-DEIM with 12 nonlinear modes, c) the ROM-DEIM with 20 nonlinear modes, d) the ROM-QDEIM with 12 nonlinear modes, e) the ROM-QDEIM with 20 nonlinear modes.

Chapter 3. Construction and implementation of a nonlinear projection-based ROM for the compressible Navier-Stokes equations

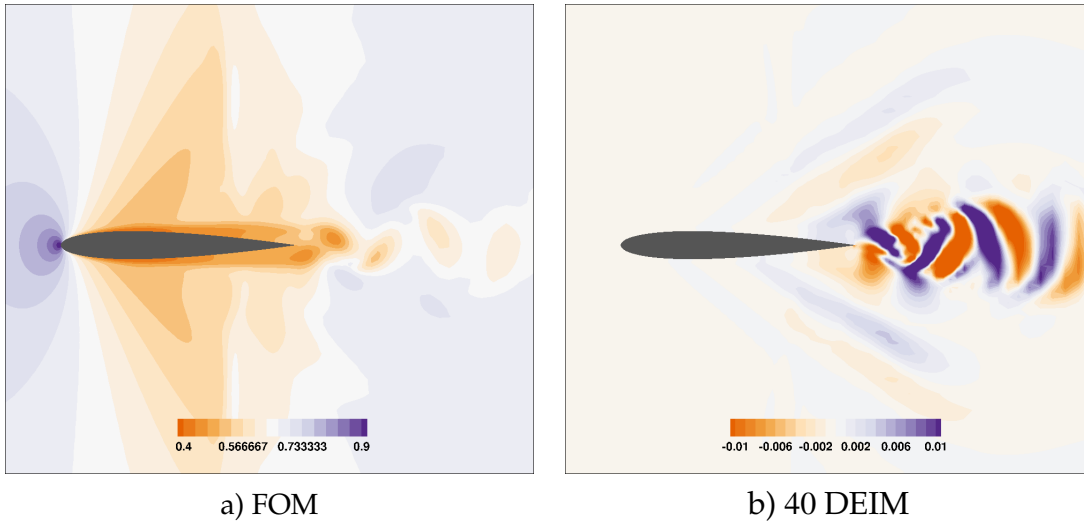


Figure 3.17 $Re = 10000$, $M = 0.85$, $\alpha = 0^\circ$: a) FOM density instantaneous snapshot of the flow for the last time instance of the sampled vortex shedding period; b) density fields absolute difference between the FOM and the ROM-DEIM with 40 nonlinear modes.

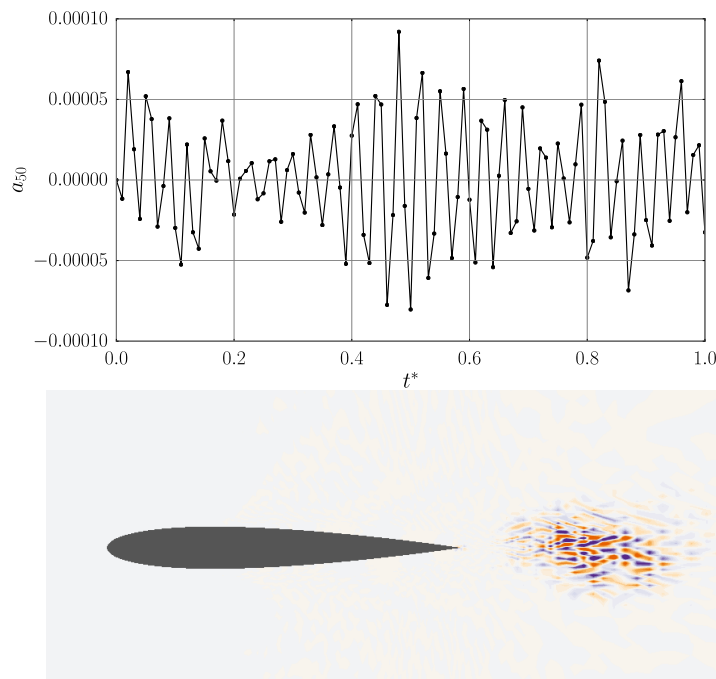


Figure 3.18 The 50th amplitude and nonlinear mode for the flow at $Re = 10000$.

3.5. Assessment of the performance of the masked projection techniques in fluid dynamics applications



Figure 3.19 $Re = 10000$, $M = 0.85$, $\alpha = 0^\circ$: a) FOM density instantaneous snapshot of the flow for the last time instance of the sampled vortex shedding period; density fields absolute difference between the FOM and: b) the ROM-QDEIM with 12 nonlinear modes, c) the ROM-QDEIM with 20 nonlinear modes, d) the ROM-QDEIM with 30 nonlinear modes, e) the ROM-QDEIM with 40 nonlinear modes, e) the ROM-QDEIM with 50 nonlinear modes.

Chapter 3. Construction and implementation of a nonlinear projection-based ROM for the compressible Navier-Stokes equations

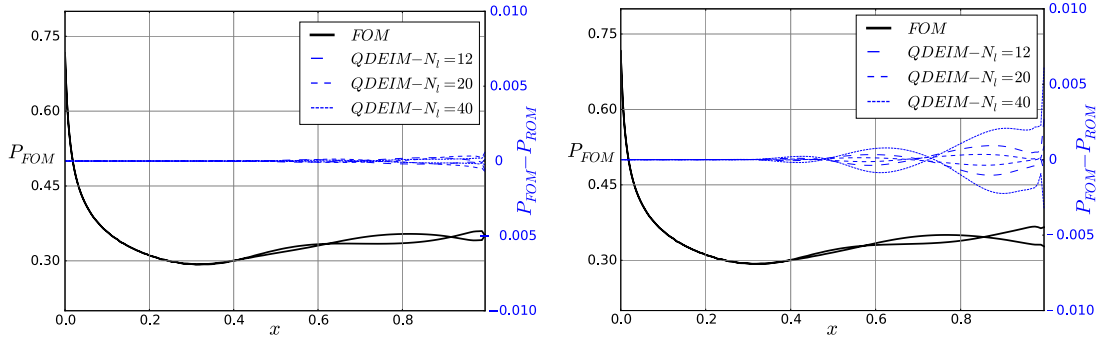


Figure 3.20 $Re = 10000$, $M = 0.85$, $\alpha = 0^\circ$: on the left axis the wall pressure reference in black and on the right axis the wall pressure differences for different p in blue. On the left for $t = T/2$ and on the right at the end the cycle $t = T$.

3.5.2 High incidence flow around a NACA 0012 airfoil

In this section, two additional test-cases are considered. The first one is the flow around a fixed NACA 0012 airfoil set at an incidence of $\alpha = 10^\circ$ with the flow parameters $M = 0.2$ and $Re = 5000$. For the second one the airfoil is set at $\alpha = 20^\circ$ with the flow parameters $M = 0.2$ and $Re = 1000$. The same grid as the one employed in the previous section is used. The flow can be considered as slightly compressible. With a preliminary steady solution as initial condition, an unsteady simulation is performed with the Backward Euler scheme and the Dual Time Step acceleration technique. The maximal number of sub-iterations is set to 50 and the adimensional timestep, computed with respect to the chord length and the far field velocity, is set to 0.01. After a transient phase a periodic vortex shedding phenomenon is observed. A sampling of 100 snapshots on one vortex-shedding cycle is employed in order to construct the POD basis for the flow solution and for the non-linear residual term. For these test cases, the vortex shedding spreads over a wider area behind the airfoil compared to the previous ones as shown in the density field related to the last time instance of the sampled vortex shedding period in Fig.3.21. The energy distribution of the solution POD modes is compared in Fig.3.14 to the one of the previous test cases of Section 3.5.1.

For the reduced order model, the dimension of the solution POD basis is set to $m = 12$ and the the ROM is integrated in time using the 4th order Runge-Kutta explicit scheme. In both cases, the choice of the basis dimension is done according to the value $E_m = \sum_{i=1}^m \sigma_i^2 / \sum_{i=1}^r \sigma_i^2$ that, for $m = 12$, is already over 0.9999.

The ROMs constructed using the DEIM approach and its variation the QDEIM approach always fail so that it is impossible to reach the end of a vortex shedding cycle before divergence occurs. The two methods are tested and compared using an increasing number of nonlinear modes from 10 to 40. Oversampling seems to be mandatory in these cases for the construction of an acceptable nonlinear ROM. The block adaptation of the DEIM (BDEIM) and of the QDEIM (BQDEIM), is analyzed

3.5. Assessment of the performance of the masked projection techniques in fluid dynamics applications

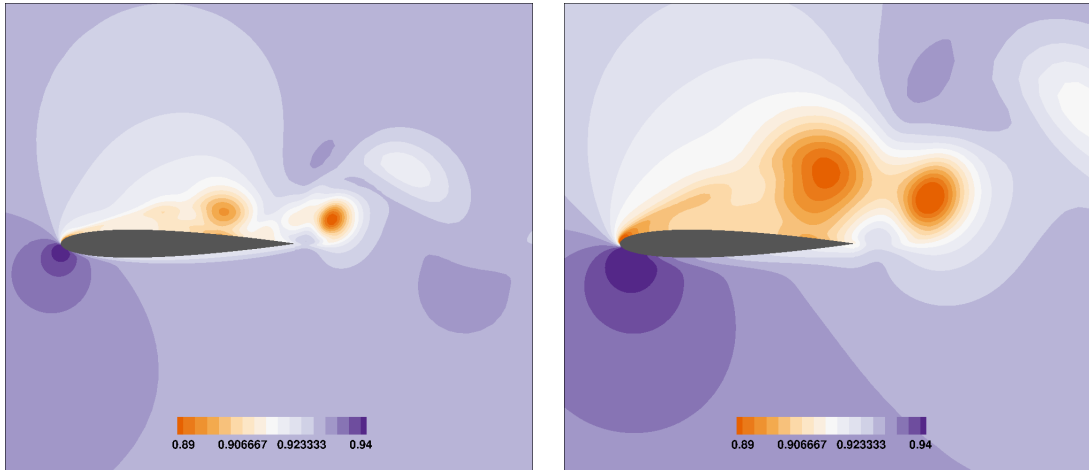


Figure 3.21 Instantaneous density field for $Re = 5000$, $M = 0.2$, $\alpha = 10^\circ$ on the left and for $Re = 1000$, $M = 0.2$, $\alpha = 20^\circ$ on the right.

with respect to the standard approach. We remind that, as the adapted Algorithm 4 (p.25) is used, the number of interpolation points is equal to the number of nonlinear modes times the number of conservative variables $f = k \cdot p$, where $k = 4$ as, in this case, a 2D configuration is considered. From now on, the ROM is intended to be constructed using the second formulation of eq.(3.34) so that, for the sake of clarity, the selected points are referred more properly as fitting points.

Chapter 3. Construction and implementation of a nonlinear projection-based ROM for the compressible Navier-Stokes equations

3.5.2.1 Flow around a NACA 0012 airfoil at $Re = 5000$, $M = 0.2$, and $\alpha = 10^\circ$

In the context of oversampling, the BDEIM/BQDEIM (respectively the BDEIM and the QBDEIM methods) detailed in Algorithm 4 (p.25) are tested using up to 60 nonlinear basis functions. The BDEIM always fails except when using 60 nonlinear POD modes which implies the use of 240 fitting points. On the contrary the QBDEIM converges with only 10 nonlinear POD modes which implies the use of 40 fitting points. We remark that the accuracy of this ROM is plotted in Fig.3.22. The accuracy of the model for the QBDEIM approach is considerably enhanced by enriching the nonlinear basis, as shown in Fig.3.23 (note the different color scale). The same trend for the wall-pressure can be observed in Fig.3.24.

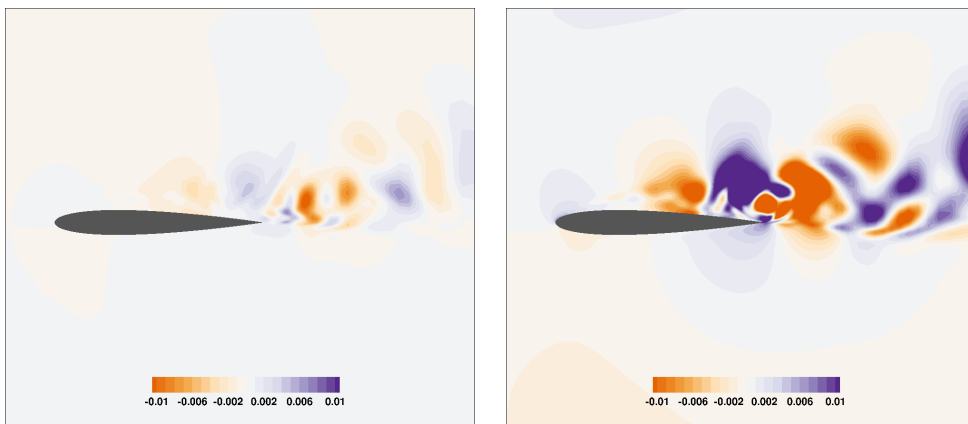


Figure 3.22 Instantaneous density fields absolute difference between the ROM and the FOM plotted in Fig.3.21 for the BDEIM adaptation using $p = 60$ nonlinear modes (and $f = 240$ fitting points) on the left, and using the BQDEIM adaptation using $p = 10$ nonlinear modes (and $f = 40$ fitting points) on the right.

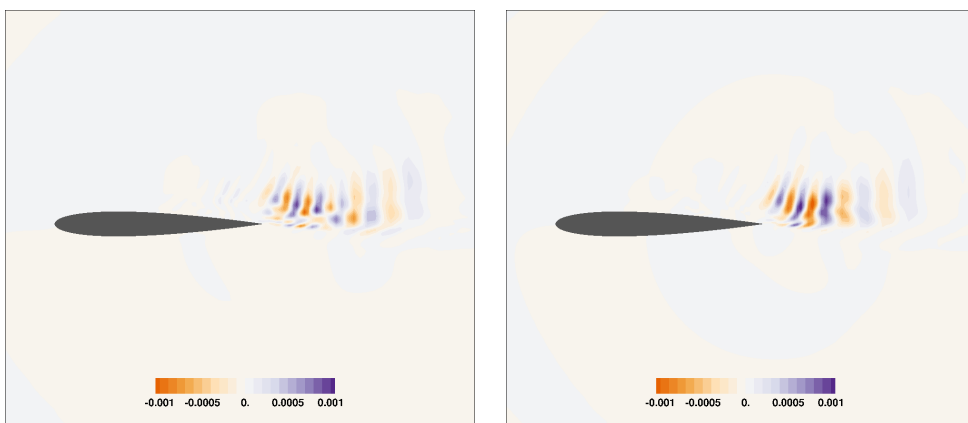


Figure 3.23 Instantaneous density fields absolute difference between the ROM and the FOM plotted in Fig.3.21 for the BQDEIM adaptation using $p = 20$ nonlinear modes (and $f = 80$ fitting points) on the left, and using the BQDEIM adaptation using $p = 30$ nonlinear modes (and $f = 120$ fitting points) on the right.

3.5. Assessment of the performance of the masked projection techniques in fluid dynamics applications

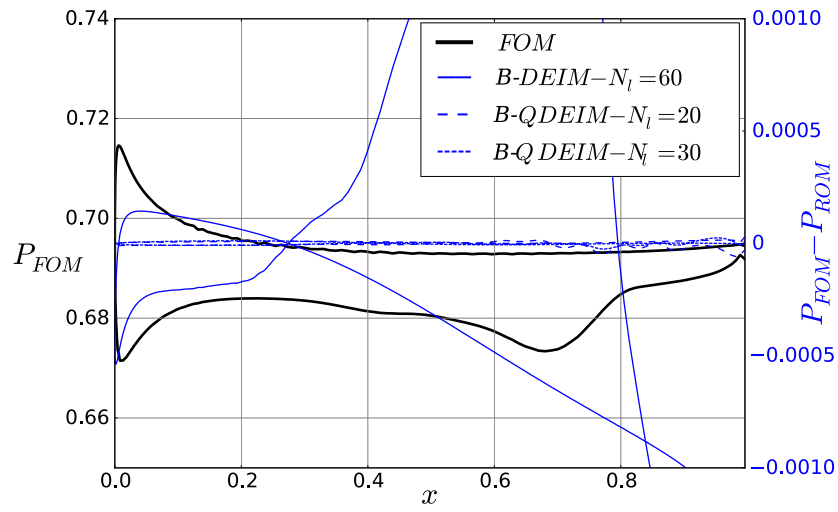


Figure 3.24 $Re = 5000$, $M = 0.2$, $\alpha = 10^\circ$: on the left axis the wall pressure reference in black and in blue on the right axis the wall pressure differences for different p at the last time instance of the vortex shedding cycle.

Chapter 3. Construction and implementation of a nonlinear projection-based ROM for the compressible Navier-Stokes equations

3.5.2.2 Flow around a NACA 0012 airfoil at $Re = 1000$, $M = 0.2$, and $\alpha = 20^\circ$

For the last test case, the BDEIM and the QBDEIM are tested using up to 60 nonlinear basis functions. In Fig.3.25 the benefit of the QBDEIM with respect to the BDEIM is clearly shown, indeed using half of nonlinear modes and fitting points, the QBDEIM results in a more accurate ROM. To achieve a similar accuracy in the density field as the one obtained with a QBDEIM approximation with 10 nonlinear modes, the use of 40 nonlinear modes is required for the BDEIM (Fig.3.26). Finally, the best accuracy for the model is achieved using the QBDEIM approach constructed using 20 nonlinear modes (and 80 fitting points) as shown in Fig.3.27.

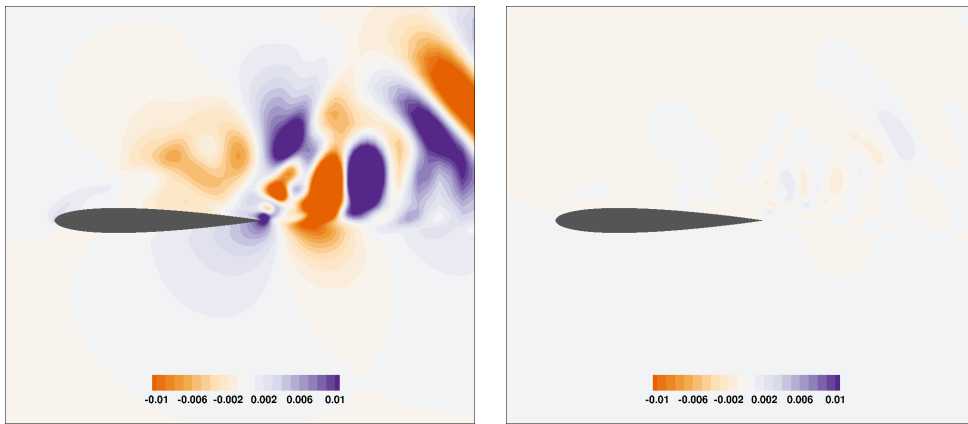


Figure 3.25 Instantaneous density fields difference between the ROM and the FOM plotted in Fig.3.21 for the BDEIM adaptation using $p = 20$ nonlinear modes (and $f = 80$ fitting points) on the left, and using the BQDEIM adaptation using $p = 10$ nonlinear modes (and $f = 40$ fitting points) on the right.

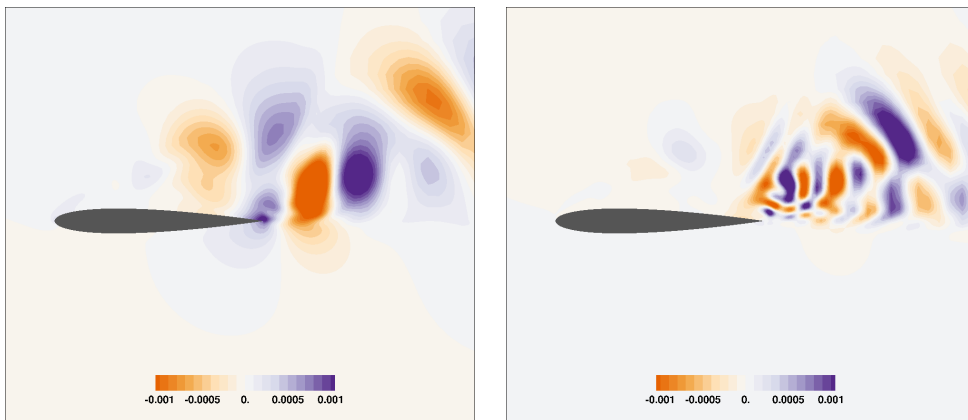


Figure 3.26 Instantaneous density fields difference between the ROM and the FOM plotted in Fig.3.21 for the BDEIM adaptation using $p = 40$ nonlinear modes (and $f = 160$ fitting points) on the left, and using the BQDEIM adaptation using $p = 10$ nonlinear modes (and $f = 40$ fitting points) on the right.

3.6. Conclusions

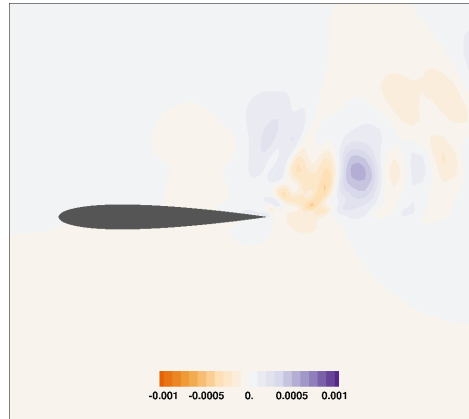


Figure 3.27 Instantaneous density fields difference between the ROM and the FOM plotted in Fig.3.21 for the BQDEIM adaptation using $p = 20$ nonlinear modes (and $f = 80$ fitting points).

3.6 Conclusions

In this chapter, a nonlinear ROM for the compressible Navier-Stokes equations has been implemented and tested. It has been based on the theoretical derivation of Chapter 2 for a general nonlinear problem and subsequently adapted for a fluid dynamics context. All the different steps of the ROM implementation process have been explained from both a theoretical and a practical point of views, by using test cases of increasing complexity. Particular attention is given to the development of the masked projection approaches with respect to the employed selection algorithm. To summarize, the following are the key take away points from the study carried out in this chapter:

- The 99,99% energy cut-off condition to select the number of POD modes for the ROM approximation is commonly employed in model reduction and is suitable in many cases. However, in some cases, it can represent a source of inaccuracy and a further *a posteriori* analysis should be conducted in order to determine the cut-off condition of the POD basis.
- The DEIM and QDEIM masked projection approaches are simple to implement and their application requires a low computational cost. However, they may be inaccurate and exhibit a limit: the increase of the number of interpolation points requires the gradual enlargement of the nonlinear POD basis using progressively higher order non linear modes. Such modes could include into the reduced system numerical fluctuations leading to divergence.
- The BDEIM/BQDEIM algorithms are adaptation of the DEIM/QDEIM algorithms that allow oversampling without affecting the size of the nonlinear POD basis. Furthermore, such approaches imply a computational complexity which does not scale with the number of degrees of freedom of the system so that they keep a low computational cost.

Chapter 3. Construction and implementation of a nonlinear projection-based ROM for the compressible Navier-Stokes equations

To conclude, a nonlinear ROM for the Navier-Stokes equations using masked approaches has been validated in a fixed mesh scenario. In the next chapter, the adaptation of this ROM to aeroelastic application dealing with moving or deforming meshes is investigated, that is the main objective of this dissertation.

Adaptation of a nonlinear ALE-based reduced order model of the Navier-Stokes equations for aeroelasticity

Contents

4.1 Introduction	70
4.2 Projection of the Arbitrary Lagrangian-Eulerian formulation of the Navier-Stokes equations	70
4.2.1 Computation of the POD modes of a flow configuration with deforming mesh	72
4.2.2 Nonlinear ROM adaptation for non-autonomous systems	73
4.2.3 Alternative centering of the snapshot collection	73
4.2.4 Practical adaptation of an ALE-based nonlinear reduced order model	75
4.3 Numerical integration of the nonlinear ALE-based ROM of a flow around a cylinder in forced motion at low Reynolds	76
4.3.1 Adaptation of the ALE-based nonlinear ROM for a new parameter configuration	85
4.3.2 Numerical integration of the adapted nonlinear ALE-based ROM for new motion parameters	89
4.3.3 Discussion	96
4.4 Numerical integration of an aeroelastic reduced order system: flow around a cylinder in free motion	97
4.5 Conclusions	104

4.1 Introduction

Having formulated and validated a nonlinear ROM for the Navier-Stokes equations, the goal now is to adapt such a ROM for aeroelastic simulations. Indeed, the ROM developed in the previous chapter does not take into account the additional complexity arising from the Arbitrary Lagrangian-Eulerian formulation which is necessary to solve the Navier-Stokes equations on a deforming spatial domain. First, the Arbitrary-Lagrangian Eulerian formulation of the Navier-Stokes equation is derived. The differences with respect to a purely Eulerian formulation are highlighted and, subsequently, their impact on the nonlinear ROM formulation is analyzed and a practical implementation of the ROM is illustrated.

The resulting ROM is tested for the flow around a cylinder in forced motion at different frequencies and amplitudes. A constant focus is kept on the efficiency and the stability of the ROM, so that the masked projection approach, assessed in the previous chapter, is adapted and validated also in this case. Then, a strategy for the adaptation of a pre-computed ROM to new motion parameters is presented and tested. Finally, a preliminary study for the coupling of the nonlinear ROM for aeroelasticity with a structural model is introduced. Conclusions are given in the last section.

4.2 Projection of the Arbitrary Lagrangian-Eulerian formulation of the Navier-Stokes equations

The conservation laws of fluid mechanics are expressed in eq.(3.1), (3.2), (3.3) for the material (Lagrangian) time derivatives of the density, the momentum and the energy. Using the chain rule, these derivatives are split into a partial time derivative term at a given spatial location plus an additional convective term due to the transport of the particle so that the conservation laws can be dealt with in an Eulerian framework on a fixed spatial domain of interest. However some parts of the spatial domain of interest may be subject to some deformations (e. g. for aeroelastic or free surface problems) in which case a Lagrangian approach would be more convenient to describe the motion of the boundary and its close neighborhood. The purpose of the Arbitrary Lagrangian-Eulerian (ALE) formulation is to combine the advantages of both the Lagrangian and the Eulerian approaches. Following the derivation of Donea *et al.* [126], if we consider an entrained and/or deformable $\Omega(t)$ computational domain, of boundary $\partial\Omega(t)$ with the unit external normal $\mathbf{n}(t)$ and velocity $\mathbf{s}(t)$ respective to an absolute reference domain frame, the following ALE integral form for the Navier-Stokes equations can be written:

$$\frac{d}{dt} \int_{\Omega(t)} \mathbf{w} d\Omega + \oint_{\partial\Omega(t)} \mathbf{F}_c(\mathbf{w}, \mathbf{s}) \cdot \mathbf{n} d\Sigma + \oint_{\partial\Omega(t)} \mathbf{F}_d(\mathbf{w}) \cdot \mathbf{n} d\Sigma = \mathbf{0}, \quad (4.1)$$

4.2. Projection of the Arbitrary Lagrangian-Eulerian formulation of the Navier-Stokes equations

where the velocity s includes both the velocity linked to the domain deformation and/or the entrainment movement velocity. In this integral formulation, with respect to eq.(3.13) the only different term is the convective flux:

$$\oint_{\partial\Omega(t)} \mathbf{F}_c(\mathbf{w}, s) \cdot \mathbf{n} d\Sigma = \begin{pmatrix} \oint_{\partial\Omega(t)} \rho(\mathbf{U} - s) \cdot \mathbf{n} d\Sigma \\ \oint_{\partial\Omega(t)} [\rho\mathbf{U} \otimes (\mathbf{U} - s) + p\mathbf{I}] \cdot \mathbf{n} d\Sigma \\ \oint_{\partial\Omega(t)} [\rho E(\mathbf{U} - s) + p\mathbf{U}] \cdot \mathbf{n} d\Sigma \end{pmatrix}. \quad (4.2)$$

If we consider a computational domain discretized in a system of elementary *hexahedral* cells, we can write the semi-discrete formulation for eq.(4.1):

$$\frac{d}{dt} \int_{\Omega(t)} \mathbf{w} d\Omega = - \sum_{i=1}^6 \int_{\Sigma_i(t)} [\mathbf{F}_c(\mathbf{w}, s) + \mathbf{F}_d(\mathbf{w})] \cdot \mathbf{n} d\Sigma, \quad (4.3)$$

where Σ_i represents the i -th face of the *hexahedral* cell considered in the mesh. Then, the average of the conservative variables \mathbf{w} in the cell Ω can be defined as:

$$\mathbf{w}_\Omega = \frac{1}{\mathcal{V}(\Omega)(t)} \int_{\Omega(t)} \mathbf{w} d\Omega, \quad (4.4)$$

where $\mathcal{V}(\Omega)$ is the **time-dependent** volume of the related cell. By substituting such a term in eq.(4.3), we can write:

$$\frac{d \mathcal{V}(\Omega) \mathbf{w}_\Omega}{dt} = -\mathbf{R}_\Omega(\mathbf{w}_\Omega, t), \quad (4.5)$$

where \mathbf{R}_Ω is a non-linear residual operator that computes the flux balance for each cell. After developing the derivative, eq.(4.5) can be written as:

$$\frac{d \mathbf{w}_\Omega}{dt} = -\frac{\mathbf{R}_\Omega(\mathbf{w}_\Omega, t)}{\mathcal{V}(\Omega)} - \frac{\mathbf{w}_\Omega}{\mathcal{V}(\Omega)} \frac{d \mathcal{V}(\Omega)}{dt}. \quad (4.6)$$

With respect to eq.(3.20), an additional source term is included in the right-hand side of the FOM eq.(4.6) to take into account the variation of the cell volumes. For a preliminary study, this last source term can be neglected so that the following formulation is obtained:

$$\frac{d \mathbf{w}_\Omega}{dt} = -\frac{\mathbf{R}_\Omega(\mathbf{w}_\Omega, t)}{\mathcal{V}(\Omega)} = \mathbf{f}_\Omega(\mathbf{w}_\Omega, t). \quad (4.7)$$

In order to relax the notation, the subscript Ω can be omitted so that the following equation is obtained:

$$\frac{d \mathbf{w}(t)}{dt} = \mathbf{f}(\mathbf{w}(t), t). \quad (4.8)$$

Chapter 4. Adaptation of a nonlinear ALE-based reduced order model of the Navier-Stokes equations for aeroelasticity

The previous equation and eq.(3.21) differ only in the time dependency of the mesh metric for the fluxes balance computation. This implies that the system is non-autonomous and the nonlinear ROM mathematical formulation reported in eq.(3.34) can be adapted as:

$$\frac{d\mathbf{a}(t)}{dt} = \mathbf{\Phi}^T \mathbf{f}(\mathbf{w}_0, t_0) + \mathbf{\Phi}^T \mathbf{U} (\mathbf{U}^T \mathbf{P} \mathbf{P}^T \mathbf{U})^{-1} \mathbf{U}^T \mathbf{P} \left(\mathbf{f}_P(\tilde{\mathbf{P}}^T \tilde{\mathbf{w}}(t), t) - \mathbf{P}^T \mathbf{f}(\mathbf{w}_0, t_0) \right), \quad (4.9)$$

where the use of the BQDEIM is implied given the assessment study of Section 3.5. Consequently, the ROM implementation reported in Algorithm 6 (presented at p.53) is valid also for the nonlinear ALE-based ROM with a few but important differences illustrated in the following sections.

4.2.1 Computation of the POD modes of a flow configuration with deforming mesh

When considering a deforming domain, the spatial correlation between different snapshots in the collection \mathbf{W} is lost because each finite volume is moving and deforming during the numerical simulation. As a result, the POD formulation requires an adaptation. More specifically, the snapshot sequence \mathbf{W} of line 1 of Algorithm 6 (p.53) is provided by preserving the spatial location of each cell along the different lines. In such a way, the POD modes of the system can be obtained by performing the SVD of \mathbf{W} in accordance with the POD theory reported in Section 2.3. If the snapshots are solutions of the ALE formulation of eq.(4.8), as the mesh is deforming the spatial correlation is lost and it would result in a biased POD formulation. To overcome such an issue, Anttonen *et al.* [48] argued that, even if the mesh is moving or deforming, the whole index numbering does not change during the simulation. As a consequence, if the snapshots are stored in such a way that each line corresponds to a given cell index, the resulting modes are no longer ‘spatial’ modes since the cell position has changed, but rather ‘index’ modes.

Alternative formulations are reported in Chapter 1 but they consider either incompressible formulation or polynomial nonlinearities in the Navier-Stokes formulation all in a continuous framework and thereby preventing the use of the masked projection approaches investigated in previous chapters. The approach proposed by Anttonen *et al.* [48] is suitable for the masked projection approach as it is formulated in a discrete framework. If the original masked projection selects a set of cells to perform an interpolation (or fitting) of the nonlinear term, following the index-based POD formulation the masked projection approach will select a set of index which identifies a set of moving or deforming cells. Obviously, during the ROM integration, the motion and/or the deformation of such a set of cells must be taken into account. This last aspect will be dealt with in next Section 4.2.2.

4.2. Projection of the Arbitrary Lagrangian-Eulerian formulation of the Navier-Stokes equations

4.2.2 Nonlinear ROM adaptation for non-autonomous systems

As highlighted above, with respect to eq.(3.21), the system of eq.(4.8) is non-autonomous. Indeed, the right-hand side depends on time t because the mesh deforms during the time integration. The nonlinear term f stands for the fluxes balance computation of the ALE-formulation of the Navier-Stokes equations divided by the concerning cell volumes. Consequently, during the ROM integration, the metric must be updated for the fluxes balance through the deforming cell faces. A brief discussion of the model reduction of non-autonomous systems has been mentioned in Section 2.6 with a focus on the adaptation of Algorithm 5 (p.27) and in particular on the computation of the operator $f_P(\tilde{\mathbf{P}}^T \Phi \mathbf{a}(t), t)$. In this case, the related $f_P(\tilde{\mathbf{P}}^T \tilde{\mathbf{w}}, t)$ operator computes the flux balances for the selected cells by the masked projection approach and divides them by the related cell volumes. As a consequence, such a nonlinear term is strictly dependent on the instantaneous mesh metric. This reflects on the ROM online phase implementation because the metric of the cells selected by $\tilde{\mathbf{P}}^T$ must be updated at each time step of the time integration.

4.2.3 Alternative centering of the snapshot collection

In Section 3.3.2 the common practice of centering the snapshot collection with respect to a reference state $\tilde{\mathbf{w}}$ has been introduced. When considering fixed mesh configurations, a common choice is to set $\tilde{\mathbf{w}}$ as the time-averaged flow field (see Chapter 3). In the present ALE-based ROM formulation, the snapshot collection is centered around the initial flow field $\tilde{\mathbf{w}} = \mathbf{w}(t_0) = \mathbf{w}_0$ so that the snapshot collection for the POD becomes $\mathbf{W} = [\mathbf{w}(t_0) - \mathbf{w}(t_0), \mathbf{w}(t_1) - \mathbf{w}(t_0), \dots, \mathbf{w}(t_{N_t}) - \mathbf{w}(t_0)]$, with $\mathbf{W} \in \mathbb{R}^{n \times N_t}$ and the flow is approximated as:

$$\tilde{\mathbf{w}}(t) \approx \mathbf{w}_0 + \Phi \mathbf{a}(t). \quad (4.10)$$

Thus, the eq.(3.29) for the computation of the initial amplitudes \mathbf{a}_0 can be avoided and the initial condition can be directly defined as:

$$\mathbf{a}_0 = \mathbf{0}. \quad (4.11)$$

The reason motivating the choice of such a centering is linked to the computation of the ROM for a new different flow parameter (*off-reference condition*). In such circumstances, an adaptation of the current ROM is required in order to avoid the computational burden behind the construction of a new ROM. Such adaptations usually require interpolation techniques that inevitably introduce some error. Assuming a centering with respect to the averaged flow field, interpolation techniques are introduced for $\tilde{\mathbf{w}}$. Then, concerning \mathbf{a}_0 either a new interpolation is performed, or a reference initial condition like $\mathbf{a}_0 = \Phi^T \mathbf{w}_\infty$ can be used, where \mathbf{w}_∞ is the far field uniform solution. In this latter case, the robustness of the ROM together with a transient phase towards the established periodic condition must be assumed. Instead,

Chapter 4. Adaptation of a nonlinear ALE-based reduced order model of the Navier-Stokes equations for aeroelasticity

by using the proposed snapshot centering, \mathbf{a}_0 is fixed to zero for any flow field configuration and the interpolation error is introduced only for the adaptation of the new off-reference initial flow field \mathbf{w}_0 .

4.2. Projection of the Arbitrary Lagrangian-Eulerian formulation of the Navier-Stokes equations

4.2.4 Practical adaptation of an ALE-based nonlinear reduced order model

All previous considerations lead to the construction of an ALE-based nonlinear ROM for the Navier-Stokes equations which requires some adjustments with respect to the one formulated in Chapter 3 for fixed mesh configurations and outlined in Algorithm 6 (p.53). As a consequence, all the phases of the ALE-based nonlinear ROM for the compressible Navier-Stokes equations are detailed in Algorithm 7 and the adjustments with respect to Algorithm 6 are highlighted in blue color.

Algorithm 7 Nonlinear ALE-based ROM of the Navier-Stokes equations

Offline phase:

- 1: Generate the **index-based** snapshot sequences $\mathbf{W} \in \mathbb{R}^{n \times N_t}$ for the solution and $\mathbf{F} \in \mathbb{R}^{n \times N_t}$ for the nonlinear term using the FOM solver with subtraction respectively of \mathbf{w}_0 and $\mathbf{f}(\mathbf{w}_0, t_0)$
- 2: Construct $\Phi \in \mathbb{R}^{n \times m}$ using POD via Algorithm 1 with input \mathbf{W}
- 3: Construct $\mathbf{U} \in \mathbb{R}^{n \times p}$ using POD via Algorithm 1 with input \mathbf{F}
- 4: Construct masked projection matrix \mathbf{P} via Algorithm 2,3 or 4 with input \mathbf{U}
- 5: **if** Algorithm 2 or 3 is chosen **then**
- 6: $\mathbf{P} \in \mathbb{R}^{n \times p}$
- 7: Compute the matrix operations of eq.(3.34) once and for all: $\Phi^T \mathbf{U} (\mathbf{P}^T \mathbf{U})^{-1}$, $\Phi^T \mathbf{f}(\mathbf{w}_0, t_0)$ and $\mathbf{P}^T \mathbf{f}(\mathbf{w}_0, t_0)$
- 8: **else if** Algorithm 4 is chosen **then**
- 9: $\mathbf{P} \in \mathbb{R}^{n \times kp}$
- 10: Compute the matrix operations of eq.(3.34) once and for all: $\Phi^T \mathbf{U} (\mathbf{U}^T \mathbf{P} \mathbf{P}^T \mathbf{U})^{-1} \mathbf{U}^T \mathbf{P}$, $\Phi^T \mathbf{f}(\mathbf{w}_0, t_0)$ and $\mathbf{P}^T \mathbf{f}(\mathbf{w}_0, t_0)$
- 11: **end if**

Online phase:

Input: Initial value for $\mathbf{a}_0 = \mathbf{0}$ and mesh metric and cell volumes $\mathcal{V}(\Omega)$ for $t = t_0$

Output: Time discrete response for the vector amplitudes $\mathbf{a} \in \mathbb{R}^{m \times N_t}$

- 1: Compute $\mathbf{f}_P(\tilde{\mathbf{P}}^T \mathbf{w}_0, t_0)$
 - 2: Integrate in time eq.(3.34) for \mathbf{a}_1
 - 3: $\mathbf{a} \leftarrow [\mathbf{a}_1]$
 - 4: **for** $i = 2$ to N_t **do**
 - 5: **Construct the nonlinear operator $\mathbf{f}_P(\tilde{\mathbf{P}}^T \tilde{\mathbf{w}}, t)$ with the updated metric and volumes $\mathcal{V}(\Omega)$, for $t = t_{i-1}$**
 - 6: Compute $\mathbf{f}_P(\tilde{\mathbf{P}}^T \tilde{\mathbf{w}}, t_{i-1}) - \mathbf{P}^T \mathbf{f}(\mathbf{w}_0, t_0)$
 - 7: Integrate in time eq.(3.34) for \mathbf{a}_i
 - 8: $\mathbf{a} \leftarrow [\mathbf{a} \ \mathbf{a}_i]$
 - 9: **end for**
-

4.3 Numerical integration of the nonlinear ALE-based ROM of a flow around a cylinder in forced motion at low Reynolds

In this section the numerical performance of the proposed strategy for the integration of ROMs for the ALE formulation of the Navier-Stokes equations (Algorithm 7) is tested. Primarily, the numerical results are presented by looking at the comparison between the amplitudes vectors $\mathbf{a}(t)$ and its high-order counterpart represented by the vector ΣV^T (see eq.(3.25)). In some cases, the reconstructed density field is also analyzed.

We consider a two-dimensional uniform flow past a circular cylinder subjected to a vertical forced motion at Reynolds number $Re = 185$ and Mach $M = 0.2$. The computational domain, is shown in Fig.3.1 and discretized with 11958 unstructured triangular finite volumes. The boundary conditions and numerical parameters are analogous to those reported in Section 3.3.1. The vertical oscillatory movement is imposed at the center of the cylinder following the law $y(t) = A \sin(2\pi ft)$. During the computation the mesh is deformed following the *spring analogy*: all point-to-point connections within the mesh are replaced by linear springs and point motion is obtained as a response to boundary displacement. The parameters A and f are normalized by the cylinder diameter D and the vortex shedding frequency f_{st} so that $A_e = A/D$ and $f_r = f/f_{st}$. The numerical simulations at the basis of the FOM are performed by means of the same solver used in Section 3.3 and validated with respect to the reference [127]. A vortex shedding phenomenon developing at the same oscillation frequency has been observed for $f_r < 1$, while for $f_r > 1$, secondary frequencies are detected (Fig.4.1).

In the following sections, two different vertical oscillation configurations will be analyzed: $(A_e, f_r) = (0.2, 0.8)$ and $(A_e, f_r) = (0.5, 1.2)$ in order to test the ROM on increasingly challenging configurations.

Test case: flow around an oscillating cylinder in forced motion at $Re = 185$, $M = 0.2$ and $(A_e, f_r) = (0.2, 0.8)$

For the first test-case, the cylinder is oscillating at $(A_e, f_r) = (0.2, 0.8)$. With a uniform flow as initial condition a FOM unsteady simulation is performed with the Backward Euler scheme and the Dual Time Step technique. The time-step is set as $\Delta t = 5 \times 10^{-9} s$. In such conditions, Guilmineau *et al.* [127] observed a vortex shedding phenomenon, whose instantaneous density field is shown in Fig.4.2, developing at a frequency equal to the oscillation frequency $f_r = 1$. The energy distribution of the solution POD modes is plotted in Fig. 4.3.

For the reduced order model, the POD basis is truncated to $m = 12$ such that

4.3. Numerical integration of the nonlinear ALE-based ROM of a flow around a cylinder in forced motion at low Reynolds

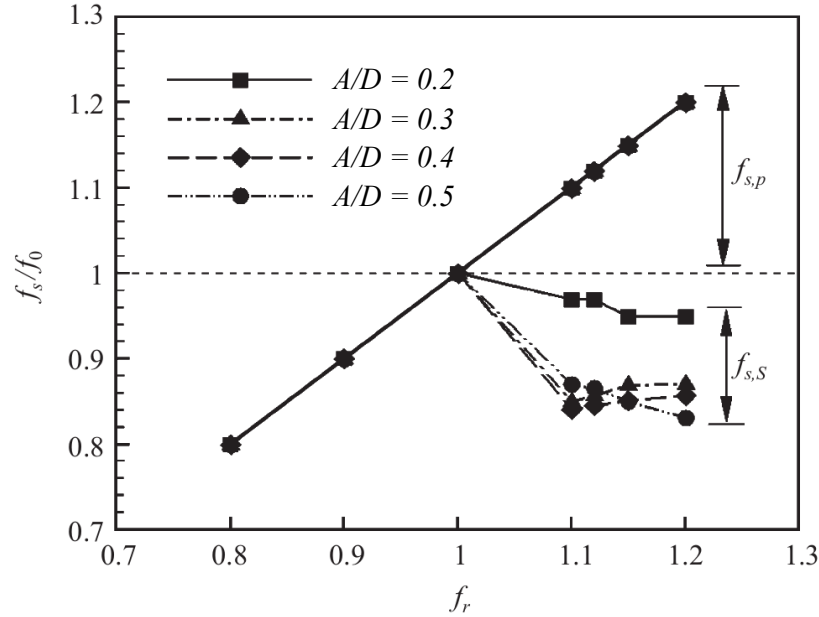


Figure 4.1 Normalized vortex shedding frequency f_s by the shedding frequency of the fixed cylinder configuration f_0 as a function of the f_r for different A_e , where $f_{s,p}$ and $f_{s,S}$ are the primary and secondary frequencies of f_s , respectively [128].

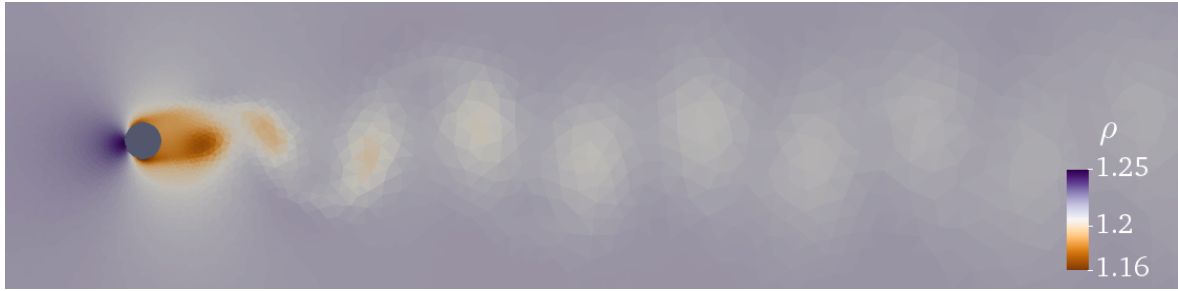


Figure 4.2 Instantaneous density field of a flow around a vertically oscillating cylinder at $Re = 185$, $A_e = 0.2$ and $f_r = 0.8$.

$E_m > 0.9999$. The first 6 density POD modes are depicted in Fig.4.4¹. The ROM outlined in Algorithm 7 (p.75) is integrated using the 4th order Runge-Kutta explicit scheme by using 12 POD modes for the solution basis. Firstly, the nonlinear ROM is integrated without any masked projection approximation. In Fig.4.5 the time history of the first six amplitudes of the ROM reveals a very good accuracy with respect to its FOM counterpart. Indeed, the absolute error, reported to the right axis oscillates between very low values. In order to speed up the evaluation of the nonlinear term and to ensure the overall ROM efficiency, a BQDEIM masked projection approach (provided in eq.(4.9)) is introduced. The ROM is integrated with an approximation

¹We remind that the modes are obtained by an index-based POD formulation. This means that the local value depicted in the plot is related to the cell rather than to the spatial location. In particular, the modes are depicted on the mesh at $t = t_0$.

Chapter 4. Adaptation of a nonlinear ALE-based reduced order model of the Navier-Stokes equations for aeroelasticity

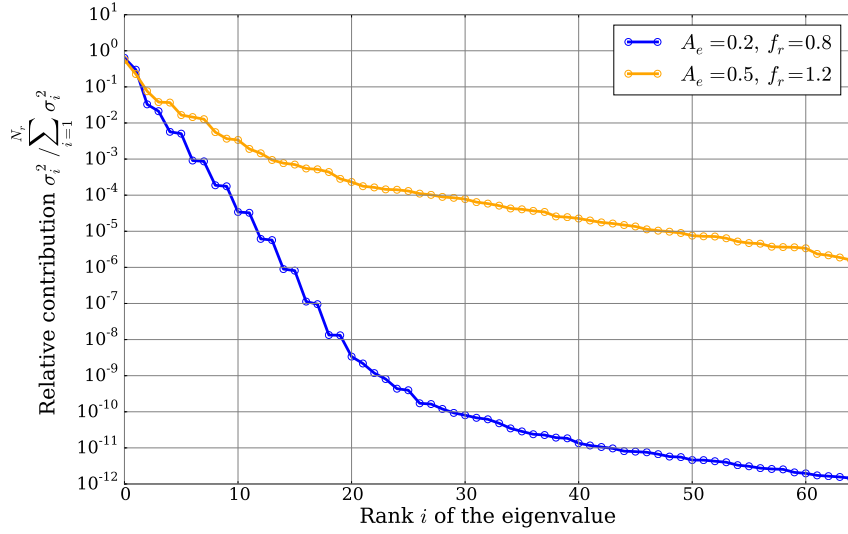


Figure 4.3 Energy distribution of the solution POD modes for the cases of a flow around a vertically oscillating cylinder at $Re = 185$ and $M = 0.2$ for two different sets of forced motion parameters.

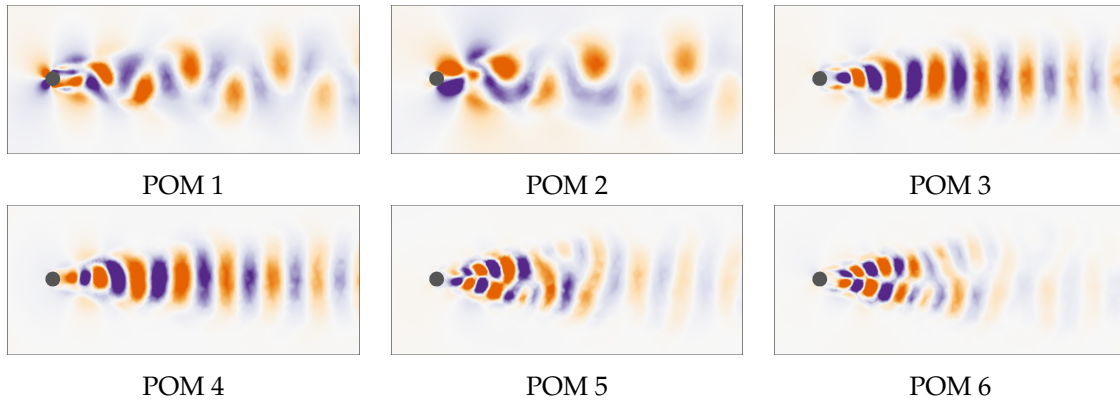


Figure 4.4 First to 6th density proper orthogonal mode (POM) for the flow around a vertically oscillating cylinder at $Re = 185$ and $(A_e, f_r) = (0.2, 0.8)$.

of the nonlinear term involving 14 nonlinear POD modes (and $14 \times 4 = 56$ fitting points, where 4 is the number of conservative variables). Fig.4.6 depicts the time history of the first six amplitudes with respect to the FOM. Although the error with respect to the ROM without masked projection is slightly augmented, the overall accuracy still remains reasonable. To demonstrate this, the difference between the density field obtained by the ROM and the FOM at the last time step of the simulation is shown in Fig.4.7. The local relative error $\frac{\rho_{FOM} - \rho_{ROM}}{\rho_{FOM}} \times 100$ never exceeds 1.2%.

4.3. Numerical integration of the nonlinear ALE-based ROM of a flow around a cylinder in forced motion at low Reynolds

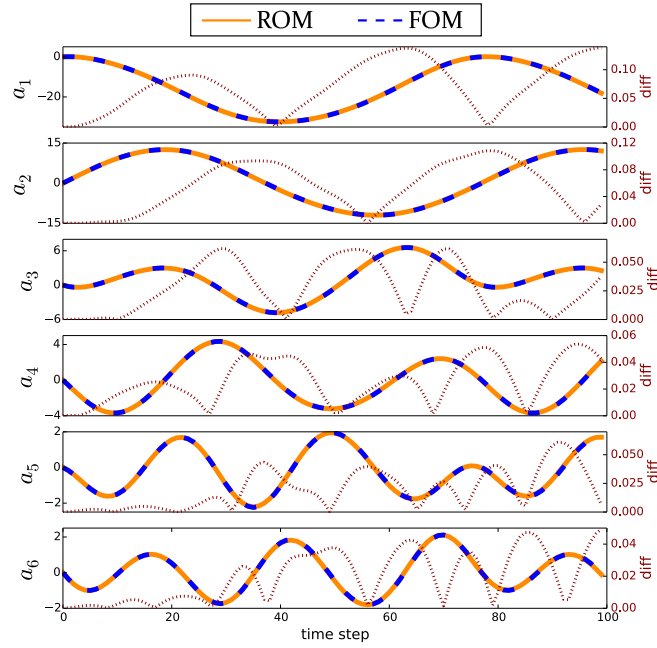


Figure 4.5 On the left axis: time history of the first 6 POD modes amplitudes for the case at $(A_e, f_r) = (0.2, 0.8)$; results obtained for the nonlinear ALE-based ROM without any masked projection. On the right axis: the respective absolute error $|a_{FOM} - a_{ROM}|$ (red dotted plot).

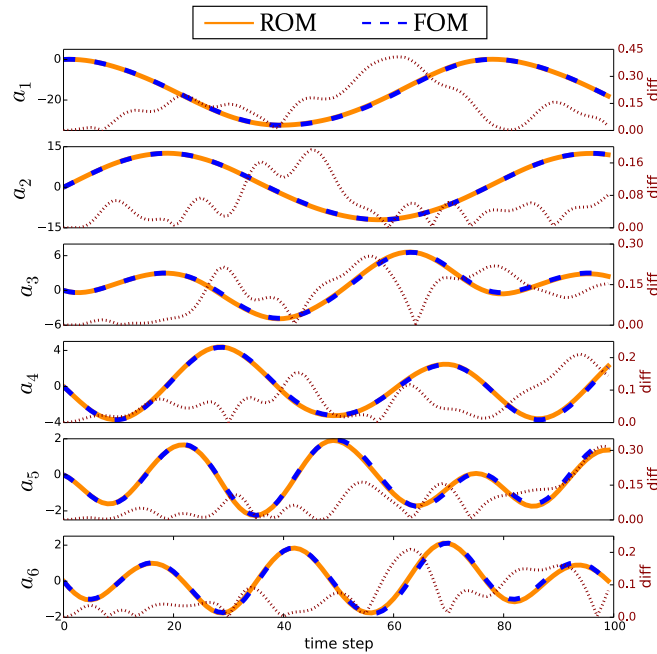


Figure 4.6 On the left axis: time history of the first 6 POD modes amplitudes for the case at $(A_e, f_r) = (0.2, 0.8)$; results obtained for the nonlinear ALE-based ROM with the use of the BQDEIM approach by using 14 nonlinear POD modes (and $14 \times 4 = 56$ fitting points). On the right axis: the respective absolute error $|a_{FOM} - a_{ROM}|$ (red dotted plot).

Chapter 4. Adaptation of a nonlinear ALE-based reduced order model of the Navier-Stokes equations for aeroelasticity

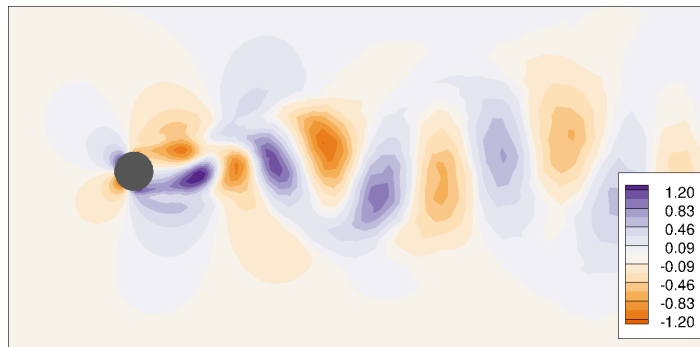


Figure 4.7 Relative error (in percentage) of the density field for the last time step of the ROM simulation: results obtained for the nonlinear ALE-based ROM with the use of the BQDEIM approach by using 14 nonlinear POD modes (and $14 \times 4 = 56$ fitting points).

4.3. Numerical integration of the nonlinear ALE-based ROM of a flow around a cylinder in forced motion at low Reynolds

Test case: flow around an oscillating cylinder in forced motion at $Re = 185$, $M = 0.2$ and $(A_e, f_r) = (0.5, 1.2)$

For the second test-case, the cylinder is oscillating at higher amplitude and frequency $(A_e, f_r) = (0.5, 1.2)$. With a uniform flow as initial condition a FOM unsteady simulation is performed with the same numerical schemes and parameters as the previous test case. In such conditions, a similar vortex shedding phenomenon is observed but a more complex dynamics of the flow is detected as seen in the energy distribution of the solution POD modes plotted in Fig.4.3. Indeed, in order to involve an equal percentage of energy with respect to the previous test case at least 40 POD modes are required. Also, the usual in pairs clustering of the singular values lacks from the 11-th singular values forward. Such a test case is chosen in order to test the nonlinear ROM with a more challenging test case. The instantaneous density field is depicted in Fig.4.8, showing the presence of more complex flow structures interacting in the vicinity of the cylinder.

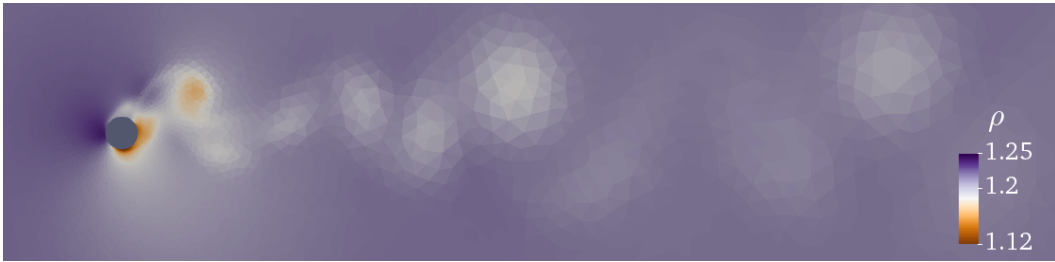


Figure 4.8 Instantaneous density field of a flow around a vertically oscillating cylinder at $Re = 185$, $A_e = 0.5$ and $f_r = 1.2$.

In Fig.4.9 we can see the time history of the first six amplitudes of the ROM integrated without the use of any masked projection revealing very good accuracy with respect to its FOM counterpart. Then the masked projection is introduced by using 40 nonlinear POD modes. As explained in Section 2.5 and confirmed by the results in Section 3.5 in the case of fixed mesh, the BQDEIM approach reported in Algorithm 4 with $k = 4$ blocks led to the most accurate results among the different masked projection approaches analyzed. For the present case with deforming mesh, the BQDEIM is firstly set with only $k = 4$ blocks, in accordance with the results of the assessment study of Section 3.5 for the case of fixed meshes. For this more challenging test case, the BQDEIM approach with $k = 4$ the nonlinear ROM is not able to converge. Further investigations revealed that the number of interpolation points ($40 \times 4 = 160$) is insufficient. As a consequence, the number of interpolation points is increased by rising the number of blocks until $k = 20$ so that $40 \times 20 = 800$ fitting points are obtained. More specifically, when using $k = 4$ the QDEIM algorithm is applied for each block conservative variable separately; then, by using $k = 20$ the QDEIM algorithm is applied for each conservative block variable itself decomposed in other 5 additional blocks, see Fig.4.10.

Chapter 4. Adaptation of a nonlinear ALE-based reduced order model of the Navier-Stokes equations for aeroelasticity

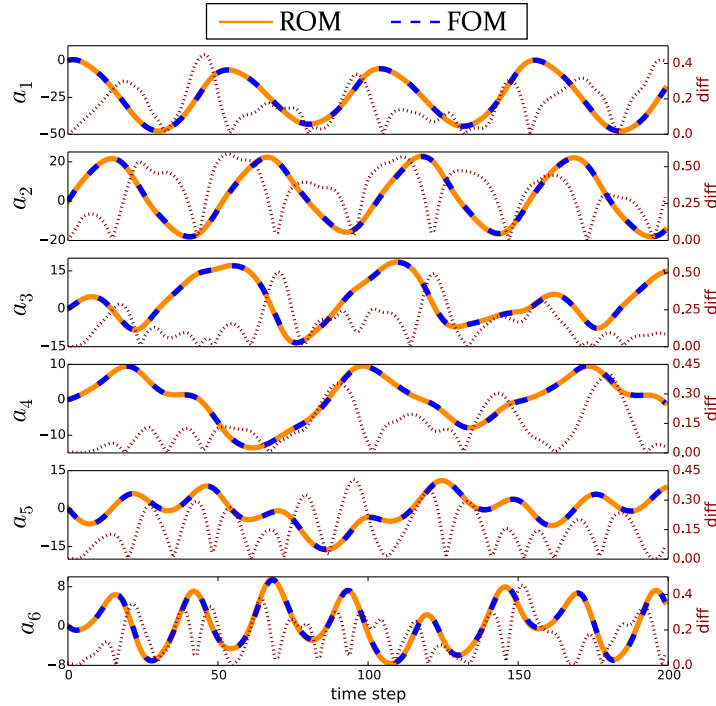


Figure 4.9 On the left axis: time history of the first 6 POD modes amplitudes for the case at $(A_e, f_r) = (0.5, 1.2)$; results obtained for the nonlinear ALE-based ROM without any masked projection. On the right axis: the respective absolute error $|a_{FOM} - a_{ROM}|$ (red dotted plot).

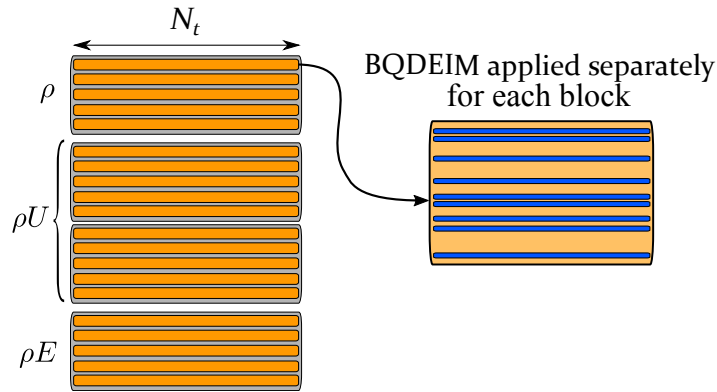


Figure 4.10 Illustrative scheme of the application of the selection algorithm for each conservative block variable itself decomposed in other 5 additional blocks.

The locations of the interpolation points are highlighted in the reference mesh in Fig.4.11. In such conditions, the nonlinear ROM is integrated successfully and the comparison of the first six amplitudes with respect to their FOM counterpart is plotted in Fig.4.12.

4.3. Numerical integration of the nonlinear ALE-based ROM of a flow around a cylinder in forced motion at low Reynolds

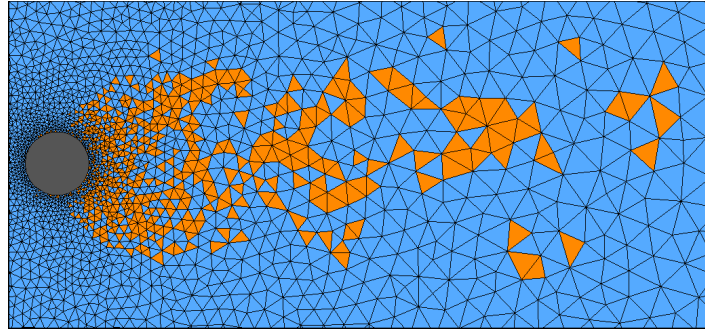


Figure 4.11 Spatial location of the 800 cells selected using the block-adapted masked projection using 20 blocks and 40 nonlinear POD modes .

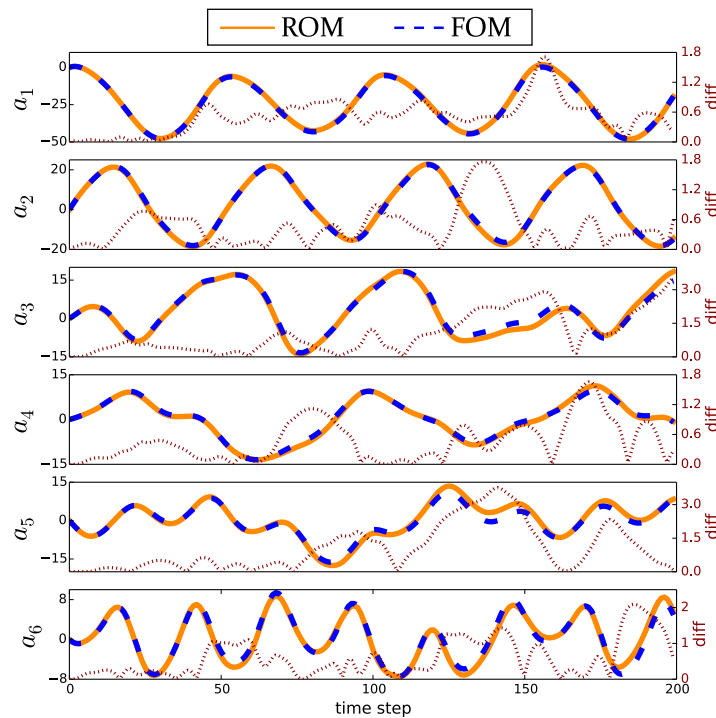


Figure 4.12 On the left axis: time history of the first 6 POD modes amplitudes for the case at $(A_e, f_r) = (0.5, 1.2)$; results obtained for the nonlinear ALE-based ROM with the use of the BQDEIM approach by using 40 nonlinear POD modes (and $40 \times 20 = 800$ fitting points). On the right axis: the respective absolute error $|a_{FOM} - a_{ROM}|$ (red dotted plot).

Even in this case, although the error with respect to the ROM without masked projection is slightly augmented, the overall accuracy still remains suitable. To demonstrate this, the difference between the density fields obtained by the ROM and the FOM at the last time step of the simulation is shown in Fig.4.13. The local relative error $\frac{\rho_{FOM} - \rho_{ROM}}{\rho_{FOM}} \times 100$ never exceeds the 3%, a value that is widely acceptable.

Chapter 4. Adaptation of a nonlinear ALE-based reduced order model of the Navier-Stokes equations for aeroelasticity

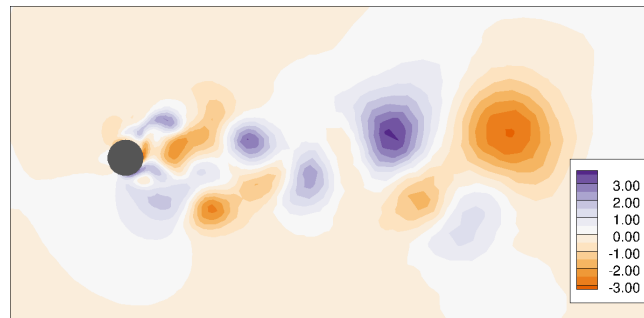


Figure 4.13 Relative error (in percentage) for the density field for the last time step of the ROM simulation for the case at $(A_e, f_r) = (0.5, 1.2)$: results obtained for the nonlinear ALE-based ROM with the use of the BQDEIM approach by using 40 nonlinear POD modes (and $40 \times 20 = 800$ fitting points).

4.3. Numerical integration of the nonlinear ALE-based ROM of a flow around a cylinder in forced motion at low Reynolds

4.3.1 Adaptation of the ALE-based nonlinear ROM for a new parameter configuration

The previous examples have been developed and shown to produce numerical results that compare well with those generated by their high-fidelity nonlinear counterparts. In this section, the adaptation of pre-computed ROMs to changes in the physical or modeling parameters is studied. ROMs have seen a growing interest in the aeroelastic community because their lower dimensionality implies reduced computational cost. Such an interest would inevitably decline if a new ROM is required for every new parameter value. Indeed, reconstructing a ROM involves generating solutions of the high-fidelity model, and solving matrix equations that, being computationally intensive, undermine the purpose which ROMs are designed for. This issue underlines the need for new strategies to adapt pre-computed ROMs to new sets of parameters.

Ideally, given a set of parameters $\boldsymbol{\mu} \in \mathbb{R}^{N_p}$ with N_p equal to the number of the parameters of the nonlinear system, the FOM of eq.(4.8) becomes:

$$\frac{d\mathbf{w}(t; \boldsymbol{\mu})}{dt} = \mathbf{f}(\mathbf{w}(t), t; \boldsymbol{\mu}). \quad (4.12)$$

For different sets of parameters, called *operating points*, Algorithm 7 (p.75) can be used in order to construct the nonlinear ROM. The aim of this section is to use only some pre-computed ROMs with respect to a limited number N_{ref} of operating points $\boldsymbol{\mu}_i$

$$\Lambda = \{\boldsymbol{\mu}_1, \boldsymbol{\mu}_2, \dots, \boldsymbol{\mu}_{N_{ref}}\}, \quad (4.13)$$

that will constitute the database to use for the adaptation of the ROM for a new parameter $\boldsymbol{\mu}^* \notin \Lambda$. Interpolation is a natural and attractive idea for adapting ROMs to a new operating point. Unfortunately, it is not a straightforward task.

Typical changing parameters for aerodynamic applications are the Reynolds number, the Mach number, angle of attack etc. [37], [49], [59], [76], [85]. Here the focus is placed on parameters that could be involved in the description of the structural motion in the ROM for aeroelasticity, namely the amplitude A_e and the frequency f_r .

Practical implementation of an off-reference ALE-based nonlinear ROM

In order to avoid the reconstruction of a new ROM for every new operating point the whole *offline* phase of Algorithm 7 (presented at p.75) must be overcome and reimplemented; instead the *online* phase of Algorithm 7 remains unchanged. In this section, a demonstrative example of two scalar operating points $\Lambda = \{\mu_1, \mu_2\}$ (for two different fairly close values of A_e or f_r) and a new parameter $\mu_1 < \mu_* < \mu_2$ is considered². A summary of the different matrices or vectors with their respec-

² The present example can be easily extended to a largest set of operating points.

Chapter 4. Adaptation of a nonlinear ALE-based reduced order model of the Navier-Stokes equations for aeroelasticity

tive sizes obtained during the *offline* phase and required during the *online* phase is provided in Table 4.1.

Vector/Matrix	\mathbf{w}_0	$f(\mathbf{w}_0)$	Φ	U	\mathbf{P}
Size	n	n	$n \times m$	$n \times p$	$n \times kp$

Table 4.1 Summary table of the matrices and vectors with their respective size computed during the offline phase of the nonlinear ROM for the Navier-Stokes equations.

These vectors/matrices given for μ_1 and μ_2 , the different tasks for the computation of such vectors/matrices for the new operating point μ_\star are:

\mathbf{w}_0 : the initial condition (or average flow) for a new operating point is usually obtained through interpolation (for example Lagrangian [59]). In the example of interest of a bidimensional cylinder in forced vertical oscillation (for different values of A_e or f_r), the flow may present similar structures evolving at different frequencies and/or amplitudes. For this reason, the initial conditions for the operating points must be selected so that they present similar flow structures at similar spatial locations in order to be able to perform a proper interpolation between the two fields. For this purpose, the set of snapshots $\mathbf{W} \in \mathbb{R}^{n \times N_t}$ and so the initial condition \mathbf{w}_0 are extracted on a time window with similar fixed characteristics. Given an established periodic dynamics of the flow and the imposed oscillatory movement $y(t) = A \sin(2\pi ft)$, the left boundary of the time window is selected in order to coincide with an instantaneous vertical position equal to the average vertical position ($y = 0$ in this case), in the *descending* part of the motion ($\dot{y} < 0$) (see Fig.4.14). Starting from the snapshot related to such a position, the time window is completed using at least the following 1000 snapshots and always in order to complete a period of oscillation. As an example, the initial condition $\mathbf{w}_0(\mu_1 = (A_e = 0.2, f_r = 0.8))$ and $\mathbf{w}_0(\mu_2 = (A_e = 0.4, f_r = 0.8))$ with the true and the interpolated initial condition $\mathbf{w}_0(\mu_\star = (A_e = 0.3, f_r = 0.8))$ are shown in Fig.4.15. The aforementioned precaution on the snapshots selection window provides interpolated initial conditions that present a similar topology of the flow structures together with a low difference with respect to the real initial condition field. In such a way, a proper interpolation of the initial condition can be computed.

$f(\mathbf{w}_0, t_0)$: in this work, the nonlinear term represents the right-hand side of the Navier-Stokes eq.(4.8) divided by the respective cell volumes. As a consequence, in order to compute the term $f(\mathbf{w}_0, t_0)$ it is sufficient to use the high-fidelity model, with the updated parameters for μ_\star , in order to compute the fluxes balance and divide it by the cell volumes.

Φ : in the context of POD method, it is not recommended to perform a linear interpolation between Φ_{μ_1} and Φ_{μ_2} for the computation of a new operating point

4.3. Numerical integration of the nonlinear ALE-based ROM of a flow around a cylinder in forced motion at low Reynolds

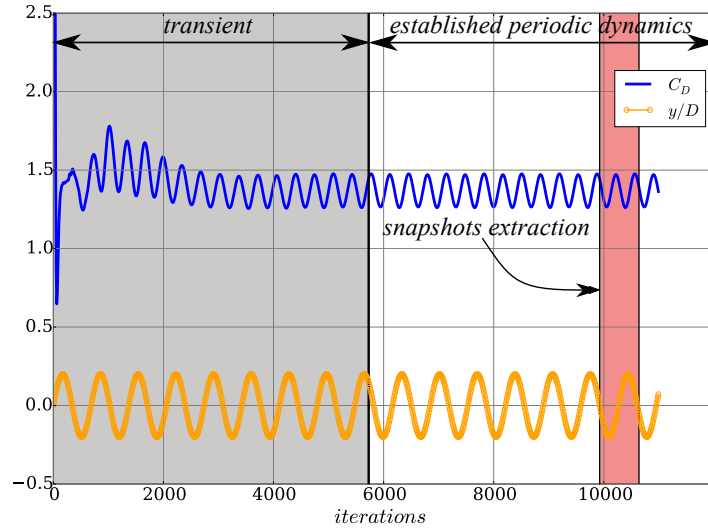


Figure 4.14 Selection of the time window for the extraction of the set of snapshots that would be the basis for nonlinear ROM. Such a procedure is necessary in order to perform a proper interpolation for the off-reference initial condition $\mathbf{w}_0(\mu_\star)$.

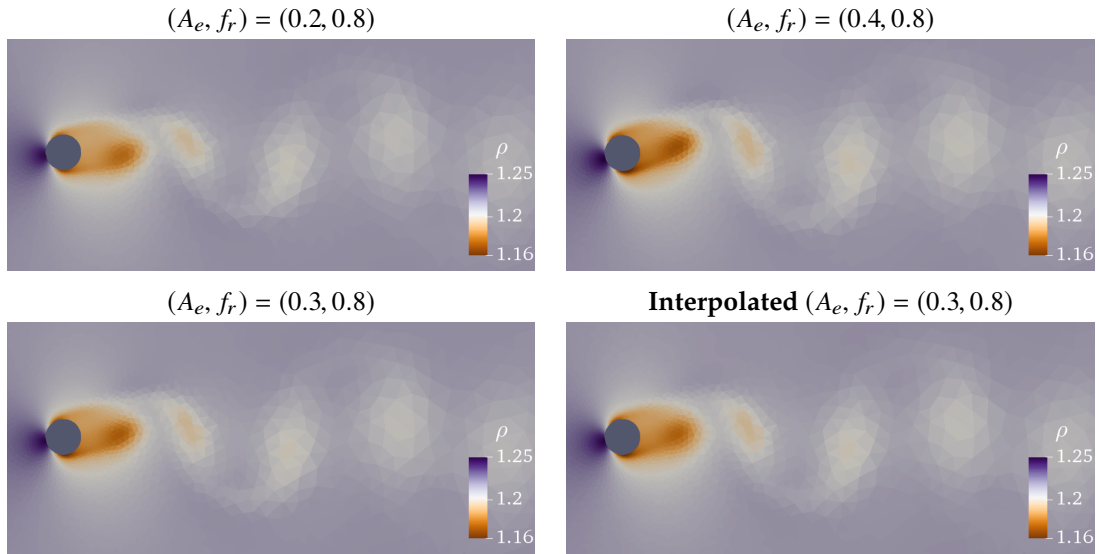


Figure 4.15 Initial conditions \mathbf{w}_0 at different values of A_e and the related interpolated field.

POD basis Φ_{μ_\star} . Indeed this simple approach is doomed to failure for two key reasons. A linear interpolation of POD bases, which are orthogonal, is not guaranteed to construct a new set of orthogonal vectors. More generally, the standard interpolation of a set of bases does not necessarily produce a basis [86]. In literature, in the context of POD method, a global POD (GPOD) method has been applied in the unsteady aerodynamic domain [129]. The aim of the GPOD approach is to enrich the snapshot matrix with solutions corresponding to different values of the varied parameters. In other words, the snapshots related to different operating points parameters are included in a

Chapter 4. Adaptation of a nonlinear ALE-based reduced order model of the Navier-Stokes equations for aeroelasticity

matrix:

$$\mathbf{W}_{\mu_\star} = [\mathbf{w}(t_1, \mu_1), \dots, \mathbf{w}(t_{N_r}, \mu_1), \mathbf{w}(t_1, \mu_2), \dots, \mathbf{w}(t_{N_r}, \mu_2)], \quad (4.14)$$

and a global POD basis is obtained by application of Algorithm 1 (p.18). The computation of such a GPOD basis could be computationally very expensive when a large number of parameters is considered. For this work, a slight adjustment to the GPOD is made. The different POD bases related to the different operating points (obtained by Algorithm 1 at p.18) are included in a global matrix:

$$\mathbf{W}_{\mu_\star} = [\Phi_{\mu_1}, \Phi_{\mu_2}], \quad (4.15)$$

Although the different flow structures related to the different flow parameters μ_1 and μ_2 are included in the matrix \mathbf{W}_{μ_\star} , it has not retained the orthogonality property of a POD basis. Then, in order to avoid any redundancy in the global basis and to restore the orthogonality property, a SVD of the matrix \mathbf{W}_{μ_\star} is performed. Such a procedure is described in Algorithm 8.

Algorithm 8 Global POD basis computation.

Input: A set of POD bases for different operating points in Λ : $\{\Phi_{\mu_1}, \Phi_{\mu_2}, \dots, \Phi_{\mu_{N_{ref}}}\}$

Output: POD basis for any new operating point $\Phi_{\mu_\star} \in \mathbb{R}^{n \times m}$

- 1: Inclusion in a single matrix of the different POD bases: $\mathbf{W}_{\mu_\star} = [\Phi_{\mu_1}, \Phi_{\mu_2}, \dots, \Phi_{\mu_{N_{ref}}}]$
 - 2: Compute the thin SVD: $\mathbf{W}_{\mu_\star} = \Phi_{\mu_\star} \Sigma \mathbf{V}^T$
 - 3: Choose a cutoff condition (if any) for $\Phi_{\mu_\star} \in \mathbb{R}^{n \times r}$
 - 4: Truncate the basis $\Phi_{\mu_\star} \in \mathbb{R}^{n \times m}$ with $m \leq r$
-

U: as discussed in Section 2.5, for the computation of \mathbf{U} a POD of the nonlinear term snapshots is performed by applying Algorithm 1 (p.18) to the matrix collection \mathbf{F} . As a consequence, equivalently to the previous point, Algorithm 8 can be applied to a set of nonlinear term basis collection as $\{\mathbf{U}_{\mu_1}, \mathbf{U}_{\mu_2}, \dots, \mathbf{U}_{\mu_{N_{ref}}}\}$ in order to obtain a new nonlinear term POD basis \mathbf{U}_{μ_\star} that could be used for any new operating point.

P: in order to obtain the new masked matrix \mathbf{P} , Algorithm 4 (p.25) with input basis \mathbf{U}_{μ_\star} is computed.

Finally, the construction and adaptation of the nonlinear operator $f_{\mathbf{P}}(\tilde{\mathbf{P}}^T \tilde{\mathbf{w}}, t)$ must be addressed. Obviously, as the mask matrix \mathbf{P} changes, the set of fitting points changes as a result. This implies that the adapted ROM requires a new selection operator $\tilde{\mathbf{P}} \in \mathbb{R}^{n \times s}$ which includes the points selected by \mathbf{P} plus the neighbor points to complete the stencil. Such a selection operator is assumed to be valid for all the new operating points included in the set of parameters the ROM is built for. On

4.3. Numerical integration of the nonlinear ALE-based ROM of a flow around a cylinder in forced motion at low Reynolds

the contrary, the nonlinear operator $f_P(\tilde{\mathbf{P}}^T \tilde{\mathbf{w}}, t)$ must be updated for each new investigated operating parameter according to the mesh motion/deformation since the computation of the fluxes balances has to be performed on the updated cell metrics.

A summary of the offline procedures leading to the adaptation of the nonlinear ALE-based ROM for off-reference conditions is presented in Algorithm 9.

Algorithm 9 Offline phase for the nonlinear ALE-based model-order reduction of the Navier-Stokes equations.

Input: Sets of POD bases for different operating points: for the solution field $\Omega = [\Phi_{\mu_1}, \Phi_{\mu_2}, \dots, \Phi_{\mu_{N_{ref}}}]$ and for the nonlinear term $\Omega_{NL} = [U_{\mu_1}, U_{\mu_2}, \dots, U_{\mu_{N_{ref}}}]$.

- 1: Construct $\Phi_{\mu_\star} \in \mathbb{R}^{n \times m}$ using Global POD approach via Algorithm 8 with input Ω
 - 2: Construct $U_{\mu_\star} \in \mathbb{R}^{n \times p}$ using Global POD approach via Algorithm 8 with input Ω_{NL}
 - 3: Construct masked projection matrix \mathbf{P} via Algorithm 2,3 or 4 with input U_{μ_\star}
 - 4: **if** Algorithm 2 or 3 is chosen **then**
 - 5: $\mathbf{P} \in \mathbb{R}^{n \times p}$
 - 6: Compute the matrix operations of eq.(3.34) once and for all: $\Phi_{\mu_\star}^T U_{\mu_\star} (\mathbf{P}^T U_{\mu_\star})^{-1}$, $\Phi_{\mu_\star}^T f(\mathbf{w}_0, t_0)$ and $\mathbf{P}^T f(\mathbf{w}_0, t_0)$
 - 7: **else if** Algorithm 4 is chosen **then**
 - 8: $\mathbf{P} \in \mathbb{R}^{n \times kp}$
 - 9: Compute the matrix operations of eq.(3.34) once and for all: $\Phi_{\mu_\star}^T U_{\mu_\star} (U_{\mu_\star}^T \mathbf{P} \mathbf{P}^T U_{\mu_\star})^{-1} U_{\mu_\star}^T \mathbf{P}$, $\Phi_{\mu_\star}^T f(\mathbf{w}_0)$ and $\mathbf{P}^T f(\mathbf{w}_0)$
 - 10: **end if**
-

4.3.2 Numerical integration of the adapted nonlinear ALE-based ROM for new motion parameters

In this section, the numerical performance of the proposed strategy for the adaptation of ROMs for new parameters configurations is investigated. The numerical results cannot be presented as in the previous section because the high-fidelity amplitudes related to the global basis are not available. Consequently, in order to evaluate the performance of the adapted ROM, firstly the aerodynamic field resulted from the adapted ROM is reconstructed and collected in a matrix \mathbf{W}_{ROM} for different time-steps. Then, it is projected onto $\Phi_{\mu_\star}^{(e)}$, the POD basis obtained by applying Algorithm 1 (p.18) to the related high-fidelity snapshots collection $[\mathbf{w}(t_1, \mu_\star), \dots, \mathbf{w}(t_{N_t}, \mu_\star)]$:

$$\mathbf{a}^* = \Phi_{\mu_\star}^{(e)T} \underbrace{\left(\mathbf{w}_0^{(A)} + \Phi_{\mu_\star} \mathbf{a}^{(A)} \right)}_{\mathbf{W}_{ROM}}. \quad (4.16)$$

Chapter 4. Adaptation of a nonlinear ALE-based reduced order model of the Navier-Stokes equations for aeroelasticity

Finally, the amplitudes vector \mathbf{a}^* can be compared to its high-fidelity counterpart $\Sigma \mathbf{V}^T$ (see eq.(3.25)).

Two numerical demonstrative examples of the adapted nonlinear ALE-based ROM are shown. In particular, the adaptation is tested with respect to the variation of both motion parameters A_e and f_r . The high-fidelity numerical simulations are performed by means of the same solver and numerical parameters as those of Section 4.3. For the first test case the frequency of the vertical harmonic motion is changed by varying the parameter $f_r = f/f_{st}$. Thus, two operating points are considered $[(A_e, f_r) = (0.2, 0.8), (A_e, f_r) = (0.2, 0.9)]$ and the ROM is adapted for an intermediate frequency $(A_e, f_r) = (0.2, 0.85)$. For the second test case the amplitude of the vertical harmonic motion is changed by varying the parameter $A_e = A/D$. Thus, two operating points are considered $[(A_e, f_r) = (0.2, 0.8), (A_e, f_r) = (0.4, 0.8)]$ and the ROM is adapted for an intermediate amplitude $(A_e, f_r) = (0.3, 0.8)$.

4.3.2.1 Test case 1: oscillation frequency variation

For the first test case, ROM is adapted for $(A_e, f_r) = (0.2, 0.85)$ between the operating points $(A_e, f_r) = (0.2, 0.8)$ and $(A_e, f_r) = (0.2, 0.9)$. Given the two POD bases for the operating points, each with 12 POD modes, a global basis must be computed. To do so, the Algorithm 8 (p.88) is applied and the singular values distribution is depicted in Fig.4.16. A sort of drop is found after the first 12 modes. However, the relative contribution for the remaining 12 modes is still relevant since the gap of the relative contribution after the drop is less than one order of magnitude. As a consequence for the construction of the global basis all the 24 POD modes are retained. Fig.4.17

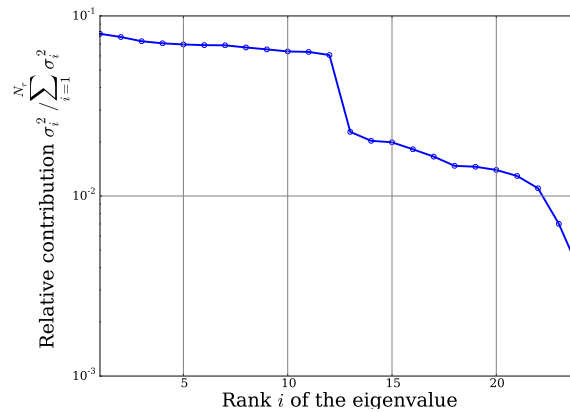


Figure 4.16 Singular values distribution for the global POD approach reported in Algorithm 8 between the operating points $(A_e, f_r) = (0.2, 0.8)$ and $(A_e, f_r) = (0.2, 0.9)$.

depicts the time history of the first six amplitudes \mathbf{a}^* of the ROM integrated without the use of any masked projection with respect to its FOM counterpart.

The accuracy achieved in this first result is very encouraging even if the overall ROM efficiency is not increased to the maximum of the potentialities. Indeed, without the use of any masked projection, the computational time benefit of the ROM

4.3. Numerical integration of the nonlinear ALE-based ROM of a flow around a cylinder in forced motion at low Reynolds

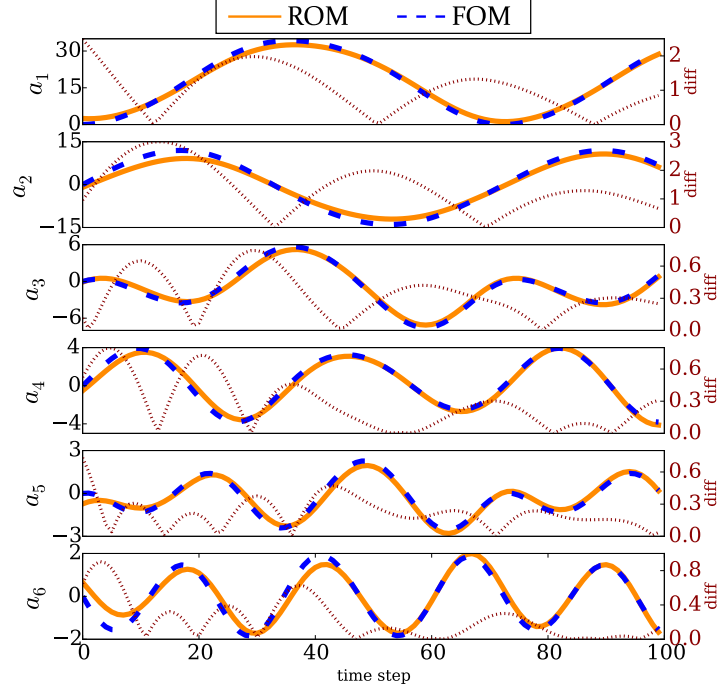


Figure 4.17 On the left axis: time history of the first 6 POD modes amplitudes of eq.(4.16) for the interpolated case at $(A_e, f_r) = (0.2, 0.85)$; results obtained for the nonlinear ALE-based ROM without the use of any masked projection approach. On the right axis: the respective absolute error $|a_{FOM} - a_{ROM}^*|$ (red dotted plot).

lies only in the time integration that is performed using an explicit scheme with a higher time-step with respect to the high-fidelity implicit counterpart. Furthermore, the matrices involved in the system resolution have lower dimension.

Finally, the masked projection approach is considered in order to maximize the computational efficiency of the ROM while introducing a further approximation. A BQDEIM formulation and the global approach of Algorithm 8 (p.88) are used so that, given that $U_{\mu_*} \in \mathbb{R}^{n \times 24}$, $24 \times 4 = 96$ fitting points are used. Fig.4.18 depicts the time history of the first six amplitudes a^* of the ROM integrated with the use of the BQDEIM with respect to its FOM counterpart. It is evident that the introduction of the masked projection approach deteriorates the accuracy of the results. However, the difference between the density fields obtained by the adapted ROM and the FOM at the last time step of the simulation, reported in Fig.4.19, never exceeds the 1% that is still widely acceptable.

To conclude, the absolute error seems to gradually decrease during the numerical integration in Fig.4.17. In other words, it seems that the initial amplitude discrepancy (attributable to the initial condition interpolation error) is gradually mitigated during the ROM simulation. In order to investigate such a feature of the ROM, a long-term numerical simulation of the ROM with and without masked projection is performed. In this regard, the time history of the difference between the first

Chapter 4. Adaptation of a nonlinear ALE-based reduced order model of the Navier-Stokes equations for aeroelasticity

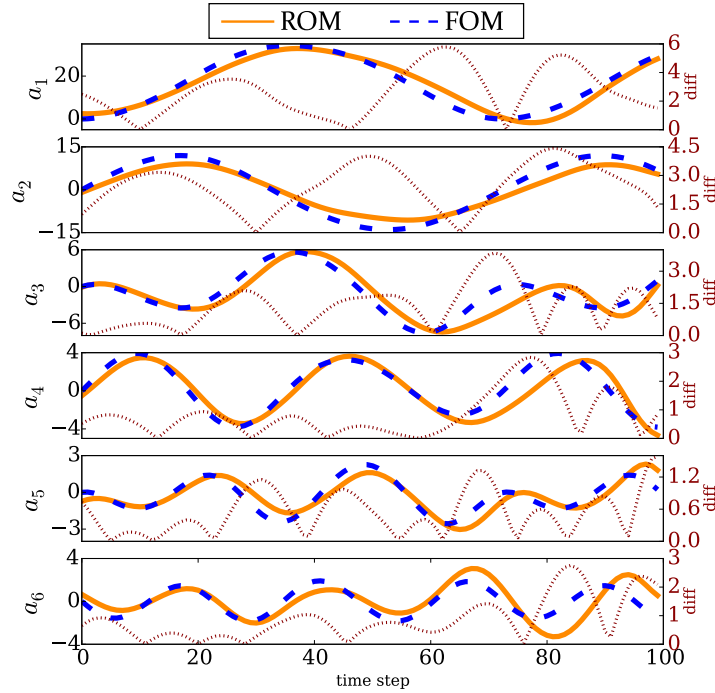


Figure 4.18 On the left axis: time history of the first 6 POD modes amplitudes of eq.(4.16) for the interpolated case at $(A_e, f_r) = (0.2, 0.85)$; results obtained for the nonlinear ALE-based ROM with the use of the BQDEIM approach by using 24 nonlinear POD modes (and $24 \times 4 = 96$ fitting points). On the right axis: the respective absolute error $|a_{FOM} - a_{ROM}^*|$ (red dotted plot).

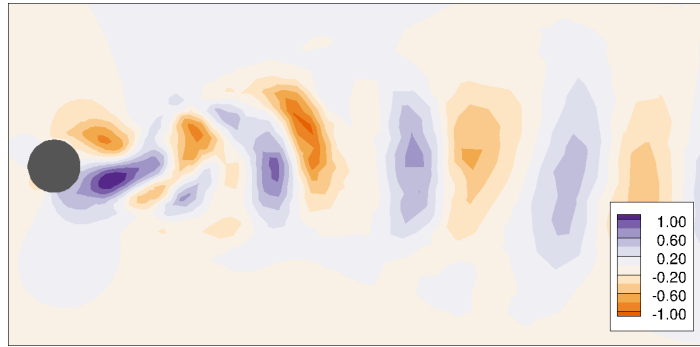


Figure 4.19 Relative error (in percentage) for the density field for the last time step of the ROM simulation for the interpolated case at $(A_e, f_r) = (0.2, 0.85)$; results obtained with the use of the BQDEIM approach by using 24 nonlinear POD modes (and $24 \times 4 = 96$ fitting points).

ROM amplitude a_1^* (see eq.(4.16)) and its FOM counterpart for both cases is shown in Fig.4.20. For the case without any masked projection, although the initial trend of the error is decreasing, the long-term behaviour is stabilized at a given oscillating error. On the contrary, the approximation introduced with the masked projection approach leads to divergence after a cycle of oscillation. Obviously this feature would be emphasized when few interpolation points are used in the masked projection approximations. Such a trend, that is not unusual for (Galerkin-) projection based

4.3. Numerical integration of the nonlinear ALE-based ROM of a flow around a cylinder in forced motion at low Reynolds

ROMs (see Section 2.4), has motivated the work that will be presented in Chapter 6 to provide a priori stable ROMs for periodic flows. However, such an issue does not divert the attention from this kind of model reduction techniques that are still of great interest in the ROM community [24], [27], [49], [79], [130]. Indeed, for the presented test case, one cycle of oscillation is sufficient to reproduce correctly the established periodic regime contained in the extraction window of interest. In this context, the adaptation of the ROM for off-reference conditions might be of primary interest, rather than the respective long term behaviour.

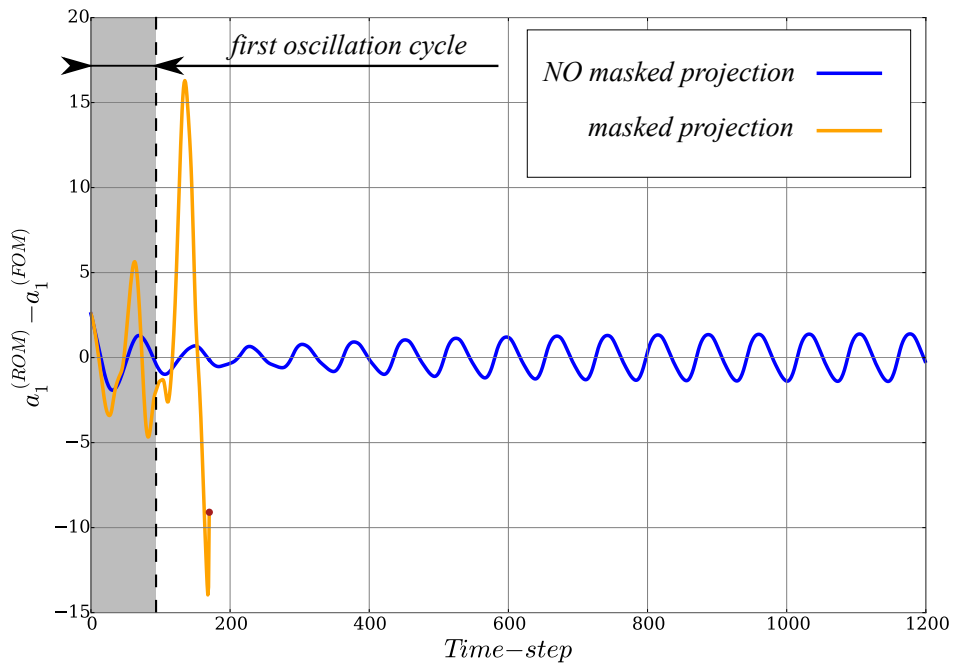


Figure 4.20 Difference between the ROM first amplitude a_1^* (see eq.(4.16)), obtained from a long-term ROM simulation without any masked projection, and its FOM counterpart.

4.3.2.2 Test case 2: amplitude variation

For the second test case, the ROM is adapted for $(A_e, f_r) = (0.3, 0.8)$ between the operating points $(A_e, f_r) = (0.2, 0.8)$ and $(A_e, f_r) = (0.4, 0.8)$. The two POD bases given for the operating points, each with 12 POD modes, a global basis must be computed. To do so, the Algorithm 8 (p.88) is applied and the singular values distribution is depicted in Fig.4.21. A sort of drop is found after the first 12 modes. However, the relative contribution for the remaining 12 modes is still relevant on the economy of the overall spectrum (the difference is of just one order of magnitude). As a consequence for the construction of the global basis all the 24 POD modes are retained.

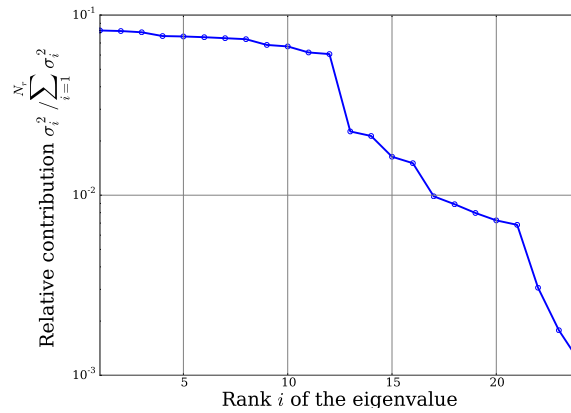


Figure 4.21 Singular values distribution for the global POD approach reported in Algorithm 8 between the operating points $(A_e, f_r) = (0.2, 0.8)$ and $(A_e, f_r) = (0.4, 0.8)$.

Fig.4.22 depicts the time history of the first six amplitudes \mathbf{a}^* of the ROM integrated without the use of any masked projection with respect to its FOM counterpart. An overall better accuracy is detected with respect to the previous example. In particular, the interpolated initial condition is closer to the reference one. This implies that the variation from $A_e = 0.2$ to $A_e = 0.4$ slightly affects the topology of the flow so that its related interpolation presents a lower discrepancy with respect to the reference. As a consequence, a more suitable initial condition has led to better results.

Finally, the masked projection approach is considered in order to maximize the computational efficiency of the ROM while introducing a further approximation. However, the classic BQDEIM approach with $k = 4$ diverges. Further investigations revealed that the number of interpolation points ($24 \times 4 = 96$) is insufficient. As shown in Section 4.3, the number of blocks can be increased in order to obtain a larger number of fitting points. The number of blocks k is thus increased to $k = 20$ so that $24 \times 20 = 480$ fitting points are obtained. In such conditions, the nonlinear adapted ROM is integrated successfully and the comparison of the first six amplitudes \mathbf{a}^* with respect to their FOM counterpart is plotted in Fig.4.23. It is evident that the introduction of the masked projection approach deteriorates the

4.3. Numerical integration of the nonlinear ALE-based ROM of a flow around a cylinder in forced motion at low Reynolds

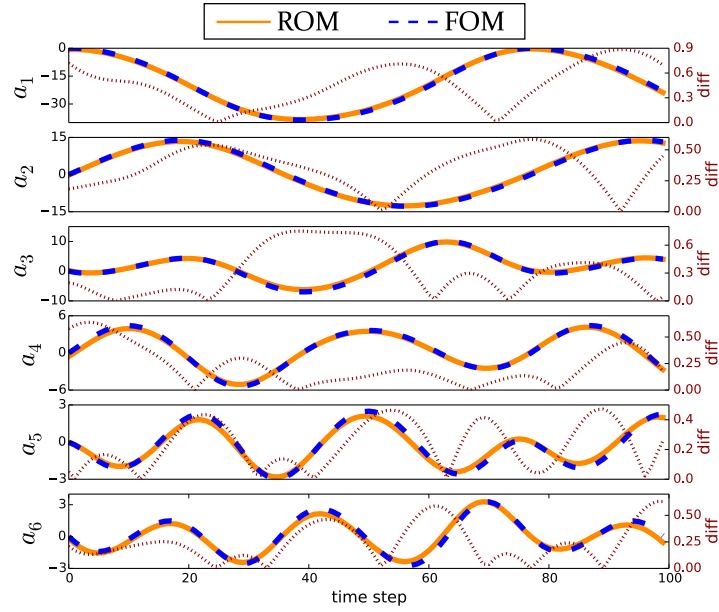


Figure 4.22 On the left axis: time history of the first 6 POD modes amplitudes of eq.(4.16) for the interpolated case at $(A_e, f_r) = (0.3, 0.8)$; results obtained for the nonlinear ALE-based ROM without the use of any masked projection approach. On the right axis: the respective absolute error $|a_{FOM} - a_{ROM}^*|$ (red dotted plot).

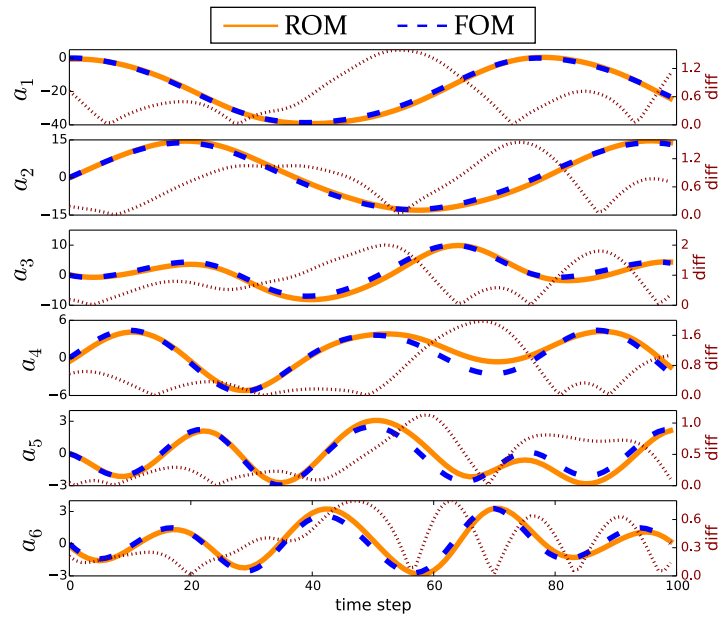


Figure 4.23 On the left axis: time history of the first 6 POD modes amplitudes of eq.(4.16) for the interpolated case at $(A_e, f_r) = (0.3, 0.8)$; results obtained for the nonlinear ALE-based ROM with the use of the BQDEIM approach by using 24 nonlinear POD modes (and $24 \times 20 = 480$ fitting points). On the right axis: the respective absolute error $|a_{FOM} - a_{ROM}^*|$ (red dotted plot).

accuracy of the results. However, the difference between the density fields obtained by the adapted ROM and the FOM at the last time step of the simulation, reported

in Fig.4.24, never exceeds the 1.5% that is still widely acceptable.

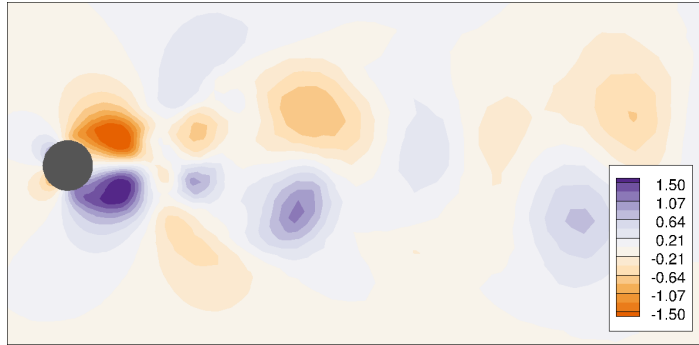


Figure 4.24 Relative error (in percentage) for the density field for the last time step of the ROM simulation for the interpolated case at $(A_e, f_r) = (0.3, 0.8)$; results obtained with the use of the BQDEIM approach by using 24 nonlinear POD modes (and $24 \times 20 = 480$ fitting points).

4.3.3 Discussion

In previous sections, a strategy for the construction of a parametric projection-based nonlinear ALE-based ROM with masked projection has been presented. In this initial stage, test cases with only two operating points and one new intermediate parameter have been investigated and successfully validated. Such test cases also revealed a limitation linked to the presented strategy: switching from *Test case 1* to *Test case 2*, with a fixed number of nonlinear term modes, a different number of interpolation cells was required. In particular, 480 cells were necessary for *Test case 2* as against the 96 cells of the *Test case 1*. Unfortunately, such a parameter of the parametric ROM cannot be established a priori. To overcome this issue, *predictor-corrector* strategies may be introduced which, as illustrated in Fig.4.25, seeks to evaluate the ROM for an increasing number of interpolation points until convergence is attained. Alternatively, other a priori strategies may be proposed which aims to select a particular zone of the mesh that potentially will include the cells that would be involved by the selection algorithm [95], [124]. For example, once the interpolation points for the different operating points are identified, a *sub-mesh* including all the selected cells can be used to identify the interpolation points for the integration of the ROM for a new parameter.

The presented *global ROM strategy* to address parametric problems, might yield inefficient ROM approximations because of the unaffordable large sets of global basis functions to approximate both the solution and the nonlinear terms. This happens when the solutions manifold (that is, the set of all solutions of the FOM for varying parameters) is characterized by large parameter variations, different physical regimes, or moving features such as shocks. In such a situation, the solution can be better approximated in a lower-dimensional subspace generated by local basis vectors, rather than in a unique subspace spanned by global basis vectors.

4.4. Numerical integration of an aeroelastic reduced order system: flow around a cylinder in free motion

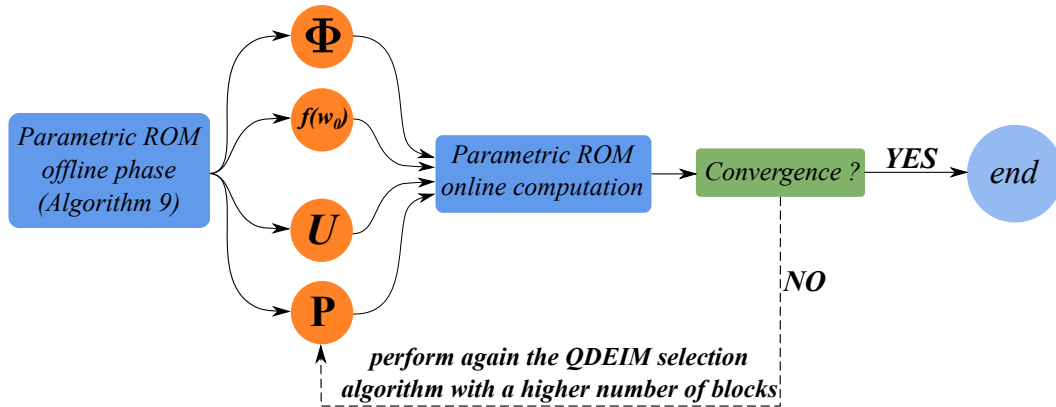


Figure 4.25 Illustrative scheme of the predictor-corrector procedure for the determination of the number of interpolation points for the parametric nonlinear ROM.

To enhance computational efficiency in this context, several strategies have been proposed in literature, relying on local reduced basis spaces possibly coupled with adaptive or interpolation procedures for their construction. This results in a clustering procedure of the solution manifold parameters accordingly to a given criterion; then, *locally global* POD bases can be used to construct nonlinear ROM that are switched while ranging in the whole set of parameters.

In this work, we do not elaborate this topic, as the focus is placed on showing that the presented ROM can actually work in such a parametric context.

4.4 Numerical integration of an aeroelastic reduced order system: flow around a cylinder in free motion

The objective of this section is to couple a nonlinear ROM for compressible aerodynamics with a structural model in order to perform a reduced order fluid-structure interaction computation. The fluid dynamics part of the system is represented by the ALE-based ROM presented in the previous sections, while the structural part is represented by a simple one degree of freedom rigid body dynamics, which simplifies the numerical implementation for such a demonstrative example. Starting from the configuration investigated in the previous section of a two-dimensional circular cylinder immersed in a uniform flow, here the cylinder is free to perform oscillation perpendicular to the direction of the far-field fluid flow. This problem has been addressed experimentally, for example by Anagnostopoulos *et al.* [131] and numerically, for example by Dettmer *et al.* [132]. It is observed that there is an interval of far field flow velocities for which the vortex shedding frequency coincides with the natural frequency of the cylinder-spring system (*lock-in* phenomenon). Within this interval of configurations, the cylinder performs stable oscillations.

In a standard manner, the degree of freedom of the cylinder is associated with

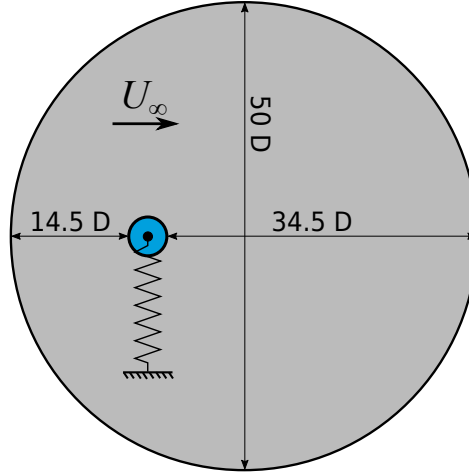


Figure 4.26 Computational domain for the two-dimensional cylinder configuration in transverse free-motion.

corresponding inertia, damping and stiffness. By assuming a linear and uncoupled behaviour of the rigid body supports, the conservation of momentum of a rigid body may be expressed as:

$$m\ddot{y}(t) + c\dot{y}(t) + ky(t) = L(t), \quad (4.17)$$

where y denotes the degree of freedom and the scalars m , c and k denote the mass, the damping and the stiffness of the spring system. The values of m and k are dimensioned according to the experiments conducted by Anagnostopoulos *et al.* [131]. The scalar L represents the component of the aerodynamic force along the direction perpendicular to the far-field fluid flow, obtained from the full order or reduced order flow field. The system configuration is represented in Fig.4.26. The system can be rearranged in matrix form as:

$$\mathbf{M}\dot{\mathbf{y}}(t) + \mathbf{K}\mathbf{y}(t) = \mathbf{L}(t), \quad (4.18)$$

where:

$$\mathbf{y} = \begin{pmatrix} y \\ \dot{y} \end{pmatrix}, \quad \mathbf{M} = \begin{bmatrix} 1 & \\ & m \end{bmatrix}, \quad \mathbf{K} = \begin{bmatrix} 0 & -1 \\ k & c \end{bmatrix}, \quad \mathbf{L} = \begin{pmatrix} 0 \\ L \end{pmatrix}. \quad (4.19)$$

A second order scheme is chosen for the time derivative discretization:

$$\mathbf{M} \frac{3\mathbf{y}^{j+1} - 4\mathbf{y}^j + \mathbf{y}^{j-1}}{2\Delta t} + \mathbf{K}\mathbf{y}^{j+1} = \mathbf{L}, \quad (4.20)$$

and the resulting system is solved by using a LU factorization. The last question before integrating the coupled problem is related to the computation of the aerodynamic force contribution \mathbf{L} and in particular to the update of the fluid mesh. More specifically, a coupling also referred to as *weak coupling* is used: at each physical iteration j , the aerodynamic force contribution \mathbf{L}^{j+1} is computed, then eq.(4.20) can be

4.4. Numerical integration of an aeroelastic reduced order system: flow around a cylinder in free motion

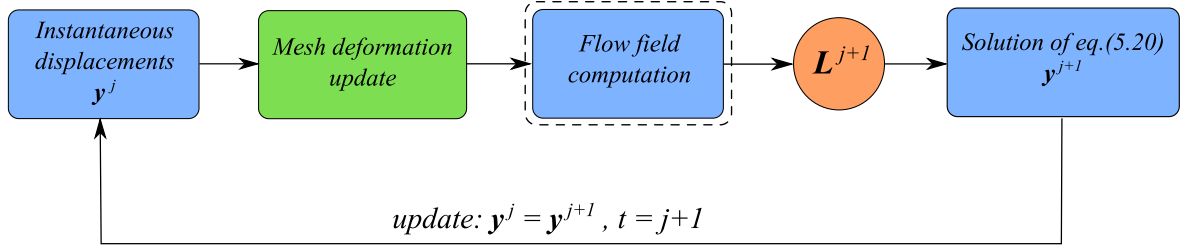


Figure 4.27 Illustrative scheme for the weak coupled fluid structure system.

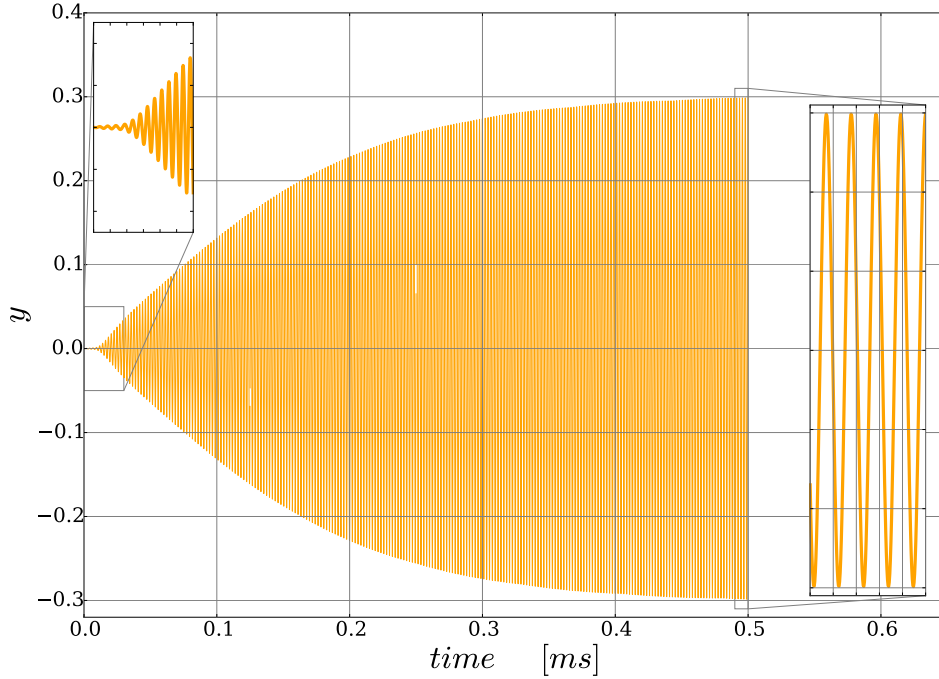


Figure 4.28 Time history of the displacement y of the cylinder in transverse free motion immersed in a uniform flow for $Re = 110$ and $M = 0.2$.

solved for the displacement \mathbf{y}^{j+1} and so on. An illustrative scheme of such a coupled system is depicted in Fig.4.27. Firstly, for the reference FOM, the flow field computation highlighted in Fig.4.27 is represented by the second order cell-centered finite-volume solver used in the previous section. Time integration is performed with a fully implicit second-order scheme that combines LU-SGS with dual time-stepping method and the updated mesh is kept unchanged during the pseudo time-step resolutions. The full order simulation is initialized with a uniform far-field condition and the initial displacement $\mathbf{y}(t = 0) = \mathbf{0}$. The test case is performed for the free-stream parameters $Re = 110$, $M = 0.2$. For this demonstrative example, a coarser mesh of 11958 triangular finite volumes is used. In Fig.4.28 the time history of the displacement y is plotted. After a transient phase the cylinder performs stable oscillations. Thus, the snapshots for the construction of the ROM are extracted during the established periodic dynamics in order to complete at least one cycle of oscillation.

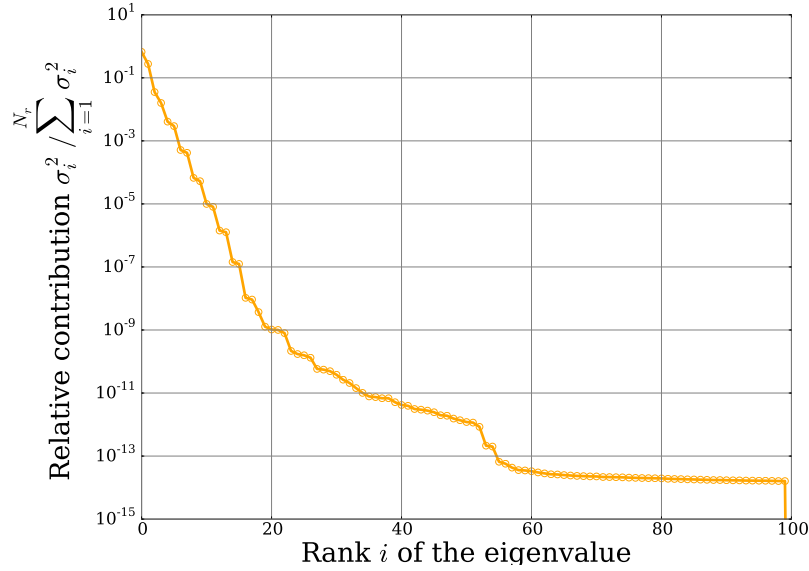


Figure 4.29 Singular values distribution of the POD for flow around a cylinder in free transverse motion at $Re = 110$.

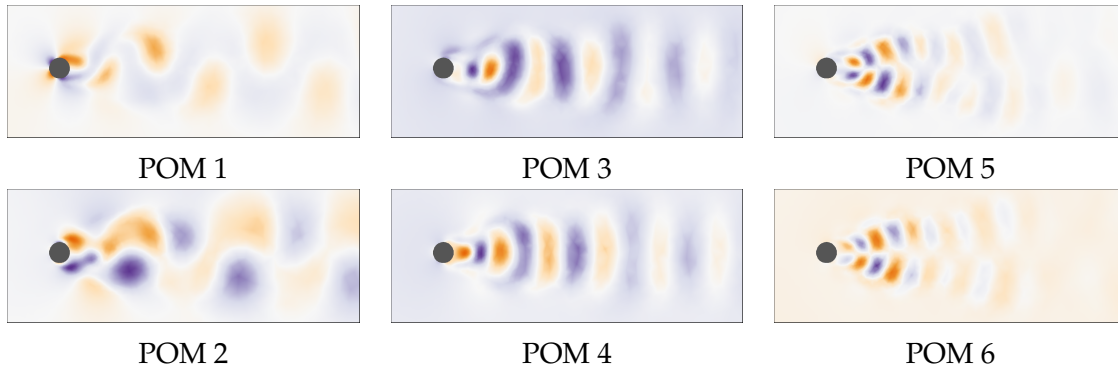


Figure 4.30 First to 6th density proper orthogonal mode (POM) for the flow around a cylinder in free transverse motion at $Re = 110$.

The nonlinear ROM described in Algorithm 7 (p.75) is integrated. The energy distribution of the solution POD modes is plotted in Fig.4.29. The POD basis is truncated to $m = 20$ such that $E_m > 0.9999$. The first 6 density POD modes are depicted in Fig.4.30.

Concerning the ROM online evaluation, the main difference with respect to the case of the cylinder in forced motion consists in the update of the mesh during the time integration. Indeed, for the case in forced motion, the instantaneous position of the cylinder and so the instantaneous mesh and cells velocities can be computed on the basis of the analytical expression for the cylinder motion. Thus, during the sub-iterations of the 4th order Runge-Kutta explicit time integration of the eq.(4.9) (see Algorithm 7 at p.75), the mesh can be easily updated. Instead, in this weak coupled scenario, once the mesh is updated as a result of the solution of eq.(4.20), it

4.4. Numerical integration of an aeroelastic reduced order system: flow around a cylinder in free motion

is kept unchanged during the Runge-Kutta sub-iterations.

Firstly, the nonlinear ROM is integrated without the use of any masked projection. For a preliminary study, the initial solution is chosen equal to the first snapshot of the sampled time period and the same time-step of the FOM is used. The time history of the position of the center of the cylinder y and of the lift coefficient c_L are shown in Fig.4.31. The amplitude of oscillation of the lift coefficient is reproduced accurately, but, moving forward in time, a slight phase shift is detected with respect to the FOM counterpart. Such a phase shift is obviously detected also in the time history of the amplitudes associated to the POMs (see Fig.4.32). This results from the different time integration algorithms used for the integration of the ROM and the FOM. Indeed, for the FOM an implicit time integrator is used, while, for the ROM, an explicit time integrator is used. This, added to the fact that the mesh is kept unchanged during the explicit Runge-Kutta sub-iterations, reflects on a higher dissipation of the ROM coupled system. In Fig.4.33 the phase portrait of the position of the center of the cylinder y and of the lift coefficient c_L for a time window which extends over the sampled time period is shown. In this case, the effect of the discrepancy between the lift derived by the ROM and the FOM reflects on the long time period oscillation. Indeed the error between the coupled ROM and its FOM counterpart gradually increases and the systems is attracted to a slightly different limit cycle of oscillation.

At this point, the effect of the masked projection approach is investigated by using different numbers of nonlinear POD modes p and of interpolation degree of freedoms f . A BQDEIM approach is used (provided in eq.(4.9)) and the reconstructed lift coefficients for the different cases are shown in Fig.4.34. If 20 nonlinear modes are used, at least 800 interpolation points are required in order to avoid the divergence of the model before the end sampled time period. Then, the discrepancy between FOM and ROM slightly reduces switching from 800 to 3200 interpolation points, but the error is still important. Divergence also occurs when using 40 nonlinear modes and 160 interpolation points. However, in such a case, the use of up to 1600 interpolation points leads to a more accurate reproduction of the amplitude of the lift coefficient but an important phase shift is still detected. Then, the best results are obtained by using 60 nonlinear modes and 9600 interpolation points. In conclusion, in this coupled ROM scenario, the accuracy of the masked projection approach is increased monotonically by adding nonlinear modes or interpolation points in the masked projection approach. However, the overall level of accuracy is not satisfactory because discrepancies are still observed in the best tested case. Furthermore, in order to perform the time integration without diverging, a high number of nonlinear modes and interpolation points are required and this reduces the benefit of the masked projection approaches.

Chapter 4. Adaptation of a nonlinear ALE-based reduced order model of the Navier-Stokes equations for aeroelasticity

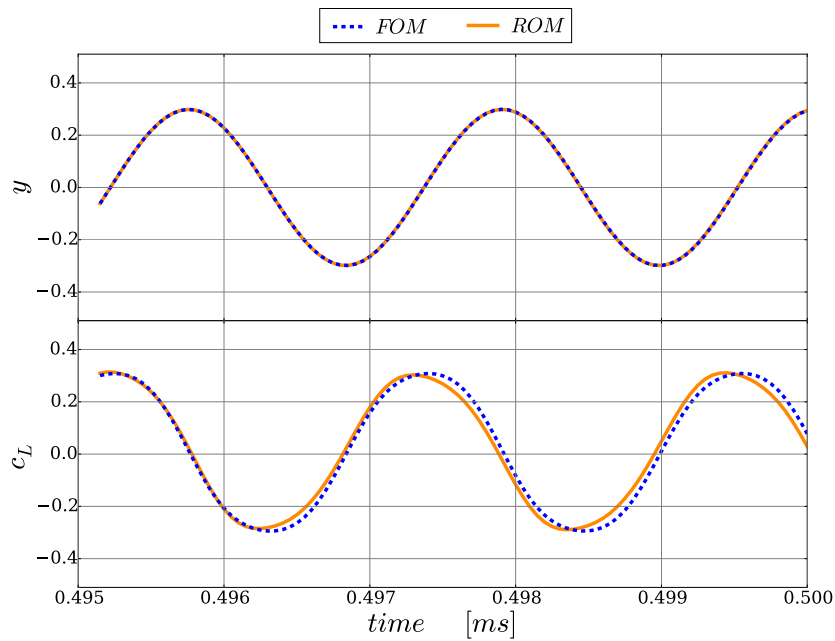


Figure 4.31 Time history of the position of the center of the cylinder y (top) and of the lift coefficient c_L (bottom) for the case of a cylinder in free transverse motion at $Re = 110$.

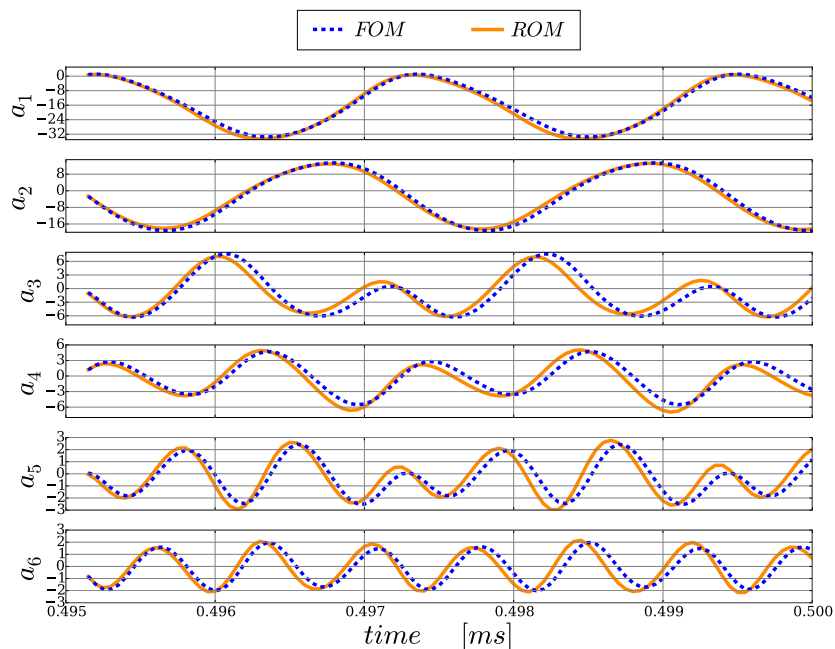


Figure 4.32 Time history of the first six amplitudes for the coupled ROM and the FOM for the case of a cylinder in free transverse motion at $Re = 110$.

4.4. Numerical integration of an aeroelastic reduced order system: flow around a cylinder in free motion

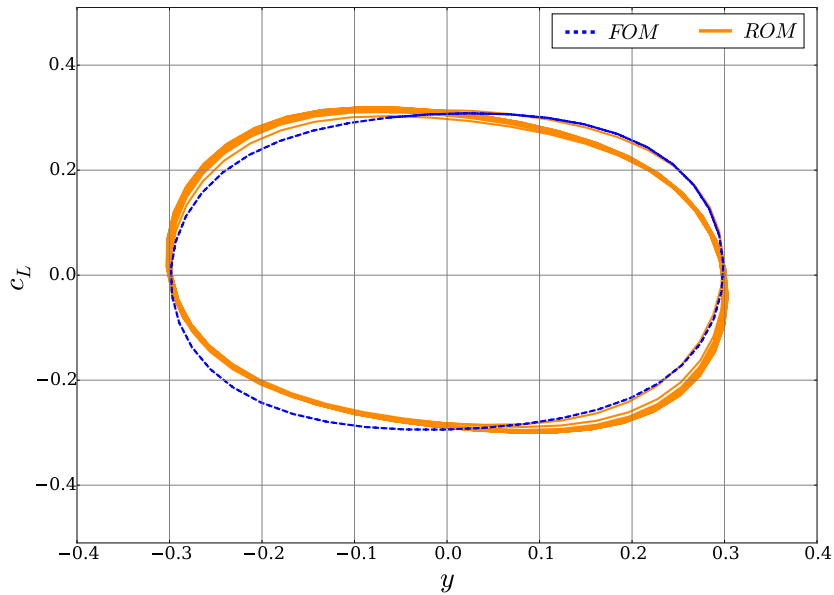


Figure 4.33 Lift coefficient and displacement phase portrait for the coupled ROM and the FOM of a cylinder in free transverse motion at $Re = 110$.

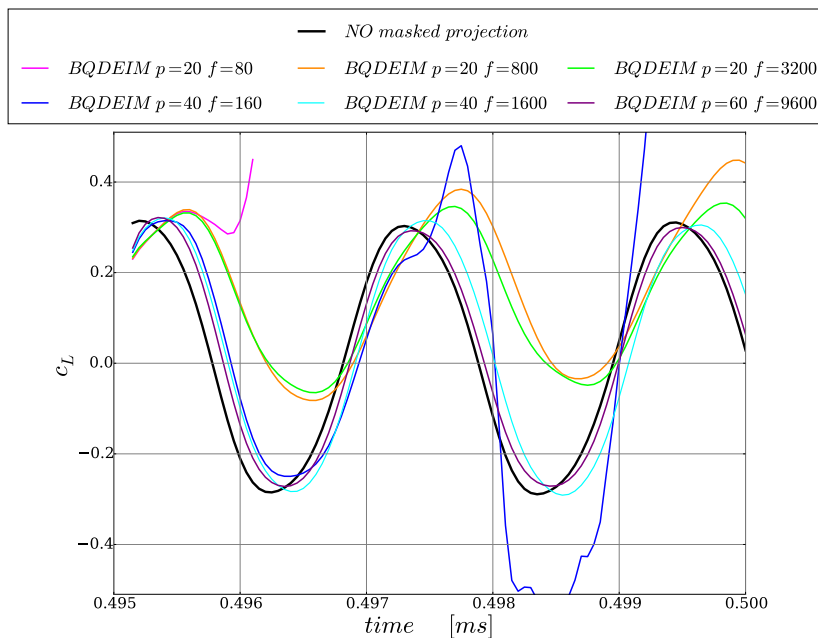


Figure 4.34 Time history of the lift coefficients for the coupled ROM for different parameters used in the masked projection approach.

4.5 Conclusions

In this chapter, the focus is placed on the construction of a nonlinear ROM of the Navier-Stokes equations for aeroelasticity. The main feature of this scenario is that the mesh is moving and deforming during the simulation. Thus, an Arbitrary Lagrangian-Eulerian (ALE) formulation of the Navier-Stokes equations is required in order to take into account the mesh motion and/or deformation. As a consequence, the dynamical system to be reduced is non-autonomous and some adaptation must be provided with respect to the nonlinear ROM developed in Chapter 2.

Firstly, the new ROM is validated with the configuration of a cylinder at $Re = 100$ in forced vertical motion. Test cases of increasing complexity with respect to the amplitude and frequency of oscillation are studied. The masked projection approach, validated in Chapter 2, is tested. In particular for the most complex test-case an adjustment is required in order to extend the set of fitting points for the masked projection approach and integrate an entire cycle of oscillation with an acceptable error.

Then, the proposed ROM is tested with respect to a parametric change and a GPOD approach with a slight modification is investigated. On the basis of certain configuration parameters, a global ROM is constructed that can be used for a new set of parameters. In this aeroelastic context, the parametric change has involved the motion parameters, that are the frequency and amplitude of oscillation. Also in this parametric case, the masked projection approach is validated.

Finally, the preliminary validation of a fully coupled aeroelastic system is investigated. In particular, the cylinder is free to perform vertical oscillations and the structural system is represented by a simple one degree of freedom rigid body system. The nonlinear ROM developed so far becomes a *module* of a more comprehensive system. The interface between structural and fluid model has been presented and a simple test case is investigated. In such a case, the explicit time integrator used for the ROM has an evident impact on the accuracy of the results, in contrast with all previous test cases. Also the masked projection approaches have demonstrated their limitations in this coupled scenario. However, in literature different approaches based, for example, on the use of the Jacobian, or data assimilation techniques and machine learning techniques have been proposed to increase the accuracy of nonlinear ROMs. Also in this application context, such techniques could represent a viable alternative to extend and improve the nonlinear ROM for aeroelasticity presented in this chapter.

Construction of a Reduced Order Time Spectral Model for the compressible ALE-based Navier-Stokes equations

Contents

5.1	Introduction	105
5.2	Formulation of the ROTSM for the compressible ALE-based Navier-Stokes equations	106
5.3	Numerical integration of the nonlinear ROTSM of a transonic flow around an oscillating airfoil	108
5.3.1	1 harmonic test case	110
5.3.2	3 harmonics test case	112
5.4	Numerical integration of the parametric ROTSM: Mach number variation	114
5.5	Conclusions	123

5.1 Introduction

The work presented in this chapter substantially addresses two important issues linked to the nonlinear ROM presented in previous chapters. The first one has already been introduced in Section 2.7 and concerns the long-term stability issues typically related to the projection-based ROMs. As outlined in Chapter 1, such an issue has been widely dealt with in literature with respect to two well-known destabilizing causes:

- the POD truncation reported in Algorithm 1 (presented at p.18) filters the low energy modes which account for the smaller spatial structures essential for the energy processes at the basis of fluid dynamics.
- the use of Galerkin projection does not ensure the stability and might lead to inaccurate long-term responses when dealing with nonlinear cases such as the ones proposed in this thesis.

Chapter 5. Construction of a Reduced Order Time Spectral Model for the compressible ALE-based Navier-Stokes equations

The second issue is strictly linked to the first one and concerns the simulation of challenging and highly nonlinear test cases such as flows with moving discontinuities. In such a context, accuracy problems are detected that consequently challenges the stability of the model. This can occur even with apparently simple test cases (see Appendix B).

In this context, the limitations of the nonlinear ROM presented in the previous chapters are emphasized. This pushed the scientific community to propose model corrections such as closure model strategies in ROMs in order to model the contribution of such small scales (as for example in references [19], [20], [133]), or the use of a different inner product for the Galerkin projection or alternative Petrov-Galerkin projection techniques [27] (see Section 2.4). Also, a posteriori stabilization techniques have been introduced in order to enhance the accuracy and stability. For example, Placzek *et al.* [134] compared several calibration techniques revealing that, when considering a flow around a moving airfoil in transonic regimes, the calibration is no longer sufficient to produce reasonably good responses. More recently, new formulations have been proposed even in new mathematical frameworks such as System Identification and Data Assimilation [35], [135], [136].

In this Chapter we propose an alternative to tackle the issues mentioned above at the FOM level by exploiting the hypothesis of periodicity of the solution at a given frequency. The mathematical derivation of this method is described in Section 2.7.2. The theory at the basis of this formulation is similar to the one provided by Thomas *et al.* [61] in the frequency domain. More specifically, the common ground between the approach described in this chapter and the one formulated by Thomas *et al.* [61] is the use of a *Ritz-type expansion* of the POMs to approximate the solution. Besides that, Thomas *et al.* [61] propose to use a second order Taylor series expansion about a reference (set of) configuration parameter(s) in order to construct a nonlinear ROM for a new (set of) configuration parameter(s). For this purpose, Galerkin projection and automatic differentiation to derive the required Jacobian and tensors are adopted. For the approach implemented in this chapter, firstly a Petrov-Galerkin projection is used. Secondly, the system solution for a new configuration parameter is computed by avoiding the Taylor series expansion. Conversely, the solution is computed by adapting (or interpolating) the POD basis Φ that represents the subspace where the solution is sought.

5.2 Formulation of the ROTSM for the compressible ALE-based Navier-Stokes equations

Given the **the periodicity at a given frequency** $f = 1/T$ of the solution, we propose to exploit such an hypothesis at the full order level and then formulate the reduced order counterpart. More specifically, starting from eq.(4.8) and following the TSM theoretical derivation of Section 2.7, we can obtain the FOTSM equation for the ALE

5.2. Formulation of the ROTSM for the compressible ALE-based Navier-Stokes equations

Navier-Stokes equations:

$$D_t(\mathbf{w}_j) - \mathbf{f}(\mathbf{w}_j) = 0 \quad , \quad 0 \leq j \leq 2N + 1. \quad (5.1)$$

The difference with respect to the general eq.(2.38) is the definition of the nonlinear operator that, in such a case, represents the right-hand side of the Navier-Stokes equations (that is the instantaneous fluxes balance) computed at the different instances $n\Delta t$ and $\Delta t = T/(2N + 1)$, with $T = 2\pi/\omega$ the period of the system, divided by the respective instantaneous cell volumes. Such a system of coupled steady equations can be solved by using pseudo-time stepping techniques either in a semi-implicit or fully-implicit formulation outlined in Section 2.7.

Given the FOTSM, we can formulate its reduced order counterpart following the theoretical derivation of Section 2.7.2:

$$\mathcal{R}_{TSM}(\mathbf{a}_j) = D_t \Phi \mathbf{a}_j - \mathbf{f}(\Phi \mathbf{a}_j) = 0, \quad 0 \leq j < 2N + 1 \quad (5.2)$$

Applying Newton's method to solve the fully coupled system (5.2) with all instance amplitudes gathered in vector $\mathbf{a} = (\mathbf{a}_0, \mathbf{a}_1, \dots, \mathbf{a}_{2N+1})$ results in the following iterations. For $k = 1 \dots K$

$$\mathbf{A}^k \Delta \mathbf{a}^k = -\mathcal{R}_{TSM}(\mathbf{a}^k) \quad (5.3)$$

with K determined by the threshold of a convergence criterion. Basically, two alternative approaches are available which differ for the projection used for the resolution of eq.(5.3). The first one is a Petrov-Galerkin projection which corresponds to the resolution of the system in a least-square sense by using the Gauss-Newton algorithm detailed in eq.(2.50). The second one is a Galerkin projection leading to the *direct* resolution of eq.(2.52).

It is worth recalling that the ROTSM should not be referred to as a reduced order model in a strict sense because there is not any truncation in the construction of the POD basis. Basically, the use of the approximation in eq.(5.2) (or eq.(2.45)) affects two different aspects. First, the solution is sought in a subspace that is a priori suitable as a result of the POD; second, the matrices involved in the numerical resolution have smaller dimensions making it easier to handle, as previously observed in Section 2.7.2. In other words, with respect to the nonlinear ROM outlined in previous chapters, in such a case the reduced order approximation can be related to the Fourier series decomposition truncation at the basis of the FOTSM. Instead, the ROTSM may help reducing the computational time and improving the rate of convergence of the FOTSM, that is a well-suited feature when dealing with nonlinear, time periodic, unsteady problems. In conclusion, the presented approach proposes to use a limited number of harmonics to model the periodic response of a flow rather than to try to keep only a certain number of POD modes for the flow approximation. For a wide range of applications, the dynamics of the system can be properly represented with a limited number of harmonics rather than with only the most energetic structures of the flow. For example, in case of discontinuous transonic flow fields,

although linear superposition of different POD modes can achieve the reconstruction of the shock wave, similarly to the Gibbs phenomenon for a Fourier sum, the smoothness of the solution near the shock wave cannot be guaranteed leading to inaccuracy or divergence [137].

5.3 Numerical integration of the nonlinear ROTSM of a transonic flow around an oscillating airfoil

To illustrate the potentialities of the proposed ROTSM a challenging test case is studied. We have selected the test case noted as *dynamic index 55* reported by the AGARD group in reference [138]. It corresponds to an oscillating *NACA64A010* airfoil under the pitch motion defined by the function:

$$\alpha(t) = \alpha_0 + \hat{\alpha} \sin(\omega t), \quad (5.4)$$

where $\alpha_0 = -0.22^\circ$ and $\hat{\alpha} = 1.01^\circ$. The Mach number is 0.796 and the excitation frequency 34.4 Hz. Under these conditions the reduced frequency is $\kappa = \omega c / 2U_\infty = 0.41$, where c is the chord of the airfoil.

As outlined above, the FOM is represented by the TSM. The reference Euler equations solution is obtained by the industrial finite volume solver *elsA* [123], while the TSM solver has been implemented in *Python* and interfaces in a modular way with the *elsA* solver for the computation of the flux balances $f(\Phi \mathbf{a}_n)$ and the Jacobian term \mathbf{J} [139]. As a rigid motion is considered the model is formulated by taking into account an absolute velocity formulation in reference domain in rigid motion¹. In Fig.5.1 the Mach fields for three different instants of the simulation are depicted in order to show the presence of a moving shock on the airfoil.

We remind that the number N of harmonics of eq.(5.2) and so the number $(2N + 1)$ of coupled steady equations to solve is a parameter of the TSM solver. Fig.5.2 compares the aerodynamic force coefficients obtained by the TSM for different number of harmonics with respect to the solution obtained with a Finite Volume unsteady flow solver. It can be noted that to reproduce correctly the lift coefficient (on the left) 1 harmonic is sufficient. However this choice implies a significant error on the drag coefficient prediction (on the right). Finally, the non-linear effects involved in this test case require a minimum number of harmonics equal to 3 in order to correctly predict the aerodynamic coefficients.

¹The complete formulation in a possibly deforming mesh is under development. However there are no relevant differences between the two respective reduced order model formulations.

5.3. Numerical integration of the nonlinear ROTSM of a transonic flow around an oscillating airfoil

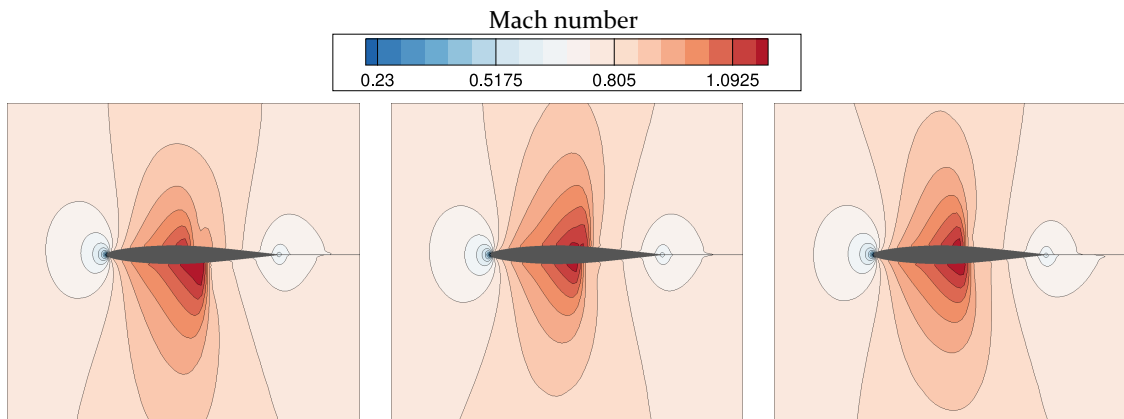


Figure 5.1 Mach fields for three different instants of the finite volume resolution of the unsteady Euler equations.

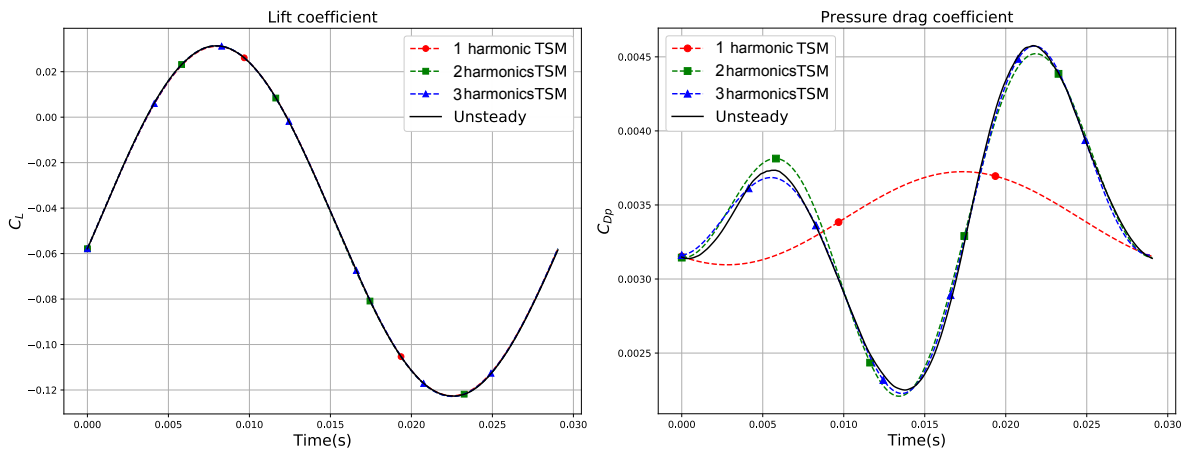


Figure 5.2 Comparison of the aerodynamic force coefficients between the finite volume solver and the TSM solver.

5.3.1 1 harmonic test case

Firstly, the ROTSM is constructed by taking into account only 1 harmonic for the TSM resolution. For this test case a semi-implicit resolution of the TSM (see Section 2.7.1) is used. Then, a POD basis is constructed using the 3 snapshots corresponding to the 3 time instances of the TSM. The 3 density POD modes are depicted in Fig.5.3.

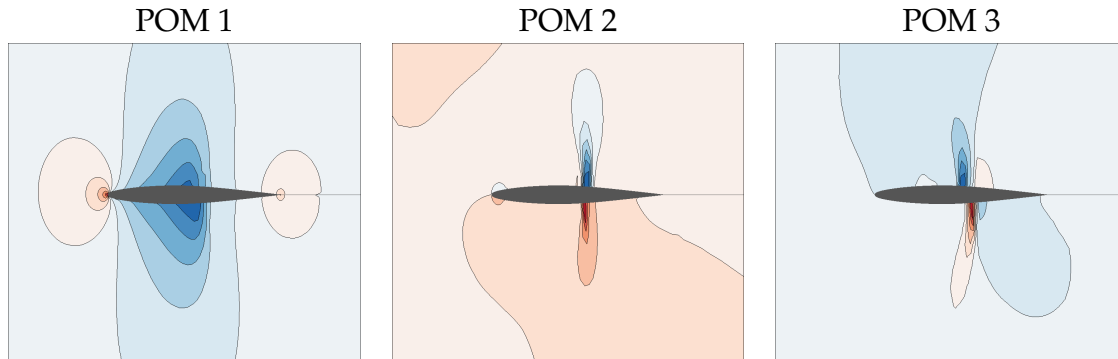


Figure 5.3 Density fields of the 3 proper orthogonal modes (POMs) composing the POD basis for the ROTSM for $N = 1$.

In Fig.5.4 the rate of convergence of the full order and the reduced order TSM is shown. Firstly, it is obvious that the ROTSM presents a much faster and more regular rate of convergence (note the different abscissa). The zoomed part of the plot emphasizes the differences between the initial guesses. Indeed, as explained in Section 2.7.2, the projection of the free-stream state vector onto the POD basis provides a different and more suitable initial guess for the ROTSM. The ROTSM requires only about 10 iterations to attain a residual comparable to the one reached by the TSM in 1000 iterations. Moreover, each iteration of the ROTSM required a smaller system to be solved resulting, globally, in a lower computational cost. We remind also that the POD basis is built from the TSM snapshots associated to a given residual norm. This norm is the convergence criterion that monitors the cost of the TSM. Since the ROTSM seeks a solution in the vector space spanned by the TSM snapshots, it is not possible to reach a better numerical accuracy than the one of the TSM simulation. Finally, in Fig.5.5 the absolute difference between the density fields related to the ROTSM and the TSM is shown as a proof of the high accuracy attained by the presented model.

5.3. Numerical integration of the nonlinear ROTSM of a transonic flow around an oscillating airfoil

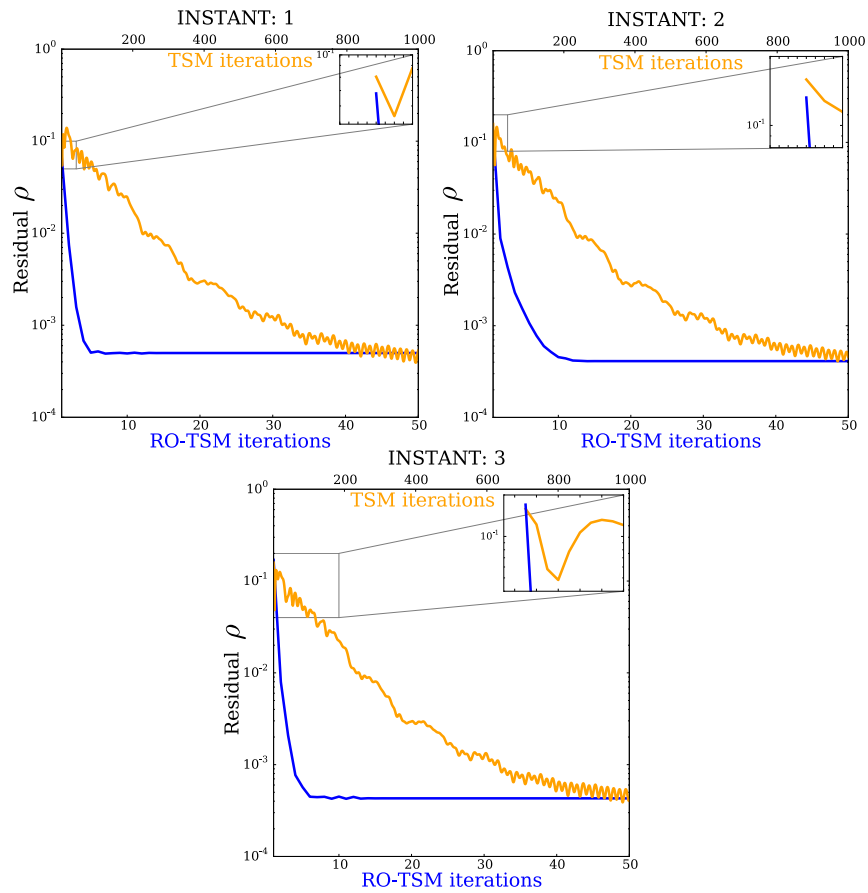


Figure 5.4 Comparison of the Euclidean norm of the density residual for the full order and the reduced order TSM. Note the different abscissa related to the two approaches.

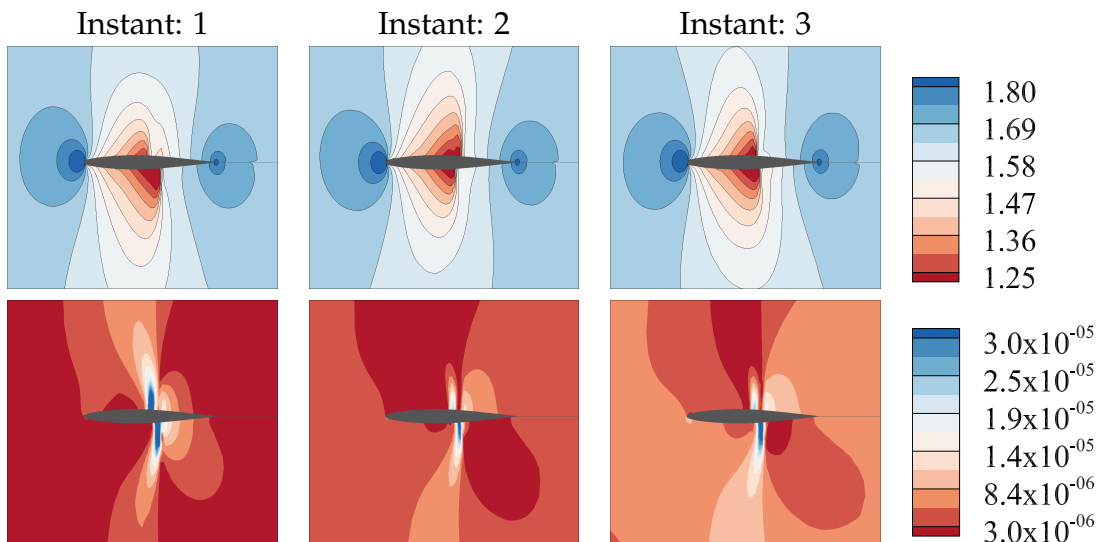


Figure 5.5 On the first line, the density fields at the 3 time instances of the TSM. On the second line, the density fields absolute difference between the ROTSM and the FOTSM density fields.

5.3.2 3 harmonics test case

As previously introduced, the non-linear effects of the presented test case require at least 3 harmonics for the TSM computation to reach an acceptable accuracy on the aerodynamic drag coefficient prediction. The choice of 3 harmonics implies 7 steady coupled equations to be solved which affects the diagonal dominance of the TSM eq.(5.3) and therefore the global complexity of the TSM resolution. This raises the convergence issues occurring when an explicit TSM solver is employed. As a consequence, a fully implicit TSM solver (with a block-Jacobi implementation [139]) is employed with a CFL number for the pseudo-time integration equal to 2.5. Once the FOTSM computation is performed, the POD basis is constructed with the resulting 7 solution field snapshots. The density POD modes are depicted in Fig.5.6.

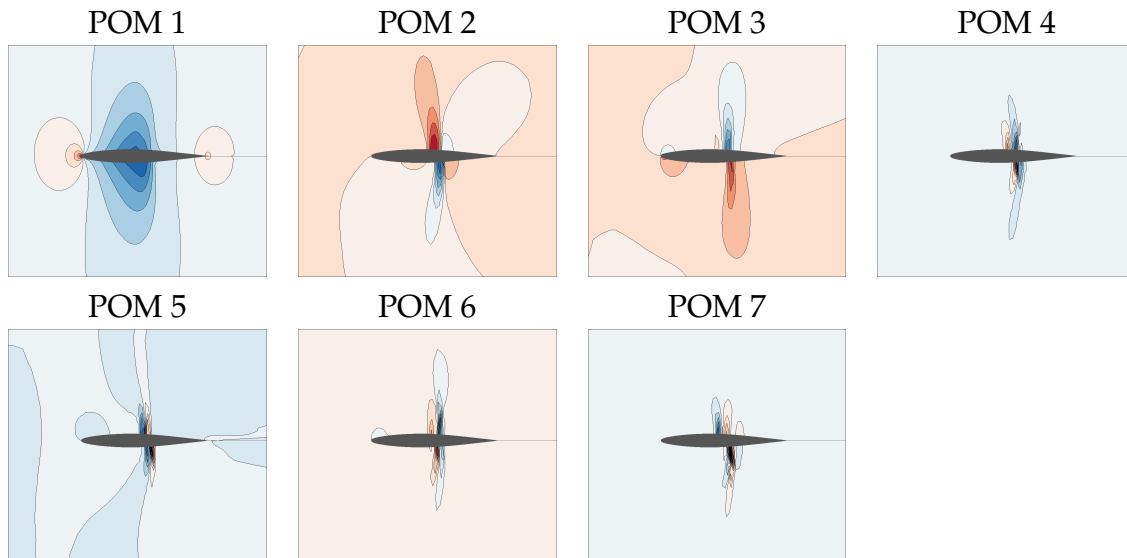


Figure 5.6 Density fields of the 7 proper orthogonal modes (POMs) composing the POD bases for the ROTSM for $N = 3$.

In Fig.5.7 the rate of convergence of the the ROTSM is shown. In contrast to the FOTSM, there are no significant differences in the stability of the model between the cases with 1 and the 3 harmonics. This is not the case for the FOTSM, which required implicitation and a low CFL condition. Instead, provided a POD basis for the involved time instances, the same ROTSM reaches a monotonic convergence. In Fig.5.8 the absolute difference between the density fields related to the ROTSM and the FOTSM is depicted in order to show the same high accuracy attained for the 3 harmonic case.

5.3. Numerical integration of the nonlinear ROTSM of a transonic flow around an oscillating airfoil

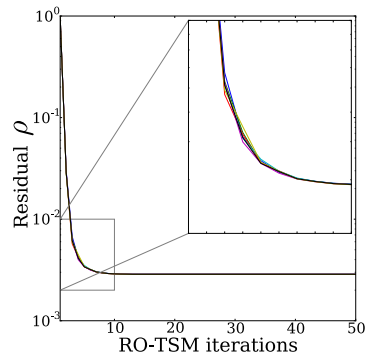


Figure 5.7 The Euclidean norm of the density residual for the 7 steady state fields of the ROTSM.

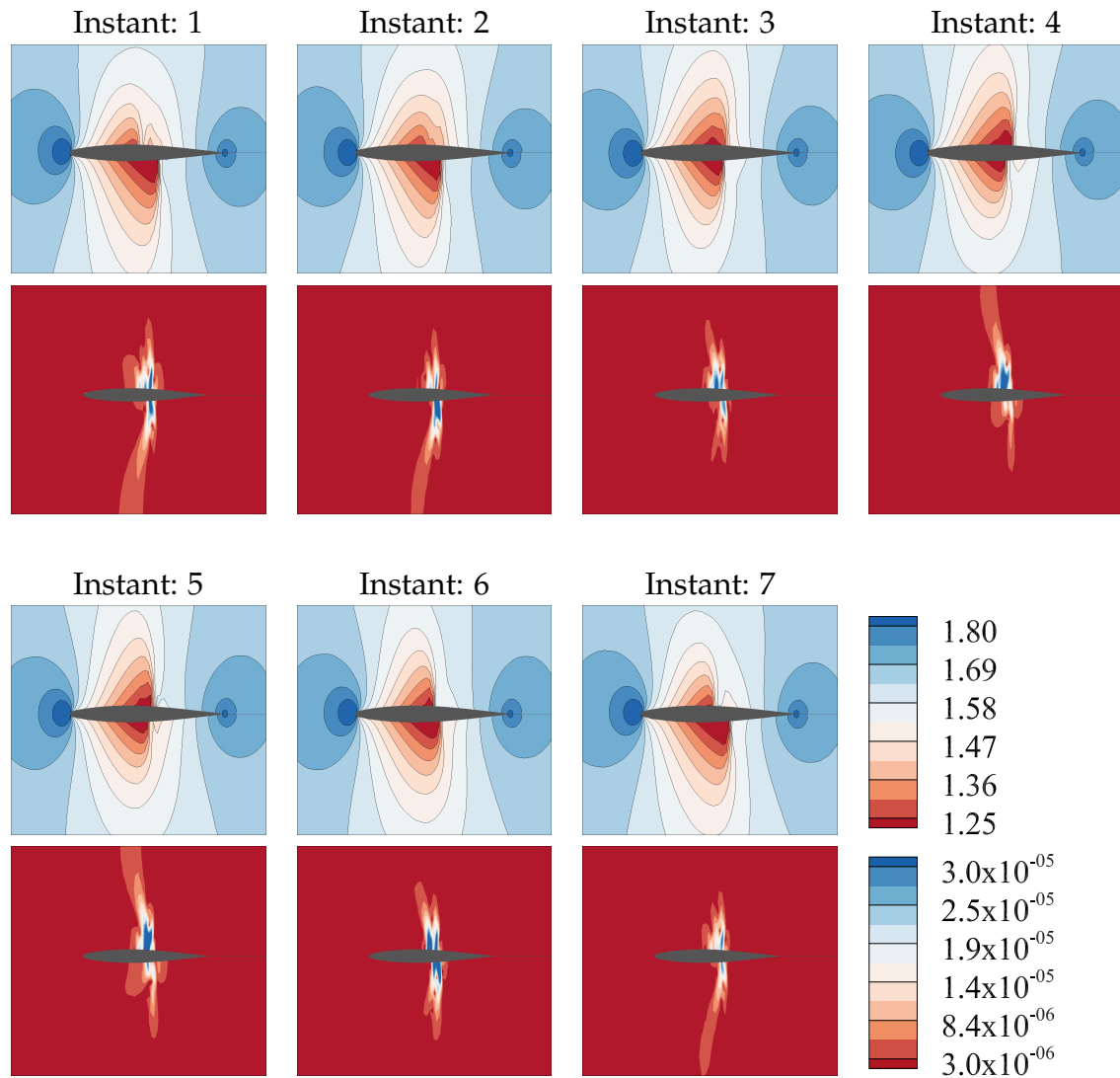


Figure 5.8 On the first line, the density fields at the seven time instances of the TSM. On the second line, the density fields absolute difference between the ROTSM and the FOTSM density fields.

5.4 Numerical integration of the parametric ROTSM: Mach number variation

One of the motivations that inspired the derivation of the ROTSM is the difficulties arising by the application of the projection-based ROMs to nonlinear problems like those encountered, for example, in transonic flows involving moving discontinuities. In Section 3.5, the case of a slightly transonic flow with a fixed shock has been addressed, but the dynamics was essentially governed by the vortex shedding and not the shock motion. In such a case, the shock is entirely included in the average term \bar{w} . On the contrary, when the shock is moving additional difficulties arise for projection-based ROMs (see Appendix B). With the ROTSM approach, such nonlinear dynamics are well detected as shown in the previous sections.

At this stage, the question of parametric investigation in nonlinear context must be addressed. Obviously, the principal parameter concerned by the subsonic/transonic/supersonic regime of the flow is the free-stream Mach number. For this reason, a set of pre-computed ROTSMs for different operating points included in Λ_{M_∞} is considered:

$$\Lambda_{M_\infty} = \{0.52, 0.56, 0.60, 0.64, 0.68, 0.72, 0.76, 0.80\}. \quad (5.5)$$

In Fig.5.9 the Mach fields for steady computations for three different free-stream Mach numbers in the operating points set are shown. It can be seen that the subsonic and transonic regimes are included in the reference solutions and, in the transonic case, a *supersonic pocket* terminated by a shock wave is detected. The reference ROTSMs are solved by using 1 harmonic so that the solution is represented by 3 instantaneous fields for each operating point.

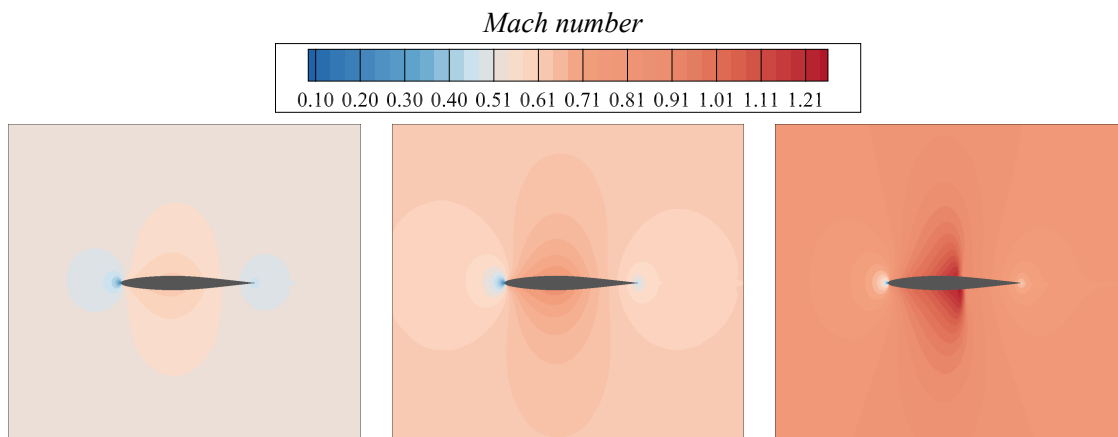


Figure 5.9 Mach steady states for three different free-stream Mach numbers in the operating points set. Left: $M_\infty = 0.52$, middle: $M_\infty = 0.68$, right: $M_\infty = 0.80$, .

5.4. Numerical integration of the parametric ROTSM: Mach number variation

The parametric study is performed on 2 off-reference Mach numbers:

$$\Lambda_{M_\infty}^* = \{0.58, 0.78\}. \quad (5.6)$$

With respect to the parametric study of the previous chapter, in such a case only the matrix Φ is required in order to solve the ROTSM for an off-reference condition.

In order to provide the POD modes Φ for an off-reference condition, the GPOD approach introduced in Section 4.3.1 is an available alternative. It implies to perform a POD of the matrix collection of the ROTSM solutions for the different Mach numbers included in Λ_{M_∞} . More specifically, given

$$\mathbf{W} = \{\mathbf{w}(j\Delta t, i), 0 \leq j \leq 2N + 1, i \in \Lambda_{M_\infty}\}, \quad (5.7)$$

with $\Delta t = T/(2N + 1)$, where T is the period of the oscillation and $N = 1$ is the number of harmonics chosen for the Fourier truncation.

Algorithm 1 can be applied with input \mathbf{W} . The singular value distribution is depicted in Fig.5.10. Eventually, the POD basis can be truncated according to the value $E_m \geq 0.9999$ so that the first 10 modes can be retained.

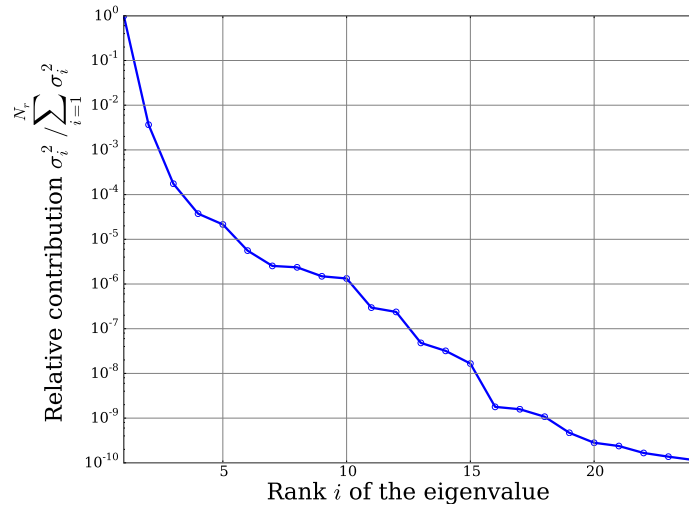


Figure 5.10 Singular values distribution of the POD computed for the matrix collection \mathbf{W} of the ROTSM solutions for different Mach numbers included in Λ_{M_∞} (eq.(5.7)).

The shapes of the density global POD modes are depicted in Fig.5.11. The first and the third modes involve regular flow structures with a continuous pattern around the airfoil. The second mode shows a sharper compression zone around the airfoil. On the contrary, from the mode 4 onward the contour around the airfoil displays ribbon patterns with alternating positive and negative values. In reference [137], these ribbons are referred to as “high frequency waves” and they are characteristic of POD bases for transonic or supersonic configurations. The linear superposition of these “high frequency waves” reproduces the shock wave dynamics of the

Chapter 5. Construction of a Reduced Order Time Spectral Model for the compressible ALE-based Navier-Stokes equations

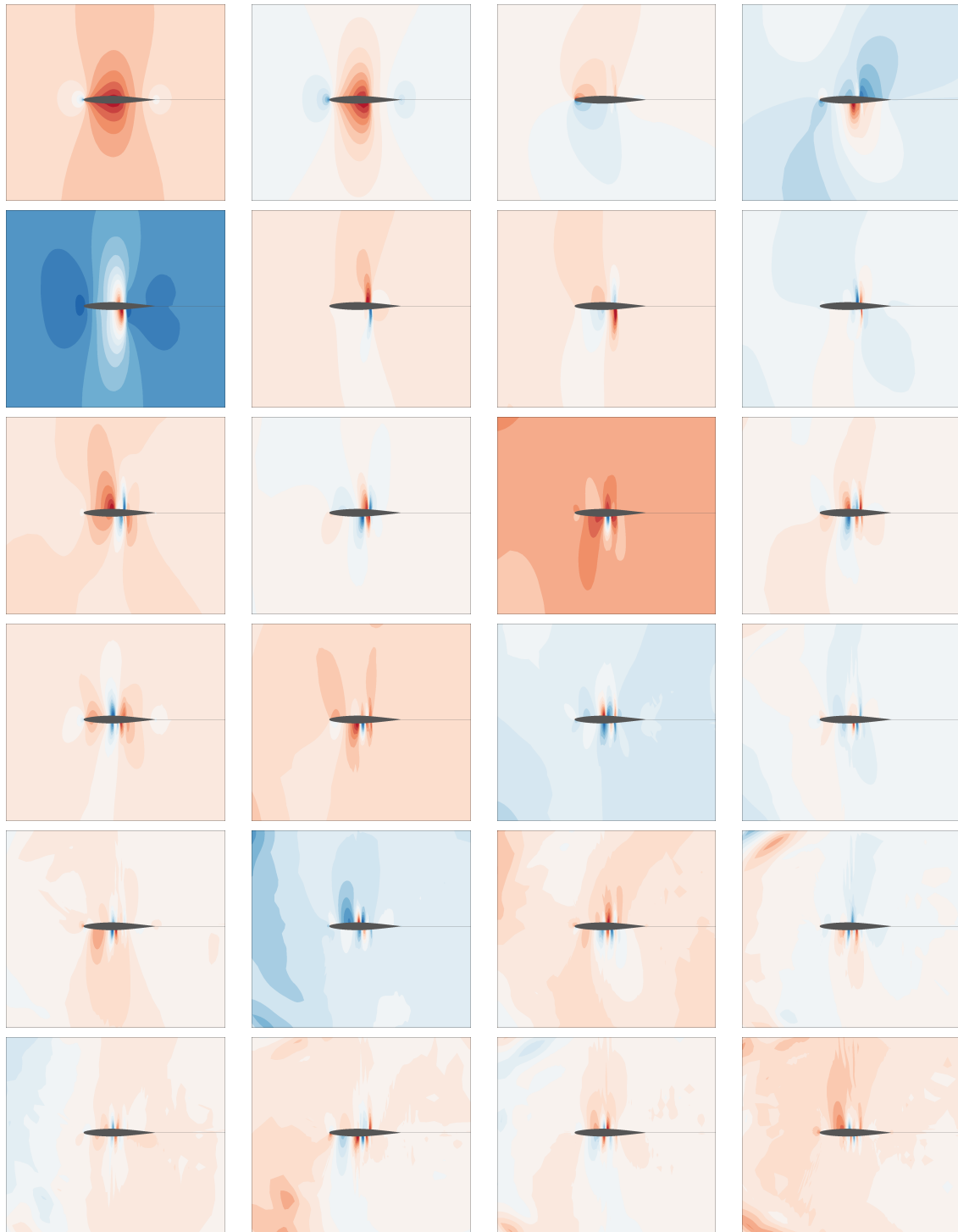


Figure 5.11 Density fields of the 24 proper orthogonal modes (POMs) composing the GPOD basis for the parametric ROTSM (sorted from left to right from the top to the bottom).

5.4. Numerical integration of the parametric ROTSM: Mach number variation

flow field. However, Li *et al.* [137] observe that the “high frequency waves” can hardly offset each other resulting in additional spurious oscillation before and after the shock. With the increase of POD modes used in the approximation basis, the oscillation frequency increases while the oscillation amplitude decreases gradually. In accordance with these deductions, it is expected a different behaviour of the ROTSM between a truncated and a full GPOD: with the truncated basis the high frequency spurious oscillations are expected to be attenuated and, in contrast, the spatial reconstruction is expected to be deteriorated with respect to the accuracy and the position of the shock.

Other studies have been presented in literature addressing a similar problem [49], [59], [68]. Particularly, results have been shown reporting the unreliability of the GPOD in the adaptation of projection based ROMs in the transonic regime. Am-sallem [86] proposed an interpolation on a tangent space of the Grassmann manifold as an alternative method for adapting pre-computed POD bases to new physical or modeling parameters. For each value of the set Λ_{M_∞} corresponding to different Mach numbers, a set of bases Φ is generated. One of the bases is taken as reference point on the Grassmann manifold and each of the remaining bases is logarithmically mapped to the tangent space at the reference point. On the tangent space, a Lagrangian interpolation is performed for the parameter of interest. Finally, the new basis is obtained through an exponential mapping [49]. For the present case, the reference point is set at $M_{\infty 0} = 0.68$. The interpolation on a tangent space of the Grassmann manifold procedure is described in Algorithm 10.

In next sections results concerning the adaptation of the ROTSM to the parameters $\Lambda_{M_\infty}^*$ are presented. In particular, three possible approaches are considered:

- a. GPOD without basis truncation;
- b. GPOD with basis truncation;
- c. interpolation on a tangent space of the Grassmann manifold.

Adaptation for $M_\infty^* = 0.58$

For this first test case, the subsonic off-reference Mach number 0.58 configuration is investigated. Reference results are obtained by using the ROTSM with a POD basis Φ obtained by using the FOTSM solutions. The three density fields at the three time instances of the TSM are shown in Fig.5.12. This result represents the reference the adapted ROTSM will be compared to.

As highlighted above, the POD basis Φ must be adapted (or interpolated) in order to investigate an off-reference condition.

In Fig.5.13, the Euclidean norm of the density residual for the different instances of the model are shown for the three different interpolation approaches with respect to the reference ROTSM counterpart. For this study, a cutoff condition in the GPOD

Chapter 5. Construction of a Reduced Order Time Spectral Model for the compressible ALE-based Navier-Stokes equations

Algorithm 10 Interpolation on a tangent space of the Grassmann manifold. [86]

Input: A set of POD bases for different operating points in Λ : $\{\Phi_{\mu_1}, \Phi_{\mu_2}, \dots, \Phi_{\mu_{N_{ref}}}\}$ and a chosen reference POD basis $\Phi_{\mu_0} \in \Lambda$

Output: POD basis for any new operating point $\Phi_{\mu_\star} \in \mathbb{R}^{n \times m}$

- 1: The remaining POD bases in $\Phi_{\mu_i} \in \Lambda - \Phi_{\mu_0}$ are logarithmically mapped using the thin SVD:

$$(\mathbf{I} - \Phi_{\mu_0} \Phi_{\mu_0}^T) \Phi_{\mu_i} (\Phi_{\mu_0}^T \Phi_{\mu_i})^{-1} = \mathbf{U}_{\mu_i} \Sigma_{\mu_i} \mathbf{V}_{\mu_i}^T$$

$$\Gamma_{\mu_i} = \mathbf{U}_{\mu_i} \tan^{-1} \Sigma_{\mu_i} \mathbf{V}_{\mu_i}^T$$

- 2: Perform the interpolation:

$$\Gamma_{\mu_\star} = \sum_{i=1}^{N_{ref}} \alpha_i \Gamma_{\mu_i},$$

where the α_i are the coefficients arising from a Lagrangian interpolation.

- 3: Compute Φ_{μ_\star} by the following exponential mapping of Γ_{μ_\star} :

$$\Gamma_{\mu_\star} = \mathbf{U}_{\mu_\star} \tan^{-1} \Sigma_{\mu_\star} \mathbf{V}_{\mu_\star}^T$$

$$\Phi_{\mu_\star} = \Phi_{\mu_0} \mathbf{V}_{\mu_\star} \cos \Sigma_{\mu_\star} + \mathbf{U}_{\mu_\star} \sin \Sigma_{\mu_\star}$$

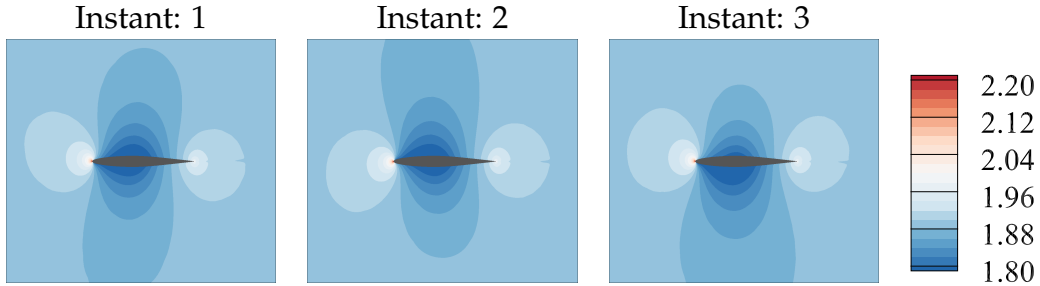


Figure 5.12 Density fields at the 3 time instances of the TSM for $M_\infty = 0.58$. Results obtained with the reference ROTSM.

has been taken into account. Given the singular values spectrum in Fig.5.10, 10 modes have been retained. First of all, the focus is on the initial guess and the initial trend of the residuals. The effect of the truncation of the GPOD does not affect the initial guess and the trend of the residuals for the first iterations. Besides, such an initial guess is different with respect to the one of reference counterpart and leads to higher residuals. Under this aspect, the case with basis interpolation presents a better initial guess being much closer to the reference ROTSM. Although the three interpolation cases exhibit a smooth and globally monotonic convergence trend, after few iterations a stagnation of the residuals at about 10^{-3} is detected, whereas the reference ROTSM converges to a value of about 10^{-8} . However, by focusing on the

5.4. Numerical integration of the parametric ROTSM: Mach number variation

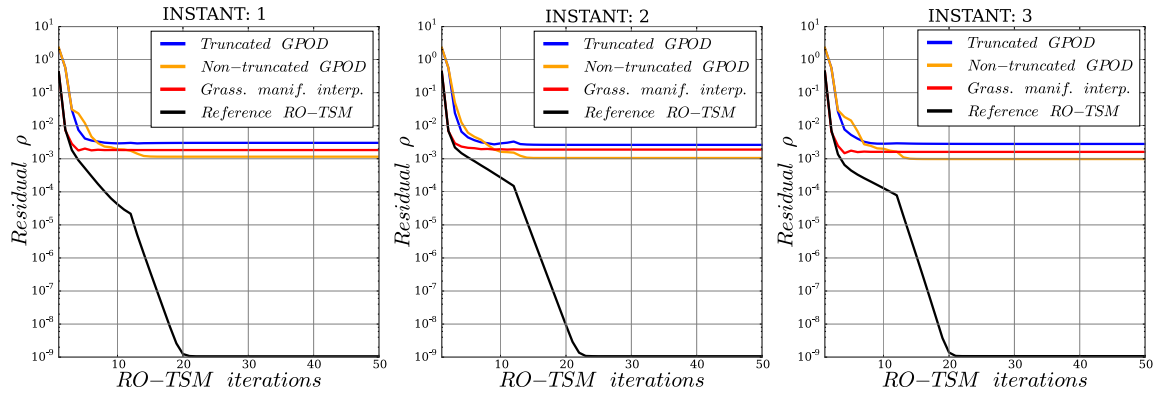


Figure 5.13 Comparison of the Euclidean norm of the density residual for the ROTSM with different interpolation approaches for $M_\infty = 0.58$. In black, the respective reference ROTSM.

absolute error on the density field in Fig. 5.14, it can be noted that for the three interpolation approaches the local error, depicted in Fig. 5.12, is always lower than 0.01 that is widely acceptable. The best results are obtained with the basis interpolated on a tangent space of the Grassmann manifold; for the GPOD with truncation, the highest error value and a concentration of the error close to the airfoil is detected (see Instant 2 in Fig. 5.14 and the values reported in Table 5.1). On the contrary the error for the GPOD approach without truncation is distributed on a wider region around the airfoil. Finally, in Table 5.1 the sum of the absolute density error over the entire mesh for each instants $\varepsilon(n\Delta t) = \sum_i | \rho_i^{\text{ROTSM}}(n\Delta t) - \rho_i^{\text{adapted ROTSM}}(n\Delta t) |$ for the different adaptation approaches is reported. Even if with a the truncated GPOD approach a higher error is locally detected, the global error over the entire mesh is lower with respect to the GPOD approach without truncation. Coherently with the plots in Fig. 5.14, the best overall accuracy is obtained with a basis interpolated on a tangent space of the Grassmann manifold.

	Instant 1		Instant 2		Instant 3	
	ε	max err	ε	max err	ε	max err
GPOD	5.52	0.006	6.08	0.007	5.45	0.006
Truncated GPOD	4.66	0.007	5.63	0.011	3.96	0.006
Grassmann manifold	2.07	0.003	1.96	0.002	1.97	0.003

Table 5.1 Sum of the absolute density error and max absolute error over the entire mesh for the different basis adaptation approaches for the 3 different instances of the TSM for the case at $M_\infty = 0.58$.

Chapter 5. Construction of a Reduced Order Time Spectral Model for the compressible ALE-based Navier-Stokes equations

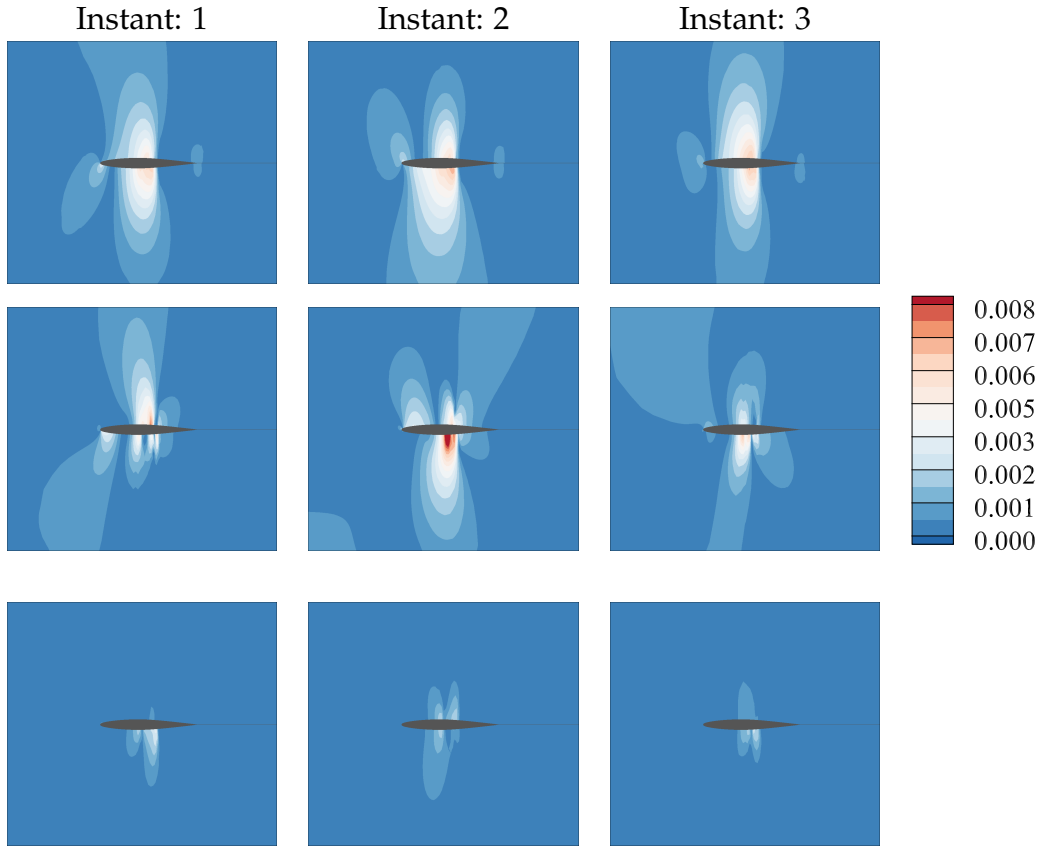


Figure 5.14 Density fields absolute difference between the reference ROTSM and the adapted ROTSM density fields at the 3 time instances for $M_\infty = 0.58$: on the first line with GPOD, on the second line with truncated GPOD and on the third line with the interpolated basis on a tangent space of the Grassmann manifold.

Adaptation for $M_\infty^* = 0.78$

For the second test case, the transonic off-reference Mach number 0.78 configuration is investigated. Reference results are obtained by using the ROTSM with a POD basis Φ obtained by using the FOTSM solutions. The three density fields at the three time instances of the TSM are shown in Fig.5.15. This result represents the reference the adapted ROTSM is compared to. With respect to the previous test case, under these transonic conditions, a *supersonic pocket* terminated by a shock wave is detected around the airfoil. Thus, the different $M_\infty^* = 0.78$ traduces in a substantially different and more challenging flow configuration. This is corroborated by the Euclidean norm of the density residual for the different instances shown in Fig.5.16. Indeed, with respect to the previous subsonic case, the level of convergence is lower of about one order of magnitude. Besides, the same characteristic of the previous test case concerning the initial guess and the trend of the residuals is detected. The lower level of convergence is also in accordance with the absolute errors of the den-

5.4. Numerical integration of the parametric ROTSM: Mach number variation

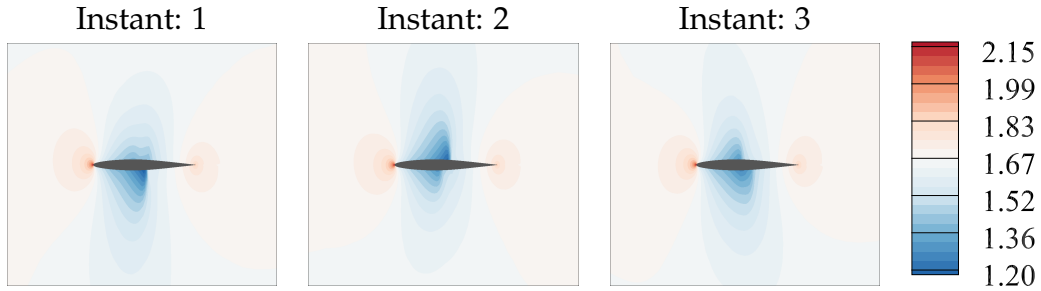


Figure 5.15 Density fields at the 3 time instances of the TSM for $M_\infty = 0.78$. Results obtained with the reference ROTSM.

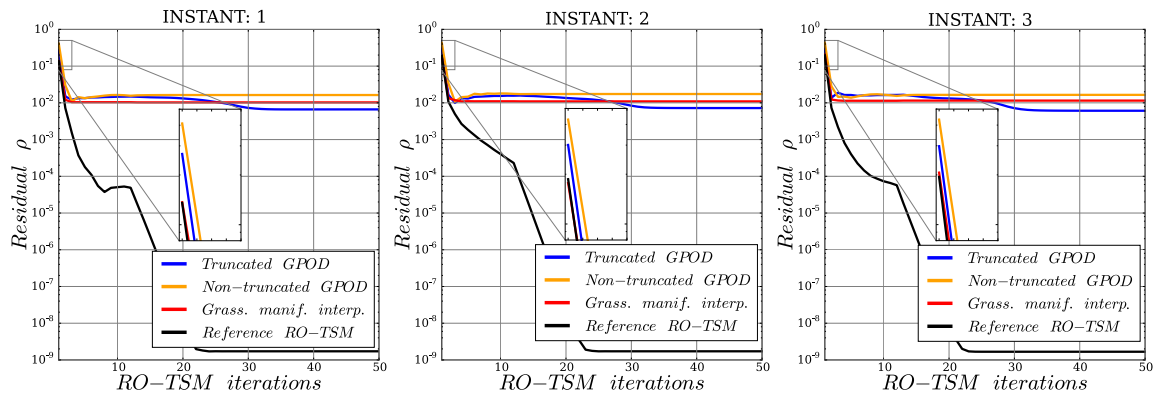


Figure 5.16 Comparison of the Euclidean norm of the density residual for the ROTSM with different interpolation approaches for $M_\infty = 0.78$. In black, the respective reference ROTSM.

sity fields depicted in Fig. 5.17. The accuracy is substantially decreased and in the worst case, the GPOD without truncation, local errors of about the 20% are detected. The highest errors are found in the zone close to the airfoil and in particular in the proximity of the shock in agreement with the considerations by Li *et al.* [137]. The lowest maximal local error between the different adapted bases approaches is not related to a particular interpolation approach (see Table 5.2). Conversely, the sum of the absolute density error over the entire mesh indicates that with the interpolation on a tangent space of the Grassmann manifold the best results are obtained (Table 5.2). To conclude, even if the adaptation of the ROTSM for a transonic off-reference condition leads to higher errors than in the subsonic case, the results with interpolation on the Grassmann manifold are still encouraging. On one side, in literature other interpolation strategies have been proposed which could fit well in the context of this study and should be subject of further investigations. On the other side, the canonical form (suggested in reference [68]) of the interpolation on a tangent space of the Grassmann manifold has been used for this example, but in literature variations and enhancements with respect to different contexts are being proposed. Thus, the study presented in this chapter could be improved also from this point of

view.

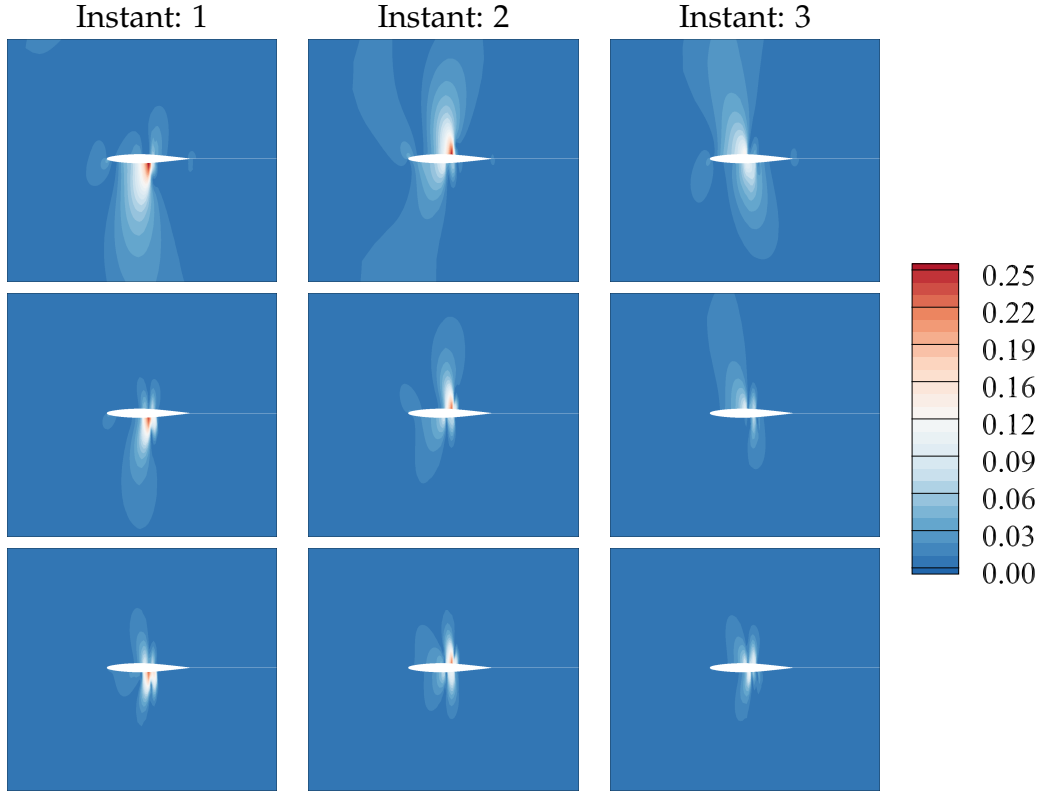


Figure 5.17 Density fields absolute difference between the reference ROTSM and the adapted ROTSM density fields at the 3 time instances for $M_\infty = 0.78$: on the first line with GPOD, on the second line with truncated GPOD and on the third line with the interpolated basis on a tangent space of the Grassmann manifold.

	Instant 1		Instant 2		Instant 3	
	ε	max err	ε	max err	ε	max err
GPOD	53.49	0.26	59.06	0.26	38.19	0.13
Truncated GPOD	96.30	0.24	104.08	0.22	91.4	0.1
Grassmann manifold	45.0	0.22	47.06	0.22	35.72	0.13

Table 5.2 Sum of the absolute density error and max absolute error over the entire mesh for the different basis adaptation approaches for the 3 different instances of the TSM for the case at $M_\infty = 0.78$.

5.5 Conclusions

This chapter has addressed the problem of long term stability related to nonlinear projection-based ROMs from a different point of view with respect to the stabilization techniques available in literature.

With the hypothesis of periodicity of the system at a given frequency, the Time Spectral Method exploits such characteristic of the flow by expressing the conservative variables as Fourier series in time with spatially varying coefficients. The reduced order counterpart (ROTSM) of this spectral method has been formulated and it presents the following main features:

- the method is a priori stable as a result of the formulation at the basis of the TSM;
- the solution is sought in a subspace that is a priori suitable as a result of the POD;
- the computational complexity of the resolution is considerably reduced with respect to its full order counterpart.

Then, the ROTSM is tested on the configuration of a moving airfoil in transonic conditions. The simulation of moving shocks with nonlinear ROMs is challenging and the proposed approach has led to accurate results.

Finally, a parametric investigation with respect to Mach variations related to different regimes of the flow has been addressed. For this purpose, three different POD basis interpolation techniques have been employed and compared. The results showed accurate results for subsonic regimes while for transonic regimes, characterized by moving discontinuities, the accuracy is gradually deteriorated. However, the presented method can be further improved, for example for the interpolation techniques adopted to compute the POD basis for a new parameter of investigation. For this reason, the presented results together with the further potential improvements are encouraging to keep studying the new approach formulated in this chapter.

Conclusions and perspectives

This thesis has provided a contribution to the development of model order reduction techniques to reduce the computational complexity of high-dimensional aeroelastic models. Indeed, when dealing with high-fidelity fluid-structure interaction problems, the resolution of the unsteady Navier-Stokes (or Euler) equations, involving a large number of degrees of freedom, is required. In the context of aeroelastic investigations (e.g. flow induced vibrations), such high-fidelity simulations require to be accomplished systematically resulting in a prohibitive (and often unaffordable) computational cost. Thus, the main objective of this thesis has been to construct a ROM for the Navier-Stokes equations taking into account moving and/or deforming meshes.

In Chapter 1 of this dissertation, a study about the current state of the art in the field of nonlinear ROM for fluid-dynamics, with a focus on fluid-structure applications, has been conducted. It has been observed that the nonlinear ROMs based on discrete Galerkin projection and POD are still of remarkable interest in this application scenario. They seek an approximated solution in the low-dimensional subspace, computed through the POD, which captures the dominant physical behavior of the system. However, when dealing with this kind of ROMs, some problems have been identified. They involve: the computation of non-polynomial nonlinearities arising from the compressible Navier-Stokes formulations; the additional complexity related to the treatment of moving and/or deforming meshes; the lack of any guarantee of long-term stability of this kind of ROMs. These issues have been addressed gradually. In Chapter 2 the mathematical guidelines for the construction of a nonlinear projection-based ROM in a general framework have been presented. In Chapter 3 the reduction of the Navier-Stokes equations has been addressed with test cases (with fixed meshes) of increasing complexity. Firstly, the validation of the ROM has been performed on the classical configuration of the flow around a two-dimensional cylinder at $Re = 100$. Within this validation study, the different implementation steps of the nonlinear ROM based on the discrete Galerkin projection and POD have been examined. Then, the focus is placed on the treatment of the nonlinearity and in particular on the performance of the masked projection techniques. This kind of approaches approximates the nonlinear term by interpolating (or fitting) it on the basis of judiciously selected points of the computational domain. The different algorithms proposed in literature providing the interpolation (or fitting) points have been explored with different test cases involving the flow around a fixed two dimensional NACA 0012 airfoil at different angles of incidence and Reynolds numbers. However, the need of an increased number of interpolation (or fitting) points might imply the occurrence of stability and accuracy problems. Thus, a slight adaptation of such masked projection selection algorithms is proposed in order to overcome this issue. This has enabled the simulation of a non-

Chapter 5. Construction of a Reduced Order Time Spectral Model for the compressible ALE-based Navier-Stokes equations

linear ROM for the flow around a fixed two-dimensional NACA 0012 airfoil at high incidence. In Chapter 4, the nonlinear ROM, validated before for fixed meshes, has been adapted in the case of moving and/or deforming meshes. In particular, an Arbitrary Lagrangian-Eulerian formulation is required to solve the Navier-Stokes equations on a deforming spatial domain. Such a formulation results in a nonlinear non-autonomous system and so the nonlinear ROM developed in the previous chapter has required some adjustments. The moving domain affects also the classical spatial POD formulation requiring a particular precaution in order to perform an index-based POD formulation. More specifically, if the mesh is moving and/or deforming during the simulation the spatial correlation at the basis of the classical POD formulation is lost. However, if the mesh index numbering does not change during the simulation, the POD can be computed on the basis of an index correlation and the resulting POD modes are no longer ‘spatial’, but rather ‘index’ modes. It has been observed that such an index-based formulation is also suitable for the masked projection approaches investigated previously for the case of fixed meshes. The vortex-shedding phenomenon, related to the flow around a two-dimensional cylinder in forced oscillatory vertical motion, has been investigated for two different values of amplitude and frequency of oscillation. In particular, the case at highest amplitude and frequency of oscillation, being the most challenging, has emphasized the relevance and the benefit of the adapted masked projection selection algorithms provided in the previous chapter. Then, a strategy to perform a parametric study with respect to the parameters involved in the description of the structural motion is proposed and tested. In the final part of this chapter, a preliminary study about the coupling of the nonlinear ROM with a structural model is performed. The objective has been to construct a reduced order fluid-structure interaction model. The investigated configuration is represented by a two-dimensional cylinder immersed in a uniform flow. The cylinder is free to perform oscillations perpendicular to the direction of the far-field fluid flow. Albeit preliminary, the results are promising. However, in this coupled scenario some limitations have emerged: from one side, the use of a *weak coupling* together with an explicit time integrator can potentially imply a dissipation which negatively affects the results, while, on the other side, the masked projection approaches have demonstrated their limitations leading to a significant inaccuracy. More specifically, the number of interpolation points, required to obtain an acceptable level of accuracy, is comparable to the number of degrees of freedom of the system and this impairs the benefit accruing to the masked projection approaches. The proposed coupling method and reduced order fluid-structure interaction model, being the last development of the thesis, still require further analyses and improvements, including the investigation of their robustness, sensitivity and stability. In Chapter 5, the problem of long-term stability related to the projection-based nonlinear ROMs is addressed. An alternative technique to tackle these issues has been proposed. Given the periodicity at a given frequency of the solution, the proposed alternative model aims to exploit such an hypothe-

5.5. Conclusions

sis at the FOM level by using the Time Spectral Method (TSM). This method consists in the use of a Fourier representation with N harmonics for the time evolution of the system so that the periodicity is directly enforced. Then, casting back the equations into the time domain, the time derivative appears as a high-order central difference formula coupling a set of $2N + 1$ steady equations related to different instances corresponding to a uniform sampling of the time period. The reduced order counterpart (ROTSM) is formulated by using a POD basis in order to improve the convergence properties and the computational complexity. The computational gain has been shown with respect to two different test cases involving the transonic inviscid flow around an oscillating NACA 64A010 airfoil with up to 3 harmonics for the Fourier series truncation. It has been observed that in order to adapt such a method for a new configuration parameter, the POD basis must be adapted. Hence, the proposed method is also suitable for the application of the different POD basis interpolation algorithms available in literature. A parametric study with respect to Mach number variations has been performed with a comparison between three different interpolation techniques. The range of variation of the Mach number involves subsonic and transonic regimes, which increases the complexity of the parametric investigation. Globally, the results have shown accurate results for subsonic flow regimes while for transonic flow regimes, characterized by moving discontinuities, the accuracy is gradually deteriorated. Moreover, it has been observed that the best performance has been obtained with the use of the POD basis interpolation on a tangent space to the Grassmann manifold.

In summary, the potential of the projection-based ROMs via Galerkin projection and POD basis for application with moving and deforming meshes has been demonstrated on test cases involving the rigid movement of a cylinder immersed in a uniform flow. In this application scenario, the different masked projection approaches have been explored and a slight adaptation has been necessary to reproduce the FOM with an acceptable accuracy. A parametric problem with respect to the parameters involved in the description of the structural motion has also been approached and has shown promising results. This dissertation provides also an alternative formulation, the ROTSM, for a nonlinear ROM for periodic flows that is *a priori* immune to long-term stability problems. Although it is not the only approach of its type with respect to the literature, to the knowledge of the author, the ROTSM is the first approach based on the TSM that has enabled a parametric study by using the interpolation POD basis techniques.

From a computational complexity point of view, it is worth noting that this dissertation does not provide any comparison of wall-clock computational time between the FOM and the involved ROM. Indeed, most of the time, for example, a comparison between the number of degrees of freedom involved in the model and the time step of the time integration have been argued to justify the computational gain related to the use of the ROM with respect to the FOM counterpart. Indeed, from a computing point of view, the work presented in this thesis has been devel-

Chapter 5. Construction of a Reduced Order Time Spectral Model for the compressible ALE-based Navier-Stokes equations

oped in *Python* language and some critical issues have been found in the interface between the ROM and the FOM. For example the evaluation of the nonlinear term, required by the ROM, via the FOM is subjected to systematic operations of *writing* and *reading* of files that are obsolete and time consuming. Also, in the computation of the nonlinear term for some isolated cells of the domain, a moderate level of intrusiveness into the FOM flow solver must be provided and it has not been considered of primary interest for this dissertation. A further computing development effort for a complete and optimized interface between ROM and FOM shall be provided in order to be able to compare the wall-clock time gain related to the proposed ROMs.

To conclude this dissertation, the following key open issues and areas of future research are proposed in the view of improving and promoting the construction of reduced order model for the compressible Navier-Stokes equations for aeroelastic applications:

- **the use of additional techniques to enhance the performance of masked projection approaches:** when dealing with complex and nonlinear cases, e.g. a coupled fluid-structure system, it has been shown that the masked projection approaches can be affected by accuracy problems and fail. In this context, alternative techniques can be explored to improve the performance of masked projection approaches. For example the technique proposed by de Pando *et al.* [25] requires the use of the Jacobian to complement the masked projection approaches. More specifically, in this dissertation the whole right-hand-side of the Navier-Stokes equations has been approximated via masked projection approaches. Instead, de Pando *et al.* [25] propose to approximate the linear part of the right-hand-side of the Navier-Stokes equations by using the Jacobian operator and therefore only the strictly nonlinear dynamics will be computed via the masked projection approaches. Alternatively, also other techniques based on data assimilation or machine learning algorithms [35], [140], [141] are of great interest in this context to complement the masked approaches when the discrepancy in the solution becomes important.
- **take into account a deforming structure:** considering the encouraging results for the test cases of a cylinder in rigid motion, it would be interesting, for example, to take into account also structural deformation of the cylinder. The deformation of the structure might imply an important volume variation of the cells in the proximity of the cylinder and therefore the source term of eq.(4.6) can no longer be neglected.
- **integration of the ROM in a decoupled system for more realistic text cases:** given the encouraging results when considering the flow around a cylinder

5.5. Conclusions

in forced vertical motion, it would be interesting to extend the ROM within a decoupled frequency-domain nonlinear harmonic method. In this decoupled approach, the nonlinear ROM for the fluid is solved with respect to each natural vibration mode of the structure separately and the resulting aerodynamic forces are subsequently integrated in the modal dynamical equation.

- **integration of the ROM in a fully coupled system:** the implementation of an implicit integrator for the nonlinear ROM with a more suitable *strong* coupling strategy could be addressed in order to pursue the preliminary investigation for a fully coupled fluid-structure ROM of Chapter 4.
- **comparison and improvements of the POD bases interpolation techniques:** starting from the literature [38], [69], [82]–[89], a study about the improvement of the bases interpolation or bases clustering techniques could be performed in order to enhance the performance of the parametric ROTSM in transonic regimes. For example it should be interesting to investigate the approach, recently proposed by Mosquera *et al.* [89], about the adaptation of the interpolation on a tangent space to the Grassmann manifold by using the Inverse Distance Weighting (IDW). The advantages of such an approach is to overcome the choice of a reference point on the Grassmann manifold which is arbitrary and could affect the performance of the POD basis interpolation.

Appendices

Preliminary investigation of a Reduced Order Model for the URANS formulation of the Navier-Stokes equations

The domain of projection-based ROMs for aerodynamics provides a large number of possibilities to reduce the computational cost of the Navier-Stokes equations in different flow configurations. URANS equations for turbulent cases represent a very challenging scenario for the application of projection-based ROMs. Nevertheless, to date, there is not any exhaustive study that investigates the applicability of this kind of ROM for the URANS equations. At first sight, one can suggest to construct a ROM for the URANS formulation simply adding the turbulent variables to the state vector and projecting the system of Navier-Stokes and turbulent equations entirely. In such a case, the ROM used so far does not require any adaptation and could be applied directly. However, all the conducted tests failed in a preliminary stage. The dynamics governing the amplitudes of the turbulent variables modes is very complex and different with respect to the conservative variables dynamics leading the ROM to divergence. This suggests to investigate an appropriate and separate model for the eddy viscosity to be integrated into the nonlinear ROM constructed in Chapter 2. The precursor of this kind of model is considered a constant eddy viscosity fixed at the average value on the sampling time period Placzek [142].

The simulation which represents the FOM is a two-dimensional flow around a NACA 0012 airfoil at incidence $\alpha = 20^\circ$. The flow parameters are $Re = 20000$ and $M = 0.5$ and the turbulence model $k - \omega$ proposed by Menter [143] is employed¹. The industrial finite volume solver *elsA* [123] is used for the FOM simulation. Three instantaneous snapshots of the flow field are shown in Fig.A.1.

The ROM presented in Chapter 3 is integrated over a vortex shedding cycle with a constant eddy viscosity fixed at the average value on the sampling time period. The 4th order Runge-Kutta explicit time integrator is used. Firstly, no masked projection is employed in order to avoid the related additional approximation. For this preliminary test, the ROM is integrated for the vortex shedding cycle and the absolute

¹This configuration represents just a preliminary test case to test the method and its physical meaning is not in question.

Appendix A. Preliminary investigation of a Reduced Order Model for the URANS formulation of the Navier-Stokes equations

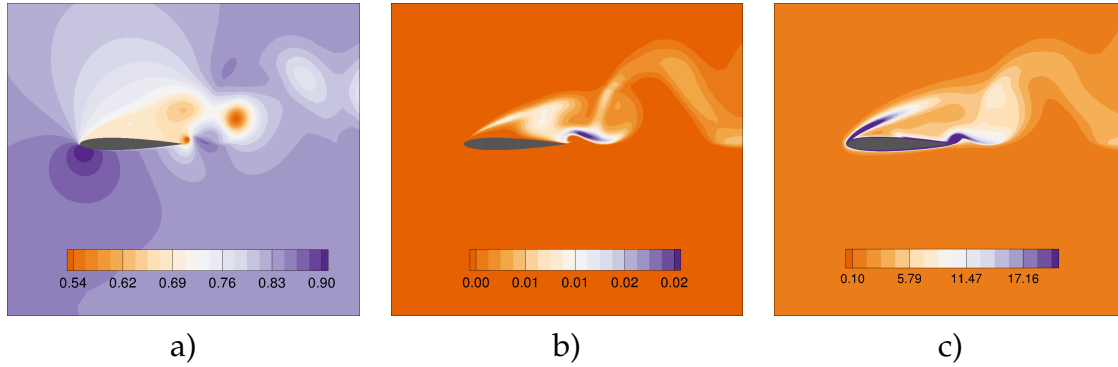


Figure A.1 Instantaneous snapshots of the field of an URANS simulation of a flow around a NACA-0012 airfoil at $\alpha = 20^\circ$, $Re = 20000$ and $M = 0.5$, using the $k - \omega$ turbulent model: a) density field, b) ρk field, c) $\rho \omega$ field.

error on the amplitudes related to the POD modes between the FOM and the ROM is depicted in Fig.A.2 for different sizes of the POD basis. The use of 4 modes implies an important error in particular for the 3-rd and 4-th amplitude. Then, by using 8, 12 and 20 modes the error decrease monotonically. In Fig.A.3, the trends of the force coefficients for different sizes of the POD basis are depicted and a small discrepancy is detected in each cases. Moreover, the slight error on the amplitudes with respect to different POD basis sizes showed before, does not reflects on the prediction of the aerodynamic force coefficients.

Finally, a study is performed by using 12 POD modes and the DEIM masked projection approach with 20 nonlinear modes in order to investigate the influence of the time-step on the ROM performance. Different simulations have been performed with different time-steps for the ROM integration being multiples of the FOM time-step δt . In Fig.A.4, the time averages for the absolute value of the error between the POM amplitudes are plotted. Globally, switching from $8\delta t$ towards $4\delta t$, the error decreases as a smaller time-step is used. In contrast, it is interesting to note that, by reducing again the time-step from $4\delta t$ to $2\delta t$ or $1\delta t$, the error tends to increase. In this case, the use of a very small time-step, even though it is a benefit when using an explicit time integrator, involves the computation of the masked projection interpolation for a higher number of times for a single integration. This results in an increasing approximation error which accumulates more frequently over the time integration. In such a case, the time-step must be chosen as a compromise to take into account this counterintuitive behavior.

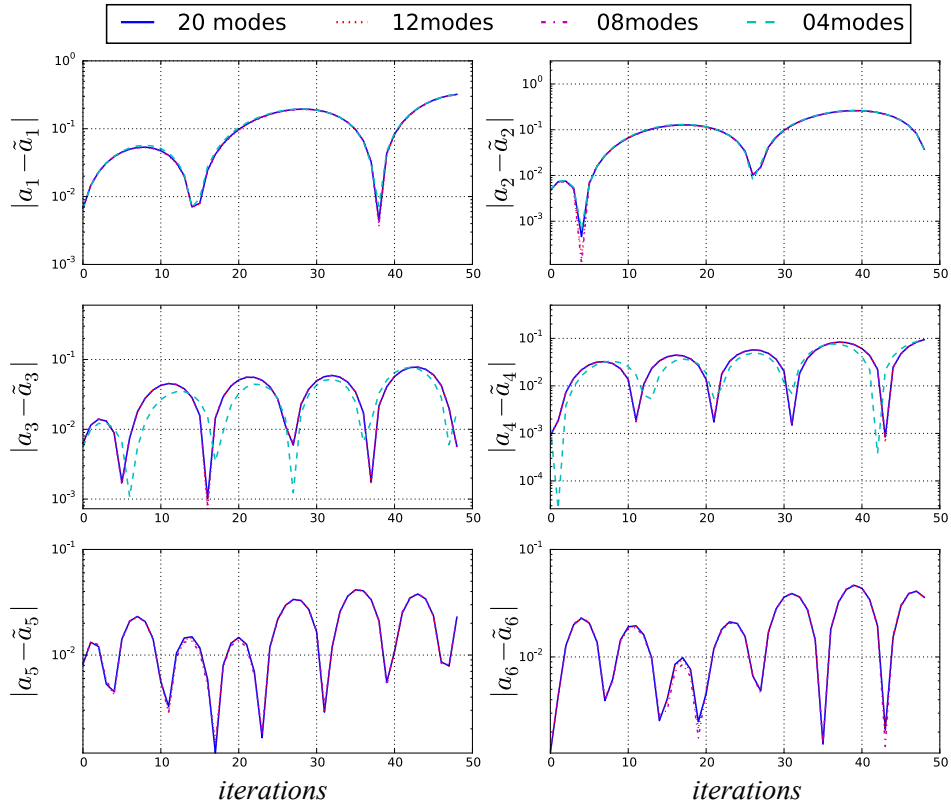


Figure A.2 Absolute error on the amplitudes related to the POD modes between FOM simulation and the ROM using a constant average eddy viscosity: flow around a NACA-0012 airfoil at $\alpha = 20^\circ$, $Re = 20000$ and $M = 0.5$, using the $k - \omega$ turbulent model.

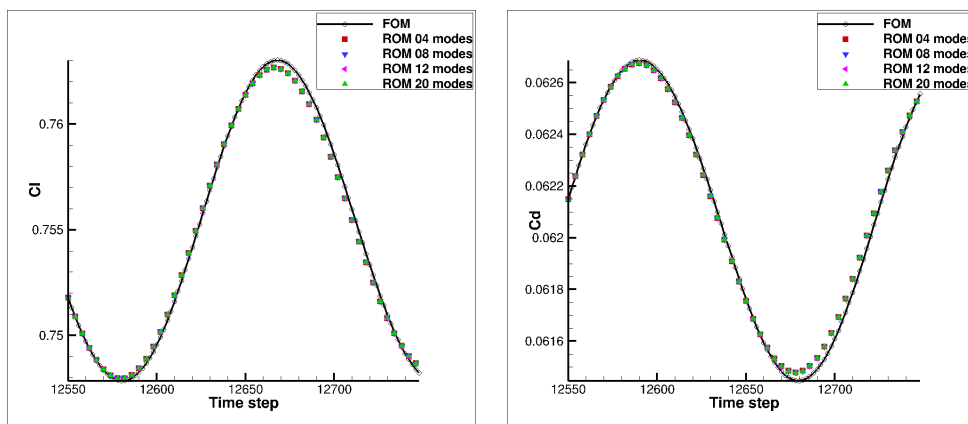


Figure A.3 Aerodynamic force coefficients for a flow around a NACA-0012 airfoil at $\alpha = 20^\circ$, $Re = 20000$ and $M = 0.5$, using the $k - \omega$ turbulent model: comparison between FOM simulation and the ROM using a constant average eddy viscosity.

Appendix A. Preliminary investigation of a Reduced Order Model for the URANS formulation of the Navier-Stokes equations

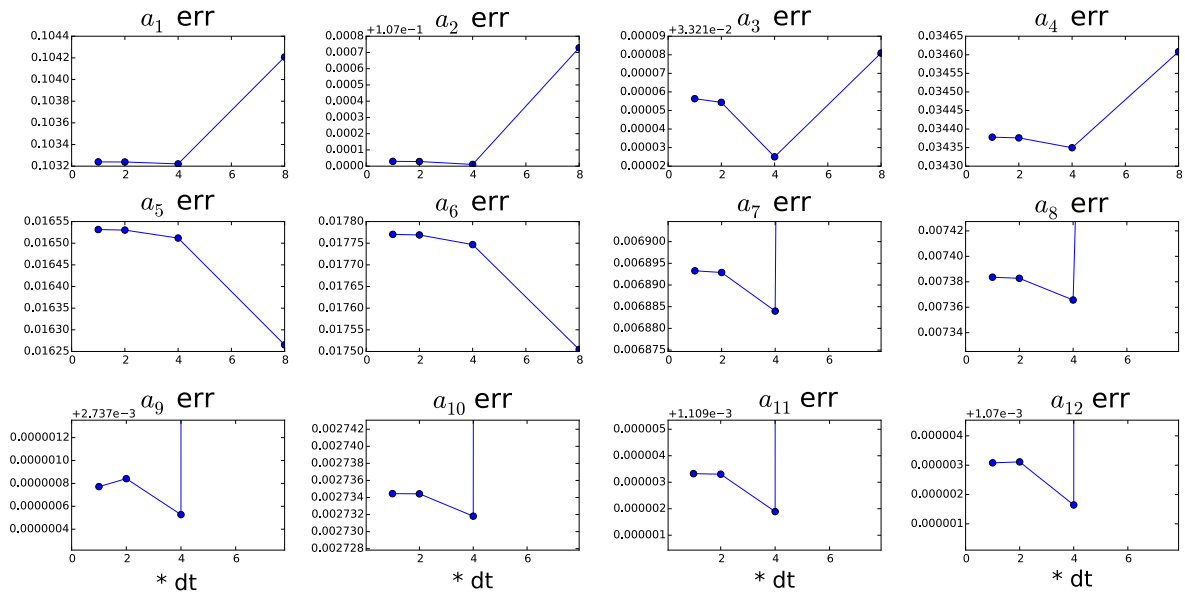


Figure A.4 Absolute error on the amplitudes related to the POD modes between FOM simulation and the ROM using a constant average eddy viscosity: flow around a NACA-0012 airfoil at $\alpha = 20^\circ$, $Re = 20000$ and $M = 0.5$, using the $k - \omega$ turbulent model.

Integration of a projection-based ROM for the subsonic Euler equations

In this section, the nonlinear ROM presented in Chapter 3 is adapted and integrated for the inviscid Navier-Stokes equations (Euler equations). A finite volume solver for the Euler equations is used as FOM. The studied configuration is the inviscid flow around an oscillating NACA 0012 airfoil under a prescribed harmonic pitch motion. The motion is sinusoidal with an angle of attack defined by the function

$$\alpha(t) = \alpha_0 + \hat{\alpha} \sin(\omega t) \quad (\text{B.1})$$

where $\alpha_0 = 0.016^\circ$ is the mean angle of attack and $\hat{\alpha} = 2.51^\circ$ is the amplitude of the pitch motion. The flow parameters are those of the reference CT5 [144] except for the Mach number set to $M = 0.5$. Under these conditions the reduced frequency is $\kappa = \omega c / 2U_\infty = 0.125$. A sampling of 1000 snapshots over a cycle of oscillation is employed in order to construct the POD basis for the flow solution and for the nonlinear residual term. The energy distribution of the solution POD modes is plotted in Fig. B.1. The value of $E_{N_m} = \sum_{i=1}^{N_m} \sigma_i / \sum_{i=1}^{N_r} \sigma_i$ for $N_m = 10$ is already over 0.9999. The first 2 density POD modes are depicted in Fig. B.2. The ROM is integrated using the DEIM and the QDEIM as masked projection techniques.

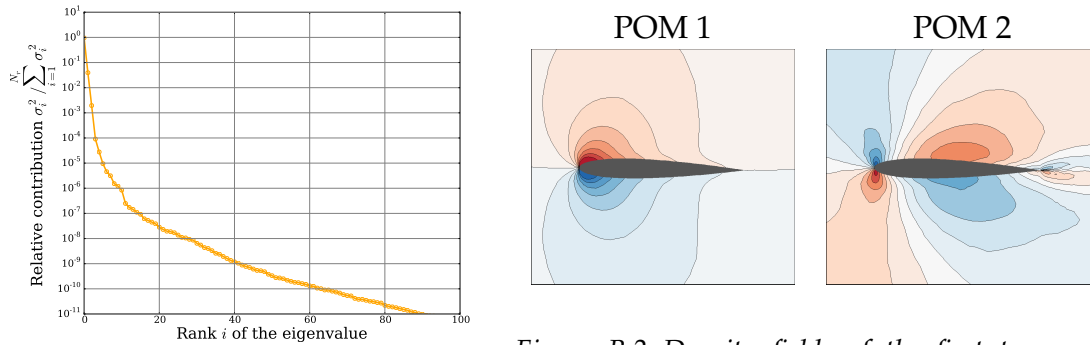


Figure B.1 Proper orthogonal eigenvalue proper orthogonal modes (POMs) for the inviscid flow of the reference CT5 [144].

Figure B.2 Density fields of the first two proper orthogonal modes (POMs) for the inviscid flow of the reference CT5 [144].

The test case is apparently not challenging, considering the moderate reduced frequency κ and the regular structures of the POD modes. Nevertheless, using from 5 to 40 non-linear POD modes and the DEIM/QDEIM as masked projection, the ROM has always diverged before the end of the first cycle. Then, the ROM is integrated without using any kind of masked projection. In such a case, the ROM is

Appendix B. Integration of a projection-based ROM for the subsonic Euler equations

integrated successfully for the oscillation cycle but the efficiency is compromised. However, the ROM always diverges when the long term stability (beyond the time sampling interval) is investigated. In Fig. B.3 the evolution of the amplitudes related to first 3 (and most energetic) modes is shown. It can be seen that after the first oscillation cycle the ROM diverges after few iterations.

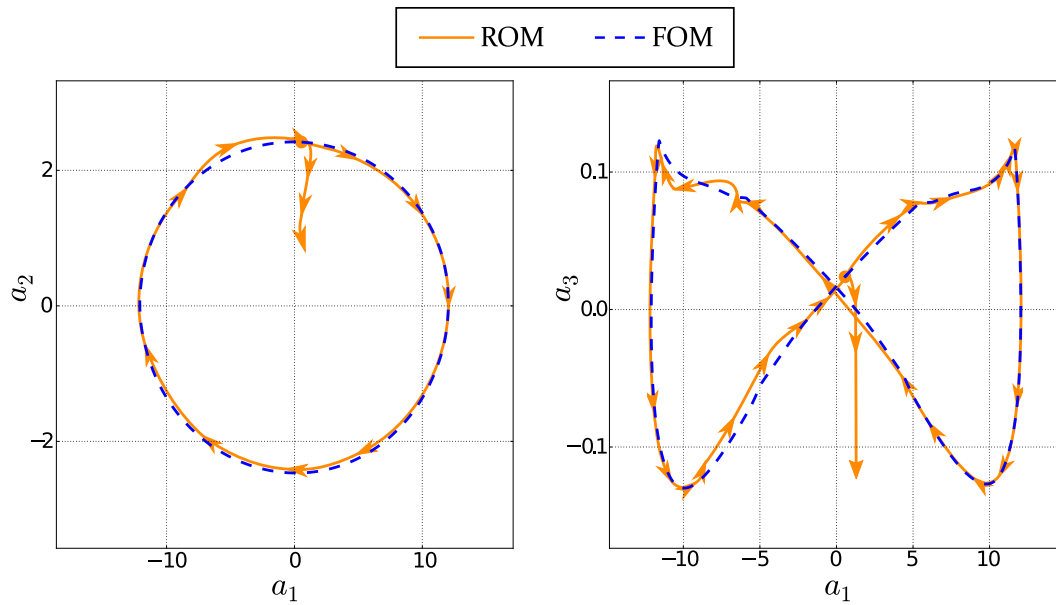


Figure B.3 Comparison of the first 3 modal coordinates \mathbf{a}_i computed as the solution of the projection based ROM and of the reference modal coordinates for the test case defined in reference CT5 [144].

Bibliography

- [1] A. Forrester, A. Sobester, and A. Keane, *Engineering design via surrogate modelling: A practical guide*. Wiley, Jul. 2008.
- [2] L. Le Gratiet, “Multi-fidelity Gaussian process regression for computer experiments”, PhD Thesis, Université Paris-Diderot - Paris VII, 2013.
- [3] C. Durantin, J. Rouxel, J.-A. Désidéri, and A. Glière, “Multifidelity surrogate modeling based on radial basis functions”, *Structural and Multidisciplinary Optimization*, vol. 56, no. 5, pp. 1061–1075, 2017.
- [4] A. Antoulas, *Approximation of large-scale dynamical systems.*: Society for Industrial and Applied Mathematics, 2005.
- [5] K. Taira, S. L. Brunton, S. T. M. Dawson, C. W. Rowley, T. Colonius, B. J. McKeon, O. T. Schmidt, S. Gordeyev, V. Theofilis, and L. S. Ukeiley, “Modal analysis of fluid flows: An overview”, *AIAA Journal*, vol. 55, no. 12, pp. 4013–4041, 2017.
- [6] K. Taira, M. S. Hemati, S. L. Brunton, Y. Sun, K. Duraisamy, S. Bagheri, S. T. M. Dawson, and C.-A. Yeh, “Modal analysis of fluid flows: Applications and outlook”, *AIAA Journal*, pp. 1–25, 2019.
- [7] A. Towne, O. T. Schmidt, and T. Colonius, “Spectral Proper Orthogonal Decomposition and its relationship to Dynamic Mode Decomposition and resolvent analysis”, *Journal of Fluid Mechanics*, vol. 847, pp. 821–867, 2018.
- [8] J. L. Lumley, “The Structure of Inhomogeneous Turbulent Flows”, *Atmospheric turbulence and radio propagation*, A. M. Yaglom and V. I. Tatarski, Eds., pp. 166–178, 1967.
- [9] L. Sirovich, “Turbulence and the dynamics of coherent structures. I - Coherent structures. II - Symmetries and transformations. III - Dynamics and scaling”, *Quarterly of Applied Mathematics*, vol. XLV, Oct. 1987.
- [10] I. Kalashnikova and M. F. Barone, “On the stability and convergence of a galerkin reduced order model (ROM) of compressible flow with solid wall and far-field boundary treatment”, *International Journal for Numerical Methods in Engineering*, vol. 83, no. 10, pp. 1345–1375, 2010.
- [11] I. Kalashnikova, M. F. Barone, S. Arunajatesan, and B. G. van Bloemen Waanders, “Construction of energy-stable projection-based reduced order models”, *Applied Mathematics and Computation*, vol. 249, pp. 569–596, 2014.
- [12] K. Carlberg, M. F. Barone, and H. Antil, “Galerkin v. discrete-optimal projection in nonlinear model reduction”, *CoRR*, vol. abs/1504.03749, 2015.

-
- [13] A. Iollo, A. Dervieux, J.-A. Désidéri, and S. Lanteri, “Two stable POD-based approximations to the Navier-Stokes equations”, *Computing and Visualization in Science*, vol. 3, no. 1, pp. 61–66, 2000.
- [14] A. Iollo, S. Lanteri, and J.-A. Désidéri, “Stability properties of POD-galerkin approximations for the compressible Navier-Stokes equations”, *Theoretical and Computational Fluid Dynamics*, vol. 13, no. 6, pp. 377–396, 2000.
- [15] M. Kirby, “Minimal dynamical systems from PDEs using Sobolev eigenfunctions”, *Physica D: Nonlinear Phenomena*, vol. 57, no. 3, pp. 466–475, 1992.
- [16] D. Xiao, F. Fang, J. Du, C. Pain, I. Navon, A. Buchan, A. Elsheikh, and G. Hu, “Non-linear Petrov-Galerkin methods for reduced order modelling of the Navier-Stokes equations using a mixed finite element pair”, *Computer Methods in Applied Mechanics and Engineering*, vol. 255, pp. 147–157, Mar. 2013.
- [17] C. Leblond, C. Allery, and C. Inard, “An optimal projection method for the reduced-order modeling of incompressible flows”, *Computer Methods in Applied Mechanics and Engineering*, vol. 200, no. 33, pp. 2507–2527, 2011.
- [18] F. Sabetghadam and A. Jafarpour, “ α regularization of the POD-Galerkin dynamical systems of the Kuramoto–Sivashinsky equation”, *Applied Mathematics and Computation*, vol. 218, no. 10, pp. 6012–6026, 2012.
- [19] J. Östh, B. R. Noack, S. Krajnović, D. Barros, and J. Borée, “On the need for a nonlinear subscale turbulence term in POD models as exemplified for a high-Reynolds-number flow over an Ahmed body”, *Journal of Fluid Mechanics*, vol. 747, pp. 518–544, 2014.
- [20] B. Protas, B. R. Noack, and J. Östh, “Optimal nonlinear eddy viscosity in Galerkin models of turbulent flows”, *Journal of Fluid Mechanics*, vol. 766, pp. 337–367, 2015.
- [21] M. Balajewicz, E. Dowell, and I. Tezaur, “Minimal subspace rotation on the Stiefel manifold for stabilization and enhancement of projection-based reduced order models for the compressible Navier-Stokes equations”, *Journal of Computational Physics*, vol. 321, pp. 224–241, 2016.
- [22] J. Baiges, R. Codina, and S. Idelsohn, “Reduced-order subscales for pod models”, *Computer Methods in Applied Mechanics and Engineering*, vol. 291, Jan. 2014.
- [23] M. Bergmann, T. Colin, A. Iollo, D. Lombardi, O. Saut, and H. Telib, “Reduced Order Models at work”, in *Modeling, Simulation and Applications*, A. Quarteroni, Ed., vol. 9, Springer, 2013.
- [24] S. R. Reddy, B. A. Freno, P. G. Cizmas, S. Gokaltun, D. McDaniel, and G. S. Dulikravich, “Constrained Reduced-Order Models based on Proper Orthogonal Decomposition”, *Computer Methods in Applied Mechanics and Engineering*, vol. 321, pp. 18–34, 2017.

Bibliography

- [25] M. F. de Pando, P. J. Schmid, and D. Sipp, “Nonlinear model-order reduction for compressible flow solvers using the Discrete Empirical Interpolation Method”, *Journal of Computational Physics*, vol. 324, pp. 194–209, 2016.
- [26] G. Stabile and G. Rozza, “Finite volume pod-galerkin stabilised reduced order methods for the parametrised incompressible navier-stokes equations”, *Computers and Fluids*, vol. 173, pp. 273–284, 2018.
- [27] K. Carlberg, M. Barone, and H. Antil, “Galerkin v. least-squares Petrov–Galerkin projection in nonlinear model reduction”, *Journal of Computational Physics*, vol. 330, pp. 693–734, 2017.
- [28] D. Amsallem, M. J. Zahr, and C. Farhat, “Nonlinear model order reduction based on local reduced-order bases”, *International Journal for Numerical Methods in Engineering*, vol. 92, no. 10, pp. 891–916, 2012.
- [29] B. Galletti, A. Bottaro, C.-H. Bruneau, and A. Iollo, “Accurate model reduction of transient and forced wakes”, *European Journal of Mechanics*, vol. 26, pp. 354–366, 2007.
- [30] M. Couplet, C. Basdevant, and P. Sagaut, “Calibrated reduced-order POD-Galerkin system for fluid flow modelling”, *Journal of Computational Physics*, vol. 207, pp. 192–220, 2005.
- [31] R. Bourguet, M. Braza, A. Sevrain, and A. Bouhadji, “Capturing transition features around a wing by reduced-order modeling based on compressible Navier-Stokes equations”, *Physics of Fluids*, vol. 21, no. 9, Sep. 2009.
- [32] L. Cordier, B. Abou El Majd, and J. Favier, “Calibration of POD reduced-order models using Tikhonov regularization”, *International Journal for Numerical Methods in Fluids*, vol. 63, no. 2, pp. 269–296, May 2009.
- [33] X. Gloerfelt, “Compressible POD/Galerkin Reduced-Order Model of Self-Sustained Oscillations in a Cavity”, *Collection of Technical Papers - 12th AIAA/CEAS Aeroacoustics Conference*, vol. 1, May 2006.
- [34] S. Giere, T. Iliescu, V. John, and D. Wells, “SUPG reduced order models for convection-dominated convection-diffusion-reaction equations”, *Computer Methods in Applied Mechanics and Engineering*, vol. 289, pp. 454–474, 2015.
- [35] J.-C. Loiseau and S. L. Brunton, “Constrained sparse Galerkin regression”, *Journal of Fluid Mechanics*, vol. 838, pp. 42–67, 2018.
- [36] S. L. Brunton, J. L. Proctor, and J. N. Kutz, “Discovering governing equations from data by sparse identification of nonlinear dynamical systems”, *Proceedings of the National Academy of Sciences*, vol. 113, no. 15, pp. 3932–3937, 2016.
- [37] V. Shinde, E. Longatte, F. Baj, Y. Hoarau, and M. Braza, “A Galerkin-free model reduction approach for the Navier–Stokes equations”, *Journal of Computational Physics*, vol. 309, pp. 148–163, 2016.

-
- [38] M. Oulghelou and C. Allery, “Non intrusive method for parametric model order reduction using a bi-calibrated interpolation on the Grassmann manifold”, 2018. eprint: [1901.03177](#).
- [39] P. Astrid, S. Weiland, K. Willcox, and T. Backx, “Missing Point Estimation in Models Described by Proper Orthogonal Decomposition”, *IEEE Transactions on Automatic Control*, vol. 53, no. 10, pp. 2237–2251, 2008.
- [40] S. Sargsyan, S. L. Brunton, and J. N. Kutz, “Nonlinear model reduction for dynamical systems using sparse sensor locations from learned libraries”, *Phys. Rev. E*, vol. 92, p. 033304, 3 2015.
- [41] R. Zimmermann and K. Willcox, “An accelerated greedy missing point estimation procedure”, *SIAM J. Scientific Computing*, vol. 38, no. 5, A2827–A2850, 2016.
- [42] S. Chaturantabut and D. C. Sorensen, “Nonlinear Model Reduction via Discrete Empirical Interpolation”, *SIAM Journal on Scientific Computing*, vol. 32, no. 5, pp. 2737–2764, 2010.
- [43] M. Barrault, Y. Maday, N. C. Nguyen, and A. T. Patera, “An ‘empirical interpolation’ method: Application to efficient reduced-basis discretization of partial differential equations”, *Comptes Rendus Mathematique*, vol. 339, no. 9, pp. 667–672, 2004.
- [44] Z. Drmac and S. Gugercin, “A New Selection Operator for the Discrete Empirical Interpolation Method - improved a priori error bound and extensions”, *CoRR*, vol. abs/1505.00370, 2015.
- [45] B. Peherstorfer, Z. Drmač, and S. Gugercin, *Stabilizing discrete empirical interpolation via randomized and deterministic oversampling*, 2018. arXiv: [1808.10473 \[math.NA\]](#).
- [46] S. Sargsyan, S. L. Brunton, and J. N. Kutz, “Online interpolation point refinement for reduced order models using a genetic algorithm”, *SIAM J. Scientific Computing*, vol. 40, 2016.
- [47] G. Dimitriu, R. Ștefănescu, and I. M. Navon, “Comparative numerical analysis using reduced-order modeling strategies for nonlinear large-scale systems”, *Journal of Computational and Applied Mathematics*, vol. 310, pp. 32–43, 2017, Numerical Algorithms for Scientific and Engineering Applications.
- [48] J. Anttonen, P. King, and P. Beran, “POD-Based reduced-order models with deforming grids”, *Mathematical and Computer Modelling*, vol. 38, no. 1, pp. 41–62, 2003.
- [49] B. A. Freno, N. R. Matula, R. L. Fontenot, and P. G. Cizmas, “The use of dynamic basis functions in proper orthogonal decomposition”, *Journal of Fluids and Structures*, vol. 54, pp. 332–360, 2015.

Bibliography

- [50] G. C. Lewin and H. Haj-Hariri, “Reduced-Order Modeling of a Heaving Airfoil”, en, *AIAA Journal*, vol. 43, no. 2, pp. 270–283, Feb. 2005.
- [51] A. Placzek, “Construction de modèles d’ordre réduit non-linéaires basés sur la décomposition orthogonale propre pour l’aéroélasticité”, Thèse de doctorat dirigée par Ohayon, Roger Mécanique Paris, CNAM 2009, PhD thesis, 2009, 1 vol. (290 p.)
- [52] R. Bourguet, M. Braza, and A. Dervieux, “Reduced-order modeling of transonic flows around an airfoil submitted to small deformations”, *J. Comput. Phys.*, vol. 230, no. 1, pp. 159–184, Jan. 2011.
- [53] V. Troshin, A. Seifert, D. Sidilkover, and G. Tadmor, “Proper Orthogonal Decomposition of flow-field in non-stationary geometry”, *Journal of Computational Physics*, vol. 311, pp. 329–337, 2016.
- [54] E. Liberge and A. Hamdouni, “Reduced order modelling method via proper orthogonal decomposition (POD) for flow around an oscillating cylinder”, en, *Journal of Fluids and Structures*, vol. 26, no. 2, pp. 292–311, Feb. 2010.
- [55] A. Falaize, E. Liberge, and A. Hamdouni, “POD-based reduced order model for flows induced by rigid bodies in forced rotation”, *Journal of Fluids and Structures*, 2019.
- [56] E. Longatte, E. Liberge, M. Pomarede, J.-F. Sigrist, and A. Hamdouni, “Parametric study of flow-induced vibrations in cylinder arrays under single-phase fluid cross flows using POD-ROM”, *Journal of Fluids and Structures*, vol. 78, pp. 314–330, 2018.
- [57] W. Stankiewicz, M. Morzyński, R. Roszak, B. R. Noack, and G. Tadmor, “Reduced order modelling of a flow around an airfoil with a changing angle of attack”, *Archives of Mechanics*, vol. 60, no. 6, pp. 509–526, 2008.
- [58] W. Stankiewicz, R. Roszak, and M. Morzyński, “Arbitrary Lagrangian-Eulerian approach in reduced order modeling of a flow with a moving boundary”, P. Reijasse, D. Knight, M. Ivanov, and I. Lipatov, Eds., EDP Sciences, Jun. 2013, pp. 109–124.
- [59] B. A. Freno and P. G. Cizmas, “A proper orthogonal decomposition method for nonlinear flows with deforming meshes”, *International Journal of Heat and Fluid Flow*, vol. 50, pp. 145–159, Dec. 2014.
- [60] V. Shinde, E. Longatte, F. Baj, Y. Hoarau, and M. Braza, “Galerkin-free model reduction for fluid-structure interaction using proper orthogonal decomposition”, *Journal of Computational Physics*, vol. 396, pp. 579–595, 2019.
- [61] J. P. Thomas, E. H. Dowell, and K. C. Hall, “Using automatic differentiation to create a nonlinear reduced-order-model aerodynamic solver”, *AIAA Journal*, vol. 48, no. 1, pp. 19–24, 2010.

- [62] K. C. Hall, J. P. Thomas, and W. S. Clark, "Computation of unsteady nonlinear flows in cascades using a harmonic balance technique", *AIAA Journal*, vol. 40, no. 5, pp. 879–886, 2002.
- [63] G. Chen, Y. Zuo, J. Sun, and Y. Li, "Support-vector-machine-based reduced-order model for limit cycle oscillation prediction of nonlinear aeroelastic system", *Mathematical Problems in Engineering*, vol. 2012, Feb. 2012.
- [64] A. Mannarino and E. H. Dowell, "Reduced-Order Models for Computational-Fluid-Dynamics-based nonlinear aeroelastic problems", *AIAA Journal*, vol. 53, no. 9, pp. 2671–2685, 2015.
- [65] A. Mannarino and P. Mantegazza, "Nonlinear aerodynamic reduced order modeling by discrete time recurrent neural networks", *Aerospace Science and Technology*, vol. 47, pp. 406–419, 2015.
- [66] J. Kou and W. Zhang, "Layered reduced-order models for nonlinear aerodynamics and aeroelasticity", *Journal of Fluids and Structures*, vol. 68, pp. 174–193, 2017.
- [67] T. Bui-Thanh, K. Willcox, and O. Ghattas, "Parametric Reduced-Order Models for Probabilistic Analysis of Unsteady Aerodynamic Applications", *AIAA Journal*, vol. 46, no. 10, pp. 2520–2529, 2008.
- [68] C. Farhat and D. Amsallem, "Recent Advances in Reduced-Order Modeling and Application to Nonlinear Computational Aeroelasticity", *46th AIAA Aerospace Sciences Meeting and Exhibit*, 2008.
- [69] F. Vetrano, C. Garrec, G. Mortchelewicz, and R. Ohayon, "Assessment of strategies for interpolating pod based reduced order models and application to aeroelasticity", *Journal of Aeroelasticity and Structural Dynamics*, vol. 2, pp. 85–104, Jan. 2011.
- [70] T. Kim, "Parametric model reduction for aeroelastic systems: Invariant aeroelastic modes", *Journal of Fluids and Structures*, vol. 65, pp. 196–216, 2016.
- [71] M. Winter, F. M. Heckmeier, and C. Breitsamter, "CFD-based aeroelastic reduced-order modeling robust to structural parameter variations", en, *Aerospace Science and Technology*, vol. 67, pp. 13–30, Aug. 2017.
- [72] J. P. Thomas, E. H. Dowell, and K. C. Hall, "Three-Dimensional Transonic Aeroelasticity Using Proper Orthogonal Decomposition-Based Reduced-Order Models", en, *Journal of Aircraft*, vol. 40, no. 3, pp. 544–551, May 2003.
- [73] J. Anttonen, P. King, and P. Beran, "Applications of multi-POD to a pitching and plunging airfoil", *Mathematical and Computer Modelling*, vol. 42, no. 3-4, pp. 245–259, Aug. 2005.
- [74] M. A. Grepl and A. T. Patera, "A posteriori error bounds for reduced-basis approximations of parametrized parabolic partial differential equations", *ESAIM: M2AN*, vol. 39, no. 1, pp. 157–181, 2005.

Bibliography

- [75] J. Burkardt, M. Gunzburger, and H.-C. Lee, “Pod and cvt-based reduced-order modeling of navier–stokes flows”, *Computer Methods in Applied Mechanics and Engineering*, vol. 196, no. 1, pp. 337–355, 2006.
- [76] D. Amsallem, J. Cortial, and C. Farhat, “On-Demand CFD-Based Aeroelastic Predictions Using a Database of Reduced-Order Bases and Models”, *47th AIAA Aerospace Sciences Meeting including The New Horizons Forum and Aerospace Exposition*, 2009.
- [77] J. Eftang, D. Knezevic, and A. Patera, “An hp certified reduced basis method for parametrized parabolic partial differential equations”, *Mathematical and Computer Modelling of Dynamical Systems*, vol. 17, pp. 395–422, Jan. 2011.
- [78] A. Paul-Dubois-Taine and D. Amsallem, “An adaptive and efficient greedy procedure for the optimal training of parametric reduced-order models”, *International Journal for Numerical Methods in Engineering*, vol. 102, Sep. 2014.
- [79] S. Pagani, A. Manzoni, and A. Quarteroni, “Numerical approximation of parametrized problems in cardiac electrophysiology by a local reduced basis method”, *Computer Methods in Applied Mechanics and Engineering*, vol. 340, pp. 530–558, 2018.
- [80] E. Kaiser, M. Morzyński, G. Daviller, J. N. Kutz, B. W. Brunton, and S. L. Brunton, “Sparsity enabled cluster reduced-order models for control”, *Journal of Computational Physics*, vol. 352, pp. 388–409, 2018.
- [81] P. Benner, S. Gugercin, and K. Willcox, “A Survey of Projection-Based Model Reduction Methods for Parametric Dynamical Systems”, *SIAM Review*, vol. 57, no. 4, pp. 483–531, 2015.
- [82] A. Hay, J. Borggaard, and D. Pelletier, “Local improvements to reduced-order models using sensitivity analysis of the proper orthogonal decomposition”, *Journal of Fluid Mechanics*, vol. 629, pp. 41–72, 2009.
- [83] A. Hay, J. Borggaard, A. Imran, and D. Pelletier, “Reduced-order models for parameter dependent geometries based on shape sensitivity analysis of the pod”, *Journal of Computational Physics*, vol. 229, pp. 1327–1352, 2010.
- [84] M. Zahr and C. Farhat, “Progressive construction of a parametric reduced-order model for pde-constrained optimization”, *International Journal for Numerical Methods in Engineering*, vol. 102, Dec. 2014.
- [85] T. Lieu, C. Farhat, and M. Lesoinne, “Reduced-order fluid/structure modeling of a complete aircraft configuration”, *Computer Methods in Applied Mechanics and Engineering*, vol. 195, no. 41-43, pp. 5730–5742, Aug. 2006.
- [86] D. Amsallem, “Interpolation on manifolds of CFD-based fluid and finite element-based structural reduced-order models for on-line aeroelastic predictions”, PhD thesis, Stanford University, 2010.

-
- [87] B. Haasdonk, M. Ohlberger, and G. Rozza, “A Reduced Basis Method for evolution schemes with parameter-dependent explicit operators”, *Electronic Transactions on Numerical Analysis*, vol. 32, Jan. 2008.
- [88] T. Lassila, A. Manzoni, A. Quarteroni, and G. Rozza, “Generalized reduced basis methods and n-width estimates for the approximation of the solution manifold of parametric PDEs”, *Bollettino della Unione Matematica Italiana. Series IX*, vol. 1, Feb. 2013.
- [89] R. Mosquera, A. Hamdouni, A. el hamidi, and C. Allery, “POD basis interpolation via Inverse Distance Weighting on Grassmann manifolds”, *Discrete and Continuous Dynamical Systems-S*, vol. 12, pp. 1743–1759, Jan. 2018.
- [90] K. Kunisch and S. Volkwein, “Galerkin proper orthogonal decomposition methods for a general equation in fluid dynamics”, *SIAM Journal on Numerical Analysis*, vol. 40, no. 2, pp. 492–515, 2002.
- [91] A. Quarteroni, A. Manzoni, and F. Negri, *Reduced basis methods for partial differential equations: An introduction*. Jan. 2015, pp. 1–263.
- [92] L. Cordier and M. Bergmann, “Proper Orthogonal Decomposition: an overview”, in *Lecture series 2002-04, 2003-03 and 2008-01 on post-processing of experimental and numerical data*, VKI, 2008.
- [93] C. Airiau, “Active flow control of a two-dimensional compressible cavity flow using direct output feedback law”, Sep. 2013.
- [94] A. E. Deane, I. G. Kevrekidis, G. E. Karniadakis, and S. A. Orszag, “Low-dimensional models for complex geometry flows: Application to grooved channels and circular cylinders”, *Physics of Fluids A: Fluid Dynamics*, vol. 3, no. 10, pp. 2337–2354, 1991.
- [95] K. Carlberg, C. Farhat, J. Cortial, and A. D., “The GNAT method for nonlinear model reduction: Effective implementation and application to computational fluid dynamics and turbulent flows”, *Journal of Computational Physics*, vol. 242, pp. 623–647, 2013.
- [96] F. A. Lülfi, D.-M. Tran, H. G. Matthies, and R. Ohayon, “An integrated method for the transient solution of reduced order models of geometrically nonlinear structures”, *Computational Mechanics*, vol. 55, no. 2, pp. 327–344, 2015.
- [97] D. J. Lucia and P. S. Beran, “Projection methods for reduced order models of compressible flows”, *Journal of Computational Physics*, vol. 188, pp. 252–280, Jun. 2003.
- [98] P. Galan del Sastre and R. Bermejo, “Error estimates of proper orthogonal decomposition eigenvectors and Galerkin projection for a general dynamical system arising in fluid models”, *Numerische Mathematik*, vol. 110, no. 1, pp. 49–81, 2008.

Bibliography

- [99] S. Sirisup and G. E. Karniadakis, “A spectral viscosity method for correcting the long-term behavior of pod models”, *Journal of Computational Physics*, vol. 194, pp. 92–116, 2004.
- [100] K. Carlberg, C. Farhat, and C. Bou-Mosleh, “Efficient non-linear model reduction via a least-squares Petrov–Galerkin projection and compressive tensor approximations”, *International Journal for Numerical Methods in Engineering*, vol. 86, pp. 155–181, 2011.
- [101] N. Nguyen, A. T. Patera, and J. Peraire, “A ‘best points’ interpolation method for efficient approximation of parametrized function”, *International Journal for Numerical Methods in Engineering*, vol. 73, pp. 521–543, Jan. 2008.
- [102] A. Hochman, B. N. Bond, and J. K. White, “A stabilized discrete empirical interpolation method for model reduction of electrical, thermal, and microelectromechanical systems”, in *2011 48th ACM/EDAC/IEEE Design Automation Conference (DAC)*, Jun. 2011, pp. 540–545.
- [103] P. Tiso and D. J. Rixen, “Discrete Empirical Interpolation Method for Finite Element Structural Dynamics”, in *Topics in Nonlinear Dynamics, Volume 1*, G. Kerschen, D. Adams, and A. Carrella, Eds., New York, NY: Springer New York, 2013, pp. 203–212.
- [104] B. Peherstorfer, D. Butnaru, K. Willcox, and H. Bungartz, “Localized Discrete Empirical Interpolation Method”, *SIAM Journal on Scientific Computing*, vol. 36, no. 1, A168–A192, 2014.
- [105] A. Radermacher and S. Reese, “POD-based model reduction with empirical interpolation applied to nonlinear elasticity”, *International Journal for Numerical Methods in Engineering*, vol. 107, no. 6, pp. 477–495, 2016.
- [106] Y. B. Zhou, “Model reduction for nonlinear dynamical systems with parametric uncertainties”, Master’s thesis, 2012.
- [107] M. Drohmann, B. Haasdonk, and M. Ohlberger, “Reduced basis approximation for nonlinear parametrized evolution equations based on empirical operator interpolation”, *SIAM Journal on Scientific Computing*, vol. 34, no. 2, A937–A969, 2012.
- [108] X. Xie, M. Mohebujjaman, L. G. Rebholz, and T. Iliescu, “Data-driven filtered reduced order modeling of fluid flows”, *SIAM Journal on Scientific Computing*, vol. 40, 2017.
- [109] Z. Wang, A. Imran, J. Borggaard, and T. Iliescu, “Proper orthogonal decomposition closure models for turbulent flows: A numerical comparison”, *Computer Methods in Applied Mechanics and Engineering*, vol. 237, 2011.

- [110] D. Wells, Z. Wang, X. Xie, and T. Iliescu, “An evolve-then-filter regularized reduced order model for convection-dominated flows: Evolve-then-filter regularized reduced order model”, *International Journal for Numerical Methods in Fluids*, vol. 84, 2017.
- [111] K. Hall, J. Thomas, K. Ekici, and D. Voytovich, “Frequency domain techniques for complex and nonlinear flows in turbomachinery”, in *33rd AIAA Fluid Dynamics Conference and Exhibit*, 2012. eprint: <https://arc.aiaa.org/doi/pdf/10.2514/6.2003-3998>.
- [112] A. Gopinath and A. Jameson, “Time Spectral Method for Periodic Unsteady Computations over Two- and Three- Dimensional Bodies”, in *43rd AIAA Aerospace Sciences Meeting and Exhibit*, 2012.
- [113] —, “Application of the Time Spectral Method to Periodic Unsteady Vortex Shedding”, in *44th AIAA Aerospace Sciences Meeting and Exhibit*, 2012.
- [114] E. van der Weide, A. Gopinath, and A. Jameson, “Turbomachinery Applications with the Time Spectral Method”, in *35th AIAA Fluid Dynamics Conference and Exhibit*, 2012.
- [115] F. Sicot, G. Puigt, and M. Montagnac, “Block-jacobi implicit algorithms for the time spectral method”, *AIAA Journal*, vol. 46, no. 12, pp. 3080–3089, 2008.
- [116] S. Labit, “Formulations temporelle et fréquentielle pour la simulation numérique d’écoulements transsoniques en oscillations forcées”, PhD thesis, 2013.
- [117] J.-C. Chassaing, S. Khelladi, and X. Nogueira, “Accuracy assessment of a high-order moving least squares finite volume method for compressible flows”, *Computers & Fluids*, vol. 71, pp. 41–53, 2013.
- [118] V. Mons, J.-C. Chassaing, T. Gomez, and P. Sagaut, “Reconstruction of unsteady viscous flows using data assimilation schemes”, *Journal of Computational Physics*, vol. 316, pp. 255–280, 2016.
- [119] J. Favier, S. Orioux, and L. Cordier, “Accurate POD reduced-order models of massively separated flows”, in *IUTAM Symposium of Unsteady Separated Flows and their Control*, Corfu (Greece), 2007.
- [120] G. Kerschen and J.-C. Golinval, “Physical interpretation of the proper orthogonal modes using the singular value decomposition”, *Journal of Sound and Vibration*, vol. 249, pp. 849–865, 2002.
- [121] A. Iollo, S. Lanteri, and J.-A. Désidéri, “Stability properties of pod–galerkin approximations for the compressible navier–stokes equations”, *Theoretical and Computational Fluid Dynamics*, vol. 13, no. 6, pp. 377–396, 2000.
- [122] M. Couplet, P. Sagaut, and C. Basdevant, “Intermodal energy transfers in a proper orthogonal decomposition–galerkin representation of a turbulent separated flow”, *Journal of Fluid Mechanics*, vol. 491, pp. 275–284, 2003.

Bibliography

- [123] L. Cambier, S. Heib, and S. Plot, “The Onera elsA CFD software: Input from research and feedback from industry”, vol. 14, pp. 159–174, Jun. 2013.
- [124] F. Di Donfrancesco, A. Placzek, and J.-C. Chassaing, “A CFD supported reduced order model using a goal-oriented domain restriction”, in *Model Reduction of Parametrized Systems IV*, Nantes (France), Apr. 2018.
- [125] R. Bourguet, M. Braza, and A. Dervieux, “Reduced-order modeling for unsteady transonic flows around an airfoil”, *Physics of Fluids*, vol. 19, no. 11, p. 111701, 2007.
- [126] J. Donea, A. Huerta, J.-P. Ponthot, and A. Rodríguez-Ferran, “Arbitrary Lagrangian–Eulerian Methods”, in *Encyclopedia of Computational Mechanics*. American Cancer Society, 2004, ch. 14.
- [127] E. Guilmineau and P. Queutey, “a Numerical Simulation of Vortex Shedding from AN Oscillating Circular Cylinder”, *Journal of Fluids and Structures*, vol. 16, pp. 773–794, 2002.
- [128] A.-H. Pham, C.-Y. Lee, J.-H. Seo, H. Chun, K. Jung Hee, H.-S. Yoon, J.-H. Kim, D.-W. Park, and I. R. Park, “Laminar flow past an oscillating circular cylinder in cross flow”, *Journal of Marine Science and Technology*, vol. 18, Jun. 2010.
- [129] R. Schmit and M. Glauser, “Improvements in Low Dimensional Tools for Flow-Structure Interaction Problems: Using Global POD”, *42nd AIAA Aerospace Sciences Meeting and Exhibit*, 2004.
- [130] A. A. Shah, W. W. Xing, and V. Triantafyllidis, “Reduced-order modelling of parameter-dependent, linear and nonlinear dynamic partial differential equation models”, *Proceedings of the Royal Society A: Mathematical, Physical and Engineering Sciences*, vol. 473, no. 2200, 2017.
- [131] P. Anagnostopoulos and P. Bearman, “Response characteristics of a vortex-excited cylinder at low reynolds number”, *Journal of Fluids and Structures*, vol. 6, pp. 39–50, Jan. 1992.
- [132] W. Dettmer and D. Perić, “A computational framework for fluid–rigid body interaction: Finite element formulation and applications”, *Computer Methods in Applied Mechanics and Engineering*, vol. 195, no. 13, pp. 1633–1666, 2006, A Tribute to Thomas J.R. Hughes on the Occasion of his 60th Birthday.
- [133] O. San and T. Iliescu, “A stabilized proper orthogonal decomposition reduced-order model for large scale quasigeostrophic ocean circulation”, *Advances in Computational Mathematics*, vol. 41, no. 5, pp. 1289–1319, 2015.
- [134] A. Placzek, D.-M. Tran, and R. Ohayon, “A nonlinear POD-Galerkin reduced-order model for compressible flows taking into account rigid body motions”, *Computer Methods in Applied Mechanics and Engineering*, vol. 200, no. 49, pp. 3497–3514, 2011.

- [135] B. Peherstorfer and K. Willcox, “Data-driven operator inference for noninvasive projection-based model reduction”, *Computer Methods in Applied Mechanics and Engineering*, vol. 306, pp. 196–215, 2016.
- [136] M. Benosman, J. Borggaard, O. San, and B. Kramer, “Learning-based robust stabilization for reduced-order models of 2D and 3D Boussinesq equations”, *Applied Mathematical Modelling*, vol. 49, pp. 162–181, 2017.
- [137] J. Li and W. Zhang, “The performance of proper orthogonal decomposition in discontinuous flows”, *Theoretical and Applied Mechanics Letters*, vol. 6, no. 5, pp. 236–243, 2016.
- [138] S. S. Davis, “NACA 64A010 (NASA Ames model) oscillatory pitching”, *Technical report 702*, 1982.
- [139] C. Blondeau and C. Liauzun, “A Modular Time Spectral Implementation Method for Aeroelastic Analysis and Optimization on Structured Meshes International Forum on Aeroelasticity and Structural Dynamics Motivation”, in *International Forum on Aeroelasticity & Structural Dynamics*, Jun. 2019.
- [140] A. Mannarino and P. Mantegazza, “Nonlinear aerodynamic reduced order modeling by discrete time recurrent neural networks”, *Aerospace Science and Technology*, vol. 47, pp. 406–419, 2015.
- [141] K. Lee and K. Carlberg, “Model reduction of dynamical systems on nonlinear manifolds using deep convolutional autoencoders”, *CoRR*, vol. abs/1812.08373, 2018.
- [142] A. Placzek, “PR ARTIST : Non-linear ALE-based reduced-order model of the Navier-Stokes equations for aeroelasticity”, ONERA, Technical Report RT 4/22294, 2015.
- [143] F. R. Menter, “Two-equation eddy-viscosity turbulence models for engineering applications”, *AIAA journal*, vol. 32, no. 8, pp. 1598–1605, 1994.
- [144] R. H. Landon, “NACA 0012 Oscillatory and Transient Pitching”, *Technical report*, p. 16, Oct. 2000.

Bibliography
